SISSA
Scuola Internazionale Superiore di Studi Avanzati

Neuroscience Area – PhD course in

Neurobiology

Novel insights on the physiological roles of the Stomatin-like protein-3 and the Calcium-activated chloride channel TMEM16A in the mouse olfactory epithelium

Candidate:

Emilio Agostinelli

Advisor:

Prof. Simone Pifferi

Co-advisors:

Prof. Anna Menini

Academic Year 2019-20

Scuola Internazionale di Studi Avanzati
Trieste

Novel insights on the physiological roles of the Stomatin-like protein-3 and the Calcium-activated chloride channel TMEM16A in the mouse olfactory epithelium

Thesis submitted for the degree of "Doctor Philosophiae"
Academic Year 2019/2020

CANDIDATE
Emilio Agostinelli

SUPERVISOR
Prof. Simone Pifferi

CO-SUPERVISOR
Prof. Anna Menini

ABSTRACT

The possibility to perceive external stimuli from the surrounding environment to correctly interact with it has always represented a leading evolutionary drive for life as we know it today. The ancient sense of smell allows animals to locate food or mates and to escape from predators or hazardous, and it is dramatically important to control animal behaviour and survival. In most mammals, the main olfactory epithelium is the major intranasal system devoted to the discrimination of a plethora of chemical molecules called odorants.

The main olfactory epithelium is located within the nasal cavity, and it is a specialized pseudostratified columnar epithelium composed of different types of cells population. The olfactory sensory neurons and the supporting cells are the most abundant cells that detect odorant and preserve tissue integrity, respectively.

The mammals' olfactory sensory neurons are small bipolar neurons with a round cell soma, a long and unbranched axon, and a dendrite that projects toward the apical epithelial portion. From the ending of each dendrite called knobs, several immotile cilia protrude in the mucus layer that covers the olfactory epithelium. In these fine structures take place the olfactory transduction that starts with the binding of an odorant to a specific odorant receptor. This binding switch on the G_{olf} protein that in turn activates the adenylyl cyclase III. This produces an increase of ciliary cAMP that gates the CNG channels allowing the influx of sodium and calcium. The calcium eventually opens the calcium-activated chloride channel TMEM16B resulting into a chloride efflux that further contributes to depolarize the neuron.

Recently, it is emerging that other proteins could modulate the olfactory signalling cascade interacting with the well-known transduction machinery. There is evidence that some members of the stomatin family have a high expression rate in the main olfactory epithelium. Moreover, the proteins from the stomatin family are involved in the modulation of ion channels and transporters, and in the transduction pathways of other sensory systems as well.

Since it has been reported that the stomatin-like protein-3 (STOML-3) is highly expressed in the cilia of olfactory sensory neurons where the olfactory transduction takes place, we decided to investigate whether this member of the stomatin family could have a role also in the olfactory system signalling. To answer this question, we decided to take advantage of a well-characterized STOML-3 knock-out mouse model.

Firstly, we assessed if olfactory sensory neurons from STOML-3 KO mice had defects in their cilia or an altered rate of proliferation, using immunohistochemistry. Moreover, we studied if the transduction machinery is disrupted by the STOML-3 deletion looking at the expression level of the adenylyl cyclase III, CNGA2, and TMEM16B channels by western-blot assay and immunostaining. Our analysis did not reveal morphological alterations in olfactory sensory neurons lacking STOML-3. Furthermore, performing whole-cell voltage-clamp experiments, we recorded voltage-gated currents and resting membrane potentials of olfactory sensory neurons from STOML-3 KO mice, and we calculated their input resistance values. Again, we did not observe differences among olfactory sensory neurons from WT and KO mice.

Extracellular recordings achieved with the loose-patch technique revealed that the spontaneous firing is significantly lower in olfactory neurons in which STOML-3 has been deleted. Then, we tested if STOML-3 affects the olfactory transduction stimulating the olfactory sensory neurons with IBMX and odorants. Loose-patch experiments demonstrated that the olfactory response is significantly shorter in olfactory sensory neurons from STOML-3 KO mice. Altogether, these results indicate that STOML-3 contributes to the regulation of the olfactory signalling cascade. Other experiments are necessary to elucidate the role of STOML-3 in the olfactory system and to identify the molecular mechanisms underlying its activity.

The supporting cells are tightly packed apically in the main olfactory epithelium above the layer of the olfactory sensory neurons. They have a columnar cell body from which several microvilli protrude in the mucus layer, while a thin basolateral process extends to the basal membrane. Several essential functions for preserving the tissue physiology have been ascribed to supporting cells: endocytosis, metabolism of toxicants, mucus secretion, regulation of the extracellular ionic composition, and phagocytosis of dead cells.

By immunohistochemistry, our lab and others have recently reported that supporting cells of the olfactory epithelium express TMEM16A, a calcium-activated chloride channel. The TMEM16A channel is involved in the regulation of the extracellular ionic composition in many other epithelia, and it could play a similar role in the olfactory system.

We firstly investigated if the TMEM16A expression is restricted to supporting cells from a specific portion of the main olfactory epithelium. Immunohistochemical results confirmed that TMEM16A is preferentially expressed in supporting cells from a portion of the epithelium close to the respiratory epithelium, although it is also expressed in supporting cells from the dorsal part of the main olfactory epithelium even if with a lower expression rate. Furthermore, I tested the functional expression of the channel performing whole-cell patch-clamp experiments in acute coronal slices of the mouse olfactory epithelium both in the transition and in the dorsal zone. I measured dose-response relations at different intracellular calcium concentrations, tested the ion selectivity of the currents, and used a specific inhibitor of the TMEM16A channel. I found out that supporting cells express calcium-sensitive chloride currents with very similar properties to those of the currents mediated by the native TMEM16A channels. Moreover, the amplitude of the TMEM16A mediated current is significantly smaller in the dorsal zone when compared to that from the transition zone, confirming the immunohistochemical experiments that revealed a higher expression of TMEM16A in supporting cells from the transition part of the epithelium. Moreover, I did not record any current activated by intracellular calcium in supporting cells from TMEM16A KO mice. Altogether, these results demonstrate that the TMEM16A channel is functionally expressed in supporting cells.

It has been reported that supporting cells express P2Y purinergic receptors and that they have complex calcium signalling dynamics to a similar extent to that reported in glial cells. For these reasons, I also hypothesized that the TMEM16A channel could be involved in response to physiological stimuli in the olfactory system. Here, I showed that the external application of ATP leads to a PLC-mediated calcium release from the intracellular stores that is sufficient to trigger the activation of TMEM16A mediated currents in supporting cells. Future work will elucidate the physiological role of the TMEM16A channel in the main olfactory epithelium.

To conclude, these works provided novel insights into two proteins expressed in the most abundant cell populations of the main olfactory epithelium. STOML-3 is highly expressed in the cilia of olfactory sensory neurons, and TMEM16A is highly expressed in a subpopulation of supporting cells located close to the transition zone with the respiratory epithelium. We showed that STOML-3 affects the olfactory transduction by increasing both the spontaneous firing and the duration of odorants-evoked responses. We have provided evidence that the TMEM16A channel mediates calcium-activated chloride currents in supporting cells upon activation of their purinergic pathway.

All in all, the emerging picture from these results is that both STOML-3 and TMEM16A are important candidates for future investigations aimed to elucidate new aspects of the olfactory sensory transduction and the physiology of the olfactory epithelium.

Index:

List of abbreviations:

AC(s): adenylyl cyclase(s)
ACIII: adenylate cyclase – type III
ACE2: angiotensin-converting enzyme 2
ANO1: anoctamin 1 (see TMEM16A)
ANO2: anoctamin 2 (see TMEM16B)
ASIC(s): acid-sensing ion channel(s)
ATP: adenosine triphosphate
BK: large conductance calcium-activated potassium channels
CaCC(s): calcium-activated chloride channel(s)
cAMP: cyclic adenosine monophosphate
CFTR: cystic fibrosis transmembrane conductance regulator
CNG: cyclic nucleotide – gated ion channel
CNS: central nervous system
DOG-1: discovered on gastrointestinal stromal tumours protein 1 (see TMEM16A)
GBC(s): global basal cell(s)
GIST: gastrointestinal stromal tumours
GLUT-1: glucose transporter 1
G_{olf}: olfactory-specific guanosine triphosphate (GTP)-binding protein
GPCR(s): G protein-coupled receptor(s)
GTP: guanosine triphosphate
HBC(s): horizontal basal cell(s)
IP3: inositol (1,4,5)-trisphosphate
MEC-2: mechanosensory abnormality protein 2
MOE: main olfactory epithelium
NCKX4: potassium-dependent Na^+/Ca^{2+} exchanger 4
NGEP: novel gene expressed in prostate (another name of TMEM16G)
NKCC1: Na^+-K^+-$2Cl^-$ cotransporter 1
OB: olfactory bulb
OMP: olfactory marker protein
OR(s): olfactory receptor(s)
ORAOV2: oral cancer overexpressed 2
OS: olfactory system
OSN(s): olfactory sensory neuron(s)
PACAP: pituitary adenylate cyclase-activating polypeptide
PDE(s): phosphodiesterase(s)
PDE1C: Calcium/calmodulin-dependent 3',5'-cyclic nucleotide phosphodiesterase 1C
PDE4A: cAMP-specific 3',5'-cyclic phosphodiesterase 4A
PHB domain: prohibitin homology domain
PIP_2: phosphatidylinositol (4,5)-bisphosphate
SARS-CoV-2 virus: severe acute respiratory syndrome coronavirus clade 2
SC(s): supporting cell(s)
SCP-2: sterol carrier protein-2
SK: small conductance calcium-activated potassium channels
SPFH domain: stomatin, prohibitin, flotillin, HflK/HflC domain (see PHB)

SRO: stomatin-related olfactory protein; (see STOML-3)
STOM: stomatin
STOML-1: stomatin-like protein 1
STOML-2: stomatin-like protein 2
STOML-3: stomatin-like protein 3
TAOS-2: tumour-amplified and overexpressed sequence 2
TM(s): transmembrane domain(s)
TMEM16 family: transmembrane protein family 16, comprise calcium-activated chloride channels and lipid scramblases
TMEM16A: calcium-activated chloride channel belonging to the TMEM16 family
TMEM16B: calcium-activated chloride channel belonging to the TMEM16 family
TMPRSS2: transmembrane protease, serine 2
TRPC6: transient receptor potential cation channel, subfamily C, member 6,
UNC-24: uncoordinated protein 24
VNO: vomeronasal organ

INTRODUCTION

1. The sense of smell: an overview

The ability to sense and perceive chemical stimuli from the external environment – named chemosensation – is crucial for the survival of living beings. Locate foods and mating partners or escape from predators are just a few examples that highlight the importance of this ancient sense in preserving life (Mombaerts, 2004). Several species can discriminate among a plethora of structurally diverse molecules that influence behaviour and physiology (Ferrero and Liberles, 2010; Menini et al., 2004). In most mammals, this process takes place in the nasal cavity where volatile chemicals are detected by several intranasal systems (Menco and Morrison, 2003).

The sense of smell is a complex process that starts with the binding of an odorant molecule – generally a small volatile organic compound – to a specific odorant receptor (OR). The olfactory stimuli released in the external environment are a complex mixture of several odorants (Pifferi and Menini, 2015). Indeed, for example, Ohloff (1994) reported that a rose emits more than 200 different types of volatile compounds. To match this large diversity of chemicals around 1000 ORs are expressed in the rat olfactory mucosa (Buck and Axel, 1991). This high number of ORs genes is consistent also in other mammals. However, the percentage of functional genes differs from species to species. Indeed, rodents have around 1000 – 1200 functional genes, while primates, including humans, have only about 300 – 400 functional genes with the rest of the ORs sequences that are pseudogenes. The sub-genome of the olfactory system (OS) codifying for the ORs is by far the largest gene superfamily in a mammalian genome, and perhaps in any genome (Buck, 2000; Menco and Morrison, 2003; Mombaerts, 2004; Pifferi and Menini, 2015).

The ORs are members of a G protein-coupled receptors superfamily, and they share a similar structure with seven hydrophobic membrane-spanning regions. The ORs are abundantly expressed in specific structures of the olfactory sensory neurons (OSNs) called cilia (Figure 1). In these sub-compartmentalization units are also located other members of the transduction machinery converting a chemical stimulus in an electric signal that results in the generation of action potentials, as described later (see chapter 2.6.4; Menini et al., 2004).

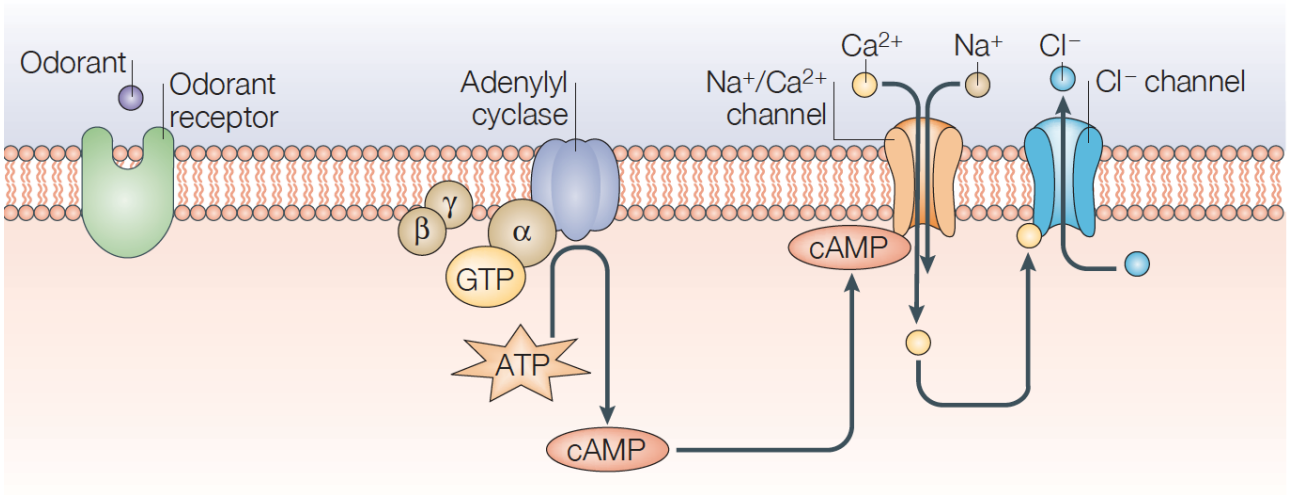

Figure 1: Olfactory transduction pathway in the cilia of the olfactory sensory neurons.

The olfactory transduction begins with odorant binding to an odorant receptor belonging the family of G-protein coupled receptors. The activation of an olfactory-specific G-protein activates an adenylate cyclase.

The resulting increase in cyclic AMP and the subsequent influx of Ca^{2+} open ion channels that permit OSNs' depolarization (image modified from Mombaerts, 2004).

Importantly, in situ hybridisation studies (Buck, 2000) and single-cell polymerase chain reaction analysis (Mombaerts, 1999) revealed that a single type of OR protein is expressed in each OSN, resulting in a better signal-to-noise ratio of the whole detection system (Mombaerts, 2004). One single odorant type could activate simultaneously different ORs. Vice versa, the same OR may be activated by several types of odorants. However, each specific odorant molecule can bind to only a unique combination of ORs. This combinatorial approach allows the OS to detect and discriminate among hundreds of thousands, if not millions of odorants (Buck, 2000; Menini et al., 2004; Mombaerts, 2004; Pifferi and Menini, 2015). Moreover, the OS can detect chemical molecules at very low concentration, and it can discriminate even small changes in the chemical structure of an odorant, being capable to distinguish the two different enantiomers of the same molecule (Pifferi and Menini, 2015).

The axons of the OSNs from the nasal cavity project to second-order neurons (mitral and tufted cells) in the olfactory bulb (OB). Axons of OSNs expressing a given OR gene project to few specific synaptic units called glomeruli. OR-specific glomeruli show a roughly symmetrical arrangement between the two halves (medial and lateral) of an OB (Figure 2). Each odorant activates a unique and specific combination of glomeruli in the OB. The convergence of axons into glomeruli provides the anatomical organisation for functional integration of sensory information codified by a specific OR (Menini et al., 2004; Mombaerts, 2004; Pifferi and Menini, 2015).

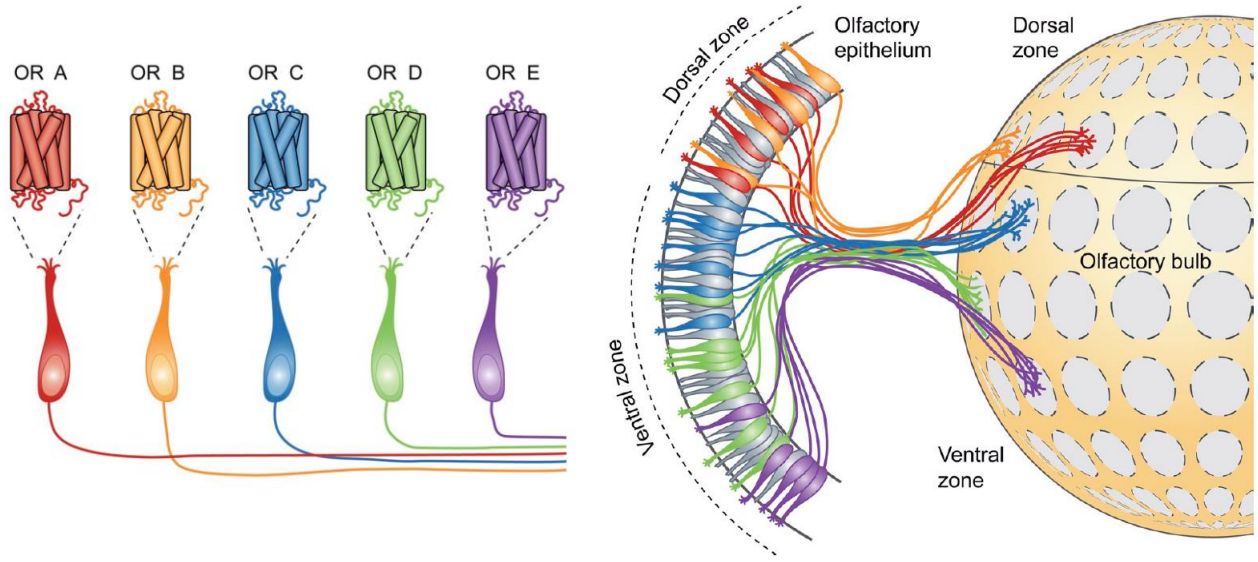

Figure 2: Glomerular organization of the olfactory bulb.

Examples of OSNs expressing different odorant receptor genes (OR A, OR B, OR C, etc.). Neurons expressing a given OR are broadly diffuse along the dorsal–ventral axis in the nasal cavity. Each OSN projects to a specific glomerulus at corresponding dorsal–ventral zones in the OB, accordingly to its OR expression. Each glomerulus thus receives innervation only from OSNs expressing the same OR (image modified from DeMaria and Ngai, 2010).

The glomeruli are the first relay station of the olfactory perception. Projections from the OB reach cortical neurons located in several anatomically distinct areas of the brain collectively named the primary

olfactory cortex, including the piriform cortex and the cortical amygdala. Moreover, each area of the olfactory cortex projects both to other cortical regions and the OB, allowing top-down modulation of these connections. Thanks to this neuroanatomical organisation, the olfactory perception is a highly regulated process that can interpret and integrate information from the binding of odorants to ORs with several other cortical processes, including learning, experience, expectations, attention, memory, and emotion (Chapuis and Wilson, 2011; Pifferi and Menini, 2015; Wilson, 2009).

2. The nasal cavity and the Main Olfactory Epithelium (MOE)

The nose is a complex organ in the upper part of the respiratory system, and it is composed of several structures that cooperatively cover various important functions. In mammals, it represents the primary site of access for inhaled air in the respiratory apparatus. The nose efficiently filters, warms, and humidifies the inhaled air to avoid trauma and severe irritation process in the more delicate distal tracheobronchial airways and alveolar parenchyma of the lung. However, the nose is not only an efficient "scrubbing tower" for the respiratory tract (Cole, 1993), but plays a leading role as the principal organ for the sense of smell (Harkema et al., 2006).

The odorants dissolved in the environmental air enter the nasal cavity during inspiration through the nostrils. This structure extends from the nostrils to the nasopharynx and is split into two symmetrical chambers with the same dimension by the nasal septum (Reznik, 1990). Several accessory structures are located in the nasal cavity: olfactory organs, nasopalatine ducts, nasolacrimal ducts, and paranasal sinuses (Alvites et al., 2018). In several mammals and especially in rodents, there are four olfactory organs (Figure 3): the main olfactory epithelium (MOE; Menco and Morrison, 2003; Moran et al., 1982) is the largest olfactory organ and is responsible for the discrimination of a large number of odorants (Getchell, 1986; Mombaerts, 2004); the vomeronasal organ (VNO; Døving and Trotier, 1998) that is involved with the intraspecific communication phenomena associated with sexual behaviour and territorial marking (Wysocki, 1979); the septal organ of Masera (Giannetti et al., 1995) that is thought to be part of a chemosensory system related to alert functions (Harkema and Morgan, 1996); and finally the Grüneberg ganglion (Storan and Key, 2006) that could be involved in the mediation of panic-like freezing behaviours in response to alarm signals, although its functions are still poorly understood (Liu et al., 2009). In humans, the principal organ responsible for smell is the MOE while it is unlikely that the other organs are present. However, in some individuals it has been found a rudimentary non-functional VNO (Døving and Trotier, 1998; Menco and Morrison, 2003).

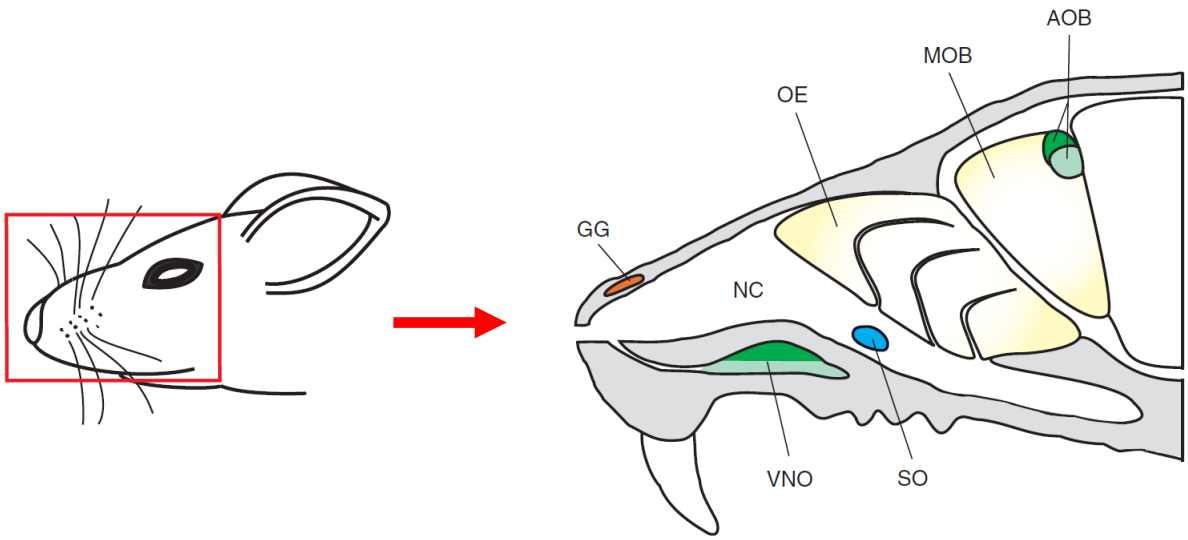

Figure 3: Olfactory organs in the murine nasal cavity.

The mouse olfactory system consists of four subsystems: the olfactory epithelium (OE), the vomeronasal organ (VNO), the Grüneberg ganglion (GG), and the septal organ of Masera (SO). Sensory neurons of the OE, SO, and GG project to the main olfactory bulb (MOB), while vomeronasal sensory neurons make synaptic connections within the accessory olfactory bulb (AOB; image obtained from Ferrero and Liberles, 2010).

The anatomical characteristics of the nasal cavity influence the breathing patterns, since rodents are obligate nose breathers, due to the close apposition of the epiglottis to the soft palate. Indeed, 20% of the inspired air reaches the olfactory region in rats, while only 5-10% in humans (Alvites et al., 2018; Kimbell, 2016; Pifferi and Menini, 2015).

Despite relatively small differences among distinct species, several excellent reviews have reported the conservation of principles between insect, amphibian, and mammalian OS. The basic organisation of the OS is conserved among several mammals, and many important contributions have been made by cross-phyla comparisons (Treloar et al., 2010). For this reason, the experimental information obtained in laboratory animal models, especially in the mouse model, is likely to apply also to humans. However, within the limitations of this reference, this chapter will focus mainly on the largest organ of the nasal cavity deputed to odorants detection in mammals: the main olfactory epithelium (MOE).

2.1 History

The first accurate description of the vertebrate olfactory mucosa is ascribed to Schultze, in 1862. He proposed that olfactory cilia of the MOE were the endings of the olfactory nerves. Schultze's astute observations are still valid up to now, and they are supported by several studies set up over the course of the following 140 years. In 1922, Parker proposed that olfactory cilia contain the receptive elements responsible for the odorants' detection, and he hypothesized that such cilia could increase the sensory surface area of the MOE. In 1847, Todd and Bowman described for the first-time glands in the lamina propria, and Kölliker named these structures Bowman's gland, in 1858 (Menco and Morrison, 2003).

After World War II, the huge developments into the electron microscopy field risen new possibility to study the cell structures. Thus in 1953, Engström and Bloom observed for the first time the human olfactory epithelium allowing to clarify the olfactory tissues' architecture (Menco and Morrison, 2003).

However, there has been an explosion of new scientific information on several aspects of the nose organisation at the macroscopic, microscopic, and molecular levels of analysis only in recent years. Several authors agree that olfactory research can be divided into two eras: before and after the discovery of ORs genes by Drs Linda Buck and Richard Axel in 1991, that started the molecular era of research into the chemical senses. Indeed, for this important milestone in the olfactory field, that boosted considerably our knowledge of how animals smell, Buck and Axel have been awarded the Nobel Prize in Physiology or Medicine in 2004 (Harkema et al., 2006; Mombaerts, 2004).

2.2 Development of the nasal cavity and MOE

The OS is one of the sensory systems that develop earlier in the embryo. The MOE derives from the olfactory placodes. These structures are specialized areas of cranial non-neural ectoderm found in the rostrolateral regions of the head (Treloar et al., 2010). Also from the olfactory placodes, some mesenchymal cells migrate to differentiate in secretory cells or glial cells (Schlosser, 2006). Soon after the closure of the neural tube, in rodents, by E10/TS16 (Embryonic day 10 / Theiler Stage 16 (Theiler, 1972), Figure 4) the olfactory placode starts to thicken and begins to invaginate. This structure is named olfactory pit and is the beginning of the nasal cavity. At E11/TS18, the nostrils are formed and twelve hours later the nasal pit further invaginates into a more complex nasal cavity. At the same time, also the VNO invaginates further into a separate, distinct cavity. Thus, MOE and VNO can be distinguished (Treloar et al., 2010).

During this period, the polarity of the OS changes dramatically. Initially, the placodes are laterally located on the embryo and they start to shift during the development process that originates the nasal cavity.

In the end, the nasal cavity shifts orientation from a rostro-lateral position to a more rostral location, until the nares form at the most rostral tip of the head (Treloar et al., 2010).

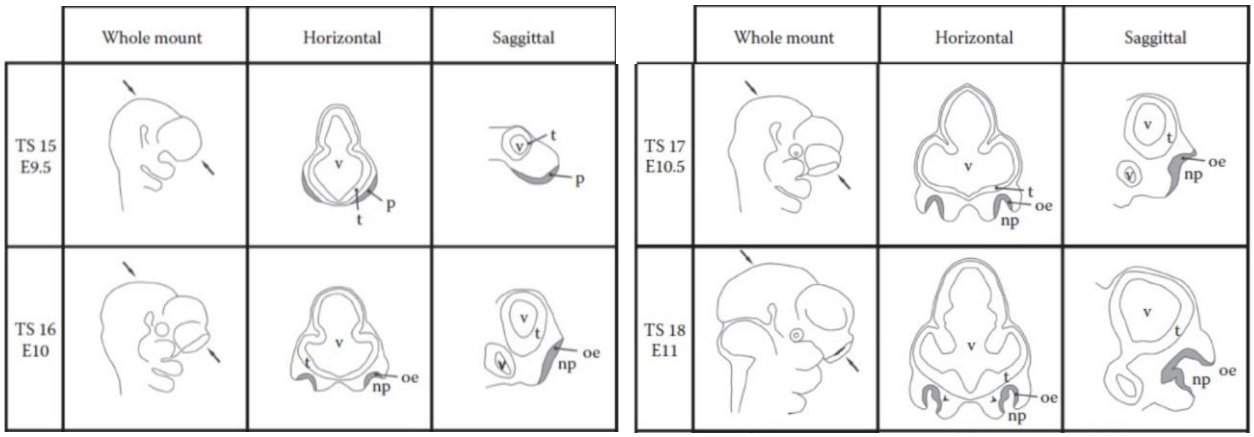

Figure 4: Development of murine nasal cavity.

At Thieler Stage (TS) 15, the olfactory placodes (shaded grey) are composed of a few cell layers thick located laterally. At TS16, the nasal pits appear after placodes invagination and they maintain a simple cuplike morphology until TS17. At TS18, a second invagination represents the initial formation of the vomeronasal organ. The arrows indicate the horizontal plane of the horizontal diagrams. Abbreviations: t, telencephalon; v, ventricle; np, nasal pit; p, placode; oe, olfactory epithelium (image modified from Treloar et al., 2010).

2.3 Gross anatomy of the nasal cavity and MOE

From cranial to caudal, we can identify four regions in the mature nasal cavity: the vestibule, the nasal valve or ostium, the main nasal chamber, and the nasopharynx. The main nasal chamber occupies most of the nasal cavity. Each nasal passage of this chamber is delimited by bone walls, and into it are located the turbinates or nasal concha. These turbinates are cartilaginous or ossified convoluted hook-shaped structures, covered by the olfactory mucosa (Alvites et al., 2018; Eiting et al., 2014). Different species have a dissimilar degree of development of these structures, accordingly to their olfactory capacity (Figure 5; Andres, 1966; Mills and Christmas, 1990). Projecting into the airway lumen of the main chamber, the nasal turbinates increase considerably the inner surface area of the nose (Harkema et al., 2006). Marked differences in airflow patterns among mammalian species are mainly due to variation in the shape of nasal turbinates. Humans have three turbinates in their nose: the superior, middle, and inferior; while other animals can have more, indeed rodents have six to eight turbinates (Alvites et al., 2018; Menco and Morrison, 2003). Moreover, humans' turbinates are relatively simple in shape compared to those from non-primate laboratory animal species (e.g., dog, rat, mouse, rabbit), that have complex folding and branching patterns (Harkema and Morgan, 1996; Harkema et al., 2006; Menco and Morrison, 2003; Mills and Christmas, 1990; Reznik, 1990). The human main nasal chamber is only about 5 to 8 cm long, and it is remarkably smaller in comparison to other mammals; however, thanks to turbinates and their branching pattern the surface area is around 150 – 200 cm^2, about four times bigger of the human trachea surface (Guilmette et al., 1989; Harkema et al., 2006).

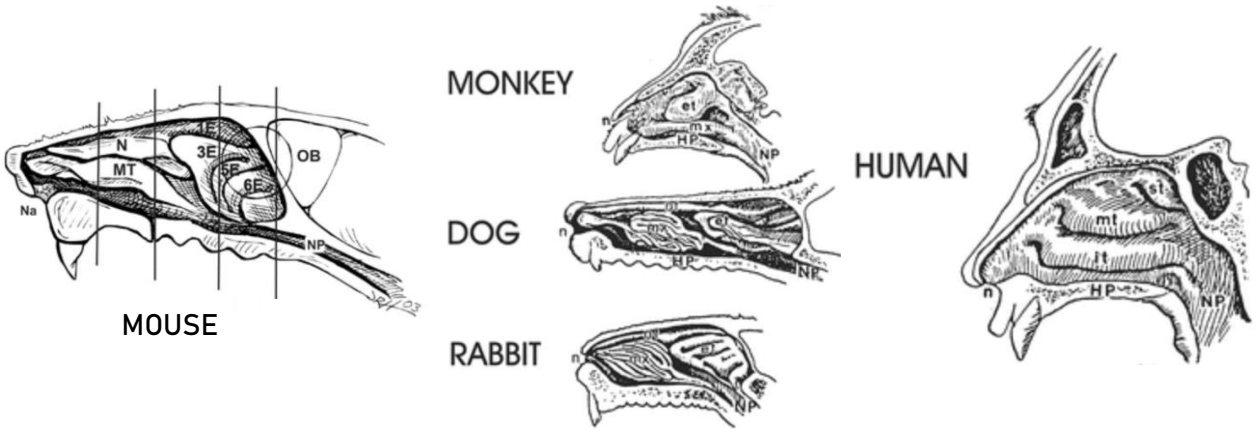

Figure 5: Comparison of the nasal cavity from different mammals.

The nasal septum has been removed to expose the nasal passage and turbinates. N = nasoturbinate; MT = maxilloturbinate; et and 1E–6E = 6 ethmoturbinates; Na and n= naris; nt = nasoturbinate; mx = maxilloturbinate; mt = middle turbinate; it = inferior turbinate; st = superior turbinate NP = Nasopharynx; HP = hard palate; OB = olfactory bulb (image modified from Harkema et al., 2006).

2.4 Histology of the nasal cavity

In the nasal cavity of several mammals are present four types of epithelia with high levels of specialization, distributed from the vestibule to the nasopharynx. They are composed of various subtypes of cells, and they are named squamous, transitional, respiratory, and main olfactory epithelium respectively (Figure 6; Uraih and Maronpot, 1990). The squamous epithelium is lightly keratinized and stratified, and it is primarily restricted to the nasal vestibule, the transitional epithelium is a nonciliated cuboidal/columnar epithelium located between squamous and respiratory epithelium mainly in the nasal valve, finally the respiratory or non-sensory, which is a ciliated pseudostratified cuboidal/columnar epithelium, and the main olfactory or sensory epithelium. The last two epithelia are the most abundant in the nasal chamber, covering the turbinates and the nasal septum (Kepler et al., 1995; Mery et al., 1994). All these mucous membranes, or mucosa, consist of two layers: the luminal surface epithelium and the underlying connective tissue of lamina propria. The olfactory lamina propria contains blood and lymphatic vessels, nerves, glands and mesenchymal cells (e.g., fibroblasts, lymphocytes, mast cells), embedded in a connective tissue matrix (Alvites et al., 2018; Harkema et al., 2006).

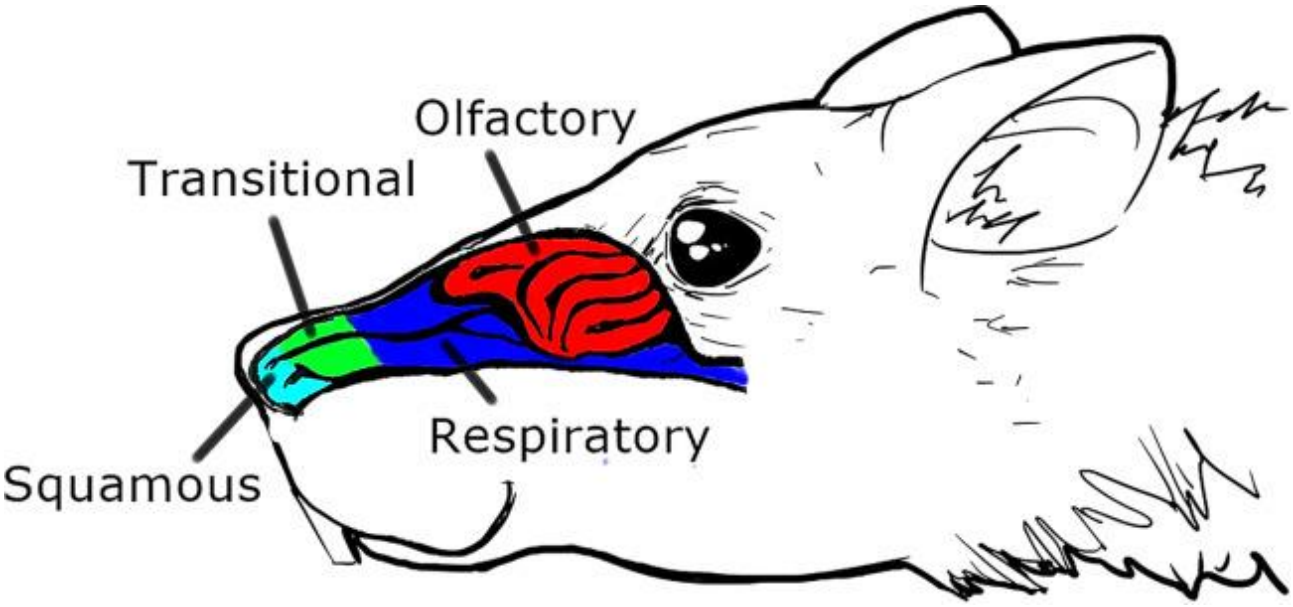

Figure 6: Distribution of different epithelia within the mouse nasal cavity.
Following the rostro-caudal axis, the four epithelia are: squamous, transitional, respiratory and olfactory epithelium (image obtained from Alvites et al., 2018).

Almost all the luminal surfaces of the nasal mucosa, especially all the lumen in the main chamber, are covered by a continuous layer of mucus. The mucus is a watery, sticky material, and it is produced by mucous (goblet) cells in the surface epithelium and subepithelial glands in the lamina propria. The mucus layer has an important role in defending the respiratory and olfactory airways, filtering the inhaled air by trapping inhaled particles and certain gases or vapours. Depending on the nasal localization, the mucus moves at different speeds and direction, and it is propelled away from the synchronized beating of underlying cilia into the luminal surface (Harkema et al., 2006). It moves very slowly on the olfactory mucosa with an estimated turnover time of day, while on the respiratory epithelium its speediness is in the range of 1 to 30 mm/min, and with a turnover time of about 10 minutes in the rat (Morgan et al., 1984). The mucus with the entrapped materials ultimately is moved distally to the naso- and oro-pharynx, and then it is swallowed into the oesophagus and cleared through the digestive tract (Harkema et al., 2006).

2.5 Histology of the MOE

The MOE is a specialized pseudostratified columnar epithelium with twice the thickness of the respiratory epithelium. The transition borders between these two types of epithelium are poorly defined and it is common to identify zones where the cell populations of each one are mixed (Chamanza and Wright, 2015). The percentage of the nasal airway that is covered by MOE is the principal difference among animal species. It covers a much higher percentage in rodents than monkeys or humans. In rats, Gross et al. (1982) morphometrically determined that approximately 50% of the nasal cavity surface is lined by the MOE. In humans, the MOE has an average surface area of approximately 2–4 cm^2, which is only 3% of the total surface area of the nasal cavity (Moran et al., 1982; Sorokin and Weiss, 1988). Mice, rabbits, and dogs are much closer to rats than primates with respect to MOE percentage in their main nasal chamber (Harkema et al., 2006).

Macroscopically, the MOE looks yellowish due to the presence of pigments in certain types of cells (Evans and Lahunta, 2013). Histologically, the MOE is primarily composed of four types of cells: olfactory sensory neurons (OSNs), sustainable or sustentacular or supporting cells (SCs), microvillous cells, and basal

cells. Basal cells are further divided into globose basal cells (GBCs) and horizontal basal cells (HBCs; Graziadei, 1973), while the OSNs in mature and immature neurons. Their nuclei are aligned in the following order, from the apical surface to the basal lamina: SCs, microvillous cells, mature OSNs, immature ONSs, GBCs, and HBCs (Figure 7). Besides, Bowman's glands and respective ducts extend from the lamina propria to the MOE. In the MOE, SCs and Bowman's glands are the only cell populations involved in those processes deputed to preserve the tissue physiology, indeed since there are no goblet cells in this epithelium, they provide mucus secretion and xenobiotic enzymatic activity (Alvites et al., 2018; Harkema et al., 2006).

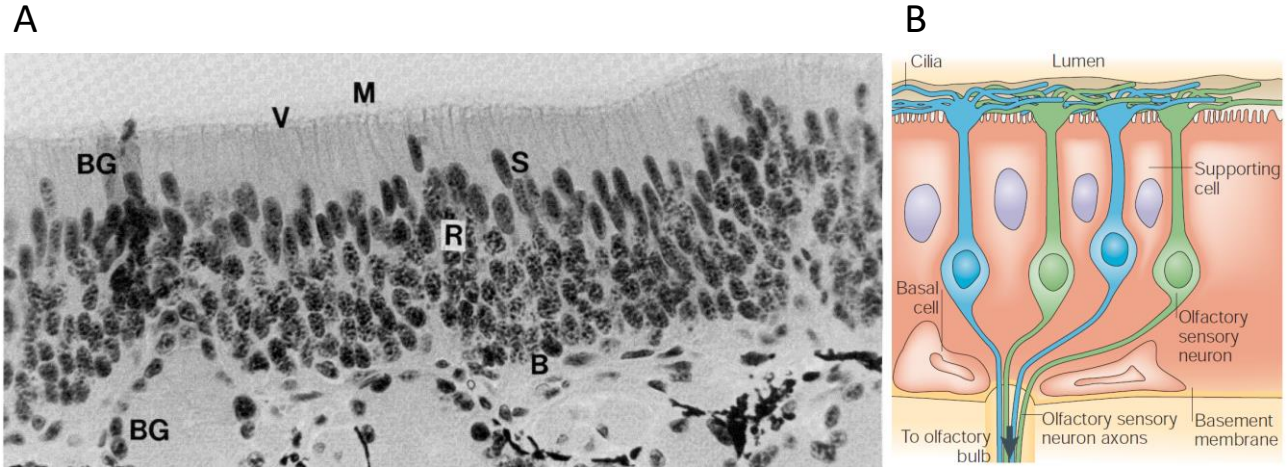

Figure 7: Cell populations of the MOE.

A- Section of the OE from tiger salamander stained with haematoxylin and eosin. Starting from the apical side: (M) mucus layer that cover the epithelium; (V) vesicles or knobs of the OSNs, (S) layer of SCs' nuclei; (R) cell bodies of the OSNs; (B) basal cells' nuclei distributed along the basal lamina and (BG) Bowman's glands extending their ducts through the epithelium surface. 400x magnification (image obtained from Masukawa et al., 1985). B- Schematic drawing of a MOE section (image modified from Mombaerts, 2004).

2.6 Olfactory sensory neurons

The OSNs from the MOE have several important features that set them apart from other types of neurons of the central nervous system (CNS). First, since they sense and detect odorants normally dissolved in the air, they are exposed to the external environment (Harkema and Morgan, 1996; Menco and Morrison, 2003; Morgan et al., 1984). Second, their axons project directly into the OB without synapsing in the thalamus (Haberly and Price, 1977; Price, 1973; Scott et al., 1980). Third, the OSNs can regenerate, and there is remarkable postnatal neurogenesis in the MOE even into old age (Altman, 1962; Brann and Firestein, 2014; Graziadei and Graziadei, 1979). Fourth, the ORs that they need to recognize odorants belong to the largest gene family in multicellular organisms, including humans (Buck and Axel, 1991; Glusman et al., 2001; Zhang and Firestein, 2002). Fifth, accordingly to the subset of ion channels expressed in their membrane, the OSNs have a really high value of input resistance in comparison with other neurons (Firestein, 2001; Kleene, 2008; Schild and Restrepo, 1998).

2.6.1 Histology

The OSNs are slender and bipolar neurons interposed between the SCs, with a density of 10^6 per cm^2 in mammals. They have a round cell soma of 5 – 7 µm in diameter located within the lower two-thirds of the epithelium (Farbman, 1994; Menco, 1980; Vollrath et al., 1985). The OSNs have a peripheral ciliated dendrite process that projects to the epithelial surface ending in a swelling called knob, or vesicle (Figure 8). The length of each dendrite varies a lot accordingly the position of the soma in the MOE (Moran et al., 1982; Morrison and Costanzo, 1990). The knobs extend usually above the MOE surface and have a typical diameter of 1 – 2 µm. Several tight-junction complexes attach the dendrite to adjacent SCs, as well as SCs to other SCs, forming a transmembrane barrier, a feature in common with other epithelia (Menco, 1980; Menco and Morrison, 2003). In mammals, several immotile cilia protrude from the knobs of the mature OSNs, on average 10 – 15, that radially project into the overlying mucus layer (Figure 8). Moreover, in most mammals, including humans, these cilia are about 50 µm in length, much longer than the non-sensory cilia of the respiratory epithelium, and have a diameter of 0.1 – 0.3 µm. However, they can reach a length of 200 µm in non-mammalian vertebrates. Overlapping with cilia of neighbouring dendrites, Menco has estimated that the OSNs' receptive surface increase by 25 – 40 -fold thanks to the ciliary apparatus (Menco, 1980; Menco and Farbman, 1985, 1992; Menco and Morrison, 2003).

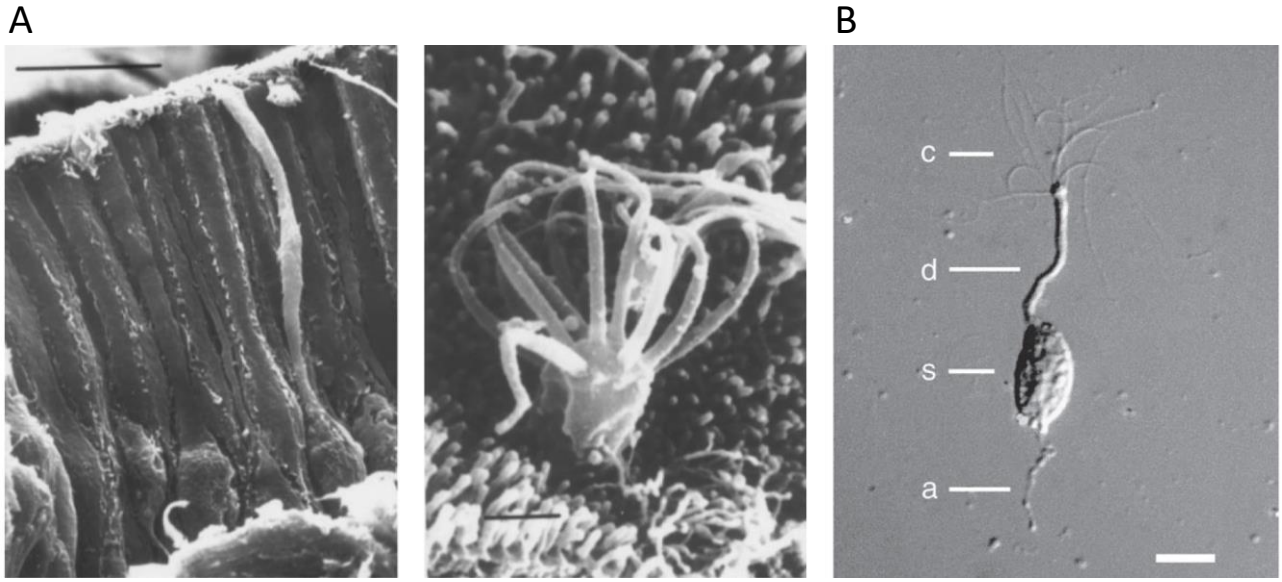

Figure 8: Histological details of OSNs.

A- Micrographs of human MOE obtained with Scanning Electron Microscopy (SEM). Left: Side view of the MOE. The OSNs are characterized by a slightly prominent dendrite (scale bar, 10 µm). Right: Surface view of the MOE showing an olfactory knob with 8 cilia (scale bar, 1 µm Images obtained from Morrison and Costanzo, 1990). B- Differential interference contrast image of an isolated frog OSN: c= cilia; d= dendrite; s= soma; a= axonal segment (scale bar, 10 µm; image obtained from Kleene, 2008).

The phospholipid bilayer covering the sensory cilia has an estimated density of intramembranous particles of about 1000 – 2000 /μm^2, about twice the value of motile cilia of respiratory ciliated cells. This is not surprising if we think that the ORs and all the transduction machinery are in the cilia of the OSNs, as confirmed from several fine structural, physiological and biochemical studies (Buck and Axel, 1991; Kleene, 2008; Menco, 1980; Menco and Farbman, 1985, 1992; Menco and Morrison, 2003; Mombaerts, 1999, 2004;

Schild and Restrepo, 1998). A typical marker of mature OSNs is the olfactory marker protein (OMP), a low molecular weight cytoplasmic protein encoded by a small intronless gene (Buiakova et al., 1994; Farbman and Margolis, 1980; Graziadei et al., 1980; Keller and Margolis, 1975). It is involved in several important process, such as: olfactory transduction (Buiakova et al., 1996; Kass et al., 2013; Reisert et al., 2007), maturation of OSNs (Holl, 2018; Lee et al., 2011) and modulation of axonal targeting (Albeanu et al., 2018; John and Key, 2005). OMP has a labelling pattern rather evenly distributed throughout the cytoplasmic compartments, including cilia (Farbman and Margolis, 1980; Graziadei et al., 1980; Keller and Margolis, 1975). From the basal portion of each OSN a long, thin, unbranched, and nonmyelinated axonal process transmits information to the brain. These axons are the smallest in the nervous system with a diameter of 0.1 – 0.7 µm (Figure 8, B; Hill et al., 2004). The OSNs' axons do not form a single olfactory nerve, but they constitute a set of small intraepithelial bundles, pass through the basal lamina, and then combine in larger fascicles (the fila olfactoria) that cross the cribriform plate of the ethmoid bone through small foramina to reach the OB. These nerve bundles are surrounded by specific glial cells called ensheathing or Schwann cells wrapping bundles of 50-200 olfactory axons that form the olfactory nerve (Doucette, 1993; Lledo et al., 2005). Interestingly, ORs are also expressed in axons and axon terminals indicating that they may have a role also for correct axonal targeting to the OB (Dang et al., 2018; Feinstein et al., 2004; Imai et al., 2006; Mombaerts, 1999; Ressler et al., 1993; Zamparo et al., 2019).

In the OB, the olfactory axons form synapses with second-order mitral and tufted neuronal cells in characteristic spherical neuropils called glomeruli (100 – 200 µm in diameter). Human glomeruli appear smaller (25 – 100 µm in diameter) and fewer in comparison with other mammals and are more widely dispersed in the OB (Mori et al., 2000; Smith et al., 1991).

2.6.2 Passive membrane properties

This paragraph reviews the passive electrical properties of the OSNs. Several studies measured the resting electrical properties of OSNs in various vertebrate and invertebrate species, reporting the values of capacitance, resting membrane resistance, and resting potential.

The capacitance is in the range from 0.7 to 35 pF, and the smallest and the largest values have been reported in zebrafish (Corotto et al., 1996) and newt (Schild and Restrepo, 1998), respectively (Table 1). Thus, the membrane surface of OSNs is in the range between 70 and 3,500 µm^2, assuming a standard value of 1 µF/cm^2 (corresponding to 1 pF/100 µm^2; Schild and Restrepo, 1998).

Species	Whole Cell Capacitance, pF
Zebrafish (*Danio rerio*)	0.7
Catfish (*Ictalurus punctatus*)	2
Rat (*Rattus rattus*)	2–4
Human (*Homo sapiens*)	4
Squid (*Loligo opalescens*)	
Floriform cells	5.7
Piriform cells	11.9
Clawed frog (*Xenopus laevis*)	4–7
Chilean toad (*Caudiverbera caudiverbera*)	5
Salamander (*Salamandra salamandra*)	6–11
Mudpuppy (*Necturus maculosus*)	16
Salamander (*Ambystoma tigrinum*)	21
Newt (*Cynops pyrrhogaster*)	35

Table 1: Value of capacitance in OSNs from different species (Data obtained from Schild and Restrepo, 1998).

Patch-clamp experiments performed on OSNs often show a similar range of values of seal resistance and resting membrane resistance (R_m), between 1 and 40 GΩ. To avoid problems in the interpretation of data, it is therefore particularly important to distinguish between the concept of resting input resistance (R_i) and R_m. In the patch-clamp whole-cell configuration, the R_i value is usually estimated using voltage clamp and applying a small electrotonic voltage pulse (Δu) to measure the asymptotic current shift (ΔI). R_i is obtained from the $\Delta u/\Delta I$ ratio and represents the combined resistance of R_m and seal resistance (R_{seal}), while the series (or access) resistance (R_s) of the pipette is negligible because it should be at least two orders of magnitude smaller than R_m or R_{seal} (Schild and Restrepo, 1998). Clearly, smaller is the ratio R_i/R_{seal} and better is the approximation $R_m \sim R_i$. Cell-attached experiments reported values of seal resistances in the range between 1 GΩ (Kurahashi and Shibuya, 1989) and 53 GΩ (Lynch and Barry, 1989) for the OSNs. Taken into account this consideration, the true membrane resistance was estimated to be 4–6 GΩ in frog OSNs, resulting in a depolarization of 5 mV following a receptor current generation of just 1 pA (Kleene, 2008; Pun and Kleene, 2004). Moreover, it is reliable that the smaller mammalian OSNs have higher resistances. Indeed, the average resting resistance was estimated to be 26 GΩ in rats (Lynch and Barry, 1991).

Several investigators reported a remarkably large range of the resting membrane potential in OSNs using the whole-cell configuration of the patch-clamp technique. The underlying zero-current potential recorded in this modality ranged between −90 mV (Frings and Lindemann, 1988) and −30 mV (Schild, 1989), as reported from Lagostena and Menini (2003). These broad difference might be explained by species heterogeneity and different conductances activated at rest (Firestein and Werblin, 1987; Schild and Restrepo, 1998). However, correcting the resting membrane potential for the high value of input resistance in frog OSNs, it was found that the resting potential is no more negative than −75 mV (Pun and Kleene, 2004). In frog, the membrane at rest is mainly permeable to K^+ ions and, to a lesser extent, to Na^+ and Ca^{2+} ions (Pun and Kleene, 2004), while the contribution of Cl^- conductance is null or neglectable in OSNs from rat (Okada et al., 2000) or frog (Pun and Kleene, 2004). Unfortunately, it is not known which cellular compartments control the resting membrane potential since OSNs contact at least 3 different extracellular environments: the apical mucus layer, the interstitial fluid, and the basolateral fluid. Moreover, it is not well known the physiological ionic compositions of these compartments and of the OSNs' cytoplasm since really few studies have analysed these aspects (Kleene, 2008).

The membrane time constant is the product between the membrane resistance and the cell capacitance, and it was measured in OSNs from various species injecting current into OSNs' membrane through a patch pipette. Since OSNs have really high value of membrane resistance, it is possible that in some species the time constant can be as long as ∼100 ms, while in those species in which the OSNs are much smaller the time constant can range between 40 and 60 ms (Schild and Restrepo, 1998). As nicely demonstrated by Lynch and Barry (1989), this implies that OSNs can be excited by very small receptor currents thanks to their high membrane resistance, but that the depolarization is relatively slow because of the long time constants.

Altogether, these passive properties make the OSNs extremely sensitive, and the binding of a few or maybe only one molecule to few or maybe one OR can excite an OSN generating an odorant response and the underlying action potentials that will send the information to the brain.

2.6.3 Voltage-gated channels involved in action potentials

This section reviews some biophysical properties of the conductances involved in the generation of action potentials in OSNs.

A. Voltage-Gated Sodium Currents

Following the binding of odorants in OSNs, the generation of a receptor potential initiates spike generation if the membrane potential reaches the firing threshold of Na^+ channels.
In some species, most of the voltage-gated Na^+ current is insensitive to tetrodotoxin, whereas it is the opposite in other species. Moreover, the threshold for activation ranging from −60 mV to −30 mV (Figure 9). This variability could be species-dependent, or it could also be ascribed to a voltage drop either along the axonal compartments or across the pipette resistance. Moreover, the amplitudes of the Na^+ currents vary considerably among species and, in some cells, Na^+ current could not be measured at all. One possible explanation could be that the channels are primarily located in the axonal membrane, which is partially lost during preparation (Schild and Restrepo, 1998).

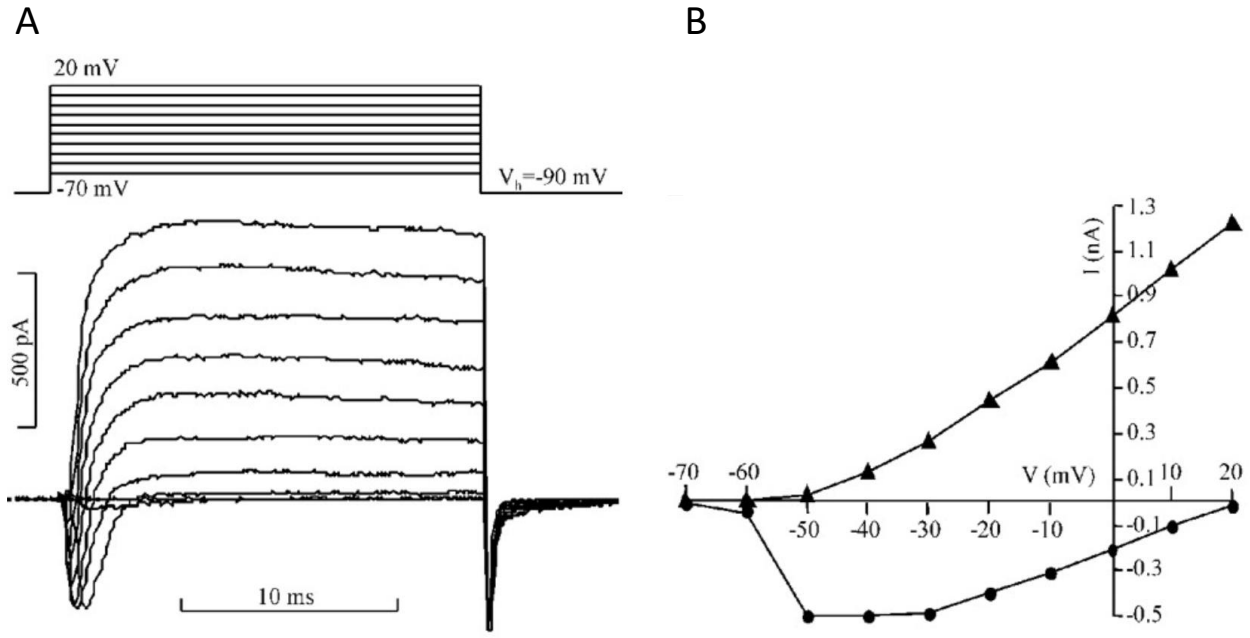

Figure 9: Voltage-gated currents recorded in whole-cell patch-clamp configuration from an isolated mouse OSN.

A- 20 ms voltage steps raging from –70 to +20 mV elicited the voltage-gated currents (holding potential of -90 mV). B- Current–voltage relationship of the traces in (A) for the peak inward current (circles) or the sustained current at the end of the voltage steps (triangles; images obtained from Lagostena and Menini, 2003).

Recently, Bolz et al. (2017) reported that the $Na_v1.7$ isoform is the most abundant subtype not only in the MOE but also in the VNO. Moreover, the $Na_v1.3$ and $Na_v1.7$ voltage-gated Na^+ channels isoforms could be strongly involved in axonal propagation of action potentials as suggested from immunohistochemical evidence. Finally, these two channels likely play a major role in the developing MOE since they specifically change subcellular localization in OSNs during the first weeks of life.

B. Voltage-Gated Calcium Currents

High-voltage-activated Ca^{2+} currents have been reported in OSNs from various species. Whole-cell patch-clamp experiments revealed that the amplitude of this current is relatively small and that the maximum current decreases with a time constant of ∼3 min (Schild, 1989). As observed in many preparations, it could be possible that this happens because of the diffusion between cytosol and patch pipette, and this phenomenon is called "washout" (Pusch and Neher, 1988).

The current threshold activation ranges between −40 and −30 mV and the Ca^{2+} current have the maximum amplitude at ∼0 mV. However, the *I-V* relationship shifts to higher voltages in some studies, and that may depend on a higher access resistances or an elevated extracellular Ca^{2+} concentration (Schild and Restrepo, 1998). Thus, high-voltage-activated Ca^{2+} channels are primarily activated during the generation of action potentials, and the resulting Ca^{2+} influx could contribute to the repolarization phase activating K^+ channels. Schild et al. (1994) have shown that these channels are mainly situated on the soma and the proximal dendrite in the frog OSNs using quantitative ratiometric Ca^{2+} imaging. However, the resolution of the method does not exclude other cellular compartmentalization in OSNs.

Finally, in few species has been reported also a low-voltage-activated Ca^{2+} current. This current may set the threshold for action potential firing at more negatively values, speeding up action potential generation. This type of current might, therefore, be extremely useful in larger OSNs that have higher capacitance and longer membrane time constant (Schild and Restrepo, 1998).

C. Potassium Conductances

Repolarization of action potentials is achieved by the activation of mainly three different types of K^+ conductances (Figure 9): a transient 4-aminopyridine-sensitive K^+ current, a Ca^{2+}-activated K^+ current, and a slow delayed rectifier-like K^+ current. All these conductances have been reported in OSNs from several species (Schild and Restrepo, 1998).

The 4-aminopyridine-sensitive K^+ current activates and inactivates rapidly, it activates at more positive potentials than those of voltage-gated Na^+ channels reported in OSNs, and it contributes strongly to the repolarization phase of action potentials (Schild, 1989).

In mouse OSNs, two types of Ca^{2+}-activated K^+ conductances have been reported: 130-pS, with voltage-dependent kinetics, and 80-pS, with voltage-insensitive kinetics, presumably corresponding to BK and SK K^+ channels, respectively (Maue and Dionne, 1987). While in other species it is not clear which type of channels are responsible for the Ca^{2+}-activated K^+ current. Ca^{2+} influx through high-voltage-activated Ca^{2+} channels seems to play the major role in activating these K^+ currents because the blockage of the high-voltage-activated Ca^{2+} channels abolished the Ca^{2+}-dependent conductances (Schild, 1989). These findings suggest that the Ca^{2+}- activated conductances, or at least a major fraction of them, may colocalize with the high-voltage-activated Ca^{2+} channels (Schild and Restrepo, 1998).

Slow delayed rectifier K^+ channels may play a role in both repolarizations of action potentials and tuning of the resting and post-stimulus impedance. Thus, this channel may play an important role in tuning the refractory period (Firestein and Werblin, 1987; Schild, 1989).

However, it is highly reliable that only a little small fraction of K^+ channels are open at rest, and this results in an extremely high resting resistance and a correspondingly high sensitivity for the OSNs from different species. The few K^+ conductances that are open at rest, presumably the inward rectifier and the delayed rectifier, would not be able to greatly contribute to the membrane repolarization because the inward rectifier is closed at depolarized voltages and the delayed rectifier has too small conductance. Thus, the repolarization is mainly achieved by transiently switching on the fast 4-aminopyridine-sensitive K^+ conductance and the fast Ca^{2+}-dependent K^+ conductance (Schild and Restrepo, 1998).

2.6.4 Transduction pathway

In the second half of the eighties, Trotier (1986) reported the first working hypothesis on the signal cascade of OSNs. He cautiously suggested that the odorant-activated response was mediated by a nonselective cation conductance and that it should be modulated by a diffusible cytosolic metabolite since there was a considerable delay (around two seconds) in the response. In the following years, Firestein, Kurahashi, and Gold laboratories independently confirmed the Trotier's hypothesis providing detailed analyses of the odorant-activated currents (Firestein and Werblin, 1989; Kurahashi, 1989; Nakamura and Gold, 1987; Schild and Restrepo, 1998). Later on, Kleene and Gesteland (1991) discovered that the "cation" current was actually a mixture of Ca^{2+}, Na^{+} and Cl^{-} currents. Nowadays, it is well known which are the main players of this process and all the steps that are involved in the olfactory response following a common pathway shared in several vertebrates (Figure 10, A).

The transduction cascade takes place in the olfactory cilia, immersed in the mucus layer that covers the luminal surface of the MOE, and starts with the binding of an odorant to a specific OR protein (Buck and Axel, 1991). The OR isomerization, in turn, activates a guanosine triphosphate (GTP)-binding protein, called G_{olf} (Jones and Reed, 1989). At this point, the GTP-bound G_{olf}-α subunit dissociates from the β and γ subunits and triggers the activation of a type III adenylyl cyclase (AC; ACIII), that converts adenosine triphosphate (ATP) into cyclic adenosine monophosphate (cAMP; Figure 10, A; Bakalyar and Reed, 1990). Surprisingly, Reisert (2010) reported that different ORs display different constitutive activity with different levels of basal transduction activity and concomitant receptor current fluctuations that drive generation of action potentials even in the absence of odorant stimulation.

The cAMP is a small and hydrophilic molecule that can rapidly diffuse into the ciliary compartment at the estimated velocity of 20 μm/s (Chen et al., 1999), playing a crucial role as the first "second-messenger" involved in the amplification of the olfactory transduction. Inside the cilium, a sufficient amount of cAMP gates the cyclic nucleotide-gated (CNG) channel, the first transduction channel in the OSNs (Figure 10, A; Nakamura and Gold, 1987). The native olfactory CNG channels are tetramer composed of 3 different subunits: 2 CNGA2, 1 CNGA4 and 1 CNGB1b (Bönigk et al., 1999; Zheng and Zagotta, 2004). The CNG channels generate a depolarizing nonselective cationic inward current that transiently increase the intraciliary Ca^{2+} concentration, the second "second-messenger" of the signal cascade amplification.

If sufficient Ca^{2+} accumulates, it opens the TMEM16B channel, a Ca^{2+}-activated Cl^{-} channel (CaCC) that is the second transduction channel (Figure 10, A; Billig et al., 2011; Kleene and Gesteland, 1991; Pifferi et al., 2009; Sagheddu et al., 2010; Schroeder et al., 2008; Stephan et al., 2009). The presence of a Na^{+}-K^{+}-$2Cl^{-}$ cotransporter, NKCC1, maintains a high Cl^{-} concentration inside the cilia (Kaneko et al., 2004; Reisert et al., 2003, 2005). Indeed, Reuter et al. (1998) found that the Cl^{-} concentration is about 70 mM in the knobs of rat OSNs and around 55 mM in the mucus layer. Therefore, the TMEM16B channels activation allows an efflux of Cl^{-} that further depolarizes the neuron. Up to 90% of the receptor current is due to the Ca^{2+}-activated Cl^{-} conductance in rodents (Figure 10, B; Boccaccio and Menini, 2007; Reisert et al., 2005).

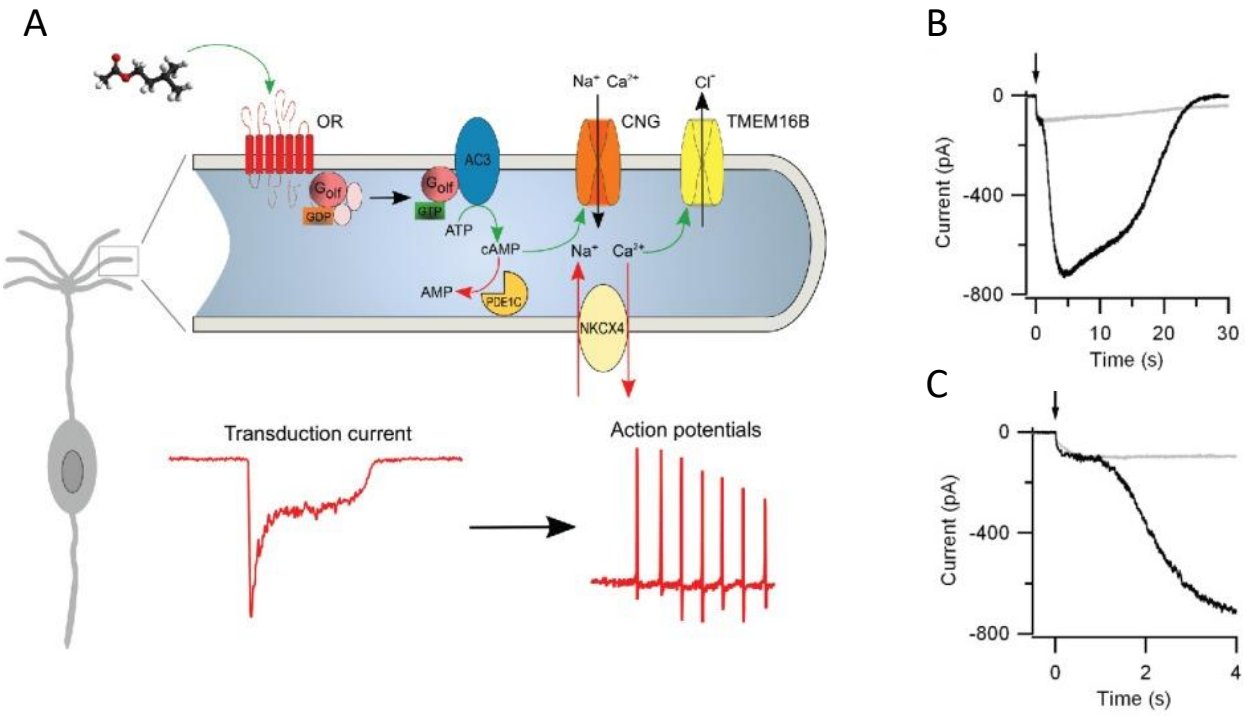

Figure 10: Transduction cascade in the cilia of OSNs.

A- The transduction cascade starts with the activation of the olfactory receptor (OR) by an odorant in the cilia of an OSN. A series of events (indicated by green arrows) eventually lead to the generation of action potentials firing that is sent to the OB in the brain. A series of negative feedbacks (indicated by red arrows) restore the ciliary homeostasis to resting levels (G_{olf} = olfactory G protein; CNG = cyclic nucleotide-gated; NCKX4 = $Na^+/Ca^{2+}/K^+$ exchanger 4; PDE1C = phosphodiesterase 1C; AC3 = adenylyl cyclase 3; image obtained from Dibattista et al., 2017). B- Transduction current recorded from a mouse OSN following photorelease of caged cAMP (in black). The Ca^{2+}-activated Cl^- current constitutes up to the 90% of the transduction current. In grey the transduction recorded from the same OSN after the blockage of the Cl^- channel by the application of niflumic acid. C- Expanded timescale of the same experiment in (B) *(Images obtained from Boccaccio and Menini, 2007).*

Importantly, the olfactory cilia not only greatly increase the OSNs surface area, and consequently the probability of interaction with odorants in the mucus (Menco, 1980; Menco and Farbman, 1985, 1992; Menco and Morrison, 2003), but rather they absolve to another important function. Indeed, enhancing the ratio between the ciliary membrane surface area and the intraciliary cytoplasmatic volume even a small change in the number of ions within the intraciliary lumen can terribly affect the ions' concentration, producing a pronounced depolarization (Getchell, 1986; Lindemann, 2001; Lowe and Gold, 1993; Reese, 1965). For this reason and the high OSNs membrane resistance, even the binding of few odorants molecules to an OR can produce a transduction current that generates action potentials (Kleene, 2008; Lindemann, 2001; Schild and Restrepo, 1998). This explains why the OS has really high detection capabilities with a very low threshold of activation. Indeed, humans can perceive ethyl mercaptan at the very low concentration of 1 part in 2.5 billion parts of air (Whisman et al., 1978), and it is added on purpose to odourless natural gas to recognize escaping gas.

Several mechanisms are involved in the termination of the response. Two different phosphodiesterases (PDEs) isoforms,PDE1C in the cilia (Cygnar and Zhao, 2009) and PDE4A in the other OSNs

compartments (Yan et al., 1995) hydrolyse cAMP into AMP (Borisy et al., 1992) and strongly reduce the amount of free cAMP (Figure 10, A). However, only knockout mice for both PDE1C and PDE4 show olfactory impairments such as a slower response termination after short odorant stimuli and a smaller adaptation in response to long stimulation (Cygnar and Zhao, 2009). Moreover, it is possible that even a simple diffusion of cAMP from the cilia is sufficient to allow a rapid response termination (Chen et al., 1999). However, another important player in the termination of the olfactory response is Ca^{2+}. The intraciliary Ca^{2+} extrusion is mainly due to the activity of the ciliary potassium-dependent Na^{+}/Ca^{2+} exchanger 4 (NCKX4; Figure 10, A; Stephan et al., 2012) Moreover, mitochondria in the dendritic knob cooperatively contribute to Ca^{2+} dynamics modulation inside the OSNs cilia. (Fluegge et al., 2012)

Furthermore, extracellular Ca^{2+} and Mg^{2+} passing through CNG channels reduce the influx of more permeant Na^{+} or K^{+} in a voltage-dependent fashion by open-channel block (Frings et al., 1995; Zufall et al., 1991, 1994). On the other hand, elevated cytoplasmic Ca^{2+}, together with one or more Ca^{2+}-binding factors such as Ca^{2+}–calmodulin, plays a strong inhibitory feedback modulation on CNG channel activity that reduces the channel sensitivity to cAMP (Kramer and Siegelbaum, 1992; Pifferi et al., 2006; Reisert and Zhao, 2011; Song et al., 2008; Trudeau and Zagotta, 2003). This mechanism is relevant for an extremely important physiological process called adaptation (Kurahashi and Menini, 1997). After a prolonged odorant stimulation, despite the continued presence of the stimulus, the receptor current decreases with time and in case of repeated stimulation, if the interval between the pulses is sufficiently short, the amplitude of the second pulse is reduced (De Palo et al., 2012; Kleene, 2008; Kurahashi and Menini, 1997). This adapted state allows a cell to work over a broad range of stimuli and to reset the OSN to discriminate higher odorant concentrations without saturating the transduction process (Kleene, 2008; Pifferi et al., 2010).

2.7 Supporting cells

Together with the OSNs, SCs are the most abundant cell population in the MOE, and they work as both epithelial and glial support cells. Indeed, as epithelial-like cells, sustentacular cells are involved in secretion (Menco and Morrison, 2003), endocytosis (Bannister and Dodson, 1992), and metabolism of toxicants (Dahl, 1988). The close association between SCs and OSNs suggest that they may function as glial-like cells insulating physically and chemically the OSNs (Breipohl et al., 1974), actively mediating phagocytose of dead cells (Suzuki et al., 1996), and regulating the extracellular ionic environment (Getchell, 1986).

2.7.1 Histology

SCs are elongated columnar non-neuronal cells that span the entire thickness of the MOE, from the airway surface to the basal lamina. Like OSNs, supporting cells exhibit a cellular polarity, with their width cell body in the apical part of the epithelium and a thin cytoplasmic foot-like process that ends in an end-foot attached to the basal lamina (Figure 11, A). Their oval elongated nuclei are the most apically located, and are aligned in a single row along the MOE (Menco, 1980; Menco and Morrison, 2003). The apical surfaces of SCs are lined by several long microvilli that extent into the mucus layer intermingling with the thin cilia of the OSNs (Figure 11, B; Andres, 1966; Morrison and Costanzo, 1990).

Ultrastructural observations have shown differences between SCs and the columnar mucus secretory goblet cells of the respiratory epithelium. Indeed, SCs contains a rich supply of organelles in their apical cytoplasm that become scarce basally suggesting that they may be involved in releasing materials in the mucus and/or absorbing substances from the mucus (Figure 11, C; Bannister and Dodson, 1992; Moran et al., 1982). Their supranuclear cytoplasm has abundant smooth endoplasmic reticulum and xenobiotic-metabolizing enzymes (e.g., cytochrome P-450, flavin-containing monooxygenases, N-acetyltransferases), thus it is thought that, together with Bowman's glands, SCs are involved in the metabolism of xenobiotic compounds. Importantly, SCs of the MOE show a specific expression pattern of ubiquitin-positive membrane array in their supranuclear region after excessive odorants exposure (Carr et al., 2001; Chen et al., 1992; Dahl and Hadley, 1991; Genter, 2004; Menco and Morrison, 2003).

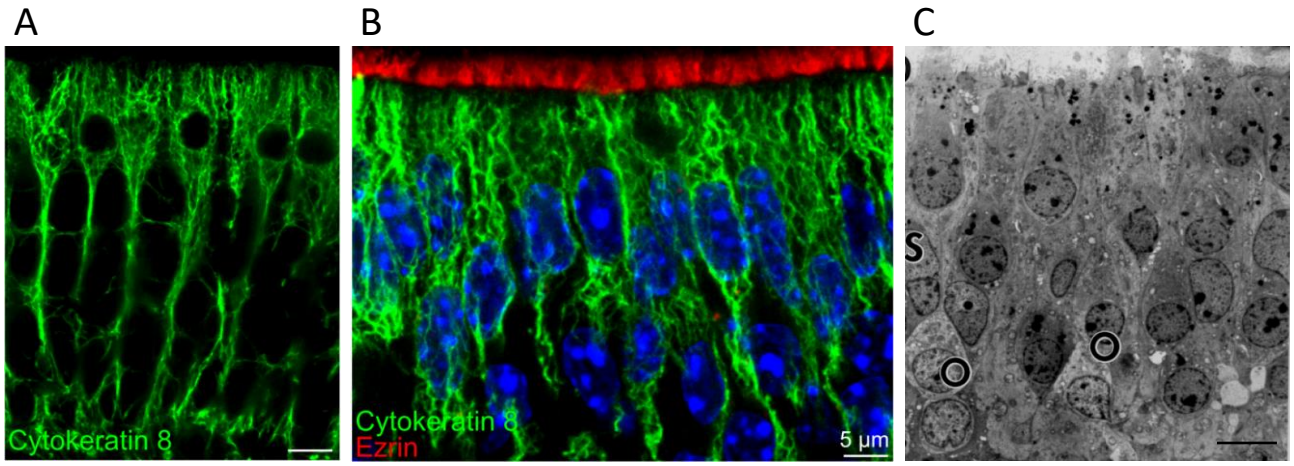

Figure 11: Cytology of olfactory sustentacular cells.

A- Typical morphology of SCs showed by the staining with Cytokeratin 8. B- Double staining of Cytokeratin 8 and the marker of microvilli ezrin. Cells nuclei stained by DAPI (scale bar, 5 µm; images modified from Maurya et al., 2015). C- Heterogeneous dark vesicles and organelles normally present in the supranuclear regions of SCs: O= OSNs; S= SCs. (scale bar, 5 µm; image modified from Menco and Morrison, 2003).

Densities of membrane-associated particles are considerably higher in the apical portion of SCs in comparison with OSNs, and several lines of evidence suggest that SCs could maintain a water and salt balance in the mucus. As a confirmation of this hypothesis, aquaporin-4 and amiloride-sensitive sodium channels have been found in the lateral membranes and in the microvilli of these cells, respectively (Lu et al., 2008; Menco, 1980; Menco et al., 1998).

Scanning microscopy has shown many fine cellular extensions that allow SCs to interact with other cells forming multiple contacts with OSNs throughout the epithelium (Breipohl et al., 1974; Morrison and Costanzo, 1990). SCs are closely associated among themselves and with the OSNs at several levels of the membrane. Indeed, several desmosomes and cell junctions can be identified between SCs and the dendrites of OSNs, and between multiple SCs as well (Menco, 1980; Menco and Morrison, 2003). Immunohistochemical analyses in the mouse MOE have shown connexin-43 immunoreactivity at discrete points on the membranes of adjacent SCs with a similar expression level both in new-born and in adult mice (Miragall et al., 1992). The connexin-45 expression has also been detected in the subapical region of the mouse MOE where the cell bodies of SCs are located (Zhang and Restrepo, 2002). This suggests that gap junctions in SCs of the mouse MOE may be composed of either connexin-43 or connexin-45 subunits or a combination of both (Martinez et al., 2002).

2.7.2 Passive membrane properties

Only a few studies, reviewed in this chapter, examined the electrical properties of SCs from different vertebrates.

Stable intracellular potentials were recorded from in vitro preparations of SCs from the salamander olfactory epithelium, and the mucus layer potential was taken as a reference. Masukawa et al. (1983) were the firsts to study the electrophysiological profile of a cell type population that accordingly its superficial location in the salamander olfactory epithelium resembled the glial-like SCs. The authors reported that these cells did not discharge action potentials but had high resting membrane potential (-50 to -104 mV) and relatively low input resistance. These cells showed opposite features to those of a second population of cells that had resting membrane potentials of -24 to -52 mV, high input resistances, and were capable to fire action potentials. The second type of cells had an intermediate location within the olfactory epithelium and presumably were OSNs. In a subsequent study Masukawa et al. (1985) used a lucifer yellow injections assay to visualize the cell type and could identify: a population of SCs characterized by a high resting potential of -95 ± 13 mV, a low input resistance of 9 ± 20 MΩ, and not capable to discharge impulses, either spontaneously or after current injection; and a population of OSNs with a lower resting membrane potential of -50 ± 15 mV, a higher input resistance of 219 ± 92 MΩ, and capable to generate action potentials.

One year later, Trotier and MacLeod (1986) reported that neither spontaneous nor evoked spike activities were recorded in SCs from an in vivo preparation of the salamander olfactory epithelium. Moreover, salamander SCs had a high resting potential of -96 ± 10 mV and low input resistance of 15 ± 12 MΩ, similar values to those reported by Masukawa et al. (1983, 1985).

Patch-clamp recordings on SCs were obtained from slices of the frog olfactory epithelium by Trotier (1998). Cell-attached single-channel recordings indicated that the intracellular potential was -68 ± 7 mV while it was -67 ± 4 mV in whole-cell conditions using Ringer's solution (in mM: NaCl 110, KCl 4, $CaCl_2$ 2, $MgCl_2$ 1, HEPES 10 and glucose 11) in the bath and a KCl based intracellular solution (in mM: KCl 100, $MgCl_2$ 1, HEPES 10, EGTA-Na_2 1.25 and $CaCl_2$ 1). The input resistance was 32 ± 14 MΩ, indicating a high membrane conductance at rest. The existence of electrical coupling between SCs was found by replacing KCI in the pipette with CsCl together with the application of octanol, a gap-junction blocker.

Whole-cell patch-clamp experiments on SCs from acute slices of the mouse MOE were performed by Vogalis et al. (2005a). They reported that mouse SCs of the MOE have on average an apparent cell capacitance of about 18.5 ± 0.5 pF and input resistance of 160 ± 11 MΩ, values that are far from those of the OSNs in which they measured 4.4 ± 0.4 pF of capacitance and 664 ± 195 MΩ of input resistance, respectively. When corrected for a seal resistance of 1 GΩ, these mean membrane resistance values were increased to 190 MΩ and 2 GΩ in SCs and OSNs, respectively. SCs had resting potentials ranging between -30 and -50 mV and were not excitable at their normal resting potential.

SCs showed a resting leak conductance that was permeable to monovalent cations and anions and was largely inhibited by substitution of external Na^+ with NMDG and by internal F^- with gluconate. This resting leak conductance deactivated up to 50% at potentials negative of −70 mV and was inhibited by 18β-glycyrrhetinic acid (20 μM) a specific gap-junction blocker (Figure 12; Davidson and Baumgarten, 1988). Application of 18β- glycyrrhetinic acid also elicited a 3.5-fold increase in the input resistance of SCs, from the averaged value of 187 ± 10 MΩ in SCs bathed in Ringer's solution to 656 ± 37 MΩ in SCs incubated with the blocker. SCs are electrically coupled by junctional resistances on the order of 300 MΩ. However, Alexa 488 added to the pipette solution failed to reveal dye coupling between SCs (Vogalis et al., 2005b).

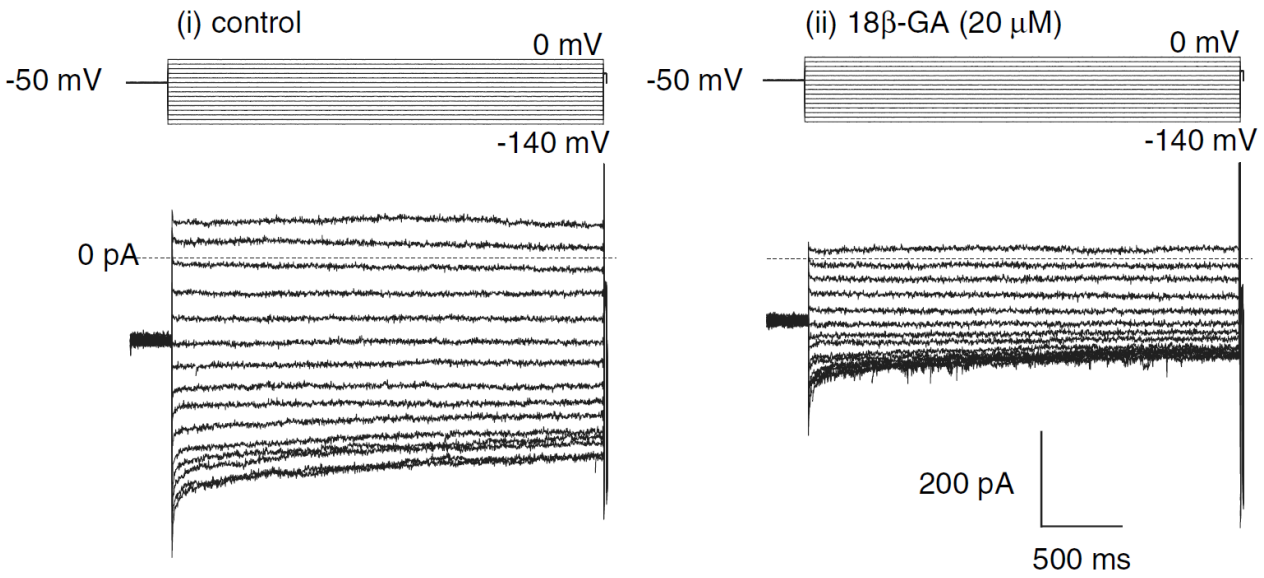

Figure 12: Resting leak conductance in mouse olfactory sustentacular cells.

Whole-cell voltage-clamp recording from a mouse SC applying voltage steps raging from –140 to 0 mV with a holding potential of -50 mV. The leak current is strongly reduced by the external application of gap junction blocker 18β-glycyrrhetinic acid (20 μM; image modified from Vogalis et al., 2005a).

2.7.3 Voltage-gated channels

Cell-attached single-channel recordings performed on SCs from slices of the frog olfactory epithelium revealed that these cells possessed voltage-gated channels in their membrane. Trotier (1998) characterized these channels after excision of the membrane patch in the inside-out configuration, identifying Ca^{2+}-dependent potassium channels of large conductance BK channels, with a conductance of 253 pS, activated by increases in intracellular Ca^{2+} concentration and by membrane depolarization.

Vogalis et al. (2005a) revealed that also SCs from acute slices of the mouse MOE have both voltage-gated K^+ and Na^+ conductances (Figure 13). From potential value more positive of −40 mV, SCs generated a 'noisy' outward K^+ current blocked by low concentrations of tetraethylammonium with little inactivation over 160 ms. This outward current was generated by the opening of charybdotoxin-sensitive BK channels with a mean conductance of 237 ± 10 pS.

Moreover, SCs generated a tetrodotoxin-resistant voltage-activated Na^+ current with a density peak at −38 mV of −44 pA pF^{-1}, much lower than the one from OSNs of -510 ± 96 pA pF^{-1}. The OSNs are also more sensitive to tetrodotoxin and this could suggest a different molecular composition of Na+ channels in SCs and OSNs of the mouse MOE. The density of Na^+ channels in SCs was sufficient to enable them to fire a single action potential, but only hyperpolarizing the membrane potential more than -80 mV. However, SCs are not excitable under resting conditions. The probable reason is the presence of the 'leak' conductance that maintains the resting potential of SCs depolarized and the Na^+ channels in the inactivated state. Regarding the location of Na^+ channels, the authors concluded that it is reasonable to think that Na^+ channels in SCs are located on the soma since the Na^+ current was adequately clamped and their recordings were obtained mainly from the cell bodies of SCs, although their presence in the process cannot be ruled out (Vogalis et al., 2005a).

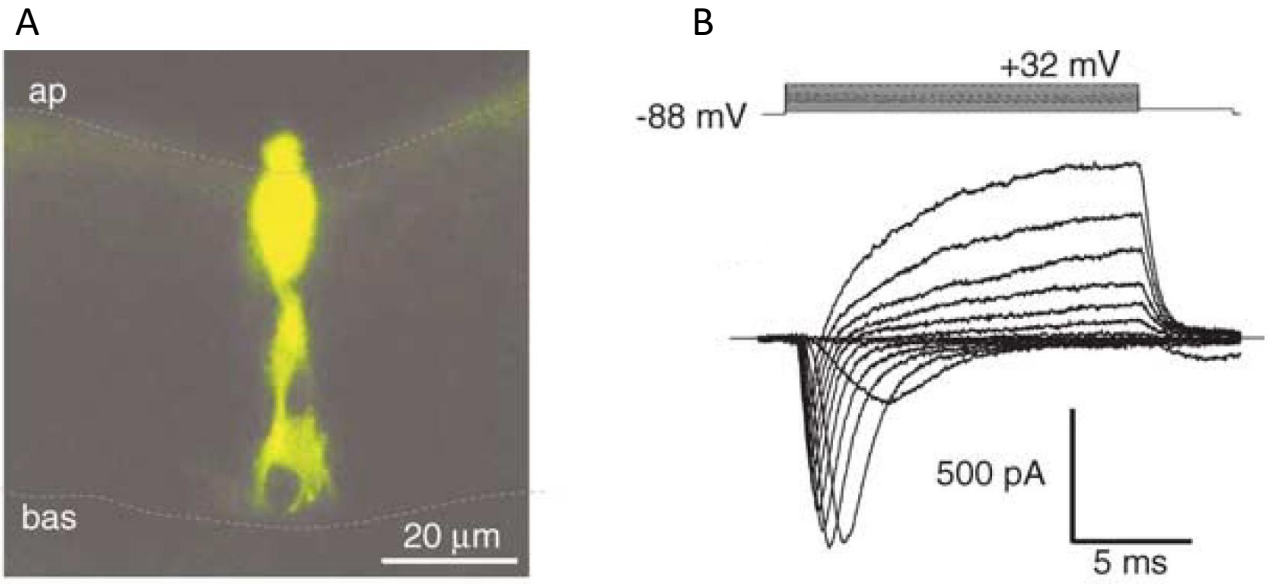

Figure 13: Voltage-gated currents recorded in whole-cell patch-clamp configuration from a mouse olfactory sustentacular cells.

A- Typical morphology of a mouse SCs filled with 0.2% Lucifer Yellow during a whole-cell patch-clamp recording (ap= apical surface; bas= basal membrane). B- Voltage steps elicited both inward and outward currents in the same cell (holding potential of -88 mV; images modified from Vogalis et al., 2005a).

2.7.4 Calcium signalling

Glial cells of the CNS have complex Ca^{2+} dynamics that regulate multiple cell functions including gene expression, cell proliferation, metabolism, ion transport systems, release of cell products, and cell death. There are two types of glial Ca^{2+} signals: intercellular and intracellular (Cornell-Bell et al., 1990; Finkbeiner, 1992; Giaume and Venance, 1998; Scemes and Giaume, 2006). The first one is characterized by Ca^{2+} waves that propagate between neighbouring cells, while the second one consists of repetitive elevations in intracellular Ca^{2+} that remain confined to single cells.

Historically, SCs have been thought of as epithelial cells, but the evidence is mounting to suggest that they share also important physiological functions typical from glial cells. Using confocal Ca^{2+} imaging of neonatal mouse MOE slices, Hegg et al. (2009) observed spontaneous intercellular Ca^{2+} and intracellular Ca^{2+} oscillations in sustentacular cells that are characteristic of glial Ca^{2+} signalling (Figure 14).

They reported that, on average, a Ca^{2+} wave travelled 107 ± 11 µm before extinguishing (Figure 14, A). Ultrastructural, immunocytochemical and electrophysiological evidence showed that sustentacular cells form gap junctions with each other and they are electrically coupled. For these reasons, SCs may be also chemically coupled and several possible intracellular messengers, including inositol trisphosphate and Ca^{2+}, may diffuse through gap junctions to neighbouring cells and potentially propagate and trigger Ca^{2+} release therein. However, the possibility that an extracellular factor, such as ATP or acetylcholine, may be involved in the propagation of these waves cannot be excluded.

Moreover, the authors found also spontaneous intracellular Ca^{2+} waves propagating in SCs. The intracellular Ca^{2+} increased in the cell soma first and slowly travelled through the thin cytoplasmic extensions

reaching the endfoot attached to the basal membrane. The wave travelled from the cell soma to the basal cell layer in 9.5 s (Figure 14, B-C).

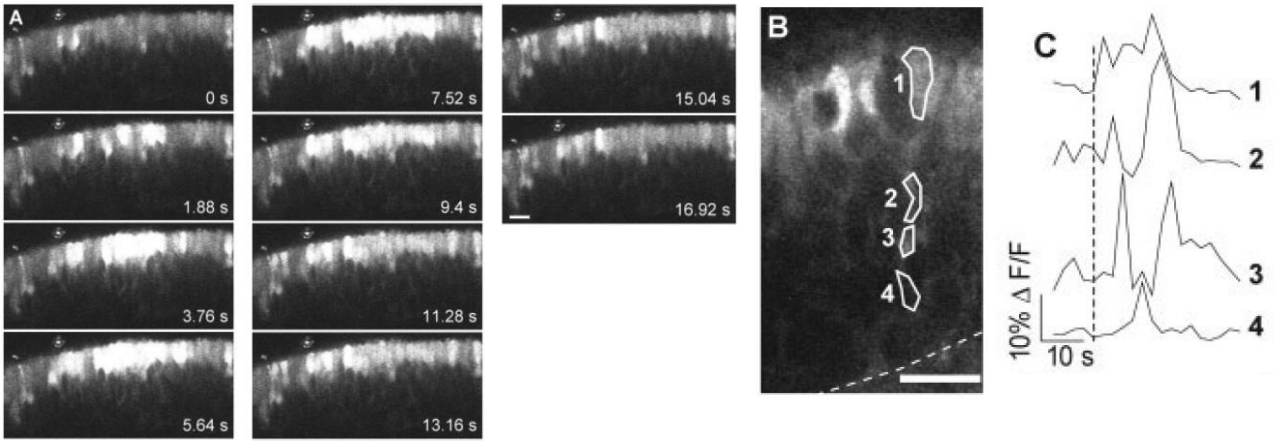

Figure 14: Complex Ca^{2+} *signalling in mouse olfactory sustentacular cells.*

A- Series of confocal Ca2+-images acquired during a spontaneous intercellular Ca2+ wave in a Fluo-4AM loaded slice of the murine MOE (scale bar, 20 µm). B- Spontaneous intracellular Ca2+ wave traveling from the apical side to the basal membrane (scale bar, 20 µm). C- Time course of the transient Ca^{2+} *increase from the numbered regions showed in (B; images modified from Hegg et al., 2009).*

Hegg et al. (2009) and Ogura et al. (2011) found that SCs can produce Ca^{2+} oscillation in response to ATP and acetylcholine, through the activation of specific G-protein coupled receptors. Like the spontaneous intracellular Ca^{2+} wave, the ATP-evoked Ca^{2+} wave initiated in the cell soma and travelled to the basal layer at an average speed of 35 ± 20 µm/s. For both stimuli, the authors observed a variability in temporal patterns for the intracellular Ca^{2+} responses. Indeed, the Ca^{2+} increase was either a single spike, multiple Ca^{2+} transients, oscillations, or a transient followed by fused oscillations leading to a sustained increase in Ca^{2+} that eventually recovered to baseline (Hegg et al., 2009). The acetylcholine induced Ca^{2+} increases showed two phases, an initial transient phase that generally decays rapidly and a second phase that consists of slow decay. Moreover, the Ca^{2+} increase evoked by the acetylcholine application is dose-dependent (Ogura et al., 2011).

The evoked Ca^{2+} transients followed the activation of the phosphoinositide phospholipase C pathway with subsequent production of inositol-1,4,5-trisphosphate. Indeed, intracellular Ca^{2+} stores depletion completely abolished the Ca^{2+} response in SCs, while the absence of Ca^{2+} in the extracellular solution did not affect the evoked Ca^{2+} transients. Inhibitors of the phospholipase C pathway (neomycin, U73122) and the application of the membrane-permeant Ca^{2+} chelator BAPTA-AM, which rapidly buffers cytosolic calcium, strongly reduced both the main monophasic Ca^{2+} transient and the oscillatory Ca^{2+} increases. These results suggest that both ryanodine and inositol trisphosphate receptors may be involved in the release of intracellular calcium (Hegg et al., 2009).

Finally, the application of atropine, an antagonist of all five muscarinic receptors, abolished the acetylcholine effects suggesting that muscarinic receptors are responsible for the Ca^{2+} increases in mouse olfactory SCs. In Ca^{2+}-free saline, the initial transient component persisted while the slow decay phase disappeared, indicating that the transient component was largely mediated by Ca^{2+} release from intracellular Ca^{2+} stores. However, information regarding the intracellular signalling pathways remains to be determined (Ogura et al., 2011).

2.7.5 Physiological functions

SCs of the MOE are involved in important physiological processes that preserve the integrity of the epithelium and that contribute to the correct functioning of the OS, acting as both epithelial- and glial-like cells.

The olfactory SCs are tightly packed on the apical portion of the epithelium and are organized in such a way to build up a barrier to humidify and warm the air and to filter it from external contaminants. Indeed, with each breath or sniff inhaled through the nose not only pleasant or unpleasant odorants reach the surface of the MOE that detects them but also a complex mix of pollutants and xenobiotics (Lucero, 2013).

There is strong evidence in the literature that olfactory SCs engage in xenobiotic metabolism and participate in odorant clearance since they express abundantly different isoforms of cytochrome P450, glutathione S-transferase and several other enzymes that can alter the odorant concentration and their chemical structure, thus modulating the detection of odorants (Chen et al., 1992; Dahl, 1988). Moreover, irritants and gases enhance the release of secretory granules from the apical portion of SCs. Electron microscopical study showed that these granules detach from their maternal SCs, floats as a droplet in the mucus, and finally, the secretory granules inside the droplet disintegrate into the mucus contributing to the continuous mucus turnover (Okano and Takagi, 1974). In olfactory SCs strong endocytosis occurs continuously to recycle their membrane and prevent the cumulation of redundant odorants and xenobiotics trapped within the epithelium. Endocytic vesicles and numerous large dense vacuoles and endosomes are closely associated with abundant fenestrated agranular endoplasmic reticulum rich of those enzymes involved in the clearance process (Bannister and Dodson, 1992). Finally, electron micrographs showed that SCs contained apoptotic bodies, cellular debris, and phagosomes in their cytoplasm, indicating that SCs in the MOE play a significant role in physiological phagocytosis in the unperturbed epithelium. Moreover, they increase their activity during acute cell death after the aforementioned events that are extremely dangerous for the MOE (Suzuki et al., 1996).

Morphologically, SCs are tightly associated with the OSNs and sleeve-like extensions envelop large amount of cell bodies, dendrites, and proximal part of the axons of several OSNs. They provide structural support for OSNs and form a barrier that protects and electrically isolates adjacent OSNs (Breipohl et al., 1974; Rafols and Getchell, 1983). SCs are bipolar elements that connect, through their apical and basal process, the epithelium surface with the basal lamina that separates the neuroepithelium from the blood vessels. Their cellular continuity from the basement membrane to the apical luminal surface may allow bidirectional movement of nutrients, wastes and hormones between capillaries and throughout the avascular olfactory epithelium (Lucero, 2013; Rafols and Getchell, 1983). However, the modalities in which this transport from capillaries into the olfactory epithelium via SCs occurs are presently unknown.

Moreover, olfactory SCs have voltage-gated ionic conductances and high resting membrane permeabilities to K^+, Na^+, and Cl^- that may play a role in mopping-up the excess of inorganic ions in the extracellular fluid compartment. Indeed, even if their large “leak” conductance clamps their membrane potential excluding a role for SCs in electrical signalling, they show a peculiar expression pattern of ion channels in their membrane (Ghiaroni et al., 2003; Vogalis et al., 2005a). Amiloride-sensitive Na^+ channels, BK channels and aquaporins are highly expressed in the microvilli and the apical region of SCs, enabling them to establish a vectorial ionic transport across the epithelium to absorb and transfer the excess of ions into the blood vessels (Menco and Morrison, 2003; Vogalis et al., 2005a). Thus, SCs may play a key role in the control of chemical composition and buffering of the intercellular fluid and mucus layer that covers the

luminal surface balancing between salts and water, which, in turn, can affect the excitability of sensory neurons.

Lateral coupling of SCs via gap junctions provides a functional syncytium for the rapid radial spread of several molecular signals across the neuroepithelium ensuring that the cellular activity can be integrated and coordinated. These coupling could facilitate the clearance of ions released by OSNs during odorant stimulation and it may assist the ionic redistribution in the epithelium between regions of unequal concentration (Masukawa et al., 1983; Trotier, 1998). Moreover, the SCs syncytium displays dynamic intracellular Ca^{2+} fluxes that can propagate through many cells resembling the typical pattern of Ca^{2+} waves that occurs in glia in the CNS (Hegg et al., 2009; Verkhratsky and Kettenmann, 1996). This widespread communication between SCs can serve as many different signals in the MOE. The Ca^{2+} fluxes could be a signal for cell turnover after injury-evoked regeneration, for secretion and calcium-dependent exocytosis to mediate vesicle release which could modify mucus composition or release growth-promoting factors that initiate proliferation acting on basal cells and neuronal precursors (Hegg et al., 2009; Lucero, 2013).

Indeed, SCs synthesize and release several important neurotrophic and neuromodulators or stress factors that regulate the physiology and pathology of the MOE. Like glia in the CNS, SCs have been shown to produce insulin, pituitary adenylate cyclase-activating polypeptide (PACAP), neuropeptide Y, endocannabinoids, ATP, and to express metabotropic P2Y purinergic receptors, muscarinic receptors, cannabinoid type 1 receptor and insulin receptor (Breunig et al., 2010a; Hansel et al., 2001; Hayoz et al., 2012; Hegg et al., 2003a, 2003b; Hutch et al., 2015; Lacroix et al., 2008; Ogura et al., 2011). The constitutive release of ATP and PACAP might be involved in normal cell turnover or modulation of odorant sensitivity in physiological conditions, while ATP-evoked ATP release following injury could lead to progenitor cell proliferation, differentiation and regeneration partially by overexpression of neuropeptide Y and heat shock protein 25 in SCs (Hassenklöver et al., 2008; Hayoz et al., 2012; Hegg and Lucero, 2006; Hegg et al., 2003b; Jia and Hegg, 2010). The release of acetylcholine is enhanced in the MOE after exposure to chemical, pathogens and thermal stimuli and it strongly increases the endocytosis activity in SCs (Fu et al., 2018). The SCs synthesize endocannabinoids that increase proliferation in neonatal and adult mouse MOE and may regulate the balance of progenitor cell survival and proliferation (Hutch and Hegg, 2016). The endocannabinoid and insulin modulation in the olfactory epithelium influence the odorant-detection thresholds accordingly to the hunger state of the animal in an opposite manner. SCs from hungry animals release more endocannabinoids rendering the OSNs more sensitive at detecting lower odorant concentrations, which probably helps the animal to locate food. Conversely, the postprandial insulin increase reversibly decreases the OSNs responsiveness to odorants (Breunig et al., 2010a, 2010b; Lacroix et al., 2008).

2.8 Other cell populations:

2.8.1 Basal cells

Basal cells are small conic stem cells capable of renewal all the cell populations that lining the MOE. There are two types of basal cells: horizontal (HBC) and globose (GBC). Both, on average, have a diameter of 4-7 µm and have a round centrally located nucleus.

The HBCs are pluripotent thin stem cells located along the basal lamina and contain keratins, intermediate filaments or tonofilaments characteristic of proliferating epithelial cells. They share similar morphologic and histochemical features with the basal cells of nasal respiratory epithelium (Holbrook et al., 1995; Menco and Morrison, 2003).

Instead, the GBCs are located above the HBCs, are not immunoreactive for keratin, and their cytoplasm is more electron-lucent and contains basal bodies. For these reasons, the GBCs appear lighter, a bit smaller, rounded and with little cytoplasm from a morphological point of view, while the HBCs are darker, thinner, and directly adhered to the basal lamina (Goldstein and Schwob, 1996; Menco and Morrison, 2003). Moreover, the GBCs have a high rate of proliferation while the HBCs have a much slower rate (Huard and Schwob, 1995).

The adult MOE is characterized by robust neurogenesis, and OSNs regenerate in humans even into old age (Holbrook et al., 2011; Murrell et al., 1996; Wolozin et al., 1992). Both HBCs and GBCs have the capacity of multipotent stem cells in the adult MOE (Caggiano et al., 1994; Leung et al., 2007; Newman et al., 2000). GBCs are a heterogeneous cell population within a hierarchy raging from stem cell to immediate neuronal precursor (Cau et al., 1997; Guo et al., 2010; Mackay-Sim et al., 2015; Manglapus et al., 2004), while HBCs are likely to be a quiescent population that requires activation by epithelial damage to re-enter the multipotent lineage (Chen et al., 2004; Iwai et al., 2008; Leung et al., 2007; Mackay-Sim et al., 2015). However, the regulation of the olfactory neurogenesis is still far to be completely understood.

2.8.2 Microvillous cells

Microvillous cells are less abundant in comparison with SCs and OSNs in the MOE, and they represent roughly 10% of the MOE's cell population. They are located primarily in the apical portion of the epithelium, neighbouring the SCs and OSNs, and are heterogeneous in terms of morphology and potential functions.

The most dominant feature of these cells is their apical microvilli that display different shapes and rigidness both among them and with those from SCs (Andres, 1966; Carr et al., 1991; Johnson et al., 1991; Menco and Jackson, 1997). Generally, the microvilli of microvillous cells are more compacted and have a more uniform diameter and a shorter length in comparison with microvilli of supporting cells. Moreover, depending on the fixation method used, the microvillous cells appear either more electron-opaque or electron-lucent than surrounding supporting cells (Bannister and Dodson, 1992; Menco and Jackson, 1997; Menco and Morrison, 2003; Moran et al., 1982; Morrison and Costanzo, 1990).

Recently, it has been identified a sub-population of microvillous cells in the MOE that expresses both the transient receptor potential channel M5 channels and cholinergic signature markers like the choline acetyltransferase and the vesicular acetylcholine transporter. This suggests that these cells are cholinergic and they could modulate the activities of neighbouring supporting cells and OSNs synthesizing and releasing locally acetylcholine (Fu et al., 2018; Hansen and Finger, 2008; Lin et al., 2008; Ogura et al., 2011). However, the exact function of these microvillous cells is still debated and the exact role of any of the microvillous cells is unknown.

2.8.3 Bowman's glands

The olfactory mucosa lays on the lamina propria made of connective tissue in which are immersed axon fascicles, blood vessels, and Bowman's glands. Bowman's glands are found in the olfactory mucosa of all vertebrates except for fish. Human Bowman's glands are composed of serous and stem cells and have a spherical (20 – 40 μm diameter) shape (Breipohl et al., 1974; Getchell and Getchell, 1992).

Bowman's glands are simple tubular-type glands that consist of small compact acini, and their ducts transverse the basal lamina at regular intervals extending through the MOE to reach the luminal surface. The central lumen of the duct is surrounded by several pyramidal serous cells, with a spherical nucleus and short stubby microvilli, while myoepithelial cells surround the acini (Menco, 1980; Menco and Morrison, 2003). At

least two types of serous cells are reported: one with electron-lucent droplets and one with opaque droplets. This suggests that the mucus is composed of multiple mucous products (Foster et al., 1991), and indeed heterogeneity and several distinct domains are founded in the mucus layer (Menco and Farbman, 1992).

Together with SCs, the Bowman's glands squeeze secretory cells and aid in moving secretory products in the mucus layer that covers the luminal surface of the MOE and regulate the microenvironment in which sensory transduction occurs. Like the SCs, several xenobiotic-metabolizing enzymes are found both in the acinar and in the duct cells of Bowman's glands (Harkema et al., 2006; Menco and Morrison, 2003).

2.9 The novel SARS-CoV-2 virus and the MOE

The novel SARS-CoV-2 virus responsible for the severe acute respiratory syndrome coronavirus clade 2 (Zhou et al., 2020) has very high infectivity causing a worldwide health crisis that is rapidly spreading around the world (Zheng, 2020). The virus infection starts with the binding of the viral Spike glycoprotein to the angiotensin-converting enzyme-2 (ACE2), followed by its priming by the TMPRSS2 serine protease, both present on the cellular membrane of the target cells (Hoffmann et al., 2020). The nasal cavity represents the main gate for SARS-CoV-2 entrance and the ciliated cells are the target in the respiratory tract (Mason, 2020). Interestingly, several reports point out that there is an association between the SARS-CoV-2 infection and olfactory dysfunctions (Parma et al., 2020; Vaira et al., 2020; Xydakis et al., 2020; Yan et al., 2020), and this could indicate that also the MOE may be a possible COVID-19 virus entry point. For this reason, several studies collected and analysed the MOE transcriptome from humans, non-human primates, and mice, looking at the coexpression of both ACE2 and TMPRSS2 genes in the same cell types.

Single-cell RNA-sequencing datasets revealed that non-neuronal cell populations of the MOE have comparable levels of ACE2 and TMPRSS2 transcripts with those from nasal ciliated cells, lung type II pneumocytes and ileal absorptive enterocytes (Brann et al., 2020; Butowt and Bilinska, 2020; Fodoulian et al., 2020; Hoffmann et al., 2020; Ziegler et al., 2020). SCs but also Bowman's glands, basal cells, microvillar cells, and nasal goblet secretory cells are supposed to be a possible cell target for the SARS-CoV-2 virus (Figure 15). It is important to note that SCs and OSNs are the most abundant cell population of the MOE, and they are in direct contact with anything that enters the nose. Moreover, SCs play a critical role in the maintenance of the neuroepithelial integrity. These considerations strongly suggest that SCs are a quite credible cell candidate for the SARS-CoV-2 virus infection, and their involvement could also explain anosmia in patients affected by COVID-19. Indeed, immunohistochemical experiments confirmed that ACE2 is broadly expressed in dorsally-located olfactory SCs (Figure 15, B; Brann et al., 2020; Fodoulian et al., 2020; Hopkins et al., 2020). CoV-2-induced inflammation, cell damage and altered cell turnover in the nasal epithelium are other possible explanations of smell dysfunction (Butowt and Bilinska, 2020; Marinosci et al., 2020).

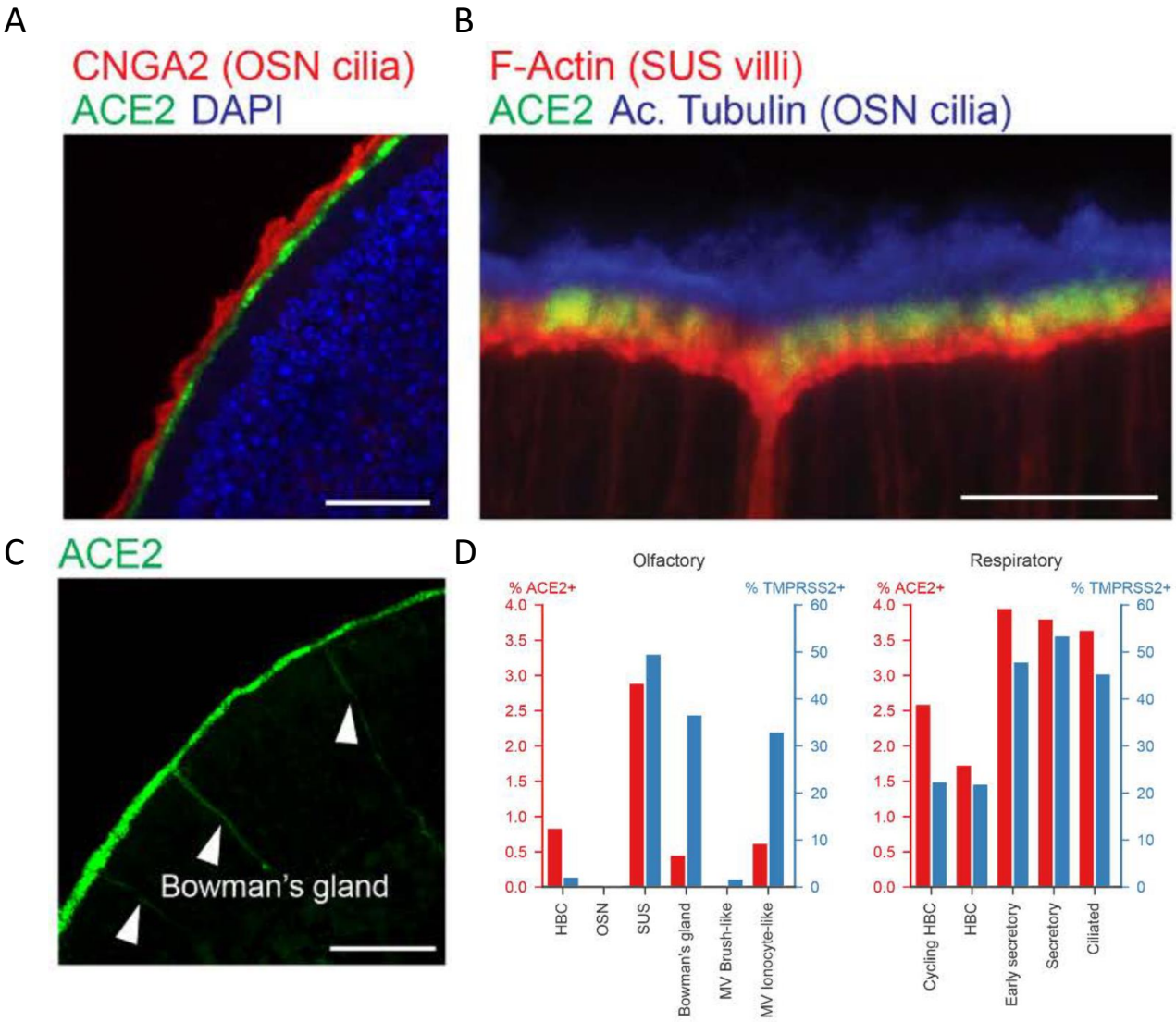

Figure 15: SARS-CoV-2 virus *s cell entry-related genes in the respiratory and olfactory epithelium.*

A- ACE2 (green) signal in the mouse dorsal MOE does not overlap with OSNs' cilia stained by CNGA2 (red; scale bar, 50 µm). B- ACE2 (green) signal is localized on mouse SCs' microvilli stained by Phalloidin (F-Actin, red), but does not overlap with OSNs' cilia stained by Acetylated Tubulin (Ac. Tubulin, blue; scale bar, 10 µm). C- Mouse Bowman's glands (arrowheads) marked by ACE2 staining (green; scale bar, 50 µm). D- Percentage of ACE2 and TMPRSS2 expression in the human respiratory and olfactory epithelium. ACE2 was detected in SCs, HBCs and other olfactory and respiratory epithelial cell types, but not in OSNs (Images modified from Brann et al., 2020).

Moreover, many viruses, including coronaviruses, have been shown to propagate from the nasal epithelium past the cribriform plate to infect the olfactory bulb and cortical areas of the brain (Hwang, 2006). Indeed, coronoviral RNA has been identified in the brains of patients and this could mediate olfactory deficits, even in the absence of lasting OE damage (Brann et al., 2020; Li et al., 2020). There are speculations about the possibility that infected people who show signs of olfactory dysfunctions may actually represent those individuals with faster and stronger immune response (Butowt and Bilinska, 2020). According to this scenario, the MOE could represent the first line of viral alert that initiates antiviral protective immune responses

shaped by the nervous system (Sepahi et al., 2019). Therefore, it could be interesting to examine groups of patients with and without the impaired sense of smell and correlate it with the severity of their symptoms and percentage of the recovery.

Furthermore, the alteration in the sense of smell reported by several patients could help to design a faster diagnosis tool to avoid the spread of the contagions. Importantly, the olfactory epithelium from the nasal cavity may be a more appropriate tissue for detection of SARS-CoV-2 virus at the earliest stages, before the onset of symptoms or even in asymptomatic people, as compared to commonly used sputum or nasopharyngeal swabs (Butowt and Bilinska, 2020). Improvements in the diagnosis of SARS-CoV-2 infection, together with effective medical treatments and vaccine, are the only way to contrast the high infectivity of this new virus and reduce its rapid spread rate.

3. Calcium-activated chloride channels

Cation channels have historically been associated with cellular excitability while chloride channels were thought to be involved more in cell-biological functions that regulate tissue homeostasis. Perhaps, for this reason, the study of anion channels has received considerably less attention. However, calcium-activated chloride channels (CaCCs) play fundamental roles in cellular physiology, including epithelial secretion of electrolytes and water, sensory transduction, regulation of neuronal and cardiac excitability, and regulation of vascular tone.

3.1 History

The first description of chloride currents mediated by channels activated upon a rise in the intracellular Ca^{2+} concentration was made by Miledi in the early 1980s in *Xenopus laevis* oocytes (Hartzell et al., 2005; Miledi, 1982). This process results in a depolarization of the oocyte's membrane that somehow prevents the fusion of additional sperm (Cross and Elinson, 1980). Later on, CaCCs have been found in several cell types including neurons; various epithelial cells; olfactory and photo-receptors; cardiac, smooth, and skeletal muscle; Sertoli cells; mast cells; neutrophils; lymphocytes; uterine muscle; brown fat adipocytes; hepatocytes; insulin-secreting beta cells; mammary glands; and sweat glands (Duran et al., 2010; Hartzell et al., 2005; Pedemonte and Galietta, 2014).

Although they have been studied for more than 30 years, their physiological roles and molecular identities have remained in question for a long time.

In 2008, three independent research teams from three continents simultaneously revealed the molecular identity of CaCCs. Using different approaches, all of them reported the same protein, TMEM16A, as a component of CaCCs (Caputo et al., 2008; Schroeder et al., 2008; Yang et al., 2008). In addition, Schroeder et al. (2008) showed that also TMEM16B is a CaCC.

The TMEM16A channel belongs to a widespread protein family of "Transmembrane proteins with unknown function 16," abbreviated as TMEM16. This family includes nine other family members labelled with letters from A to K, excluding I. TMEM16A is also known as anoctamin 1 (abbreviated ANO1, Figure 16). Since homologues are found in all eukaryotic phyla but absent in prokaryotes, this indicates that the family appeared relatively late during evolution. This family is characterized by a high degree of functional divergence, including chloride channels, phospholipid scramblases, and dual-function nonselective ion channel/phospholipid scramblases (Falzone et al., 2018; Hartzell et al., 2009; Pedemonte and Galietta, 2014).

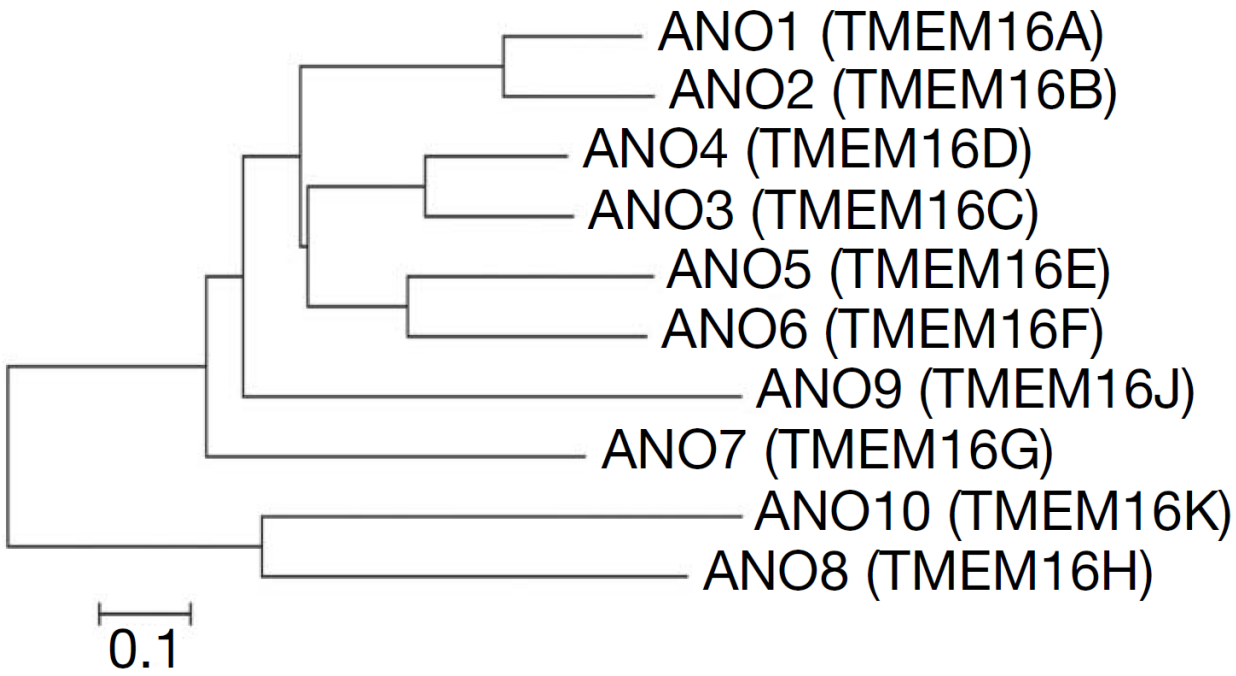

Figure 16: Phylogenetic tree of the TMEM16 family in humans.

The tree shows that TMEM16A and B share the higher amino acid identity (scale bar, 0.1 nucleotide substitutions per site; image modified from Yang et al., 2008).

3.2 Biophysical properties

CaCCs are characterized by specific biophysical hallmarks. Both the Cl^- currents elicited by TMEM16A and TMEM16B channels share very similar biophysical properties. They are activated by cytosolic Ca^{2+} and the half-maximal concentrations for their activation is in the submicromolar range. However, this Ca^{2+} concentration range varies among different cell types, possibly due to differences in molecular composition or local cellular environment (Huang et al., 2012a; Pedemonte and Galietta, 2014). TMEM16A channels have a half effective Ca^{2+} concentration of about 0.4 – 0.6 µM at positive membrane potentials (Ferrera et al., 2009), while TMEM16B channels are less Ca^{2+} sensitive, with 1 – 3 µM of half effective Ca^{2+} concentration at positive membrane potentials (Pifferi et al., 2009).

Both Cl^- channels mediate voltage- and Ca^{2+}-dependent currents. At low intracellular Ca^{2+} concentration they exhibit outward rectification of the steady-state current-voltage relationship due to activation and deactivation at positive and negative membrane potentials, respectively. At higher intracellular Ca^{2+} concentration the CaCCs' current-voltage relationship is linear (Figure 17). Moreover, the apparent affinity for Ca^{2+} increases by a change of the membrane potential to positive values (Huang et al., 2012a; Pedemonte and Galietta, 2014).

Activation and deactivation kinetics are much faster for TMEM16B channels in comparison with those of TMEM16A, with time constants differing by more than 10-fold (Caputo et al., 2008; Pifferi et al., 2009; Stephan et al., 2009). Furthermore, the value of single-channel conductance is small for TMEM16B and nearly 1 pS (Pifferi et al., 2009), while it is around 3.5 pS for TMEM16A (Adomaviciene et al., 2013). TMEM16A and TMEM16B channels are also activated by other divalent cations, such as Ba^{2+}, Sr^{2+}, and Ni^{2+}, while Zn^{2+}

has instead an inhibitory effect (Stephan et al., 2009). Finally, CaCCs preferentially permeate large anions in the following order: $SCN^- > I^- > NO_3^- > Br^- > Cl^- > F^-$ (Huang et al., 2012a; Pedemonte and Galietta, 2014).

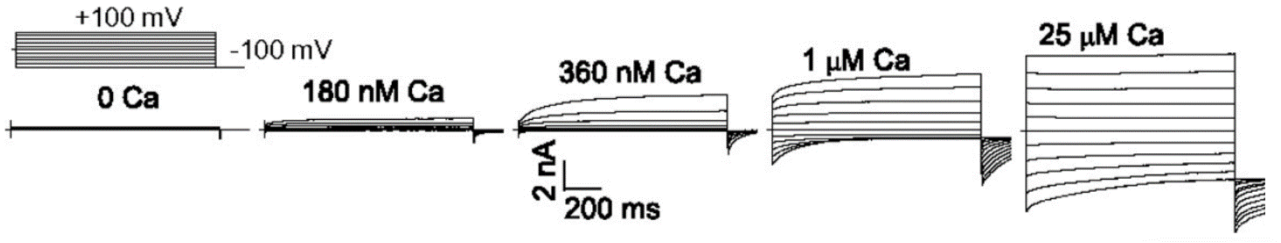

Figure 17: TMEM16A mediated currents modulated by intracellular Ca2+ and membrane potentials.

Whole-cell voltage-clamp recording from different HEK cells transfected with mTMEM16A(a,c). The voltage steps raging from –100 to 100 mV with a holding potential of 0 mV elicited TMEM16A currents with different IV relationship in presence of different amount of free intracellular Ca^{2+} (Image obtained from Xiao et al., 2011).

Another typical hallmark of CaCCs is a time-dependent current decay that occurs during prolonged stimulation by saturating Ca^{2+}, called "rundown" or "desensitization" (Huang et al., 2012a; Pedemonte and Galietta, 2014). This phenomenon produces a decrease of the CaCCs mediated currents over time that eventually leads to complete channels desensitization. It has been observed in both endogenous CaCCs (Wang and Kotlikoff, 1997) and recombinantly expressed TMEM16A (Dang et al., 2017). Moreover, Pifferi et al. (2009) found that also TMEM16B show a similar rundown at saturating Ca^{2+} concentrations both in native tissues and heterologous expression systems. The mechanisms underlying this process are still not clear. Recently, it has been proposed that it might depend on phosphatidylinositol (4,5)-bisphosphate (or simply PIP_2, Figure 18) depletion since it has been shown that PIP_2 regulates TMEM16A channel gating (Le et al., 2019; Ta et al., 2017; Tembo and Carlson, 2018; Yu et al., 2019).

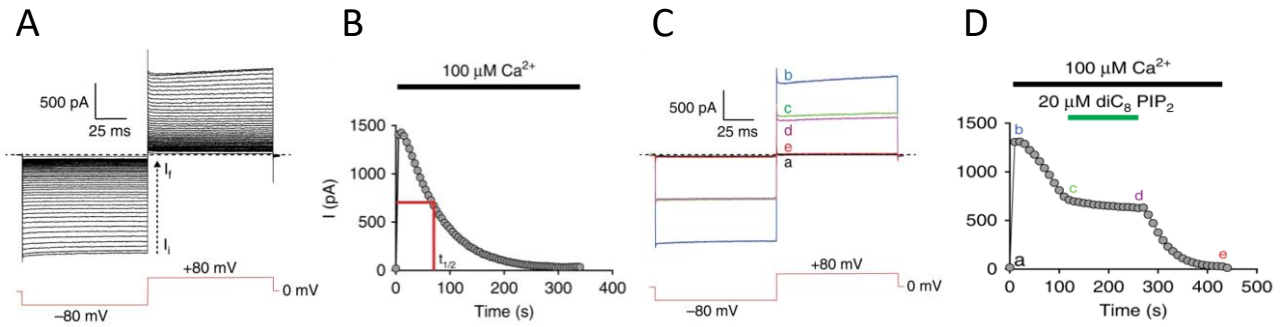

Figure 18: TMEM16A rundown is affected by PIP_2.

A- Voltage steps from -80 mV to +80 mV elicited TMEM16A mediated current in inside-out patch clamp recordings under saturating 100 µM intracellular Ca^{2+}. B- Current plot over time of the experiment shown in (A). C- Representative TMEM16A mediated current traces recorded at four time points from a different inside-out patch using the same protocol, and in the presence or absence of 20 µM diC8 PIP_2. D- Current plot over time of the experiment shown in (C). The PIP_2 application attenuates TMEM16A channel rundown (Image modified from Le et al., 2019).

3.3 Structure

Terashima et al. (2013) confirmed that purified mammalian TMEM16A proteins are the pore-forming subunits of CaCCs. Other studies suggested that these channels are dimers using electrophysiological, biochemical, and fluorescent assays (Fallah et al., 2011; Sheridan et al., 2011; Tien et al., 2013). They proposed that each monomer is independently gated by Ca^{2+} and forms a physically distinct Cl^- permeation pathway (Falzone et al., 2018; Jeng et al., 2016; Lim et al., 2016).

The structure at atomic-resolution demonstrates that TMEM16A channels are homodimers and their transmembrane region is composed of 10 helices, labelled TM1–10, for each monomer (Figure 19, B; Dang et al., 2017; Paulino et al., 2017a, 2017b). The TMEM16A channel has an extensive cytosolic domain that adopts a ferredoxin-like fold and a structured extracellular domain stabilized by four pairs of cysteine residues engaged in constitutive disulfide bonds. Each TMEM16 monomer forms an independent subunit cavity gated by two Ca^{2+}-binding sites. The hydrophilic pathway is formed by TM3–7 of each monomer (Figure 19, C). However, the pathway is partially exposed to the hydrophobic core of the membrane. These pathways have a conserved hourglass shape in which the two intracellular and extracellular vestibules are separated by a narrow constriction located just above the Ca^{2+}-binding sites. This groove-like structure lined by TM4–7, with minimal participation of TM3, forms the anion-selective pore through which Cl^- ions diffuse in the CaCCs. Several basic residues in the intra- and extracellular vestibules make the pore electropositive, suggesting electrostatic discrimination against cations (Brunner et al., 2014; Dang et al., 2017; Falzone et al., 2018; Paulino et al., 2017a, 2017b).

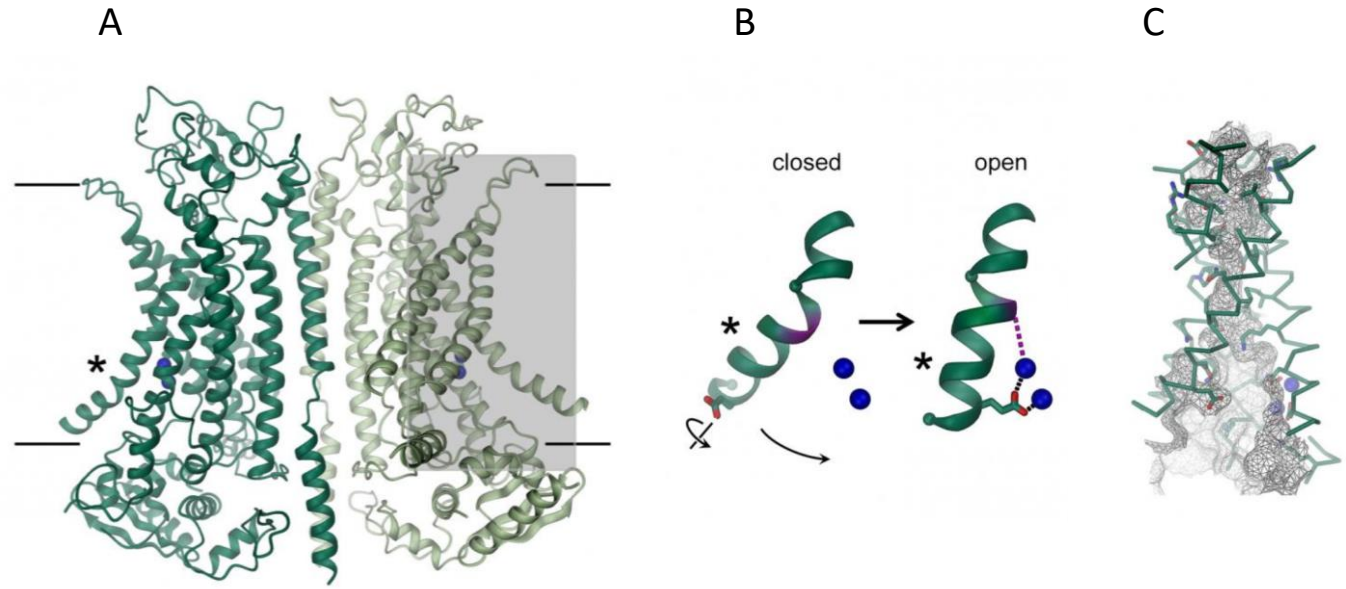

Figure 19: Structures of the mouse TMEM16A channel.

*A- Ribbon representation of the structures of the Ca^{2+}-bound mTMEM16A channel (black lines = membrane boundaries; blue spheres = Ca^{2+} ions bound to the Ca^{2+}-binding sites; * = Ca^{2+}-binding sites; grey rectangle = ion conduction pore). B- Conformational changes of the TM6 after Ca^{2+} binding (blue spheres = bound Ca^{2+} ions). C- Highlights of the ion conduction pathway of the mTMEM16A subunit (grey mesh = pore surface; blue spheres = Ca^{2+} ions; images modified from Paulino et al., 2017a).*

The Ca^{2+}-binding sites are formed by highly conserved acidic residues on TM6–8. They are located approximately at one-third of the membrane span from the inner side, rationalizing the synergistic effects of

voltage and Ca^{2+} binding on channel opening (Figure 19, A; Dang et al., 2017; Falzone et al., 2018; Paulino et al., 2017a, 2017b). A pronounced rearrangement of TM6 is the main consequence of Ca^{2+} unbinding, while the rest of the protein remains almost unchanged, as revealed by structures of TMEM16A in the presence of zero, one, and two Ca^{2+} ions. In the absence of Ca^{2+}, the intracellular portion of TM6 moves away from the TM7 domain, resulting in a pronounced narrowing of the intracellular vestibule and pore constriction. The TM6 helix appears to serve as a key allosteric connection through which Ca^{2+}, voltage, and extracellular Cl^- act to regulate the opening of the TMEM16A pore. Moreover, the Ca^{2+} unbinding alters the electrostatic environment of the pathway, and the increased electronegativity is likely to strongly impede permeation of the negatively charged Cl^- ions. This combination of steric and electrostatic effects may cooperate in the closing of the TMEM16A pore (Dang et al., 2017; Falzone et al., 2018; Paulino et al., 2017a; Peters et al., 2018).

3.4 TMEM16A

3.4.1 Expression pattern

TMEM16A is broadly expressed in airway epithelia, in acinar cells from lachrymal, airway submucosal, parotid, submandibular and pancreas glands, in the interstitial cells of Cajal of the gastrointestinal tract, in the trachea, and in smooth muscle cells of the reproductive tracts and airways, including portal vein, lymphatic vessels and pulmonary artery, in sensory neurons from rat dorsal root ganglia and vomeronasal organ (Falzone et al., 2018; Hartzell et al., 2005; Huang et al., 2012a; Pedemonte and Galietta, 2014; Whitlock and Hartzell, 2017).

The presence of alternative splicing and alternative promoters results in tissue-specific expression of different TMEM16A isoforms. A prominent functional implication of this phenomenon is that the inclusion or exclusion of different exon changes dramatically the sensitivity to cytosolic Ca^{2+}, resulting in a different modulation of the TMEM16A activity (Ferrera et al., 2009; Pedemonte and Galietta, 2014).

3.4.2 Relevant physiological roles

The transepithelial movement of Cl^- is the main driving force for fluid secretion by exocrine gland acinar cells. The Cl^- secretion requires the coordinated activity of various channels and transporters localized in the apical and basolateral epithelial membranes. The TMEM16A channel is involved in this physiological mechanism controlling processes that range from smooth muscle contractility to epithelial secretion. In particular, in cystic fibrosis patients, the TMEM16A channel has been proposed as a promising target to rescue the impaired Cl^- secretion caused by the loss of function of the cystic fibrosis transmembrane conductance regulator (CFTR) protein (Huang et al., 2012a; Pedemonte and Galietta, 2014).

CaCCs in smooth muscle cells are expected to sustain contraction producing membrane depolarization, especially in response to excitatory agonists. Several laboratories are focusing their attention to find a link between CaCCs and TMEM16A protein in smooth muscle cells. Interestingly, the TMEM16A expression is downregulated in smooth muscle cells isolated from the basilar arteries of hypertensive rats, (Wang et al., 2012) while is upregulated in pulmonary arterial smooth muscle cells with chronic hypoxia and pulmonary hypertension (Forrest et al., 2012; Manoury et al., 2010; Sun et al., 2012). TMEM16A may be a drug target to prevent bronchoconstriction in asthma and hypertension (Huang et al., 2012a; Pedemonte and Galietta, 2014).

Sensory neurons from rat dorsal root ganglia are among the first mammalian cells in which CaCCs were studied (Mayer, 1985). Liu et al. (2010) showed that bradykinin simultaneously inhibits M-type K^+ channels and activates TMEM16A in nociceptors. Both these effects contribute to membrane depolarization and the generation of ascending nociceptive signals. Moreover, Cho et al. (2012) demonstrated that sensory neurons respond to high temperature with activation of TMEM16A mediated Cl^- currents. In conclusion, TMEM16A expressed in nociceptive neurons represents an important target for analgesic therapies (Huang et al., 2012a; Pedemonte and Galietta, 2014).

3.4.3 Relevant pathological roles

Before the discovery of TMEM16A as a CaCC, the same gene was already known to oncologists by various names: discovered on gastrointestinal stromal tumours protein 1 (DOG-1), oral cancer overexpressed 2 (ORAOV2), and tumour-amplified and overexpressed sequence 2 (TAOS-2; Huang et al., 2012a; Pedemonte and Galietta, 2014). Indeed, TMEM16A is highly expressed in multiple different cancer types, including gastrointestinal stromal tumours (GIST; West et al., 2004), oral and oesophageal squamous cell carcinoma (Huang et al., 2006). Moreover, TMEM16A has been suggested to serve as a hallmark for GIST, although its function in tumour biology and the reason for its high expression is unknown. Interestingly, TMEM16A expression is associated with reduced survival and increased metastatic potential, and its knockdown or inhibition leads to reduced malignancy of the tumours (Ayoub et al., 2010; Duvvuri et al., 2012; Ruiz et al., 2012). In summary, TMEM16A is an important diagnostic and prognostic marker and may represent an important drug target in some types of human cancers (Pedemonte and Galietta, 2014).

Another relevant role of TMEM16A concerns the regulation of normal trachea development in mice, and TMEM16A deletion is lethal. Rock et al. (2008) reported that mice homozygous for a null allele of TMEM16A died within one month of birth. The death is mainly due to the presence of ventral gaps in the cartilage rings of the trachea, which caused the trachea to collapse, thus mimicking human tracheomalacia. Most probably, the cartilage defect is actually secondary to defects in the epithelium or trachealis muscle, where TMEM16A is normally expressed. Moreover, TMEM16A knock-out animals also show an accumulation of mucus and impairment of mucociliary transport in the airways, mimicking the cystic fibrosis disease phenotype (Pedemonte and Galietta, 2014).

3.5 Other TMEM16 family members:

Nowadays, it is known that the majority of the TMEM16 family members are phospholipid scramblases. However, this was completely unexpected since the first characterized homologues, TMEM16A and B, were both CaCCs, indicating that was reasonable to think that the TMEM16s were a family of CaCCs. Indeed, it was a real surprise the discover that TMEM16F was involved in phospholipid trafficking, leading to the conclusion that the TMEM16 family is composed of both ion channels and phospholipid scramblases.

3.5.1 TMEM16B

Analysis of amino acid sequence similarity within TMEM16 proteins revealed that TMEM16A and TMEM16B share the higher amino acid identity of about 62%, resulting in the closely related members belonging to the same subfamily (Milenkovic et al., 2010). Schroeder et al. (2008) were the first to show that TMEM16B was associated with CaCC activity, a result subsequently confirmed by other teams (Pifferi et al., 2009; Stephan et al., 2009; Stöhr et al., 2009).

TMEM16B is mainly expressed in neuronal tissues, and it is required for correct action-potential firing and axonal targeting in hippocampal, inferior olivary, and olfactory sensory neurons (Huang et al., 2012b; Pietra et al., 2016; Schreiber et al., 2010; Zhang et al., 2017). TMEM16B is highly expressed in the photoreceptor (cones and rods) of the mouse retina (Stöhr et al., 2009). In humans, a homozygous deletion of part of the TMEM16B gene has been found in severe von Willebrand disease type 3, a hereditary coagulation abnormality (Schneppenheim et al., 2007); while a Japanese a genome-wide association study found that TMEM16B is associated with panic disorder in the Japanese population (Otowa et al., 2009).

3.5.2 TMEM16

The TMEM16 family is functionally divergent, and it is composed of CaCCs and Ca^{2+}-dependent scramblases, some of which also mediate nonselective ion transport.

Among the TMEM16 channel/scramblase homologues, TMEM16F is one of the most highly expressed members in different tissues and cell types (Falzone et al., 2018; Schreiber et al., 2010). In humans, TMEM16F plays a key role in controlling blood coagulation, and loss-of-function mutations in the TMEM16F gene cause Scott syndrome, a mild bleeding disorder due to defective Ca^{2+}-dependent exposure of phosphatidylserine in activated platelets (Castoldi et al., 2011; Suzuki et al., 2010). Moreover, TMEM16F gene deletion in mice recapitulates well the Scott syndrome phenotype (Baig et al., 2016). Interestingly, TMEM16F is also endowed with ion channel activity, although there is no consensus about its biophysical properties among different studies (Falzone et al., 2018; Huang et al., 2012b; Pedemonte and Galietta, 2014).

The TMEM16E channel/scramblase prevalently localizes to intracellular compartments and mediates both channel and scramblase activities (Duran et al., 2011). In humans, it has been associated with a complex panoply of phenotypes, and TMEM16E mutations cause limb-girdle muscular dystrophy, Miyoshi myopathy type 3 and gnathodiaphyseal dysplasia 1, suggesting that this protein plays a role in membrane fusion and repair and bone formation (Bolduc et al., 2010; Falzone et al., 2018; Marconi et al., 2013). However, a clear picture of its functional properties is far to be reached.

Very few it is known at the moment about the other members of the TMEM16 family. TMEM16C regulates pain processing in rat sensory neurons (Huang et al., 2013), TMEM16K mutations cause autosomal recessive ataxia, attentional disorders, epilepsy, and porencephalic cysts (Chamova et al., 2012), TMEM16G (also known as NGEP) is involved in the formation of cell–cell contacts in healthy and cancerous prostate tissues (Bera et al., 2004), and it has been proposed that TMEM16J might function as a cation channel activated by the cAMP/PKA signalling pathway (Kim et al., 2018).

Collectively, these findings highlight the broad importance of the TMEM16 family members in human physiology and disease. Overall, their study remains a work in progress as novel functions are identified for known homologues, and new roles are discovered for poorly characterized ones.

3.6 CaCCs in the MOE

Both the two members of the TMEM16 family that code for CaCCs, TMEM16A and B, are found in the MOE. However, they show a different temporal and cellular expressions pattern consistent with a diverse physiological significance for the two proteins.

Few studies investigated the TMEM16A expression in the mouse MOE, finding that the protein is expressed on the apical portion of SCs and the apical membrane of Bowman's gland ducts (Figure 20; Dauner et al., 2012; Maurya and Menini, 2014; Maurya et al., 2015). Moreover, two of them reported a dynamic expression of TMEM16A during mouse embryonic development. According to the authors, TMEM16A is

expressed at the apical surface of the entire OE at embryonic day E12.5 while from E16.5 its expression is restricted to a region near the transition zone with the respiratory epithelium (Figure 20, D; Maurya and Menini, 2014; Maurya et al., 2015). Moreover, they did not find evidence of altered morphology in the MOE from TMEM16A$^{-/-}$ mice, indicating that TMEM16A does not seem to be involved in the regulation of proliferation and development of the mouse MOE (Maurya et al., 2015). However, none of the previous works confirmed the functional expression of TMEM16A in the MOE, and if it is able to mediate Cl^- currents contributing to the regulation of the extracellular ionic environment in the mucus layer that covers the epithelium.

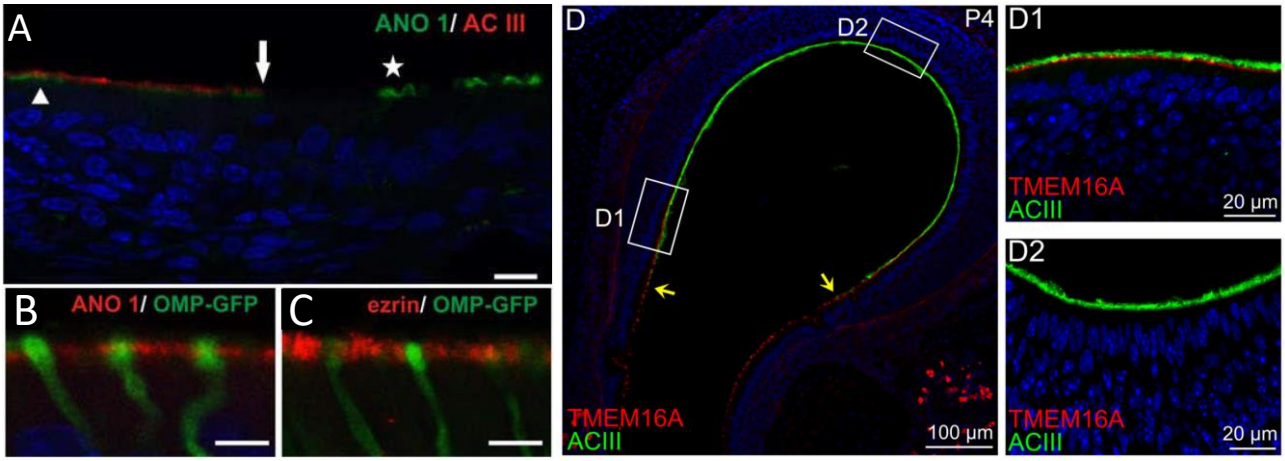

Figure 20: Expression of TMEM16A (ANO1) channels in the main olfactory epithelium.

A- Confocal image of the rat MOE and respiratory epithelium. TMEM16A (ANO1, green) is expressed both in the MOE and respiratory epithelium and it does not colocalize with ACIII (red; arrowhead = MOE; arrow = transition between the MOE and the respiratory epithelium; star = respiratory epithelium; DAPI staining for cell nuclei; scale bar, 15 µm). B,C- Apical portion of the MOE from the OMP-GFP mouse. TMEM16A (ANO1, red) is expressed on SCs' microvilli marked in red with ezrin (Images modified from Dauner et al., 2012). D- Confocal image of the mouse MOE and respiratory epithelium. TMEM16A (red) is expressed in the respiratory epithelium and in portions of the MOE in contact with the respiratory epithelium indicated by the yellow arrows. ACIII is stained in green. In D1 and D2 magnifications of the image in D. The TMEM16A and ACIII staining does not colocalize (DAPI staining for cell nuclei; images modified from Maurya et al., 2015).

In 2009, the TMEM16B channel was proposed as the olfactory CaCC. Indeed, the olfactory cilia proteome of mouse showed high levels of TMEM16B expression (Stephan et al., 2009). TMEM16B was able to mediate Cl^- currents with similar properties to those of native olfactory CaCCs when heterologously transfected (Figure 21, A-C; Pifferi et al., 2009; Stephan et al., 2009). Moreover, immunohistochemistry assays showed that it is strongly expressed in the ciliary layer of OSN (Billig et al., 2011; Rasche et al., 2010; Sagheddu et al., 2010). Three years later, Billig et al. (2011) generated the first mouse model where the TMEM16B gene was knocked out. The CaCCs mediated currents were completely abolished in OSNs from TMEM16B KO mice, confirming that TMEM16B is a mandatory part of the Cl^- channel. Surprisingly, KO mice showed no impairment in the ability to detect odorants, and the authors concluded that CaCCs are dispensable for olfaction (Billig et al., 2011). However, Pietra et al. (2016) found that the same mouse model required longer times to identify new odorants. Moreover, the TMEM16B deletion affected the firing pattern of the OSNs prolonging the action potentials train duration and increasing the number of spikes in response

to a stimulus (Figure 21, D-E). Interestingly, Neureither et al. (2017) revealed that the detection of an unfamiliar odorant and its memorization requires the TMEM16B-mediated signal amplification. TMEM16B-deficient mice display impaired cue-tracking behaviour when challenged with unfamiliar odorants at low concentrations. Li et al. (2018) found that TMEM16B mediated currents clearly predominated in the mouse olfactory responses, confirming previous results obtained in rat (Li et al., 2016). The Cl^- current activated during the olfactory transduction accounts for about the 80% of the response (Li et al., 2018). Furthermore, Zak et al. (2018) provided the *in vivo* evidence that odorant-evoked responses in TMEM16B KO mice were consistently larger for a variety of odorants and concentrations. For this reason, KO mice revealed clear olfactory behavioural deficits in an open arena, needing a much longer time to localize odorants. Finally, Reisert and Reingruber (2019) revealed that a transduction pathway based on Cl^- efflux circumvents the problems linked to a Na^+ current based signal amplification. Indeed, Na^+ currents are much more affected by changes in the external mucus composition. Moreover, the ciliary Na^+ increase would negatively affect the Ca^{2+} clearance by $Na^+/Ca^{2+}/K^+$ exchange. Finally, the dramatic change in osmotic pressure produced by intraciliary Na^+ increase would result in cilia damage. Altogether, these results indicate that the TMEM16B channel is an important player involved in the complex tuning mechanisms of the olfactory responses.

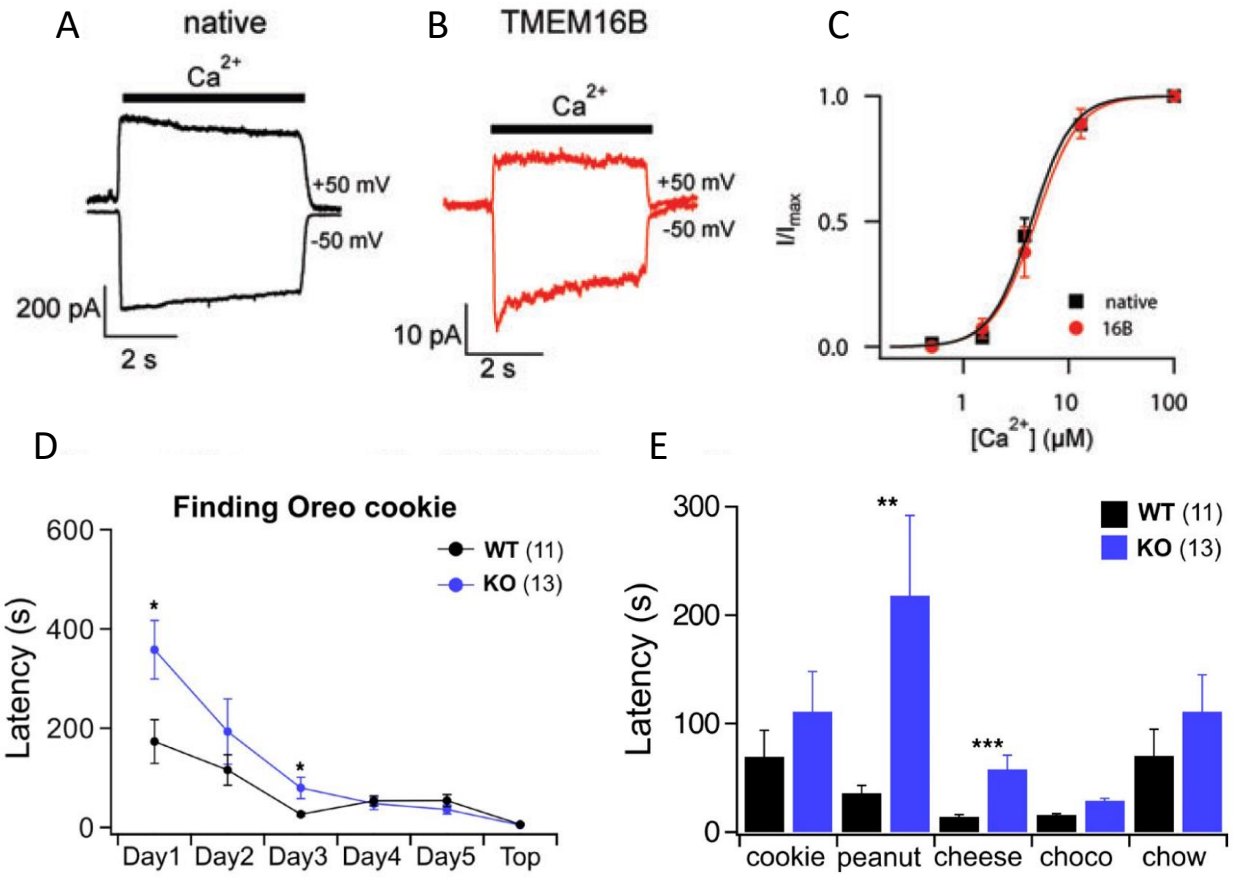

Figure 21: TMEM16B channels in the main olfactory epithelium.

A- TMEM16B mediated currents from an OSN's insid-out excised patch. The current was activated by application of 100 µM of Ca^{2+} at holding potential of – and +50 mV B- Similar results were obtaioned from TMEM16B upon heterologous expression in HEK-293 cells. C- Hill equation fitting of the normalized currents measured at −50 mV plotted versus Ca^{2+} concentrations (Images obtained from Pifferi et al., 2012). D- WT and KO mice for TMEM16B were trained to find foods buried in their cage. In the first days of the experiment

*the KO mice needed more time to localize the food. E- The same mice were exposed to known (oreo cookies and chow) and unknown odorants (peanut, cheese and chocholate). Mann-Whitney U test: *, P < 0.05; **, P < 0.01; ***, P < 0.001. Mean ± SEM from 11 WT and 13 KO mice (Images obtained from Pietra et al., 2016).*

Further studies are required to clarify more in detail the roles of the CaCCs TMEM16A and B in the MOE.

4. Stomatin family:

The stomatin family of proteins is composed of members containing a characteristic core domain called stomatin-domain. These proteins are widely expressed in various tissues and all classes of life. Several orthologues have been found in vertebrates, invertebrates, plants, and microorganisms. The ubiquity of proteins of the stomatin family and their high degree of homology suggest that they may be involved in crucial specific cellular functions, which have yet to be defined.

4.1 History

Interest in stomatin proteins family started when red blood cells of patients with the haemolytic anaemia Hereditary Stomatocytosis were found to be lacking a major membrane protein in the band 7 region. For still unknown reasons, before cellular lyse the erythrocyte morphology takes on a “mouth-shaped” area called stoma that names the disease (Figure 22). For the same reason, the founding member of this protein family was termed stomatin (Dacie, 1970; Eber et al., 1989; Hiebl-Dirschmied et al., 1991a; Lande et al., 1982; Lock et al., 1961). However, not all patients with Hereditary Stomatocytosis were lacking stomatin in the red cells. Indeed, stomatin is only missing in erythrocytes from Overhydrated Hereditary Stomatocytosis patients and not in Dehydrated Hereditary Stomatocytosis (Kanzaki and Yawata, 1992; Stewart et al., 1993).

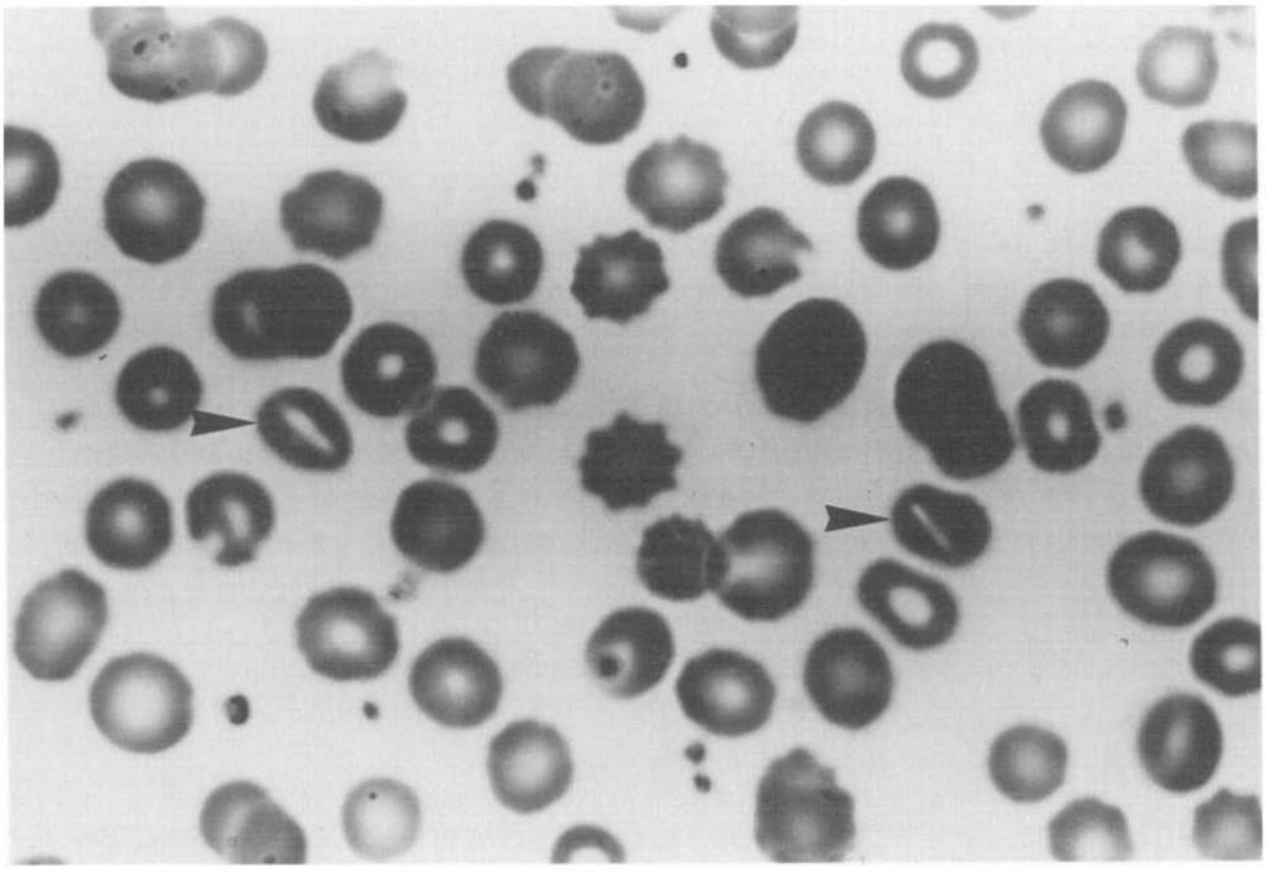

Figure 22: Mouth-shaped erythrocytes from a patient affected by overhydrated hereditary stomatocytos.

The arrows indicate stomatocytes in Wright-Giemsa-stained blood (Image obtained from Stewart et al., 1993).

After isolation and characterization of stomatin, proteomic studies on the erythrocytes from Overhydrated Stomatocytosis patients revealed the total or partial absence of stomatin proteins in the membranes of red cells (Gallagher and Forget, 1995; Stewart et al., 1993). Surprisingly, no genetic defects were found in the stomatin gene amongst patients suffering from stomatocytosis, and mice with a null allele of the stomatin gene do not display stomatocytosis (Fricke et al., 2003; Zhu et al., 1999). The erythrocytes' membrane displays a pronounced "leakiness" to monovalent cations in cases of stomatocytosis, and this led to the hypothesis that stomatin may regulate the activity of membrane channels or transporters (Stewart et al., 1993).

Following the discovery of the stomatin protein, several new members of this family have been identified. It is emerging that the stomatin-like proteins play a significant role in membrane organisation and the regulation of membrane-associated proteins, including ion channels. However, the molecular mechanisms by which members of the stomatin family mediate their effects remain still elusive (Browman et al., 2007; Lapatsina et al., 2012; Salzer et al., 2007).

4.2 Structures

All the proteins of the stomatin family are identified by the presence of the characteristic and structurally conserved stomatin-domain (Tavernarakis et al., 1999). Moreover, the same domain is found in members of the prohibitin, flotillin/reggie, erlin and bacterial HflK/HflC protein families and it has accordingly also been called the SPFH domain (Stomatin, Prohibitin, Flotillin, HflK/HflC domain) and more recently the PHB domain (prohibitin homology domain; Browman et al., 2006; Morrow and Parton, 2005; Rivera-Milla et al., 2006). The stomatin family forms a distinct branch of the SPFH family, which diverged early on from other eukaryotic SPFH proteins, such as prohibitins and flotillins, as confirmed by phylogenetic analysis (Browman et al., 2007; Lapatsina et al., 2012; Salzer et al., 2007).

Although several stomatin members are widely distributed amongst all forms of life, the amino-acid sequence of the stomatin-domain is remarkably conserved in mammals, plants, bacteria, and archaea, as revealed by genome and transcriptome analyses (Green and Young, 2008). There are five members in the mammalian stomatin family: stomatin, stomatin-like protein-1 (STOML-1), stomatin-like protein-2 (STOML-2), stomatin-like protein-3 (STOML-3) and podocin. Except for STOML-2, the other members of the family share 40 – 84% sequence similarity in the stomatin-domain and their membrane topology and primary domain organisation is quite similar (Green and Young, 2008).

The typical structure of a stomatin-domain protein is given by the presence of two principal components: a single, relatively short, hydrophobic transmembrane domain followed by the core stomatin domain (Figure 23). For this reason, the members of this family are integral membrane proteins, and only a single conserved proline residue in the hydrophobic region is required for the formation of the hairpin structure inserted in the membrane. Both N- and C-termini of the protein are intracellular (Figure 23), and they differ a lot among the family members conferring them different properties like cytoskeleton binding and homo-oligomerisation (Lapatsina et al., 2012; Salzer et al., 1993; Snyers et al., 1998, 1999).

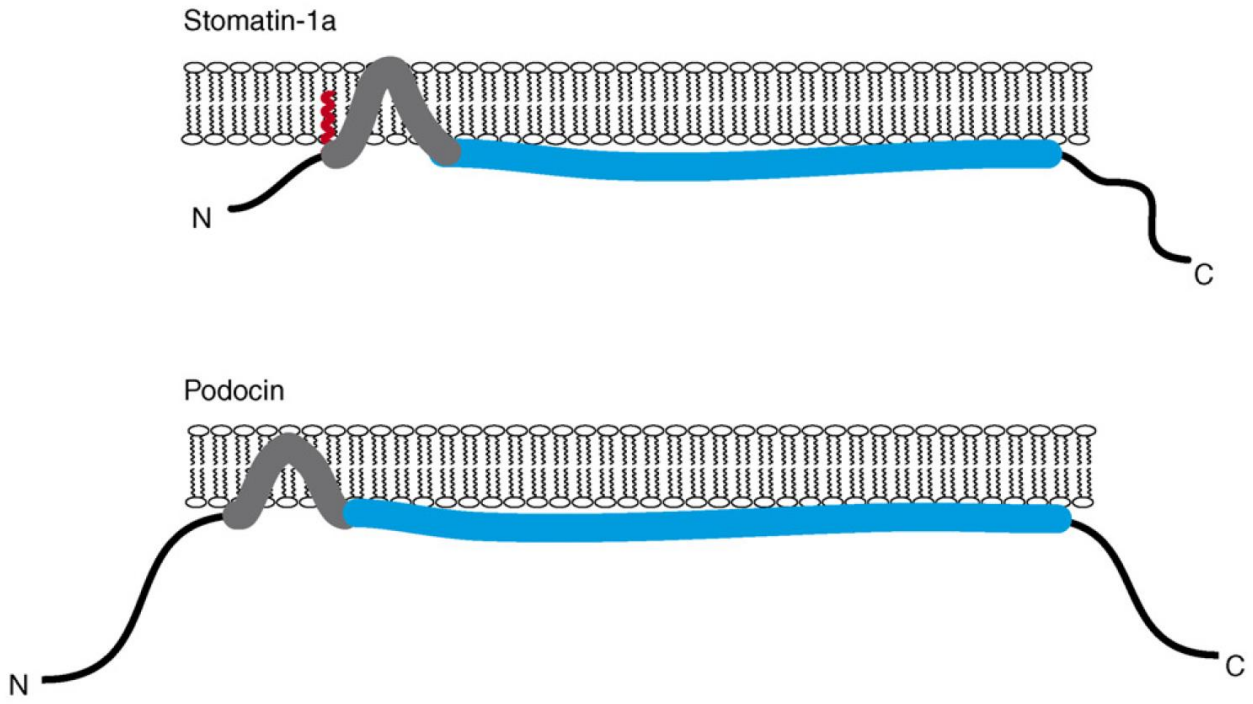

Figure 23: Predicted membrane topology of STOML-1 and Podocin.

STOML-1 shows a hairpin-like transmembrane domain (grey) that is inserted in the plasma membrane, while the N- and C- terminal are facing the cytoplasm. In blue the SPFH domain. In red is showed the palmytoilation of a N-terminal residue of the transmembrane domain. Podocin shows a similar topology but it lacks of palmytoilation and it has a longer C-terminal cytoplasmic tail (Image modified from Browman et al., 2007).

Stomatin proteins isolated by solubilization and density gradient centrifugation are organized in high-order homo-oligomers (Figure 24). The mechanism underlying the oligomer formation is still not understood. However, the stomatin chains are not covalently linked because they are readily identified by SDS-PAGE (Salzer and Prohaska, 2001; Snyers et al., 1998). Since an atomic resolution structure of the mammalian stomatin protein is still missing, it is of great interest the solved crystal structure of the archaebacterial stomatin from Pyrococcus horikoshii to predict the topological and structural characteristics of the mammalian stomatins (Figure 24). Yokoyama et al. (2008) have shown that the core stomatin-domain is per se able to oligomerise forming a stable trimer, while α helical extensions at the C-terminus may participate in membrane bending.

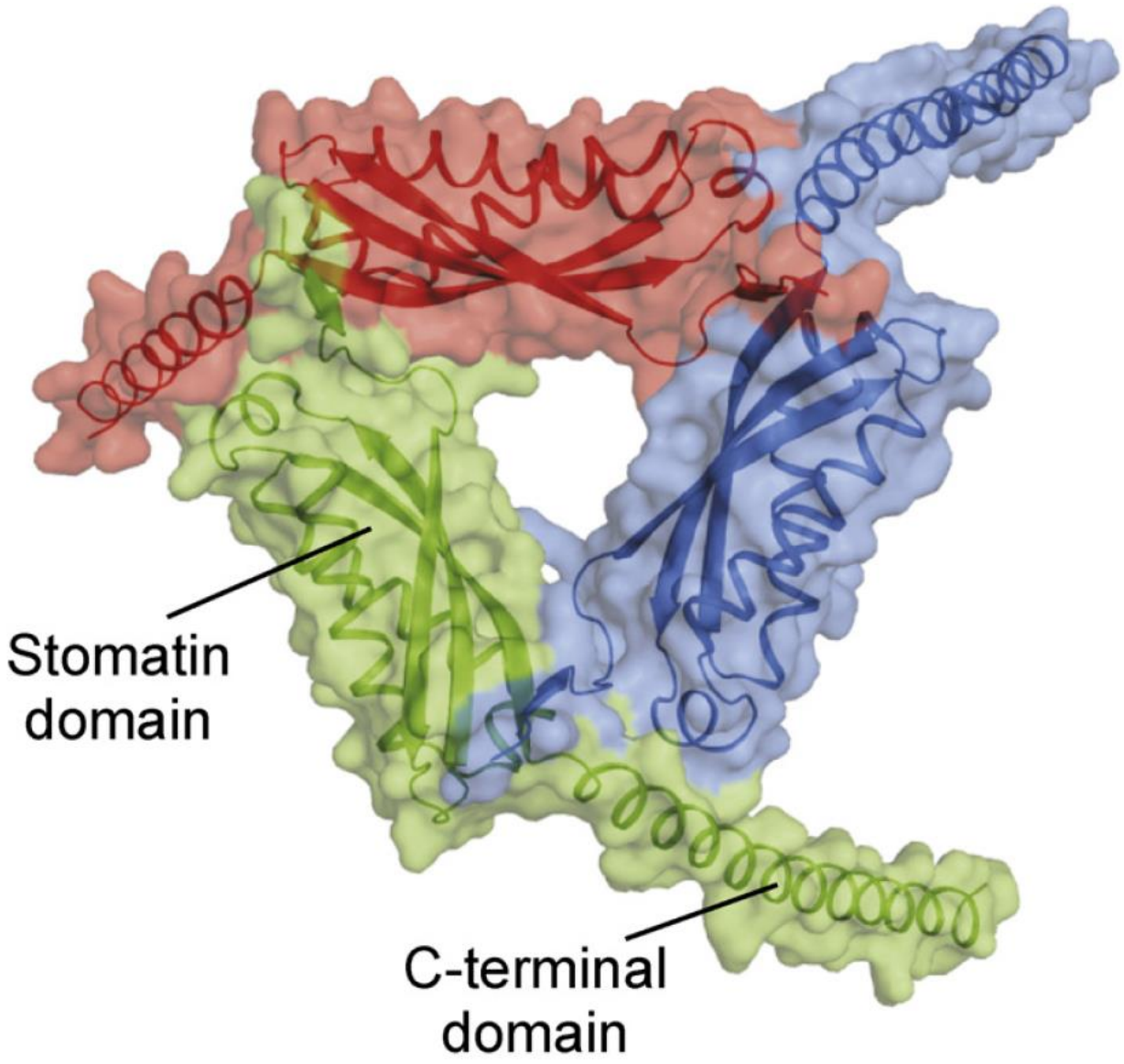

Figure 24: Predicted homology model of trimeric STOML-3 based on the known structure of the trimeric phStomatin.

The model was created using SWISS-MODEL. The C-terminal and SPFH domain are indicated (Image modified from Lapatsina et al., 2012).

4.3 Expression pattern

Apart from being a major erythrocyte membrane protein, it was immediately noticed the stomatin's widely expression in several tissues and cell types (Hiebl-Dirschmied et al., 1991b; Stewart et al., 1992). This expression is not surprising if we think that the promoter region of the stomatin gene showed typical features like those of a household gene. Moreover, Northern blot analyses and microarray databases (like the Gene Expression Atlas, at http://symatlas. gnf.org/SymAtlas/), strongly confirmed this evidence. However, the expression level of stomatin transcripts was comparatively low in the brain in comparison with other organs and tissues (Salzer et al., 2007; Unfried et al., 1995).

In nucleated cells, stomatin is found mainly in two specific cellular compartments: the plasma membrane and the juxtanuclear vesicle region (Snyers et al., 1997). A similar distribution pattern was found in epithelial cells, fibroblasts, and endothelial cells. Stomatin is particularly concentrated in the microvilli of polarized cells, and it is associated with actin microfilaments probably thanks to adaptor proteins (Browman et al., 2007; Salzer et al., 2007; Snyers et al., 1997).

When cell membranes are solubilized with Triton X-100 at a low temperature, the stomatin-domain proteins display a strong enrichment in the detergent-resistant membranes (Salzer and Prohaska, 2001; Snyers et al., 1999). For this reason, all stomatin family members, except for STOML-2 which lacks a hydrophobic intramembrane domain, have been classed as lipid raft-associated proteins (Morrow and Parton, 2005; Wang and Morrow, 2000).

4.4 Stomatin

Stomatin is the founding member of the stomatin proteins family and is a ubiquitously expressed membrane protein unrelated to any known ion channel or transporter. Like other proteins playing a structural role in plasma membrane organisation, such as ezrins and flotillins, stomatin forms higher-order oligomers, is associated with lipid rafts and is phosphorylated and palmitoylated (Gallagher and Forget, 1995; Salzer et al., 1993; Snyers et al., 1998, 1999; Stewart et al., 1993).

There is clear evidence that stomatin can directly modulate the activity of members of the acid-sensing ion channel (ASIC) family. The overexpression of stomatin in cells expressing ASIC3 and ASIC2a results into a profound loss of proton-gated currents mediated by ASIC3 and increased desensitisation of ASIC2a currents (Price et al., 2004). Proton-gated ASICs channels are expressed in different parts of the nervous system and are involved in nociception and mechanosensation (Wemmie et al., 2006). Potentially, stomatin could regulate ASICs activity in the nervous system. However, these models are based on studies using heterologous expression system, and the observed interaction still needs to be confirmed in vivo (Browman et al., 2007; Lapatsina et al., 2012).

In human erythrocytes, stomatin interacts with and modulates the activity of the glucose transporter type 1 (GLUT-1). The amount of exogenously expressed stomatin inversely correlates with GLUT-1 activity, and this reciprocal relationship was observed also in vivo studies (Montel-Hagen et al., 2008; Zhang et al., 2001). A possible explanation of the depressing effect of stomatin on the GLUT-1 activity is that reversible recruitment of GLUT-1 to stomatin-containing rafts could result in a novel mechanism of GLUT-1 regulation (Rubin and Ismail-Beigi, 2003). However, the mechanisms by which stomatin regulates the activity of GLUT-1 are far to be elucidated (Lapatsina et al., 2012; Salzer et al., 2007).

Finally, stomatin is expressed in sensory ganglia, where it may regulate ASICs channels as well as mechanosensory transduction as has been shown for mechanosensory abnormality protein 2 (MEC-2), the best characterised of the nine stomatin-like orthologues in *Caenorhabditis elegans* (Green and Young, 2008; Huang et al., 1995; Mannsfeldt et al., 1999). Indeed, a sub-population of skin mechanoreceptors from stomatin knock-out mice revealed reduced mechanosensitivity in the absence of changes in membrane excitability (Martinez-Salgado et al., 2007). However, these effects on mechanotransduction were much less pronounced than those found after gene deletion for the closely related STOML-3 (Wetzel et al., 2007).

4.5 STOML-1

STOML-1 is a membrane protein that consists of two distinct structures: a typical stomatin-domain at the N-terminus and an additional sterol carrier protein-2 (SCP-2) domain at the C-terminus. A similar

pattern has been found also for the orthologue of STOML-1 in *Caenorhabditis elegans* called uncoordinated protein 24 (UNC-24). The SCP-2 domain is involved in lipid/sterol transport and transfer (Barnes et al., 1996; Sedensky et al., 2004). Up to now, there is no clear evidence about an in vivo function for this protein. In cell lines, STOML-1 is targeted to the late endosomal compartment where it interacts with stomatin, while it is mainly expressed in the brain in comparison with other tissues (Mairhofer et al., 2009; Wang and Morrow, 2000). Unpublished studies from the Lewin group reported in Lapatsina et al. 2012, show that STOML-1 is significantly expressed in a subpopulation of sensory neurones in the dorsal root ganglia. The Lewin group has generated a mice model with a null mutation of the STOML-1 gene, and these mice may indeed have a deficit in mechanosensory function (Lapatsina et al., 2012). Further studies are necessary to elucidate the precise role of this protein in the nervous system and whether STOML-1 has a role in the physiological modulation of ion channels.

4.6 STOML-2

STOML-2 is the only stomatin-family member that lacks a hydrophobic domain for membrane anchoring at its N-terminus. It is a peripheral membrane protein that most probably separated early in the evolution from the rest of the family (Green and Young, 2008; Wang and Morrow, 2000). STOML-2 not only is expressed in mature erythrocytes, but it is widely distributed in several tissues (Wang and Morrow, 2000). Moreover, STOML-2 shows a mitochondrial localisation sequence at its N-terminus and many mitochondrial proteomic studies have confirmed its presence in mitochondria (Da Cruz et al., 2003; Reifschneider et al., 2006; Schmitt et al., 2006). In erythrocytes and neuronal cells, STOML-2 can interact with the peripheral membrane skeleton forming high-order oligomers. The membrane attachment is probably due to lipid modifications similar to the palmitoylation of stomatin (Kirchhof et al., 2008; Lapatsina et al., 2012; Wang and Morrow, 2000).Mitochondrial stress results in up-regulation of STOML-2 and increases in protein turnover. Moreover, depletion of STOML-2 was shown to lead to degradation of prohibitins and subunits of complexes I and IV of the mitochondrial respiratory chain (Schmitt et al., 2006). It has been proposed that STOML-2 may be required to protect mitochondria from stress-induced mitochondrial hyperfusion (Tondera et al., 2009).

Interestingly, STOML-2 is up-regulated in many different cancer types and premalignant lesions, thereby possibly serving as a marker for early detection of specific forms of cancer. It is associated with higher levels of mortality, and it has been reported that STOML-2 promotes cell proliferation and cell adhesion. STOML-2 may work as a transmembrane linker between the extracellular matrix and the cytoskeleton (Cui et al., 2007; Salzer et al., 2007; Zhang et al., 2006).

Finally, it is reasonable to think that STOML-2 plays a role in essential biological functions because mice carrying null alleles of the stoml-2 gene are not viable (Heppenstall, Seifert and Lewin unpublished). However, more detailed analysis of the STOML-2 physiology is required to clarify the mode of action of this intriguing protein.

4.7 STOML-3

STOML-3, also known as stomatin-related olfactory protein (SRO), was first identified as a specific protein of unknown function expressed by OSNs (Kobayakawa et al., 2002). STOML-3 is the closest relative of stomatin, and it shares about 77% of similarity in its amino acid sequence also with the stomatin orthologue MEC-2. However, STOML-3 expression is restricted to just a few neuronal tissues including mechanosensory neurones of the dorsal root ganglia, whereas stomatin is almost ubiquitously expressed

(Browman et al., 2007; Lapatsina et al., 2012). Wetzel et al. (2007) demonstrated that STOML-3 has a fundamental role in mechanosensation, suggesting that this function is conserved in mammalian systems. STOML-3-deficient mice show strongly reduced touch sensitivity, in accordance with the worm's mec-2 null phenotype, and this confirms that STOML-3 is functionally orthologous to the MEC-2 protein. The absence of response to mechanical stimuli is due to the loss of function of a subset of skin mechanoreceptors, which are dependent on STOML-3 (Wetzel et al., 2007).

In mammals, the touch sensation of the skin is thought to be mediated by the proton-gated ASIC channels that are expressed in different parts of the nervous system, since they are involved in nociception, taste and mechanosensation (Wemmie et al., 2006). Interestingly, like stomatin, STOML-3 modulates the activity of the ASIC ion channels inhibiting the amplitude of their currents. Indeed, the proton gated currents are larger in sensory neurones from STOML-3 knock-out mice (Wetzel et al., 2007). However, the molecular mechanisms that enable STOML-3 to modulate mechanotransduction channels and ASIC proteins are not yet understood.

4.8 Podocin

Podocin is exclusively expressed in kidney podocytes where it is part of a multiprotein complex that localizes on the slit diaphragm. This structure is a specialized intercellular junction in the mammalian kidney that forms a tight filtration slit around the glomerular capillaries also named the glomerular filtration barrier. Mutations in podocin or other proteins involved in the filtration barrier lead to congenital nephrotic syndromes and kidney failure (Benzing, 2004; Huber and Benzing, 2005). The podocin gene was first identified as being mutated in patients with a familial idiopathic nephrotic syndrome (Boute et al., 2000). Subsequent genetic studies reported that the most common cause of the hereditary nephrotic syndrome is ascribed to mutations in the podocin gene (Tsukaguchi et al., 2002).

In the same way as other stomatin-family members, podocin forms oligomers, and it interacts with proteins involved in tight junction formation (Shono et al., 2007). Podocin also colocalises with nephrin and cytoskeleton. Thus, it may act as a scaffolding protein that organises lipid-protein domains (Saleem et al., 2002). and it is absolutely required for the proper formation of the slit diaphragm (Roselli et al., 2004).

It has been proposed that podocin may also participate in mechanotransduction events within the slit diaphragm of the podocyte. Indeed, there is evidence that podocin associates with cholesterol in the membrane and binds directly to the TRP ion channel TRPC6 enhancing its ion channel activity (Huber et al., 2006). Interestingly, mechanical stretch leads to TRPC6 activation (Spassova et al., 2006). Therefore, podocin might be involved in mechanosensation, and it might function as a sensor of glomerular pressure or filtration rate in the kidney filtration barrier through the TRPC6 activity modulation (Huber et al., 2006).

4.9 Stomatin family members in the MOE

There is evidence in the literature that all the stomatin-domain proteins, except podocin, are expressed in the MOE. However, the expression level and compartmentalization seem to be different for each member.

In 2002, the Sakano and Reed groups independently identified STOML-3 and characterized its expression in the murine MOE by in situ hybridization and immunohistochemistry (Figure 25). Both studies revealed that STOML-3 is specifically and highly expressed in mature OSNs of the MOE but not in the VNO or other tissues, confirming its very restricted expression pattern. Moreover, western blotting and immunohistochemistry assays showed that STOML-3 is expressed in the apical portion of the OSNs, and it is

localized mainly to the membrane fraction of olfactory cilia (Figure 25, C; Goldstein et al., 2003; Kobayakawa et al., 2002).

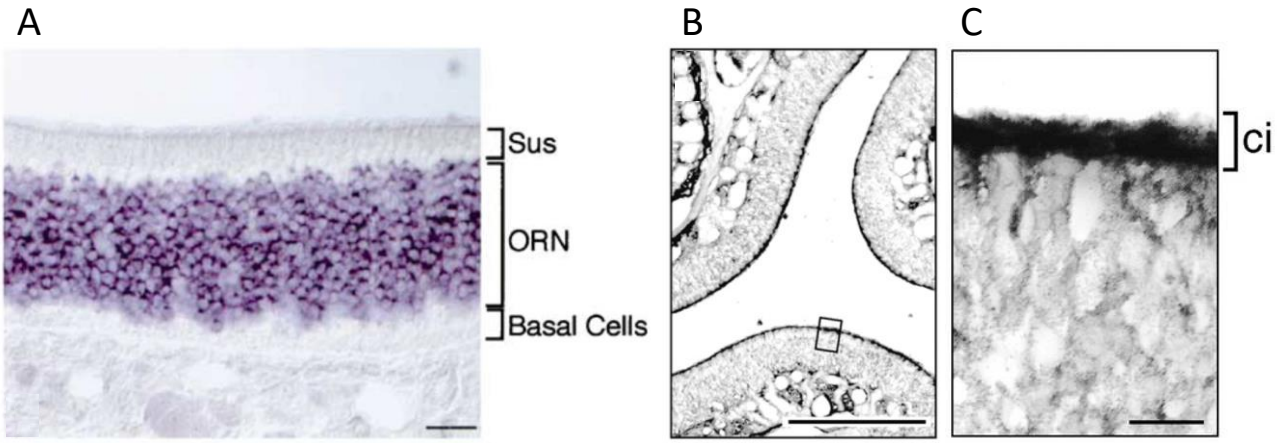

Figure 25: STOML-3 in the main olfactory epithelium.

A- In situ hybridization assay showing STOML-3 mRNA in the OSNs layer. There is no evidence of STOML-3 transcripts in SCs and basal cells (Sus = Supporting cells; ORN = Olfactory sensory neurons; scale bar, 20 µm; image modified from Goldstein et al., 2003). B- Immunohistochemical detection of STOML-3 in the cilia of mouse OSNs (scale bar, 250 µm). C- High magnification of a section from the image in (B) (ci = OSNs' cilia; scale bar, 10 µm; image modified from Kobayakawa et al., 2002).

Kobayakawa et al. (2002) also found stomatin transcripts in the murine MOE. However, it is well known that the founding member of the stomatin-family is almost ubiquitously expressed. Indeed, the same group reported that stomatin is expressed in other tissues tested, such as VNO, retina and tongue. Importantly both stomatin and STOML-3 were identified in the OSNs but not in SCs of the MOE, suggesting a specialized function for these proteins in the olfactory transduction pathway (Goldstein et al., 2003; Kobayakawa et al., 2002).

Recently, other transcriptomic studies reported that not only STOML-3 and stomatin are the most abundant members of the stomatin-domain family, but they are highly expressed also considering the whole MOE transcriptome (Fletcher et al., 2017; Kanageswaran et al., 2015; Saraiva et al., 2015). Interestingly, Wetzel et al. (2007) noticed that the expression pattern of stomatin and STOML-3 is higher in the MOE if compared with the other tissues tested. Moreover, transcriptomic and proteomic data showed that even STOML-1 and STOML-2 are expressed in the murine OE, but they displayed a lower rate of expression (Fletcher et al., 2017; Kanageswaran et al., 2015; Saraiva et al., 2015).

It is possible that some members of the stomatin-domain family, especially STOML-3, are enriched in the lipid rafts of olfactory cilia. Indeed, STOML-3 colocalized with ACIII and caveolin-1, a well-known lipid raft-associated protein marker (Kobayakawa et al., 2002). Schreiber et al. (2000) reported that important components of the olfactory transduction machinery (such as G_{olf} and ACIII) are found in the lipid rafts of OSNs' cilia. Anti-STOML-3 antibodies enhanced the cAMP production in the cilia membrane fraction, and this result confirms the interaction between ACIII and STOML-3 (Kobayakawa et al., 2002). Furthermore, stomatin and STOML-3 have a peculiar high level of expression in the MOE, and this strongly suggests that they may participate in the formation of supramolecular complexes capable to generate odorants-induced signals. At present, we are still far away from understanding if the stomatin-domain proteins are involved in the olfactory transduction, and how they could modulate it.

5. Aims:

Regarding the project focused on the investigation of STOML-3 in the modulation of the olfactory transduction in OSNs from the MOE, the aims of the work were:

- To test if the lack of the STOML-3 protein affects the growth, the morphology, and the transduction machinery of mouse OSNs comparing WT and KO mice using immunohistochemical and western-blot assays from.

- To test whether OSNs from WT and KO mice for STOML-3 have similar passive membrane properties and voltage-gated currents performing whole-cell voltage-clamp experiments.

- To investigate if the STOML-3 protein influences the spontaneous firing pattern in mouse OSNs comparing OSNs from WT and KO mice using loose-patch recordings

- To investigate the action potential firing in OSNs stimulated by IBMX and an odorant mixture comparing OSNs from WT and KO mice using loose-patch recordings

Regarding the project focused on the investigation of TMEM16A mediated current in SCs from the MOE, the aims of the work were:

- To test whether the TMEM16A channels are expressed in SCs from the entire mouse MOE or if their expression is restricted to SCs from a specific portion of the epithelium using immunohistochemical assays.

- To investigate the functional expression of the TMEM16A channels in SCs from the transition and the dorsal zone of the MOE performing whole-cell voltage-clamp experiments.

- To confirm that the TMEM16A channels expression is necessary for mediating the calcium-activated chloride current in SCs from the transition and the dorsal zone of the olfactory epithelium performing whole-cell voltage-clamp experiments in KO mice for TMEM16A.

- To investigate if ATP stimulation can induce a transient calcium increase in SCs from the MOE that leads to the activation of TMEM16A mediated currents combining confocal calcium imaging with whole-cell voltage-clamp experiments.

6. Results:

6.1 STOML3 modulates action potential firing in olfactory sensory neurons

E. Agostinelli, K.Y. Gonzalez-Velandia, E. Xerxa, A. Hernandez-Clavijo, D. K. Maurya, C. Wetzel, V. Bégay, G.R. Lewin, A. Menini, M. Dibattista and S. Pifferi;
Work in preparation.

6.2 TMEM16A calcium-activated chloride currents in supporting cells of the mouse olfactory epithelium

T. Henriques*, E. Agostinelli*, A. Hernandez-Clavijo, D. K. Maurya, J. R. Rock, B. D. Harfe, A. Menini, S. Pifferi
* These authors equally contributed to this work.
May 2019 – Journal of General Physiology; 151 (7): 954–966; https://doi.org/10.1085/jgp.201812310

STOML3 modulates action potential firing in olfactory sensory neurons

Manuscript in preparation.

Emilio Agostinelli performed and analyzed all the electrophysiological experiments.

Kevin Y. Gonzalez-Velandia performed and analyzed immunohistochemical and Western blot experiments.

Elena Xerxa performed and analyzed Western blot experiments.

Devendra Kumar Maurya (Department of Molecular Biology, Umeå University, Umeå, Sweden) contributed and analyzed some immunohistochemical experiments.

Andres Clavijo-Hernandez contributed to the experimental design of electrophysiological experiments.

Christiane Wetzel, Valérie Bégay, Gary R Lewin (Department of Neuroscience, Max Delbrück Center for Molecular Medicine, Berlin, Germany) provided STOML-3 KO mice.

Anna Menini, Michele Dibattista, and Simone Pifferi designed research, contributed to data analysis, and writing of the manuscript.

ABSTRACT

Stomatin-like protein-3 (STOML3) is an integral protein expressed in the cilia of the olfactory sensory neurons, but its functional role has never been addressed. It is also expressed in dorsal root ganglia and has been shown to be implicated in touch sensation. Due to its expression in the cilia where the first steps of olfactory transduction take place, we hypothesized that STOML3 could be involved in odorant responses in olfactory sensory neurons. We confirmed and extended previous results showing that STOML3 is mainly expressed in the knob and proximal cilia of olfactory sensory neurons and that mice lacking STOML3 have a morphologically normal olfactory epithelium. To investigate the functional role of STOML3, we performed loose patch recordings and found that mutant olfactory sensory neurons had a spontaneous firing activity with a lower mean frequency and a different interspike intervals distribution compared to control. Moreover, firing activity in response to stimuli showed a lower number of spikes and a shorter duration in neurons lacking STOML3 compared to wild type. We conclude that STOML3 has a physiological role in olfaction, modulating firing of olfactory sensory neurons.

INTRODUCTION

Olfactory perception begins with the binding of molecules to odorant receptors in the cilia of olfactory sensory neurons (OSNs) in the olfactory epithelium. This binding initiates a transduction cascade that involves the activation of G-proteins, adenylyl cyclase type III (ACIII), phosphodiesterases (PDEs), CNG and TMEM16B ion channels (Billig et al., 2011; Bönigk et al., 1999; Buck and Axel, 1991; Chen et al., 1999; Cygnar and Zhao, 2009; Kleene and Gesteland, 1991; Nakamura and Gold, 1987; Pifferi et al., 2009; Reisert, 2010; Reisert and Reingruber, 2019; Schroeder et al., 2008; Stephan et al., 2009; Yan et al., 1995; Zheng and Zagotta, 2004). The activation of the transduction cascade leads to the generation of inward currents that produce membrane depolarization, activation of voltage-gated currents and generation of action potentials that propagate along the axons of OSNs to the olfactory bulb (Dibattista et al., 2017; Firestein, 2001; Kleene, 2008; Lindemann, 2001; Menco and Morrison, 2003; Mombaerts, 2004; Pifferi et al., 2010; Schild and Restrepo, 1998).

The physiological role of several proteins highly expressed in the cilia of OSNs is still unknown, including that of stomatin-like protein-3 (STOML3). STOML3 was identified in the mouse olfactory epithelium by Kobayakawa et al. (2002) and first named SRO, and a year later Goldstein et al. (2003), who named it SLP3. STOML3 is a member of the family of stomatin proteins characterized by the presence of a structurally conserved core domain of near 120 residues called stomatin-domain, that is further related to the SPFH domain (Stomatin, Prohibitin, Flotillin, HflK/HflC; Green and Young, 2008; Lapatsina et al., 2012; Tavernarakis et al., 1999). Stomatin proteins are found in all three domains of life with a remarkable conservation, with bacterial and human homologous sharing 50% identity. In the mammalian genome, 5 members of the stomatin family have been identified all sharing 40/84% sequence similarity in the stomatin-domain and with similar membrane topology characterized by a single, relatively short, hydrophobic membrane insertion domain, followed by the core stomatin domain (Green and Young, 2008; Lapatsina et al., 2012). Several recent studies began to reveal some common aspects of the physiology of the stomatin proteins. In particular, it has been demonstrated that they can form oligomers, they mostly localize to membrane domains and they can modulate ion channel activity, even if the precise mechanisms of this regulation are still unclear (Brand et al., 2012; Lapatsina et al., 2012; Poole et al., 2014).

As aforementioned STOML3 is expressed in OSNs (Goldstein et al., 2003; Kobayakawa et al., 2002; Kulaga et al., 2004; Kurtenbach et al., 2017; Tadenev et al., 2011) and therefore might play a role in olfactory transduction, we analyzed in detail the expression and the subcellular localization of STOML3 in the mouse olfactory epithelium and confirmed its presence in the cilia of OSNs, the site of olfactory transduction. By using a knock-out (KO) mouse line for STOML3 (Wetzel et al., 2007), we first verified that mice lacking STOML3 have a morphologically normal olfactory epithelium and expression of several proteins involved in transduction. We then asked if STOML3 plays a role in OSN firing by measuring spontaneous and stimulus-induced spiking activity in the loose-patch configuration in WT and STOML3 KO mice. We found that STOML3 plays a physiological role in OSNs by regulating both spontaneous firing and responses to IBMX and odorant mixtures.

MATERIALS AND METHODS

Animals

Mice were handled in accordance with the Italian Guidelines for the Use of Laboratory Animals and European Union guidelines on animal research, under a protocol approved by the ethics committee of Scuola Internazionale Superiore di Studi Avanzati (SISSA).

Experiments were performed on tissues from STOML3 KO and WT mice derived from breeder pairs provided by G. Lewin (Wetzel et al., 2007).

Immunohistochemistry

The head containing the nasal cavity was fixed in 4% paraformaldehyde in PBS pH 7.4 for 4 hours at 4 °C. After fixing, heads of mice were incubated in 0.5 M EDTA for 2 days. The tissues were cryoprotected by incubation in 30% sucrose in PBS pH 7.4 overnight. Tissue was immersed in cryostat embedding medium (BioOptica) and immediately frozen at −80 °C. 18 µm coronal sections were cut on a cryostat and mounted on Superfrost Plus Adhesion Microscope Slides (ThermoFisher Scientific). The sections were air-dried for 3 hours. To wash the cryostat embedding medium from tissue, slices were incubated 15 minutes with PBS. Tissue was treated for 15 minutes with 0.5 % sodium dodecyl sulphate in PBS for antigen retrieval, then washed and incubated in blocking solution (2% normal goat serum, 0.2% Triton X-100 in PBS) for 90 minutes and finally overnight at 4°C in primary antibodies diluted in blocking solution. The following primary antibodies (catalog number, dilution; company) were used: mouse monoclonal anti-acetylated tubulin (T7451; 1:100; Sigma); polyclonal rabbit anti-ACIII (sc-588; 1:100, Santa Cruz Biotechnology); polyclonal goat anti-CNGA2 (sc-13700; 1:100, Santa Cruz Biotechnology); polyclonal rabbit anti-Ki67 (sc-7846, 1:250, Santa Cruz Biotechnology); polyclonal goat anti-OMP (544-10001, 1:1000, Wako); mouse monoclonal anti-p63 (CM163, 1:250, Biocare Medical); polyclonal rabbit anti-STOML3 (13316-1-AP, 1:200, Proteintech), polyclonal rabbit anti-TMEM16B (NBP1-90739,1:250, Novus). After removal of the excess of primary antibodies with PBS washes, sections were incubated with Alexa Fluor-conjugated secondary antibodies (1:500 dilution) in TPBS (Tween 20 0.2% in PBS) for 2 hours at room temperature, washed and mounted with Vectashield (Vector Laboratories) or FluoromontG (ThermoFisher). DAPI (5 µg/ml) was added in solution containing secondary antibody to stain the nuclei. Secondary antibodies used were Alexa 594-conjugated donkey anti-goat, Alexa-594 conjugated chicken anti-rabbit Alexa 488-conjugated goat anti-rabbit, Alexa 488-conjugated donkey anti-mouse (ThermoFisher). For antibodies anti-Ki67 and anti-p63 we used heat antigen retrieval protocol instead of treatment with SDS. Tissue was put in a container with sodium citrate buffer (10 mM Sodium Citrate, 0.05% Tween 20, pH 6.0) and heated at 100°C with microwave for 5 min. After cooling down, sodium citrate buffer was washed, and the rest of procedure was the same as aforementioned. To reveal anti STOML3 we applied the tyramide signal amplification method using the Tyramide SuperBoost™ Kit (ThermoFisher; Hunyady et al., 1996).

Immunoreactivity was visualized with a confocal microscope (Nikon A1R or C1). Images were acquired using NIS Element software (Nikon) at 1,024 x1,024-pixel resolution and were not modified other than to balance brightness and contrast.

Whole mount cilia staining

The olfactory turbinates were exposed by bisecting the head along the midline and removing the septum. The hemiheads were fixed with 4% paraformaldehyde in PBS pH 7.4 for 20 min at room temperature and then washed with PBS. Endogenous biotin was blocked by using Avidin/Biotin Blocking Kit (Vector Laboratories) following the manufacturer's protocol. The preparation was incubated for 2 hours with the biotinylated lectin Dolichos biflorus agglutinin (VectorLabs) at 20 µg/ml concentration in PBS, then washed at least 3 times with PBS, 10 minutes each. The preparation was incubated for 3 hours with Streptavidin-Alexa Fluor594 (ThermoFisher) diluted 1:500 in PBS and washed again. Then turbinates were dissected out from the nasal cavity and mounted on FluoroDishes (World Precision Instruments) with Vectashield (Vector Laboratories) or Fluoromont-G (ThermoFisher). A coverslip was gently placed on the tissue to press and close cilia to the glass bottom of the FluoroDish.

Western blot

Olfactory epithelium from adult mice was lysed with RIPA buffer (25 mM Tris pH 7.5, 1% NP40, 150 mM NaCl, 0.5% Deoxycholate, 0.1% SDS) containing Complete™ mini Protease Inhibitor Cocktail (Roche). 300 µl of lysis buffer was used for each mouse. Tissue was homogenized with electrical homogenizer at low speed. After lysis, the olfactory epithelium was incubated 1 hour on ice mixing gently every 15 minutes. Lysates were cleared by centrifugation 10 minutes at 10000 g at 4°C and supernatants was stored separately and their protein concentration measured with Pierce™ BCA Protein Assay Kit (ThermoScientific) according to the manufacturer's protocol.

For Western Blot, 40 µg of protein extract dissolved in Laemmli buffer (2x buffer concertation: 125 mM Tris pH 6.8, 4% SDS, 20% glycerol, 0.1% bromophenol blue and 10% β-mercaptoethanol, added fresh) were loaded in each well of an 8-12 % Acrylamide/Bis-acrilamide gel (Sigma) for SDS-PAGE electrophoresis. After separation, gel containing proteins was equilibrated 10 min in transfer buffer (25 mM Tris, 192 mM glycine pH 8.3, 15% MeOH), and then proteins were transferred to PDVF membrane with pore size of 0.45 µm (ThermoScientific). Membrane was blocked in 5% no fat milk in TBS at room temperature for 1 hour and then incubated overnight with primary antibodies diluted in 5% no fat milk in TBS. Then membrane was washed 3 times with TBS-T (0.1% Tween-20 in TBS) and incubated with horseradish peroxidase-conjugated secondary antibodies in TBS-T for 1 hour. Signal was developed using Super Signal West Pico PLUS Chemiluminescent substrate (ThermoScientific) or Super Signal West Atto ultimate Chemiluminescent substrate (ThermoScientific). The following primary antibodies (catalog number, dilution; company) were used: polyclonal rabbit anti-ACIII (sc-588; 1:1000, Santa Cruz Biotechnology); polyclonal rabbit anti-CNGA2 (ab96410; 1:500, Abcam); polyclonal goat anti-OMP (544-10001, 1:5000, Wako); polyclonal rabbit anti-STOML-3 (13316-1-AP, 1:1000, Proteintech), polyclonal rabbit anti-TMEM16B (20647-1-AP, 1:2000, Proteintech); monoclonal mouse anti-acetylated tubulin (T8203, 1:5000, Sigma). The following secondary antibodies (catalog number, dilution; company) were used: polyclonal Goat Anti-Rabbit HRP (P0448, 1:2000, Dako); polyclonal Rabbit Anti-Goat HRP (P0449, 1:2000, Dako) and polyclonal Goat Anti-Mouse HRP (P0447, 1:2000, Dako).

Electrophysiological recordings from OSNs

Acute coronal slices of the olfactory epithelium were obtained from P0-P4 mice with a method similar to those previously described (Dibattista et al., 2008; Henriques et al., 2019; Pietra et al., 2016; Shimazaki et al., 2006; Wong et al., 2018). The head without the skin of a P0-P4 mouse was dissected and embedded in

3% Type I-A agarose prepared in Ringer's solution once the solution cooled to 38°C. The Ringer's solution contained (in mM): 140 NaCl, 5 KCl, 2 CaCl2, 1 MgCl2, 10 HEPES, 10 glucose, adjusted to pH 7.4 with NaOH. Coronal slices from the mouse olfactory epithelium of 300 µm thickness were cut with a vibratome (Vibratome 1000 Plus Sectioning System) and kept in cold oxygenated Ringer's solution until use.

Slices were transferred to a recording chamber continuously perfused with oxygenated Ringer's solution at room temperature and viewed with an upright microscope (BX51WI; Olympus), equipped with infrared differential contrast optics, a camera (DFK 72BUC02; Imaging Source) and a 40 X water-immersion objective with an additional 2 X auxiliary lens. OSNs were identified by their morphology. Experiments were recorded at room temperature (20–25°C) using a MultiClamp 700B amplifier controlled by Clampex 10.6 via a Digidata 1550B (Molecular Devices). Data were low-pass filtered at 2 kHz and sampled at 10 kHz. The bath was grounded via a 3 M KCl agar bridge connected to an Ag/AgCl reference electrode. Patch pipettes were pulled from borosilicate capillaries (WPI) with a Narishige PC-10 puller.

Extracellular recordings from the soma of OSNs were obtained in the on-cell loose-patch configuration using patch pipettes of 2-3 MΩ when filled with Ringer. Seal resistances were 30-50 MΩ. Extracellular recordings were made in voltage-clamp mode with a holding potential of 0 mV. Stimuli were delivered through an 8-into-1 multi-barrel perfusion pencil connected to a ValveLink8.2 pinch valve perfusion system (Automate Scientific, Berkeley, CA, USA). To test the cell viability, a high K+ Ringer solution (25 mM KCl) was applied in 3 s pulses and experiments were performed only on OSNs responding to this stimulus.

Control experiments measuring membrane properties and voltage-gated inward and outward currents were performed in the whole-cell voltage-clamp configuration. Patch pipettes had resistances of 4-7 MΩ when filled with the intracellular solution composed of (in mM): 145 KCl, 4 MgCl2, 0.5 EGTA, and 10 HEPES, adjusted to pH 7.2 with KOH.

Heptaldehyde, Isoamyl acetate, Acetophenone, Cineole and Eugenol were dissolved in dimethyl sulfoxide (DMSO) at 5 M. The odorants mixture was prepared diluting each odorant at the final concentration of 100 µM on the day of the experiment. 3-Isobutyl-1-methylxanthine (IBMX) was prepared weekly by dissolving into Ringer's solution at the final concentration of 1 mM.

Analysis of electrophysiological data

IgorPro software (WaveMetrics) and Clampfit (Molecular Devices) were used for data analysis and figure preparation.

Recordings were filtered offline with a high-pass filter at 2 Hz to eliminate slow drifts in the baseline. Individual action potentials were identified by an event detection algorithm using an arbitrary threshold, and each event was confirmed by shape inspection. The starting time of each event was taken as the time for that individual action potential. Mean spontaneous firing frequency was calculated as the number of spikes divided by the duration of the recording. Inter-spike interval (ISI) was calculated measuring the time between consecutive spikes (second to first, third to second, and so forth). To construct the ISI distribution, we calculated the ISI for all spikes for each cell, then we grouped the ISIs in bins as indicated in the figures and divided the value of each bin by the total number of calculated ISIs for each cell. Finally, we averaged the distribution obtained from all cells of the group (Arnson and Holy, 2011). The values in y-axes represent the percentage of spikes in each bin, the area under the curve is 100%.

The averages obtained from individual experiments in different cells are presented as mean ± SEM and the number of cells recorded (n). Cells were obtained from at least 3 different WT or KO mice. When data were not normally distributed (Jarque-Bera test or Shapiro-Wilk test) statistical significance was determined by Wilcoxon-Mann-Whitney's test (U-test). Kolmogorov-Smirnov test was used to compare the cumulative distributions. P-values <0.05 were considered statistically significant.

RESULTS

STOML3 expression in the olfactory epithelium

STOML3 protein has been shown to be expressed in mouse olfactory epithelium and to localize in the mature OSNs but its functional role in the olfactory system is still elusive. We decided to investigate the role of the STOML3 protein in OSNs by taking advantage of a loss of function approach using the STOML3 KO mouse model.

First, we sought to confirm the expression pattern of STOML3 in the olfactory epithelium of the WT mice by using immunofluorescence.

Immunofluorescence for STOML3 showed a clear staining of the ciliary layer (Fig. 1). In particular, the staining pattern suggests a localization of the STOML3 in the knob and proximal part of the cilia (Fig. 1A-C). The OSNs cilia were visualized by marking the ciliary protein acetylated tubulin and we observed a partial overlap with STOML3 (Fig. 1C). While the acetylated tubulin pattern seemed unaltered in KO, the STOML3 staining was absent, thus demonstrating the specificity of our staining (Fig. 1D-F).

Beside the intense signal of the knob/cilia we could also see a sparse localization of STOML3 in the mature OSNs cell bodies, signal that disappeared in the KO (Fig. 1B,E).

Together, our data confirm and extend previous results showing that STOML3 is mainly expressed in the knob and proximal ciliary region of OSNs.

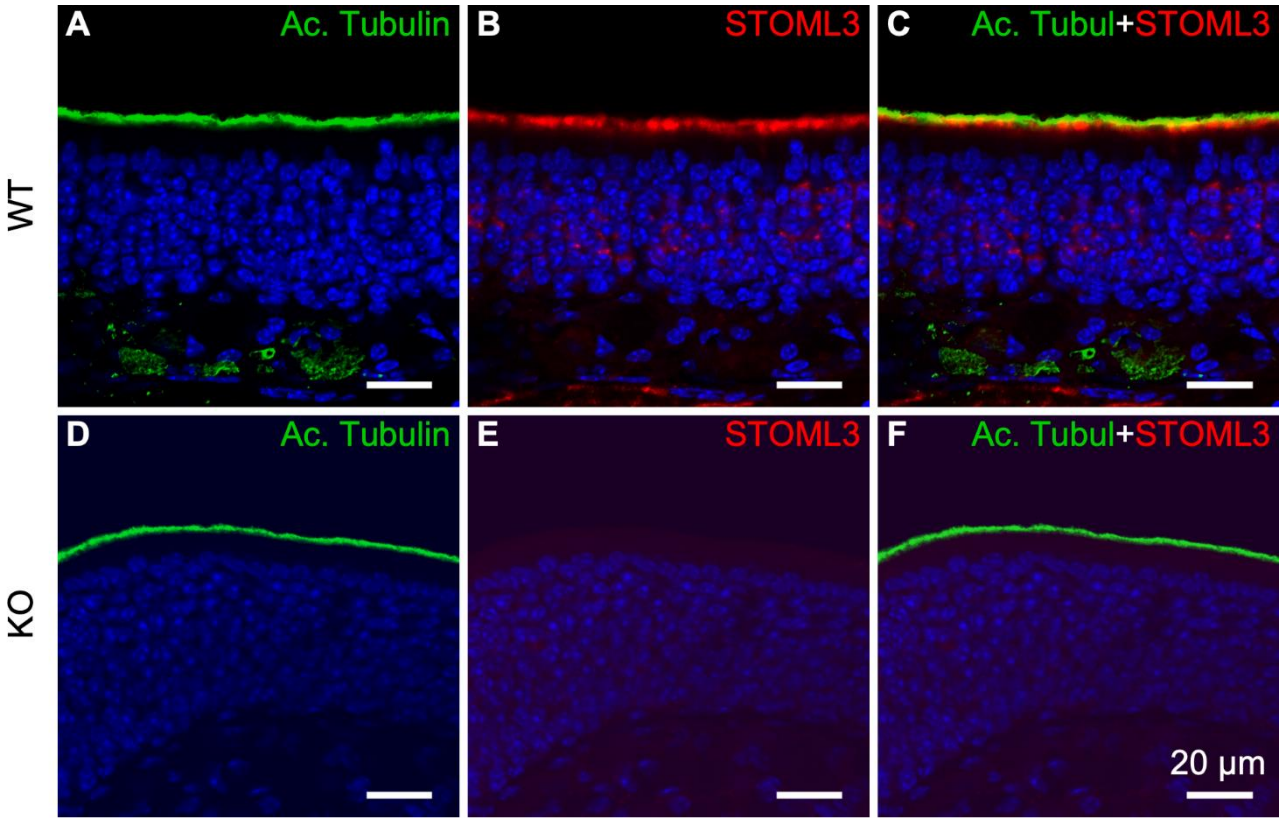

Figure 1. STOML3 is expressed in knob/proximal cilia of OSNs. A. Antibodies against Acetylated Tubulin (Ac. Tubulin) stained the ciliary region of the OE. STOML3 localized in the same ciliary region and OSNs cell bodies (**B**). A merge of the two images shows that STOML3 has a diffuse staining that co-localized with Ac. Tubulin (yellow regions in **C**) and a more defined staining of the region below the Ac. Tubulin in the region occupied by the OSN' knobs. The signal disappeared in the OE of the STOML3 KO mice (**D-F**). Nuclei were stained with DAPI (blue).

Knocking out STOML3 does not change structural and morphological properties of the olfactory epithelium

Stomatin proteins have been implicated in the structural and morphological organization of different cellular complexes (Brand et al., 2012; Browman et al., 2007; Kobayakawa et al., 2002; Lapatsina et al., 2012; Poole et al., 2014; Qi et al., 2015; Salzer et al., 2007; Sezgin et al., 2017; Simons and Toomre, 2000; Umlauf et al., 2006; Wetzel et al., 2007) and, since STOML3 shares structural features with the other proteins of the same family, we asked whether STOML3 is important for the structural organization of the olfactory epithelium and its cell types.

We performed immunostaining against the proteins of the signal transduction machinery that are abundantly expressed in the OSNs cilia. We found that ACIII, CNGA2 and TMEM16B localized to the ciliary layer together with acetylated tubulin both in WT and STOML3 KO mice (Fig. 2 A-L). By keeping the same acquisition settings, we did not observe any clear difference in staining intensity or in pattern expression in the KO.

By Western blotting, we identified a 32 kDa band in WT as expected that was absent in KO mice. We then quantified the ciliary proteins and verified that ACIII, CNGA2, TMEM16B, OMP and acetylated tubulin had similar expression levels in WT and KO mice (Fig. 2M-N).

Altogether, these results indicate that STOML3 is not involved in localization and expression levels of several members of the transduction cascade.

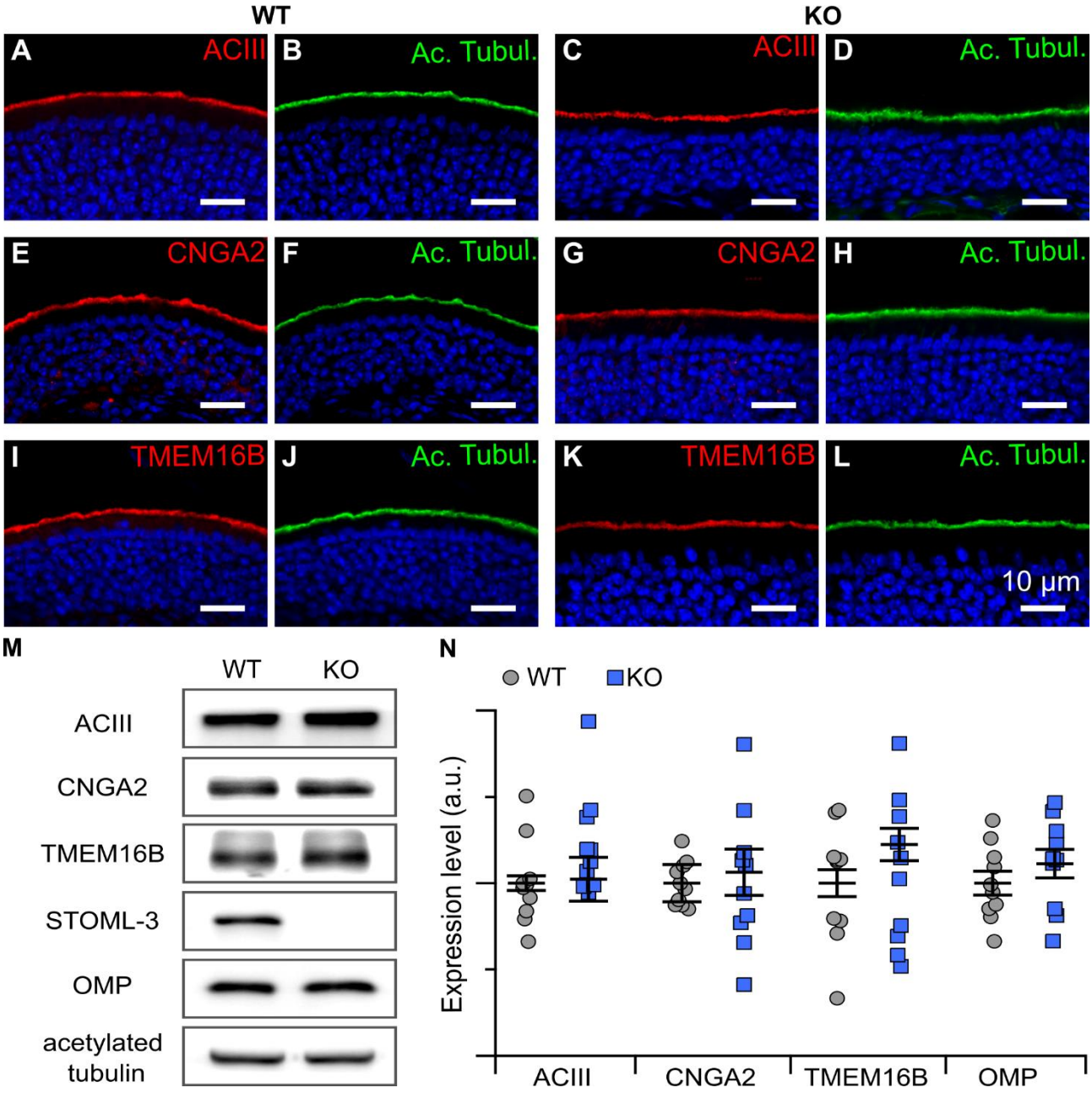

Figure 2. Staining of Acetylated tubulin, ACIII (A-D), CNGA2 (E-H), TMEM16B (I-L), are comparable between the WT and KO mice. Sections are counterstained with DAPI. Scale bar, 10 µm. **M**, Western blot analysis of total OE proteins. **N**, Expression level relative to tubulin. WT, n = 10; KO, n = 10 mice.

To better assess whether STOML3 could have a role in neuronal morphological organization we used DAB to mark the OSNs cilia for their entire length. We quantified the total ciliary length per analyzed OSNs and determined that, although there was a tendency for the KO to have a lower total ciliary length, this was not significant (Fig. 3 A-B and quantification in E). Also, the overall olfactory epithelium morphology was not changed since staining and counting of OMP positive cells did not reveal any difference in the number of OMP positive cells between WT and KO mice (Fig. 3G and 92 ± 5 for WT and 94 ± 5 for KO, n=3 mice).

To further characterize the morphology of the olfactory epithelium, we stained the population of basal cells with Ki67 and p63, markers for horizontal (HBCs) and globose basal (GBCs) cells, respectively. These cells are usually located at the base of the olfactory epithelium lying on the basal lamina. We could see

Ki67 and p63 positive cells in their supposed location in both WT and KO (Fig. 3 E-F). In addition, no differences were observed in HBCs and GBCs numbers (Fig. 3 G, Ki67: 6.3 ± 0.9 for WT and 5.6 ± 0.6 for KO n=3 mice; p63: 7.8 ± 0.8 for WT and 7.7 ± 0.4 for KO).

In summary, the absence of STOML3 did not alter the number of OSNs, HBCs and GBCs indicating that STOML3 does not contribute to the normal olfactory epithelium morphology.

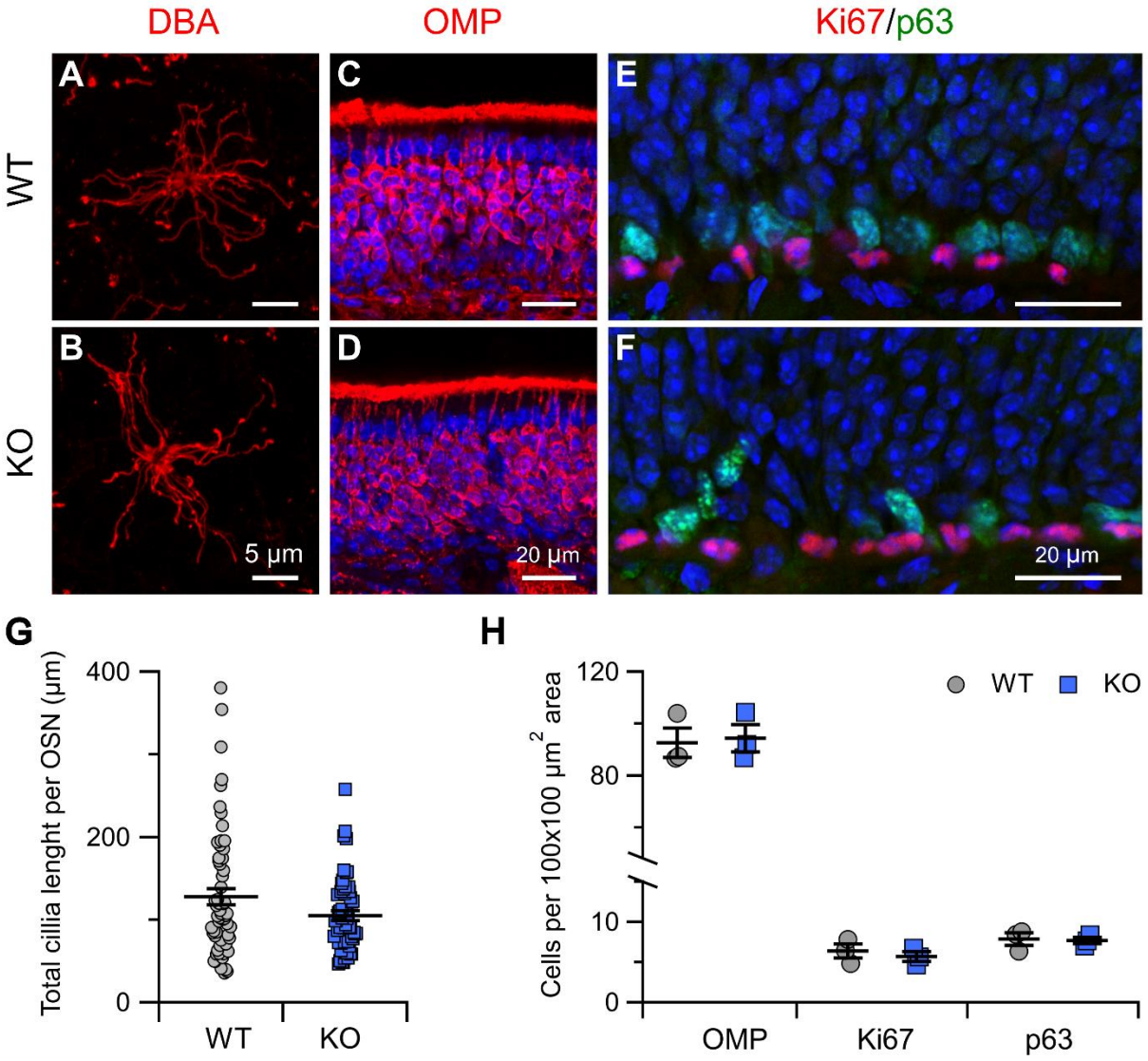

Figure 3. STOML3 KO mice have grossly normal OE. Immunofluorescent staining of OE sections from control (**A-C-E**) and conditional *STOML3* KO (**B-D-F**) mice. **A** and **B**, *En-face* view of whole-mount preparation of OE with cilia OSNs labeled by rhodamine-conjugated Dolichos biflorus agglutinin (DBA). Scale bar, 5 µm. **G**, Quantification of the total cilia length per OSN (error bars indicate SEM) for WT and KO (n=61 OSNs from 4 WT mice, n=57 OSNs from 4 KO mice). OMP stained the mature OSNs both in WT (**C**) and KO (**D**) and their quantification (**H**). **E** and **F,** basal cells positive to Ki67 (red) and p63 (green) and their quantification (**E**). Sections are counterstained with DAPI. Scale bar, 20 µm**.**

STOML3 modulates spontaneous firing frequency in OSNs

Based on recent findings on the STOML3 role in shaping the electrophysiological properties of mechanosensitive neurons (Brand et al., 2012; Lapatsina et al., 2012; Poole et al., 2014; Qi et al., 2015; Wetzel

et al., 2007) and on its expression in OSNs, we sought to investigate a possible role of STOML3 in the spontaneous and/or evoked electrical activities of OSNs.

By using loose patch recordings, we investigated the spontaneous activity of OSNs in olfactory epithelium slices from WT and STOML3 KO mice. By recording from a substantial number of cells we could appreciate the heterogeneous patterns of spontaneous activity in WT OSNs (Fig. 4 A-C). Indeed, the raster plots of 38 recorded cells showed a huge variation in patterns ranging from almost silent OSNs (upper rows in Fig. 4C) to OSNs with elevated and sustained spontaneous firing (bottom rows in Fig. 4C). In STOML3 KO mice, OSNs seemed to have lower spontaneous activity. The raster plots in Fig. 4D shows that in KO there was an increase in the number of OSNs that have lower spontaneous firing. Indeed, OSNs in KO had lower spontaneous mean frequency compared to WT mice (Fig. 4E 1.4 ± 0.3 Hz for WT and 1.1 ± 0.3 Hz for KO, n=38-37 $p<0.05$ U-test).

In addition, the ISI distribution revealed that brief ISIs were missing in STOML3 KO neurons compared to WT (Fig. 4F). The overall cumulative probability further showed that the ISI distribution was overall different between the WT and KO (Fig. 4G, $p<0.001$ Kolmogorov–Smirnov test).

These results are the first to demonstrate that STOML3 plays a role in shaping OSNs spontaneous activity by increasing their mean firing frequency and decreasing the interspike intervals.

As spontaneous firing in OSNs is mainly driven by the constitutive activity of the ORs that initiate and control the activation of the downstream signaling cascade (Connelly et al., 2013; Dibattista and Reisert, 2016; Reisert, 2010), changes in the spontaneous firing of OSNs lacking STOML3 have led us to hypothesize that STOML3 might play a role in odorant signal transduction and the electrical response to odorants.

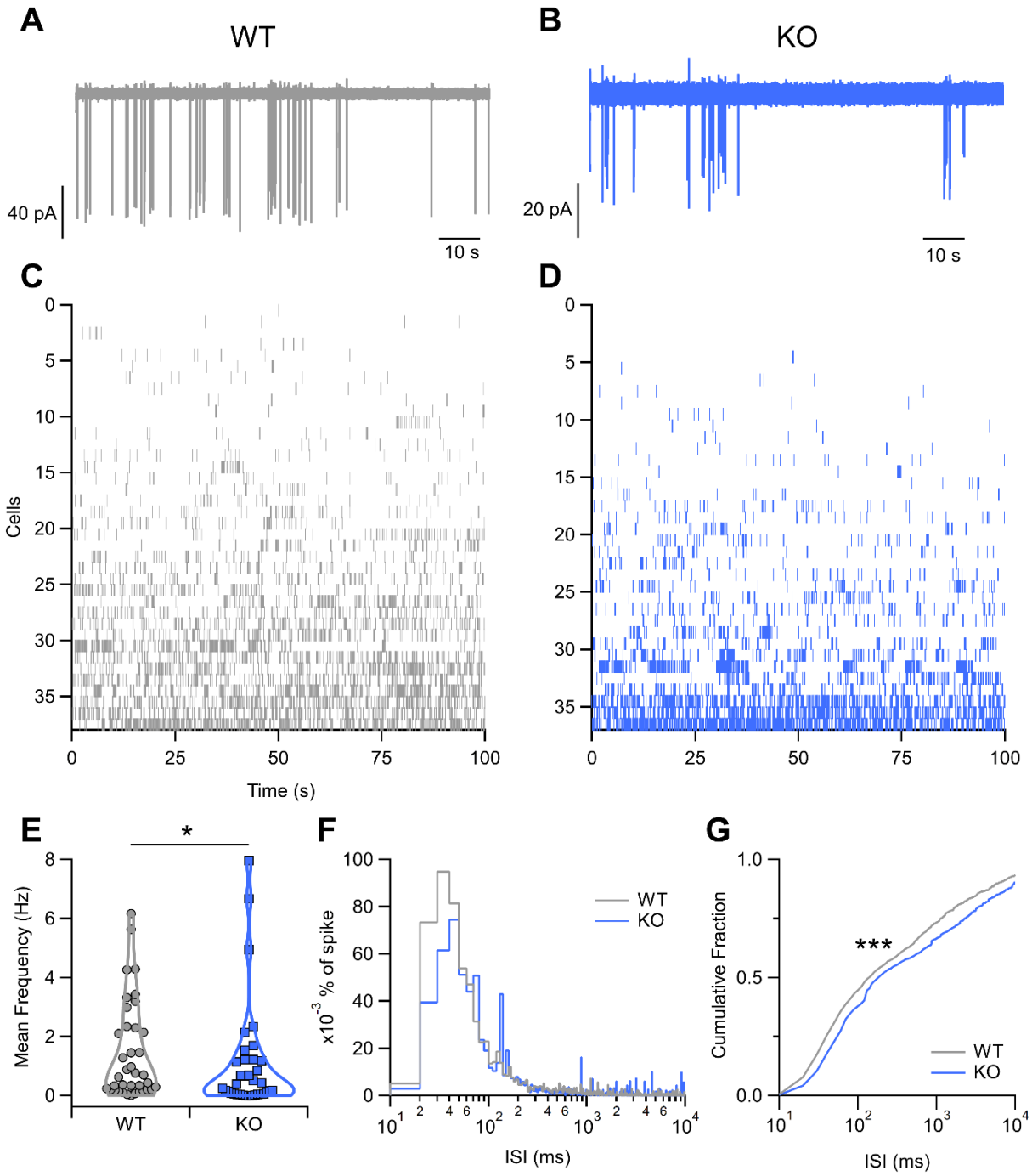

Figure 4. STOML3 modulates spontaneous firing frequency in OSNs. (**A-B**) Representative loose-patch recordings showing the spontaneous activity of OSNs from acute slices of OE from WT and KO mice. (**C-D**) Raster plots of recordings of the spontaneous activity of 38 and 37 OSNs from WT and KO mice, respectively. (**E**) Mean frequency of spontaneous activity in OSNs from WT and KO mice (n=38 for WT and n=37 for KO, *p<0.05 U-test). (**F**) Interspike interval (ISI) distributions of spontaneous firing from cells shown in C and D (bin = 5 ms). Values were normalized to the area under each curve to show the spike percentages for WT or KO mice. (**G**) Cumulative fraction of ISI distributions (***, p< 0.001, Kolmogorov-Smirnov test).

STOML3 regulates spike number and duration of the evoked response

To further understand the potential involvement of STOML3 in the transduction events we recorded action potential firing in response to the phosphodiesterase inhibitor IBMX. It has been often used as surrogate of odorants as blocking PDE reveal the basal rate of cAMP production by ACIII (Cherry and Pho, 2002; Cygnar and Zhao, 2009; Pietra et al., 2016; Wei et al., 1998).

To test if STOML3 deletion modifies OSNs passive membrane properties or voltage-gated currents, we performed whole-cell recordings with KCl in the patch pipette and we did not find any significant difference in resting potential, input resistance and voltage-gated inward and outward currents (data not shown).

In the loose patch configuration, we stimulated OSNs for 3 s with 1 mM IBMX and recorded the evoked firing activity (Fig. 5). In WT, the firing frequency of the response was on average 50 Hz and similar values were found for the KO (Fig. 5E). Surprisingly though, it was soon evident that the number of spikes was lower, and the duration of the response was shorter in KO than in WT mice. Indeed, quantification of the duration of the response and the number of spikes showed that both were significantly different between WT and KO (Fig. 5 C-D For high K^+ duration: 372 ± 49 ms n=29 for WT and 385 ± 75 ms n=23 for KO $p>0.05$ U-test; spike number: 6.0 ± 0.6 n=29 for WT n and 5.0 ± 0.5 n=23 for KO $p>0.05$ U-test; For IBMX duration: 263 ± 38 ms n=19 for WT and 135 ± 27 ms n=20 for KO $p<0.01$ U-test; spike number: 10 ± 1 n=19 for WT n and 5 ± 1 n=20 for KO $p<0.01$ U-test). These differences were due to the activity of the transduction events since stimulation with high K^+ of the same duration of IBMX did not show any alteration in firing activity duration. During IBMX stimulation, while both WT and KO showed spike trains with action potentials that were decreasing in size, only the KO fired fewer action potentials (a shorter spike train) followed by a period of "bumpy" noise (Fig. 5).

Is the odorant response too modulated by STOML3? To address this question, we stimulated OSNs for 3 s with a mix of odorants (Fig. 5F-G) and recorded the evoked firing activity. As with the IBMX stimulation, WT and KO were both responding with a series of action potentials of decreasing size and at the same frequency (Fig. 5J). Clear differences emerged when we counted the number of spikes and the duration of the response that were respectively significantly lower and shorter in the KO compared to WT (Fig 5 H-I 189 ± 34 ms for WT and 95 ± 18 ms for KO n=8 $p<0.01$ U-test; 7 ± 1 for WT and 3.5 ± 0.3 for KO n=8 $p<0.01$ U-test).

In summary, differences in evoked firing activity in response to IBMX and odorant mix indicated a possible scenario where STOML3 may participate to the transduction events. Where? This is the question that we would need to answer with future experiments.

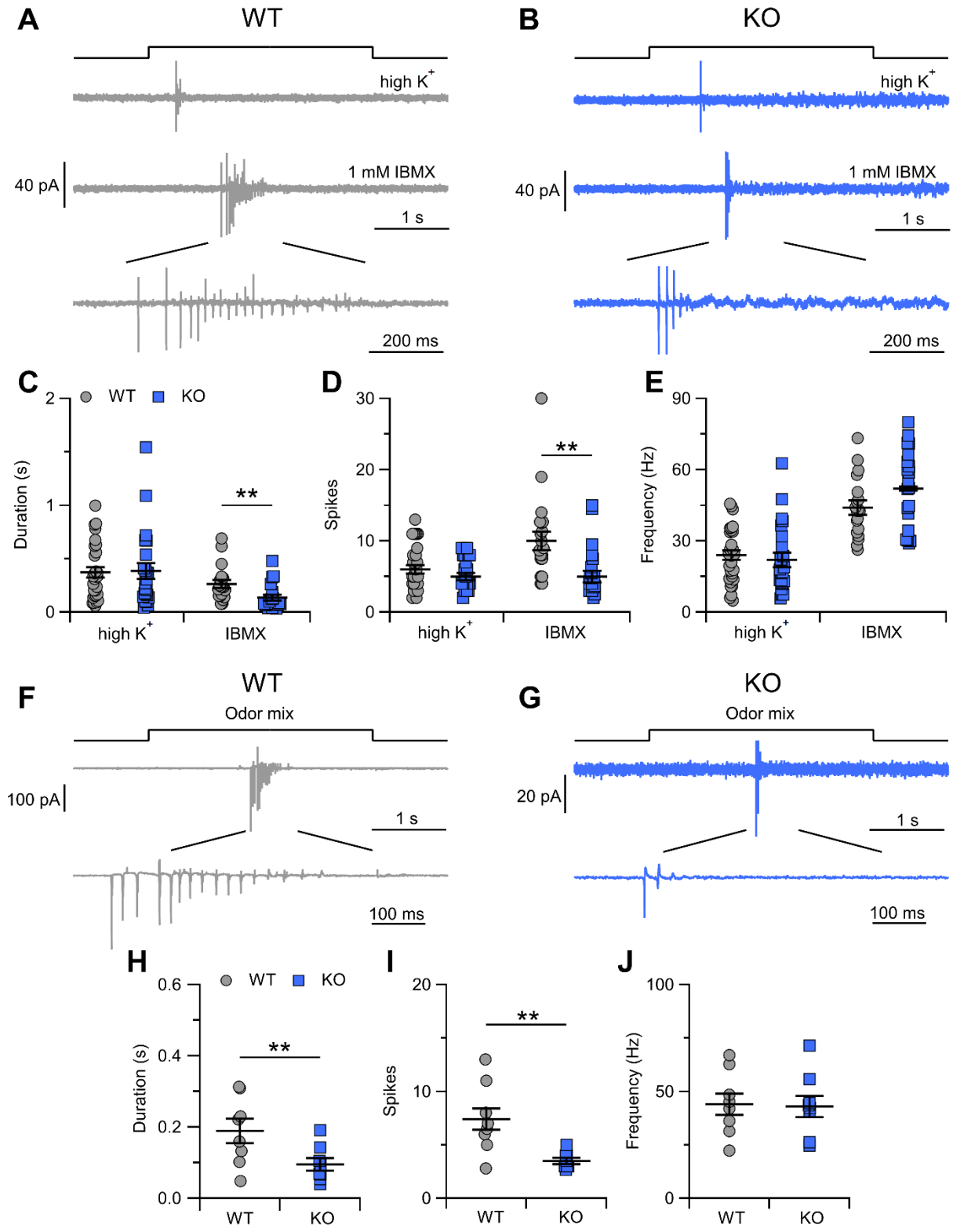

Figure 5. Representative loose-patch recordings of a OSN from WT (A) or KO (B) mice stimulated with high K^+ (upper trace) or with 1mM IBMX (middle and lower traces). Comparison of duration response (**C**), evoked spikes (**D**), mean frequency of the response (**E**) to high K^+ or 1 mM IBMX in OSNs from WT or KO (mice error bars indicate SEM). Representative loose-patch recordings of a OSN from WT (**F**) or KO (**G**) mice stimulated

with odor mixture. Comparison of duration response (**H**), evoked spikes (**I**), mean frequency of the response (**J**) to odor mixture in OSNs from WT or KO (mice error bars indicate SEM).

DISCUSSION

In this study, we sought to understand the functional role of STOML3 protein expressed in the OSNs. It was shown to be expressed in mouse olfactory epithelium in OSNs (Goldstein et al., 2003; Kobayakawa et al., 2002) and our results confirmed the knob/proximal ciliary localization of STOML3 (Fig. 1). We hypothesized a possible role in organizing and/or modulating the transduction apparatus in OSNs and tested our hypothesis by analyzing mice where STOML3 was knocked out. We determined that the loss of STOML3 does not alter the morphology of the olfactory epithelium (Fig. 3). STOML3 has been shown to be mis-localized in BBS8 KO mice (Kulaga et al., 2004; Kurtenbach et al., 2017; Tadenev et al., 2011). BBS are proteins involved in ciliogenesis and ciliary transport (Jin and Nachury, 2009; Nachury and Mick, 2019) so we tested whether STOML3 might participate in these processes as well. We did not observe any significant alteration in the organization of the transduction machinery (Fig. 2) or in the ciliary structure (Fig 3) of the KO mice, thus concluding that STOML3 is not involved in the regulation of the olfactory epithelium structural and morphological development**.**

Our main finding, though, is the involvement of STOML3 in the odorant transduction events rather.

After that STOML3 was found in the OSNs, it was shown by only using biochemical methods that it interacted with ACIII and its blockage by antibodies against STOML3 lead to an increase in cAMP concentration measured from olfactory cilia preparations. Although olfactory cilia preparation and biochemical methods have traditionally been used to understand signal transduction in OSNs (Flannery et al., 2006; Kobayakawa et al., 2002; Restrepo and Teeter, 1990; Villar et al., 2017), they lack the resolution of the electrophysiological techniques, making it difficult to clearly understand the functional role of STOML3 in OSNs.

Therefore, by using loose patch recordings, we found that spontaneous activity is altered when STOML3 is missing, indicating a potential role of STOML3 in modulating spontaneous AP firing (Figure 4). In OSNs it has been shown that spontaneous firing is dependent from the activation of the signal transduction machinery by the constitutive activity of ORs (Connelly et al., 2013; Dibattista and Reisert, 2016; Reisert, 2010). OR basal activation leads to basal cAMP oscillations that trigger the opening of CNG channels followed by that of TMEM16B. The resulting depolarization allow the OSN to fire AP, that could be suppressed by blocking TMEM16B activity or knocking down other elements of the transduction (Boccaccio and Menini, 2007; Brunet et al., 1996; Cygnar and Zhao, 2009; Ferguson and Zhao, 2017; Knott et al., 2012; Michalakis et al., 2006; Nakashima et al., 2020; Pietra et al., 2016; Qiu et al., 2016; Reisert et al., 2005; Wong et al., 2000). Our experiments excluded the possibility that a significant alteration of the voltage gated Na and K channels could be responsible for the observed firing behaviour. Because of STOML3 expression site and the origin of spontaneous activity in OSNs, we could conclude that STOML3 could be a new player in the transduction mechanisms.

In addition, we found that OSNs lacking STOML3 responded to IBMX stimulation with shorter spike trains compared to WT (Fig. 5). The spike trains in the KO rapidly shut off and did not reappeared during the duration of the entire stimulus. Same effects were observed during odor mix stimulation (Fig. 5) but not during the application of High K+, again strengthening our conclusions that STOML3 is modulating transduction events.

We could depict at least three possible scenarios for the role of STOML3 in olfactory transduction.

First, since the spontaneous firing is driven by the OR constitutive activity, STOML3 could modulate OR expression or transport of the OR to the ciliary site. Indeed, Stomatin, another protein of the same family sharing the stomatin motif, had already been shown to interact with GPCRs in erythrocytes (Mayer et al., 1998) thus making it possible that also STOML3 might work similarly in OSNs.

In particular, it could regulate OR assembly on the ciliary membrane by mitigating the translocation of ORs with medium/high basal activity to keep basal noise instructive without altering signal to noise ratio in OSNs (Connelly et al., 2013; Dibattista and Reisert, 2016; Reisert, 2010). Indeed, a higher basal rate of constitutive activity could result in an increased cAMP production rate that would soon keep the cell in a more adapted state thus limiting the AP firing (as we observed in STOML3 KO).

The second scenario is based on what we know so far of STOML3 in the OSNs: we know its expression site, we know that it interacts with ACIII and that it is involved in cAMP production. In particular blocking with antibodies raised against STOML3 it was shown that in ciliary preparation cAMP concentration was increased compared to control when stimulating ACIII with forskolin (Kobayakawa et al., 2002). In the absence of STOML3, continuous cAMP production by the transduction cascade led to OSNs being in an adapted state (Dibattista and Reisert, 2016; Reisert and Matthews, 1998; Reisert et al., 2007) which could slow down the transduction events, reducing the chance of both spontaneous and evoked AP firing. In addition, the differences in responses to IBMX between WT and KO could strengthen this scenario hypothesizing that STOML3 might participates in the poorly understood cAMP buffering system of OSN cilia. Indeed, by simply anchoring to the ciliary membrane in close proximity of the ACIII, STOML3 could buffer cAMP keeping it relatively low in close proximity of the CNG or of the PDEs.

The third scenario we propose is that of a possible interaction between STOML3 and TMEM16B channels as it happens between STOML3 and ASIC2a, ASIC2b, ASIC3 (Lapatsina et al., 2012; Wetzel et al., 2007) where it was shown a direct interaction among them. Also, STOML3 functionally interacts with the mechanosensitive ion channels Piezo-1 and Piezo-2, increasing the sensitivity of these channels to mechanical stimulations (Poole et al., 2014).

It would then be tempting to speculate a possible modulation of TMEM16B by STOML3. We have previously shown that TMEM16B is an important regulator of the spontaneous and evoked firing of the OSNs. It could both amplify and “clamp” the resulting depolarization following the activation of the signal transduction events in spontaneous as well as evoked AP firing, respectively. In this case STOML3 could modulate the TMEM16B current by fastening its kinetics so that it could operate in order to amplify the smaller spontaneous events without causing sustained depolarization that would then terminate the AP firing thus altering the spontaneous firing rate of OSNs. The same mechanism could account for the “clamping” effect of TMEM16B during evoked firing. When STOML3 was knocked out the slower TMEM16B kinetics could explain our results since it could account for the persistent depolarization that would keep the inactivation of voltage-gated channels (Trotier, 1994), allowing for less spikes to be generated over a shorter time window.

Further experiments are needed to elucidate which of the proposed scenario could be that of the OSNs. Based on our results, we can conclude that STOML3 is expressed in the knob and proximal ciliary region in the olfactory epithelium and for the first time we could show that it participates to the signal transduction events at least by regulating their output: the action potential firing. It is worth notice that lately emerging new players have been involved in the odorant transduction mechanisms (Baumgart et al., 2014; Buiakova et al., 1996; Dannecker et al., 2005; Dibattista and Reisert, 2016; Dooley et al., 2009; Ivic et al., 2000; Kaneko-Goto et al., 2013; Kerr et al., 2008; Sinnarajah et al., 2001; Talaga et al., 2017) increasing the complexity of long-known mechanisms crucial for the transformation of a chemical signal, the odorant, into an electrical one, the AP, that could then initiate the long journey to the brain.

References:

Arnson, H.A., and Holy, T.E. (2011). Chemosensory burst coding by mouse vomeronasal sensory neurons. J. Neurophysiol. *106*, 409–420.

Baumgart, S., Jansen, F., Bintig, W., Kalbe, B., Herrmann, C., Klumpers, F., Köster, S.D., Scholz, P., Rasche, S., Dooley, R., et al. (2014). The scaffold protein MUPP1 regulates odorant-mediated signaling in olfactory sensory neurons. J. Cell Sci. *127*, 2518–2527.

Billig, G.M., Pál, B., Fidzinski, P., and Jentsch, T.J. (2011). Ca2+-activated Cl− currents are dispensable for olfaction. Nat. Neurosci. *14*, 763–769.

Boccaccio, A., and Menini, A. (2007). Temporal development of cyclic nucleotide-gated and Ca2+ -activated Cl- currents in isolated mouse olfactory sensory neurons. J. Neurophysiol. *98*, 153–160.

Bönigk, W., Bradley, J., Müller, F., Sesti, F., Boekhoff, I., Ronnett, G.V., Kaupp, U.B., and Frings, S. (1999). The native rat olfactory cyclic nucleotide-gated channel is composed of three distinct subunits. J. Neurosci. Off. J. Soc. Neurosci. *19*, 5332–5347.

Brand, J., Smith, E.S.J., Schwefel, D., Lapatsina, L., Poole, K., Omerbašić, D., Kozlenkov, A., Behlke, J., Lewin, G.R., and Daumke, O. (2012). A stomatin dimer modulates the activity of acid-sensing ion channels. EMBO J. *31*, 3635–3646.

Browman, D.T., Hoegg, M.B., and Robbins, S.M. (2007). The SPFH domain-containing proteins: more than lipid raft markers. Trends Cell Biol. *17*, 394–402.

Brunet, L.J., Gold, G.H., and Ngai, J. (1996). General Anosmia Caused by a Targeted Disruption of the Mouse Olfactory Cyclic Nucleotide–Gated Cation Channel. Neuron *17*, 681–693.

Buck, L., and Axel, R. (1991). A novel multigene family may encode odorant receptors: a molecular basis for odor recognition. Cell *65*, 175–187.

Buiakova, O.I., Baker, H., Scott, J.W., Farbman, A., Kream, R., Grillo, M., Franzen, L., Richman, M., Davis, L.M., Abbondanzo, S., et al. (1996). Olfactory marker protein (OMP) gene deletion causes altered physiological activity of olfactory sensory neurons. Proc. Natl. Acad. Sci. *93*, 9858–9863.

Chen, C., Nakamura, T., and Koutalos, Y. (1999). Cyclic AMP diffusion coefficient in frog olfactory cilia. Biophys. J. *76*, 2861–2867.

Cherry, J.A., and Pho, V. (2002). Characterization of cAMP Degradation by Phosphodiesterases in the Accessory Olfactory System. Chem. Senses *27*, 643–652.

Connelly, T., Savigner, A., and Ma, M. (2013). Spontaneous and sensory-evoked activity in mouse olfactory sensory neurons with defined odorant receptors. J. Neurophysiol. *110*, 55–62.

Cygnar, K.D., and Zhao, H. (2009). Phosphodiesterase 1C is dispensable for rapid response termination of olfactory sensory neurons. Nat. Neurosci. *12*, 454–462.

Dannecker, L.E.C.V., Mercadante, A.F., and Malnic, B. (2005). Ric-8B, an Olfactory Putative GTP Exchange Factor, Amplifies Signal Transduction through the Olfactory-Specific G-Protein Gαolf. J. Neurosci. *25*, 3793–3800.

Dibattista, M., and Reisert, J. (2016). The Odorant Receptor-Dependent Role of Olfactory Marker Protein in Olfactory Receptor Neurons. J. Neurosci. *36*, 2995–3006.

Dibattista, M., Mazzatenta, A., Grassi, F., Tirindelli, R., and Menini, A. (2008). Hyperpolarization-activated cyclic nucleotide-gated channels in mouse vomeronasal sensory neurons. J. Neurophysiol. *100*, 576–586.

Dibattista, M., Pifferi, S., Boccaccio, A., Menini, A., and Reisert, J. (2017). The long tale of the calcium activated Cl- channels in olfactory transduction. Channels Austin Tex *11*, 399–414.

Dooley, R., Baumgart, S., Rasche, S., Hatt, H., and Neuhaus, E.M. (2009). Olfactory receptor signaling is regulated by the post-synaptic density 95, Drosophila discs large, zona-occludens 1 (PDZ) scaffold multi-PDZ domain protein 1. FEBS J. *276*, 7279–7290.

Ferguson, C.H., and Zhao, H. (2017). Simultaneous Loss of NCKX4 and CNG Channel Desensitization Impairs Olfactory Sensitivity. J. Neurosci. *37*, 110–119.

Firestein, S. (2001). How the olfactory system makes sense of scents. Nature *413*, 211–218.

Flannery, R.J., French, D.A., and Kleene, S.J. (2006). Clustering of cyclic-nucleotide-gated channels in olfactory cilia. Biophys. J. *91*, 179–188.

Goldstein, B.J., Kulaga, H.M., and Reed, R.R. (2003). Cloning and Characterization of SLP3: a Novel Member of the Stomatin Family Expressed by Olfactory Receptor Neurons. JARO J. Assoc. Res. Otolaryngol. *4*, 74–82.

Green, J.B., and Young, J.P.W. (2008). Slipins: ancient origin, duplication and diversification of the stomatin protein family. BMC Evol. Biol. *8*, 44.

Henriques, T., Agostinelli, E., Hernandez-Clavijo, A., Maurya, D.K., Rock, J.R., Harfe, B.D., Menini, A., and Pifferi, S. (2019). TMEM16A calcium-activated chloride currents in supporting cells of the mouse olfactory epithelium. J. Gen. Physiol. *151*, 954–966.

Hunyady, B., Krempels, K., Harta, G., and Mezey, E. (1996). Immunohistochemical signal amplification by catalyzed reporter deposition and its application in double immunostaining.: J. Histochem. Cytochem.

Ivic, L., Pyrski, M.M., Margolis, J.W., Richards, L.J., Firestein, S., and Margolis, F.L. (2000). Adenoviral vector-mediated rescue of the OMP-null phenotype in vivo. Nat. Neurosci. *3*, 1113–1120.

Jin, H., and Nachury, M.V. (2009). The BBSome. Curr. Biol. CB *19*, R472-473.

Kaneko-Goto, T., Sato, Y., Katada, S., Kinameri, E., Yoshihara, S., Nishiyori, A., Kimura, M., Fujita, H., Touhara, K., Reed, R.R., et al. (2013). Goofy Coordinates the Acuity of Olfactory Signaling. J. Neurosci. *33*, 12987–12996.

Kerr, D.S., Von Dannecker, L.E.C., Davalos, M., Michaloski, J.S., and Malnic, B. (2008). Ric-8B interacts with G alpha olf and G gamma 13 and co-localizes with G alpha olf, G beta 1 and G gamma 13 in the cilia of olfactory sensory neurons. Mol. Cell. Neurosci. *38*, 341–348.

Kleene, S.J. (2008). The Electrochemical Basis of Odor Transduction in Vertebrate Olfactory Cilia. Chem. Senses *33*, 839–859.

Kleene, S.J., and Gesteland, R.C. (1991). Calcium-activated chloride conductance in frog olfactory cilia. J. Neurosci. *11*, 3624–3629.

Knott, T.K., Madany, P.A., Faden, A.A., Xu, M., Strotmann, J., Henion, T.R., and Schwarting, G.A. (2012). Olfactory discrimination largely persists in mice with defects in odorant receptor expression and axon guidance. Neural Develop. *7*, 17.

Kobayakawa, K., Hayashi, R., Morita, K., Miyamichi, K., Oka, Y., Tsuboi, A., and Sakano, H. (2002). Stomatin-related olfactory protein, SRO, specifically expressed in the murine olfactory sensory neurons. J. Neurosci. Off. J. Soc. Neurosci. *22*, 5931–5937.

Kulaga, H.M., Leitch, C.C., Eichers, E.R., Badano, J.L., Lesemann, A., Hoskins, B.E., Lupski, J.R., Beales, P.L., Reed, R.R., and Katsanis, N. (2004). Loss of BBS proteins causes anosmia in humans and defects in olfactory cilia structure and function in the mouse. Nat. Genet. *36*, 994–998.

Kurtenbach, S., Gießl, A., Strömberg, S., Kremers, J., Atorf, J., Rasche, S., Neuhaus, E.M., Hervé, D., Brandstätter, J.H., Asan, E., et al. (2017). The BEACH Protein LRBA Promotes the Localization of the Heterotrimeric G-protein G olf to Olfactory Cilia. Sci. Rep. *7*, 8409.

Lapatsina, L., Brand, J., Poole, K., Daumke, O., and Lewin, G.R. (2012). Stomatin-domain proteins. Eur. J. Cell Biol. *91*, 240–245.

Lindemann, B. (2001). Predicted profiles of ion concentrations in olfactory cilia in the steady state. Biophys. J. *80*, 1712–1721.

Mayer, H., Breuss, J., Ziegler, S., and Prohaska, R. (1998). Molecular characterization and tissue-specific expression of a murine putative G-protein-coupled receptor. Biochim. Biophys. Acta BBA - Gene Struct. Expr. *1399*, 51–56.

Menco, B.P.M., and Morrison, E.E. (2003). Morphology of the Mammalian Olfactory Epithelium: Form, Fine Structure, Function, and Pathology. 17–49.

Michalakis, S., Reisert, J., Geiger, H., Wetzel, C., Zong, X., Bradley, J., Spehr, M., Hüttl, S., Gerstner, A., Pfeifer, A., et al. (2006). Loss of CNGB1 Protein Leads to Olfactory Dysfunction and Subciliary Cyclic Nucleotide-gated Channel Trapping. J. Biol. Chem. *281*, 35156–35166.

Mombaerts, P. (2004). Genes and ligands for odorant, vomeronasal and taste receptors. Nat. Rev. Neurosci. *5*, 263–278.

Nachury, M.V., and Mick, D.U. (2019). Establishing and regulating the composition of cilia for signal transduction. Nat. Rev. Mol. Cell Biol. *20*, 389–405.

Nakamura, T., and Gold, G.H. (1987). A cyclic nucleotide-gated conductance in olfactory receptor cilia. Nature *325*, 442–444.

Nakashima, N., Nakashima, K., Taura, A., Takaku-Nakashima, A., Ohmori, H., and Takano, M. (2020). Olfactory marker protein directly buffers cAMP to avoid depolarization-induced silencing of olfactory receptor neurons. Nat. Commun. *11*, 2188.

Pietra, G., Dibattista, M., Menini, A., Reisert, J., and Boccaccio, A. (2016). The Ca2+-activated Cl- channel TMEM16B regulates action potential firing and axonal targeting in olfactory sensory neurons. J. Gen. Physiol. *148*, 293–311.

Pifferi, S., Dibattista, M., and Menini, A. (2009). TMEM16B induces chloride currents activated by calcium in mammalian cells. Pflüg. Arch. Eur. J. Physiol. *458*, 1023–1038.

Pifferi, S., Menini, A., and Kurahashi, T. (2010). Signal Transduction in Vertebrate Olfactory Cilia. In The Neurobiology of Olfaction, A. Menini, ed. (Boca Raton (FL): CRC Press/Taylor & Francis), pp. 203–223.

Poole, K., Herget, R., Lapatsina, L., Ngo, H.-D., and Lewin, G.R. (2014). Tuning Piezo ion channels to detect molecular-scale movements relevant for fine touch. Nat. Commun. *5*, 3520.

Qi, Y., Andolfi, L., Frattini, F., Mayer, F., Lazzarino, M., and Hu, J. (2015). Membrane stiffening by STOML3 facilitates mechanosensation in sensory neurons. Nat. Commun. *6*, 8512.

Qiu, L., LeBel, R.P., Storm, D.R., and Chen, X. (2016). Type 3 adenylyl cyclase: a key enzyme mediating the cAMP signaling in neuronal cilia. Int. J. Physiol. Pathophysiol. Pharmacol. *8*, 95–108.

Reisert, J. (2010). Origin of basal activity in mammalian olfactory receptor neurons. J. Gen. Physiol. *136*, 529–540.

Reisert, J., and Matthews, H.R. (1998). Na+-dependent Ca2+ extrusion governs response recovery in frog olfactory receptor cells. J. Gen. Physiol. *112*, 529–535.

Reisert, J., and Reingruber, J. (2019). Ca2+-activated Cl- current ensures robust and reliable signal amplification in vertebrate olfactory receptor neurons. Proc. Natl. Acad. Sci. U. S. A. *116*, 1053–1058.

Reisert, J., Lai, J., Yau, K.-W., and Bradley, J. (2005). Mechanism of the Excitatory Cl− Response in Mouse Olfactory Receptor Neurons. Neuron *45*, 553–561.

Reisert, J., Yau, K.-W., and Margolis, F.L. (2007). Olfactory marker protein modulates the cAMP kinetics of the odour-induced response in cilia of mouse olfactory receptor neurons. J. Physiol. *585*, 731–740.

Restrepo, D., and Teeter, J.H. (1990). Olfactory neurons exhibit heterogeneity in depolarization-induced calcium changes. Am. J. Physiol.-Cell Physiol. *258*, C1051–C1061.

Salzer, U., Mairhofer, M., and Prohaska, R. (2007). Stomatin: A new paradigm of membrane organization emerges. Dyn. Cell Biol. *1*, 20–33.

Schild, D., and Restrepo, D. (1998). Transduction Mechanisms in Vertebrate Olfactory Receptor Cells. Physiol. Rev. *78*, 429–466.

Schroeder, B.C., Cheng, T., Jan, Y.N., and Jan, L.Y. (2008). Expression cloning of TMEM16A as a calcium-activated chloride channel subunit. Cell *134*, 1019–1029.

Sezgin, E., Levental, I., Mayor, S., and Eggeling, C. (2017). The mystery of membrane organization: composition, regulation and roles of lipid rafts. Nat. Rev. Mol. Cell Biol. *18*, 361–374.

Shimazaki, R., Boccaccio, A., Mazzatenta, A., Pinato, G., Migliore, M., and Menini, A. (2006). Electrophysiological properties and modeling of murine vomeronasal sensory neurons in acute slice preparations. Chem. Senses *31*, 425–435.

Simons, K., and Toomre, D. (2000). Lipid rafts and signal transduction. Nat. Rev. Mol. Cell Biol. *1*, 31–39.

Sinnarajah, S., Dessauer, C.W., Srikumar, D., Chen, J., Yuen, J., Yilma, S., Dennis, J.C., Morrison, E.E., Vodyanoy, V., and Kehrl, J.H. (2001). RGS2 regulates signal transduction in olfactory neurons by attenuating activation of adenylyl cyclase III. Nature *409*, 1051–1055.

Stephan, A.B., Shum, E.Y., Hirsh, S., Cygnar, K.D., Reisert, J., and Zhao, H. (2009). ANO2 is the cilial calcium-activated chloride channel that may mediate olfactory amplification. Proc. Natl. Acad. Sci. U. S. A. *106*, 11776–11781.

Tadenev, A.L.D., Kulaga, H.M., May-Simera, H.L., Kelley, M.W., Katsanis, N., and Reed, R.R. (2011). Loss of Bardet-Biedl syndrome protein-8 (BBS8) perturbs olfactory function, protein localization, and axon targeting. Proc. Natl. Acad. Sci. U. S. A. *108*, 10320–10325.

Talaga, A.K., Dong, F.N., Reisert, J., and Zhao, H. (2017). Cilia- and flagella-associated protein 69 regulates olfactory transduction kinetics in mice. J. Neurosci.

Tavernarakis, N., Driscoll, M., and Kyrpides, N.C. (1999). The SPFH domain: implicated in regulating targeted protein turnover in stomatins and other membrane-associated proteins. Trends Biochem. Sci. *24*, 425–427.

Trotier, D. (1994). Intensity coding in olfactory receptor cells. Semin. Cell Biol. *5*, 47–54.

Umlauf, E., Mairhofer, M., and Prohaska, R. (2006). Characterization of the stomatin domain involved in homo-oligomerization and lipid raft association. J. Biol. Chem. *281*, 23349–23356.

Villar, P.S., Delgado, R., Vergara, C., Reyes, J.G., and Bacigalupo, J. (2017). Energy Requirements of Odor Transduction in the Chemosensory Cilia of Olfactory Sensory Neurons Rely on Oxidative Phosphorylation and Glycolytic Processing of Extracellular Glucose. J. Neurosci. *37*, 5736–5743.

Wei, J., Zhao, A.Z., Chan, G.C.K., Baker, L.P., Impey, S., Beavo, J.A., and Storm, D.R. (1998). Phosphorylation and Inhibition of Olfactory Adenylyl Cyclase by CaM Kinase II in Neurons: a Mechanism for Attenuation of Olfactory Signals. Neuron *21*, 495–504.

Wetzel, C., Hu, J., Riethmacher, D., Benckendorff, A., Harder, L., Eilers, A., Moshourab, R., Kozlenkov, A., Labuz, D., Caspani, O., et al. (2007). A stomatin-domain protein essential for touch sensation in the mouse. Nature *445*, 206–209.

Wong, S.T., Trinh, K., Hacker, B., Chan, G.C.K., Lowe, G., Gaggar, A., Xia, Z., Gold, G.H., and Storm, D.R. (2000). Disruption of the Type III Adenylyl Cyclase Gene Leads to Peripheral and Behavioral Anosmia in Transgenic Mice. Neuron *27*, 487–497.

Wong, W.M., Nagel, M., Hernandez-Clavijo, A., Pifferi, S., Menini, A., Spehr, M., and Meeks, J.P. (2018). Sensory Adaptation to Chemical Cues by Vomeronasal Sensory Neurons. ENeuro *5*.

Yan, C., Zhao, A.Z., Bentley, J.K., Loughney, K., Ferguson, K., and Beavo, J.A. (1995). Molecular cloning and characterization of a calmodulin-dependent phosphodiesterase enriched in olfactory sensory neurons. Proc. Natl. Acad. Sci. U. S. A. *92*, 9677–9681.

Zheng, J., and Zagotta, W.N. (2004). Stoichiometry and assembly of olfactory cyclic nucleotide-gated channels. Neuron *42*, 411–421.

JGP Journal of General Physiology

COMMUNICATION

TMEM16A calcium-activated chloride currents in supporting cells of the mouse olfactory epithelium

Tiago Henriques[1*], Emilio Agostinelli[1*], Andres Hernandez-Clavijo[1], Devendra Kumar Maurya[1], Jason R. Rock[2], Brian D. Harfe[3], Anna Menini[1], and Simone Pifferi[1]

Glial-like supporting (or sustentacular) cells are important constituents of the olfactory epithelium that are involved in several physiological processes such as production of endocannabinoids, insulin, and ATP and regulation of the ionic composition of the mucus layer that covers the apical surface of the olfactory epithelium. Supporting cells express metabotropic P2Y purinergic receptors that generate ATP-induced Ca^{2+} signaling through the activation of a PLC-mediated cascade. Recently, we reported that a subpopulation of supporting cells expresses also the Ca^{2+}-activated Cl^- channel TMEM16A. Here, we sought to extend our understanding of a possible physiological role of this channel in the olfactory system by asking whether Ca^{2+} can activate Cl^- currents mediated by TMEM16A. We use whole-cell patch-clamp analysis in slices of the olfactory epithelium to measure dose–response relations in the presence of various intracellular Ca^{2+} concentrations, ion selectivity, and blockage. We find that knockout of TMEM16A abolishes Ca^{2+}-activated Cl^- currents, demonstrating that TMEM16A is essential for these currents in supporting cells. Also, by using extracellular ATP as physiological stimuli, we found that the stimulation of purinergic receptors activates a large TMEM16A-dependent Cl^- current, indicating a possible role of TMEM16A in ATP-mediated signaling. Altogether, our results establish that TMEM16A-mediated currents are functional in olfactory supporting cells and provide a foundation for future work investigating the precise physiological role of TMEM16A in the olfactory system.

Introduction

The olfactory epithelium is a pseudostratified epithelium composed of olfactory sensory neurons, glial-like supporting (or sustentacular) cells, basal cells, and microvillous cells, covered by a protective mucus layer composed of water, ions, and proteins secreted by Bowman's glands and supporting cells (Menco and Farbman, 1992; Menco et al., 1998). Although most studies concentrated on the physiological role of olfactory sensory neurons, as they detect odorant molecules, very few investigated how the supporting cells contribute to the epithelium homeostasis.

Supporting cells have columnar cell bodies that form a monolayer at the apical surface of the olfactory epithelium and basal processes extending to the basal lamina. The apical side of these cells bears several microvilli immersed in the mucus layer intermingling with cilia of olfactory sensory neurons. Supporting cells are electrically coupled by gap junctions composed at least by connexin 43 and 45, creating a syncytium for the diffusion of Ca^{2+} and other signaling molecules throughout the epithelium (Rash et al., 2005; Vogalis et al., 2005a,b).

These cells perform a large number of physiological functions. For example, they surround and provide structural support to olfactory sensory neurons, act as phagocytes of dead cells, and are involved in the metabolism of external compounds mediated by cytochrome P450 and other enzymes (Breipohl et al., 1974; Chen et al., 1992; Suzuki et al., 1996; Gu et al., 1998; Ling et al., 2004; Whitby-Logan et al., 2004). Neurotrophic and neuromodulator molecules such as endocannabinoids, insulin, and ATP are produced by supporting cells (Czesnik et al., 2007; Lacroix et al., 2008; Breunig et al., 2010; Hayoz et al., 2012). Moreover, they express metabotropic P2Y purinergic receptors, and stimulation with ATP induces Ca^{2+} signaling through the activation of a PLC-mediated cascade (Hegg et al., 2003, 2009; Gayle and Burnstock, 2005). Interestingly, several studies showed that ATP is involved in neuroprotection and neuroproliferation (Hassenklöver et al., 2009; Jia et al., 2009, 2010; Jia and Hegg, 2010). The mechanisms mediating the aforementioned functions are far from being completely elucidated.

[1]Neurobiology Group, International School for Advanced Studies, Trieste, Italy; [2]Center for Regenerative Medicine, Boston University School of Medicine, Boston, MA; [3]Department of Molecular Genetics and Microbiology Genetics Institute, University of Florida, College of Medicine, Gainesville, FL.

*T. Henriques and E. Agostinelli contributed equally to this paper; Correspondence to Simone Pifferi: spifferi@sissa.it; D. Kumar Maurya's present address is Department of Molecular Biology, Umeå University, Umeå, Sweden.

Moreover, supporting cells have peculiar electrical properties and express several channels involved in the regulation of the ionic composition of the mucus layer at the apical surface of the olfactory epithelium, contributing to the maintenance of a balance between salts and water. For example, the amiloride-sensitive Na^+ channel is highly expressed in microvilli of supporting cells (Menco et al., 1998), and it has been suggested that the cystic fibrosis transmembrane conductance regulator Cl^- channel and members of the aquaporin water channel family are possibly located in these cells, although their localization has not been conclusively demonstrated (Rochelle et al., 2000; Ablimit et al., 2006; Grubb et al., 2007; Lu et al., 2008; Merigo et al., 2011; Pfister et al., 2015).

We and others have recently shown that a relatively new discovered Ca^{2+}-activated Cl^- channel, TMEM16A, is expressed in olfactory supporting cells (Dauner et al., 2012; Maurya and Menini, 2014; Maurya et al., 2015). Interestingly, we found that TMEM16A expression is limited to supporting cells from a specific region of the olfactory epithelium (Maurya and Menini, 2014), although others, while confirming TMEM16A expression in the supporting cells, did not mention any zonal expression of the channel (Dauner et al., 2012). For this reason, here, we first tried to define whether a zonal expression of TMEM16A can be observed in the olfactory epithelium. By using immunohistochemistry on WT and TMEM16A knock out (KO) mice, we found that TMEM16A is expressed both in the ventral and dorsal zones of the olfactory epithelium, although its expression is higher in the region near the transition zone with the respiratory epithelium than in the dorsal zone.

Because TMEM16A is expressed in supporting cells, is it also mediating Ca^{2+}-activated Cl^- currents in these cells? To begin to address this question, we performed recordings in whole cells from mouse supporting cells after blocking gap junctions with 18β-glycyrrhetinic acid (18β-GA; Davidson and Baumgarten, 1988) and recorded Ca^{2+}-activated Cl^- currents in WT but not TMEM16A KO mice, showing that TMEM16A is necessary for the activation of this current in mouse olfactory supporting cells. TMEM16A controls fluid secretion in airway and intestine epithelia (Rock et al., 2009; Benedetto et al., 2017, 2019), suggesting that TMEM16A could play a similar role in supporting cells. Moreover, TMEM16A can modulate several aspects of Ca^{2+} homeostasis, consequently regulating different signaling cascades (Kunzelmann et al., 2016; Cabrita et al., 2017). What signaling pathway leads to the activation of TMEM16A-mediated currents in supporting cells? We found that stimulation of purinergic receptors with ATP activated a TMEM16A-dependent current.

In summary, TMEM16A can produce Ca^{2+}-activated Cl^- currents in response to extracellular ATP in olfactory supporting cells. Finally, we picture and discuss the different scenarios of physiological functions of supporting cells and their chloride conductance.

Materials and methods

Animals

Mice were handled in accordance with the guidelines of the Italian Animal Welfare Act and European Union guidelines on animal research under a protocol approved by the ethics committee of the International School for Advanced Studies. Postnatal days 0–4 (P0–P4) mice were decapitated before nose removal. Experiments were performed on tissues from C57BL/6 mice or from TMEM16A WT and TMEM16A KO littermate mice obtained by breeding heterozygous mice generated by Rock et al. (2008).

Immunohistochemistry

Coronal sections of the olfactory epithelium and immunohistochemistry were obtained as previously described (Maurya and Menini, 2014; Maurya et al., 2015). Briefly, the dissected nose was fixed in 4% paraformaldehyde PBS for 4 h at 4°C. Tissues were equilibrated overnight at 4°C in 30% (wt/vol) sucrose and then embedded in optimal cutting temperature compound (Bioptica) and stored at −80°C. Coronal sections 12- to 14-µm thick were cut with a cryostat. Before using primary antibodies, sections were incubated in blocking solution (2% FBS [vol/vol] and 0.2% [vol/vol] Triton X-100 in PBS) for 90 min. Then, they were incubated with the primary antibody (diluted in the blocking solution) overnight at 4°C. The following primary antibodies (catalog number, dilution; company) were used: polyclonal goat anti-OMP (544–10001, 1:1,000; Wako Chemicals), mouse monoclonal acetylated tubulin (T7451, 1:100; Sigma), and rabbit polyclonal anti-TMEM16A (ab53212, 1:50; Abcam). Sections were then rinsed with 0.1% (vol/vol) Tween 20 in PBS (PBS-T) and incubated with the fluorophore-conjugated secondary antibody (diluted in PBS-T) for 2 h at room temperature. The following secondary antibodies were used: donkey anti-rabbit Alexa Fluor 488 (A-21206; Life Technologies), donkey anti-goat Alexa Fluor 594 (A-11058; Life Technologies), and donkey anti-mouse Alexa Fluor 594 (A-21203; Life Technologies). After washing with PBS-T, sections were treated with 0.1 µg/ml DAPI for 30 min, washed with PBS-T, and mounted with Vectashield (Vector Laboratories).

Immunoreactivity was visualized with a confocal microscope (TCS SP2; Leica). Images were acquired using Leica software (at 1,024 × 1,024–pixel resolution) and were not modified other than to balance brightness and contrast, unless otherwise specified. Nuclei were stained by DAPI. Control experiments without the primary antibodies gave no signal. In addition, negative control experiments for the localization of TMEM16A were performed in tissues from TMEM16A KO mice following the same protocol used in WT mice.

Preparation of acute slices of the olfactory epithelium

Acute coronal slices of the olfactory epithelium of P0–P4 mice were prepared with slight modifications of the methods previously described to obtain slices of the vomeronasal organ (Shimazaki et al., 2006; Dibattista et al., 2008; Pietra et al., 2016; Wong et al., 2018). P0–P4 mice are suitable for this study, because TMEM16A is already expressed in the olfactory epithelium at this age (Maurya and Menini, 2014; Maurya et al., 2015). The nose of a P0–P4 mouse was dissected en bloc and embedded in 3% Type I-A agarose prepared in artificial cerebrospinal fluid (ACSF) once the solution cooled to 38°C. ACSF contained (in mM) 120 NaCl, 25 $NaHCO_3$, 5 KCl, 1 $MgSO_4$, 1 $CaCl_2$, 10 HEPES, and 10 glucose, pH 7.4, with NaOH. Coronal slices of 300-µm

thickness were cut with a vibratome (Vibratome 1000 Plus Sectioning System) and kept in cold oxygenated ACSF until use.

Whole-cell recordings from supporting cells of the olfactory epithelium

Slices were transferred to a recording chamber continuously perfused with oxygenated ACSF. Slices were viewed with an upright microscope (BX51WI; Olympus) equipped with infrared differential contrast optics, a camera (DFK 72BUC02; Imaging Source) and a 40× water-immersion objective with an additional 2× auxiliary lens. Extracellular solutions were exchanged or stimuli were delivered through an eight-in-one multibarrel perfusion pencil connected to a ValveLink8.2 pinch valve perfusion system (Automate Scientific).

Supporting cells were identified by their morphology, and whole-cell experiments were obtained by patching the apical part of supporting cells. Fluorescein (10 µg/ml) dissolved in the pipette solution diffused into the cell and allowed visualization under blue light of the fluorescence image of the cell (Fig. 2 A). Patch pipettes were pulled from borosilicate capillaries (WPI) with a Narishige PC-10 puller and had resistances of 3–5 MΩ when filled with intracellular solution. Electrophysiological recordings were obtained using a MultiClamp 700B amplifier controlled by Clampex 10.6 via a Digidata 1550B (Molecular Devices). Data were low-pass filtered at 2 kHz and sampled at 10 kHz. Experiments were performed at room temperature (20–25°C).

The extracellular Ringer's solution contained (in mM) 140 NaCl, 5 KCl, 2 $CaCl_2$, 1 $MgCl_2$, 10 HEPES, and 10 glucose, pH 7.4. For ionic selectivity experiments, NaCl in the extracellular Ringer's solution was omitted and 250 mM sucrose was added to maintain the osmolarity (sucrose Ringer's) or NaCl was replaced with equimolar NMDG-Cl (NMDG Ringer's). We used various intracellular solutions filling the patch pipette according to the type of experiment. For recordings of voltage-gated currents, the pipette solution contained (in mM): 145 KCl, 4 $MgCl_2$, 11 EGTA, and 10 HEPES, adjusted to pH 7.2 with KOH. For recordings of Ca^{2+}-activated currents, the intracellular solutions contained (in mM) 140 CsCl, 10 HEDTA, and 10 HEPES adjusted to pH 7.2 with CsOH, and no added Ca^{2+} for the nominally 0 Ca^{2+} solution or various added Ca^{2+} concentrations, as calculated with the program WinMAXC (C. Patton, Stanford University, Stanford, CA), to obtain free Ca^{2+} in the range between 0.5 and 3.8 µM (Patton et al., 2004). 10 mM HEDTA had the best buffer efficacy in the desired range of free Ca^{2+} concentrations. We added 1.242, 3.209, or 5.806 mM $CaCl_2$ to obtain 0.5, 1.5, or 3.8 µM free Ca^{2+}, respectively, as described previously (Pifferi et al., 2006, 2009; Cenedese et al., 2012; Betto et al., 2014; Amjad et al., 2015). The free Ca^{2+} concentrations were also experimentally determined by Fura-4F (Thermo Fisher Scientific) measurements by using an LS-50B luminescence spectrophotometer (PerkinElmer).

For recordings of ATP-activated currents, the pipette solution contained (in mM) 140 CsCl, 2 HEDTA, and 10 HEPES, adjusted to pH 7.2 with CsOH. I-V relations were measured using a ramp protocol from −80 mV to +80 mV at 0.16 mV/ms.

The bath was grounded via a 3 M KCl agar bridge connected to an Ag/AgCl reference electrode. Liquid junction potentials were calculated using pClamp 10.6 (based on Barry, 1994), and the applied voltages were corrected offline for the following values (in mV) in the indicated bathing solutions: −4.7 in Ringer's solution, +7.9 in sucrose Ringer's solution, and −5.7 in NMDG Ringer's solution.

The following chemicals were prepared as stock solutions as indicated and diluted to the final concentration in the bathing solution on the day of the experiment: 100 mM 18β-GA in ethanol, 30 mM ATP in Ringer's solution, stored at −20°C; and 1 mM Ani9 in DMSO, stored at +4°C. The final concentration of 18β-GA was 20 µM as previously used by Vogalis et al. (2005a,b) to substantially reduce the resting leak conductance in olfactory supporting cells. At this concentration, 18β-GA is reported to block most of the gap-junction–mediated current in fibroblasts (Davidson and Baumgarten, 1988). The final concentration of ATP was 30 µM, which is slightly higher than the concentration of 10 µM used by Hegg et al. (2003) to activate P2Y receptors expressed in supporting cells and induce an intracellular Ca^{2+} increase. All chemicals were purchased from Sigma unless otherwise specified.

Confocal Ca^{2+} imaging

Slices were loaded with 20 µM Cal-520AM (Santa Cruz Biotechnologies) for 90 min at room temperature in ACSF. The concentration of Cal-520AM required for cell loading in our slices was determined empirically after testing several dye working solutions from 10 to 20 µM, as suggested by the technical information sheet. To help dye uptake, Pluronic F-127 was added at final concentration of 0.2 mg/ml. After washing, the slices were kept in ACSF solution until use. Stock solution of Cal-520AM was prepared in DMSO at 2 mM and stored at −20°C. Pluronic F-127 was weekly dissolved in DMSO at 200 mg/ml concentration. A gravity-driven multivalve perfusion system (Automate Scientific) was used to deliver the stimuli.

An inverted Nikon A1R confocal microscope was used for data acquisition with a 60× oil-immersion objective (numerical aperture 1.3) using NIS Element software (Nikon). Cal-520 fluorescence was excited using a krypton-argon ion laser. To reduce dye bleaching and photodamage, only 1–4% of the laser power and a resonance scanning mirror was used. Fluorescence emission between 500 and 600 nm was captured using a variable band bass system. Data were recorded after averaging eight frames to get a final acquisition frequency of 0.23 Hz with 1,024 × 512–pixel resolution. Recordings were obtained 50–100 µm below the slice surface to avoid damaged cells.

Changes in fluorescence were measured in regions of interest drawn around a single supporting cell using ImageJ 1.51s (National Institutes of Health). Data are presented as normalized fluorescence changes, $\Delta F/F_0 = (F(t) - F_0)/F_0$, where F_0 is the average of fluorescence intensity before the application of the first stimulus and F(t) is the fluorescence amplitude at time t. Further analysis and figures were made with IgorPro 6.3.7.2 (WaveMetrics). In some experiments, the reduction of fluorescence signal due to photobleaching was mathematically corrected using the exponential decay observed in nonresponding cells (Thomas et al., 2000). We considered a cell responsive if (a) there was no spontaneous activity; (b) after stimulation, $\Delta F/F_0$

was higher than the average of the prestimulus (10-s time window) plus three SDs for at least 3 s; and (c) there was no response to ACSF solution application.

Analysis of electrophysiological data

IGOR Pro software (WaveMetrics) was used for data analysis and to produce the figures. All averaged data from individual experiments in different cells are presented as mean ± SEM and number of cells (n). Cells were obtained from at least three different WT or KO mice. In the box plot, horizontal lines represent the median, upper and lower box boundaries represent the 25th and 75th percentile, and upper and lower whiskers represent the 10th and 90th percentiles. Statistical analyses of normally distributed data (Jarque–Bera test) were performed using a *t* test, one-sample *t* test, or one-way ANOVA with Tukey test. For not normally distributed data, the Wilcoxon–Mann–Whitney *U* test and Kruskal–Wallis with Dunn–Holland–Wolfe test were used. P values of <0.05 were considered statistically significant.

Results

TMEM16A expression in olfactory supporting cells

Considering that the physiological role of TMEM16A in olfactory supporting cells is unknown, we started studying the TMEM16A expression in the olfactory epithelium. We previously reported a not-uniform immunoreactivity for TMEM16A in the olfactory epithelium of postnatal mice (Maurya and Menini, 2014). Indeed, we found that TMEM16A is expressed only in the supporting cells in the ventral region of olfactory epithelium close to the respiratory epithelium. However, Dauner et al. (2012) did not show this specific localization and instead found TMEM16A in supporting cells from all olfactory epithelium. For this reason, we first asked whether TMEM16A is specifically expressed only near the transition zone, and therefore has a physiological role only in that zone, or if it is also poorly expressed in other regions of the olfactory epithelium.

By immunohistochemistry, we confirmed previous results that TMEM16A is strongly expressed at the apical surface of the ventral region of the olfactory epithelium near the transition zone with the respiratory epithelium, but we also identified a weak staining for TMEM16A in the dorsal zone that could be revealed only by digital enhancement of the signal intensity (Fig. 1, A–D). We performed control experiments in the olfactory epithelium of TMEM16A KO mice following the same protocol and found no signal for TMEM16A, confirming the specificity of the immunostaining obtained in WT mice (Fig. 1, C and D). To visualize olfactory neurons, we used the olfactory marker protein, a typical marker for mature olfactory sensory neurons (Keller and Margolis, 1975), while the cilia of olfactory neurons were identified with acetylated tubulin, a canonical marker for cilia (Piperno and Fuller, 1985). In both the transition and dorsal zones, TMEM16A was expressed at the apical surface of the olfactory epithelium of WT mice, and it did not overlap with the upper layer stained by acetylated tubulin, confirming that TMEM16A was not expressed in olfactory sensory neurons but was localized at the apical portion of supporting cells.

These results confirm and extend previous data showing that TMEM16A is highly expressed in the transition zone (Fig. 1 C), while it is poorly expressed in the dorsal zone (Fig. 1 D).

Ca^{2+}-activated Cl^- currents in supporting cells of the mouse olfactory epithelium

TMEM16A is a Ca^{2+}-activated Cl^- channel, but currents caused by the activity of this channel have not yet been reported in olfactory supporting cells. Therefore, we performed electrophysiological experiments to investigate the presence of functional Ca^{2+}-activated Cl^- channels in these cells.

First, we established the viability of obtaining electrophysiological recordings from supporting cells by measuring basic electrophysiological properties and voltage-gated currents. Whole-cell recordings were obtained from supporting cells at the apical surface of neonatal mouse olfactory epithelium slices. To visually identify cells, fluorescein was included in the intracellular solution filling the patch pipette and diffused inside the cell after rupturing the membrane to obtain the whole-cell configuration. The fluorescence image in Fig. 2 A reveals the typical morphology of a supporting cell, with the cell body located in the apical region and processes extending toward the basal part of the epithelium. In this study, we only analyzed recordings from supporting cells clearly identified by their morphology. Passive membrane properties in the presence of KCl in the pipette had the following values: mean resting potential, −41 ± 1 mV (n = 18); input resistance, 261 ± 88 MΩ (n = 11); and capacitance, 17 ± 1 pF (n = 17). Next, we investigated the presence of voltage-gated currents (Fig. 2). As supporting cells have very large leak currents (see Fig. 2, D and E), voltage-gated currents could only be revealed after subtraction of the leak currents using the P/4 protocol (Fig. 2 B). Voltage steps more positive than approximately −60 mV elicited transient inward currents followed by outward currents. Average I-V relations measured at the peak of the inward currents or at the end of the sustained outward currents (Fig. 2 C) are largely similar to those previously reported by Vogalis et al. (2005a), who showed that inward and outward currents were mainly due to voltage-gated Na^+ and K^+ channels. Our results confirm the viability of electrophysiological recordings of supporting cells in our slice preparation.

Before measuring Ca^{2+}-activated currents, we tested whether we could block the large leak conductance measured in the presence of nominally 0 Ca^{2+}. Indeed, in extracellular Ringer's solution, the average current was −687 ± 206 pA at −80 mV and 3,678 ± 1,065 pA at +80 mV (n = 4), with an intracellular solution containing CsCl (Fig. 2, D and E). After pretreatment of slices for ∼1 h with 20 µM 18β-GA, a gap junction blocker, currents were significantly reduced to −174 ± 18 pA at −80 mV and 459 ± 54 pA at +80 mV (n = 17, P < 0.001, unpaired Wilcoxon–Mann–Whitney *U* test; Fig. 2, D and E), confirming that 20 µM 18β-GA partially blocks the leak currents as previously reported (Vogalis et al., 2005a,b). Thus, all the subsequent experiments were performed with intracellular CsCl after pretreatment with 20 µM 18β-GA.

To establish whether a current could be activated by Ca^{2+} in supporting cells, we compared currents measured with intracellular solutions containing various Ca^{2+} concentrations

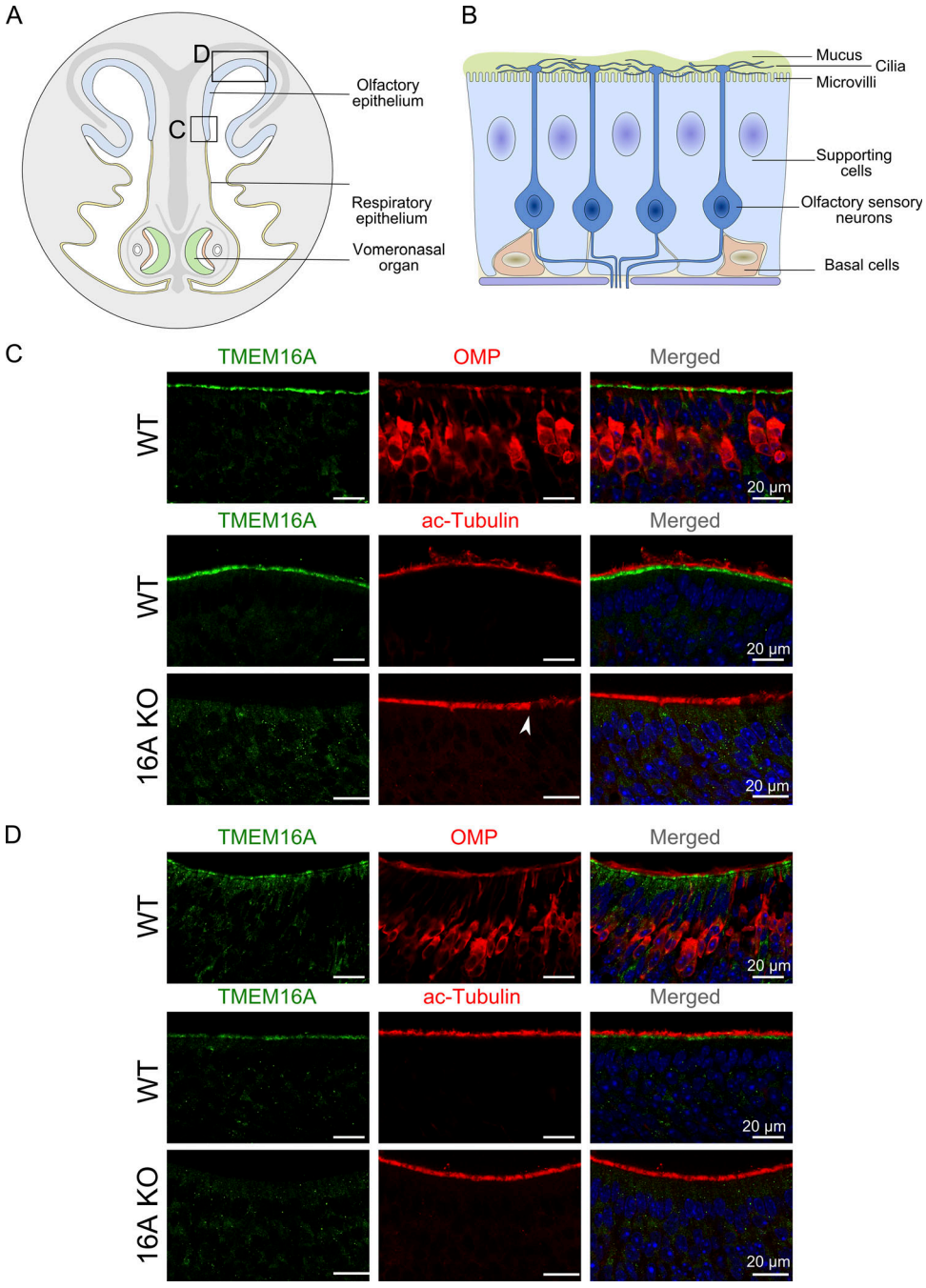

Figure 1. **TMEM16A expression in the olfactory epithelium. (A)** Schematic drawing of a nose coronal section showing the olfactory epithelium, respiratory epithelium, and vomeronasal organ. **(B)** The olfactory epithelium is composed of supporting cells, olfactory sensory neurons, and basal cells. **(C and D)** Confocal micrographs of coronal sections of the olfactory epithelium from an area near the transition zone with the respiratory epithelium (C) or from the dorsal zone (D). The signal intensity in D was digitally enhanced to reveal a weak staining for TMEM16A. No immunoreactivity to TMEM16A was detectable at the apical surface of the olfactory epithelium in TMEM16A KO mice (C and D). Arrowhead in C indicates the transition from the olfactory to respiratory epithelium. Cell nuclei were stained by DAPI. OMP, olfactory marker protein.

ranging from nominally 0 to 3.8 µM Ca^{2+}. Since we have previously shown that cells in the transition zone display a strong immunoreactivity for the Ca^{2+}-activated Cl^- channel TMEM16A (Fig. 1 C), we first recorded from supporting cells located in this area.

Fig. 3 A shows currents in the presence of increasing $[Ca^{2+}]_i$. The activation of the current by voltage steps in the presence of 0.5 and 1.5 µM Ca^{2+} was time dependent, with an instantaneous component followed by relaxation (Fig. 3 A, red and blue traces). Indeed, at +80 mV, the instantaneous outward current was followed by a small additional outward relaxation, while at −80 mV, the instantaneous inward current was followed by a more pronounced relaxation toward less negative values. Moreover, when the voltage was stepped to −80 mV at the end of the

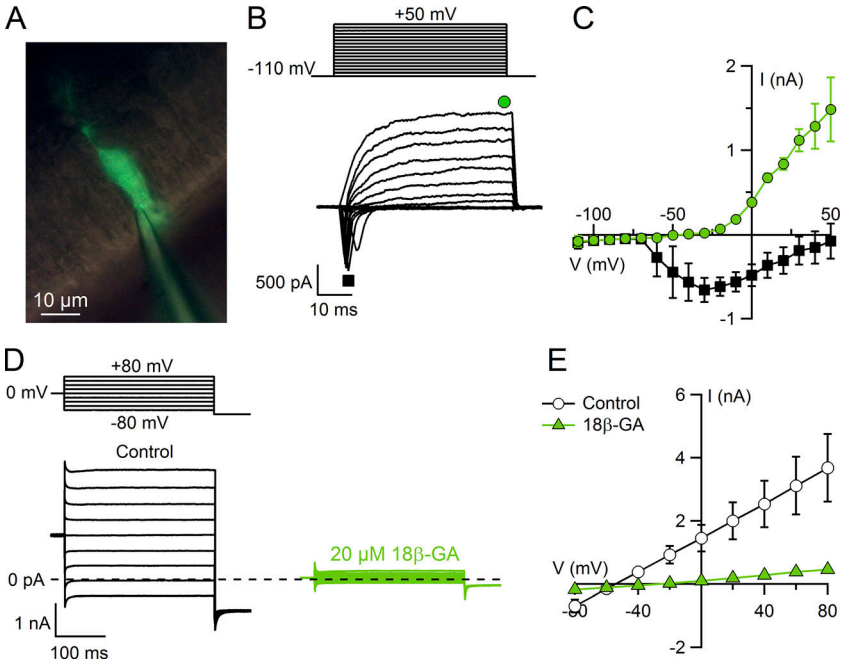

Figure 2. **Voltage-gated currents and leak currents in olfactory supporting cells. (A)** Fluorescence micrograph of a supporting cell filled with fluorescein through the patch pipette. **(B)** Representative whole-cell currents recorded using the voltage protocol indicated at the top of the panel. The holding potential was −110 mV, and voltage steps in 10-mV increments were applied up to +50 mV. Leak currents were subtracted using the P/4 protocol. **(C)** Plot of average ± SEM amplitudes of inward (black squares) and outward (green circles) currents versus the test potential (n = 3). **(D)** Representative whole-cell currents recorded from two different supporting cells in control condition (black traces) and after preincubation with 20 µM 18β-GA (green traces). The holding potential was 0 mV, and voltage steps from −80 mV to +80 mV with 20-mV increments were applied as indicated at the top of the panel. **(E)** Plot of average ± SEM current amplitudes measured at the end of voltage pulses versus the test potential from cells in control condition (white circles; n = 4) and after preincubation with 20 µM 18β-GA (green triangles; n = 17).

protocol, deactivating inward tail currents were observed. I-V relations measured at the end of voltage pulses showed an outward rectification at 0.5 µM Ca^{2+} that became less pronounced as $[Ca^{2+}]_i$ increased (Fig. 3, A and B). The rectification index, calculated as the ratio between the current at +80 and −80 mV, decreased from 4.1 ± 0.3 (n = 5) at 0.5 µM Ca^{2+} to 1.24 ± 0.06 (n = 7) at 3.8 µM (Fig. 3 C; P < 0.001, Dunn–Holland–Wolfe test).

Dose–response relations were evaluated at +80 and −80 mV. The average current at +80 mV in the presence of nominally 0 Ca^{2+} (residual leak current, I_L) was 459 ± 54 pA (n = 17), while 0.5 µM Ca^{2+} elicited comparatively larger currents (1,151 ± 192 pA, n = 5). Further increases of $[Ca^{2+}]_i$ produced currents of higher amplitudes, reaching an average of 2,268 ± 137 pA (n = 33) with 1.5 µM Ca^{2+} and 2,328 ± 296 pA (n = 7) with 3.8 µM Ca^{2+} (Fig. 3 D). The average current amplitudes were plotted versus $[Ca^{2+}]_i$ and fit at each voltage by the Hill equation:

$$I = I_L + (I_{max} - I_L)[Ca^{2+}]_i^{n_H} / ([Ca^{2+}]_i^{n_H} + K_{1/2}^{n_H}), \quad (1)$$

where I is the current, I_L is the residual leak current in the presence of nominally 0 Ca^{2+}, I_{max} is the maximal current, $K_{1/2}$ is the half-maximal $[Ca^{2+}]_i$, and n_H is the Hill coefficient. The Hill coefficient had the same value of 2.5 at both voltages, while $K_{1/2}$ decreased with membrane depolarization from 1.5 µM at −80 mV to 0.6 µM at +80 mV (Fig. 3 D), indicating that the Ca^{2+} sensitivity is slightly voltage dependent.

The ionic selectivity was evaluated by replacing NaCl in the extracellular Ringer's solution with sucrose or NMDG-Cl (Fig. 3, E–H). In the presence of low extracellular Cl^-, the reversal potential of the Ca^{2+}-activated current shifted toward positive values, as expected for Cl^--selective channels in our ionic conditions, with an average shift of reversal potential of 40 ± 4 mV (n = 7). When NaCl was replaced with NMDG-Cl, a very small shift of the reversal potential of 4.2 ± 0.2 mV (n = 4) was measured, confirming the Cl^- selectivity of these channels.

Altogether, the time dependence of current activation by voltage, change of rectification of the I-V relation depending on $[Ca^{2+}]_i$, voltage dependence of Ca^{2+} sensitivity, and Cl^- selectivity are typical hallmarks of Ca^{2+}-activated Cl^- channels (Huang et al., 2012; Pedemonte and Galietta, 2014), suggesting that these channels may be responsible for the measured currents.

As we have shown that a weak immunoreactivity for TMEM16A was also present in supporting cells from the dorsal zone of the olfactory epithelium (Fig. 1 D), we also performed electrophysiological recordings in this zone (Fig. 4). The typical features of Ca^{2+}-activated Cl^- currents were present in several cells (represented by colored traces; Fig. 4, A and B) but absent in other cells (gray traces). We estimated that in the presence of 1.5 µM Ca^{2+}, ∼65% of the measured supporting cells (16 out of 24) from the dorsal zone had a Ca^{2+}-activated current, although its amplitude was significantly smaller than that measured in cells from the transition zone (Fig. 4 C; Tukey test after one way ANOVA), confirming the lower expression of TMEM16A observed in immunohistochemistry.

Furthermore, the fit of dose–response relations measured in the dorsal zone yielded Hill coefficient values of 2.8 at −80 mV and 2.7 at +80 mV, while $K_{1/2}$ decreased with membrane depolarization from 1.2 µM at −80 mV to 0.7 µM at +80 mV (Fig. 4 D), similar to values obtained from supporting cells in the transition zone. The average shift of reversal potential upon reduction of extracellular Cl^- by replacement of NaCl with sucrose was +41 ± 4 mV (n = 6), indicating a higher permeability for Cl^- than for Na^+ (Fig. 4, E and F).

Altogether, these results indicate that although the dorsal zone has on average a lower Ca^{2+}-activated Cl^- current compared with the transition zone, the biophysical properties of the channels are the same.

To measure the extracellular pharmacological block of Ca^{2+}-activated Cl^- currents, we tested Ani9, a recently identified

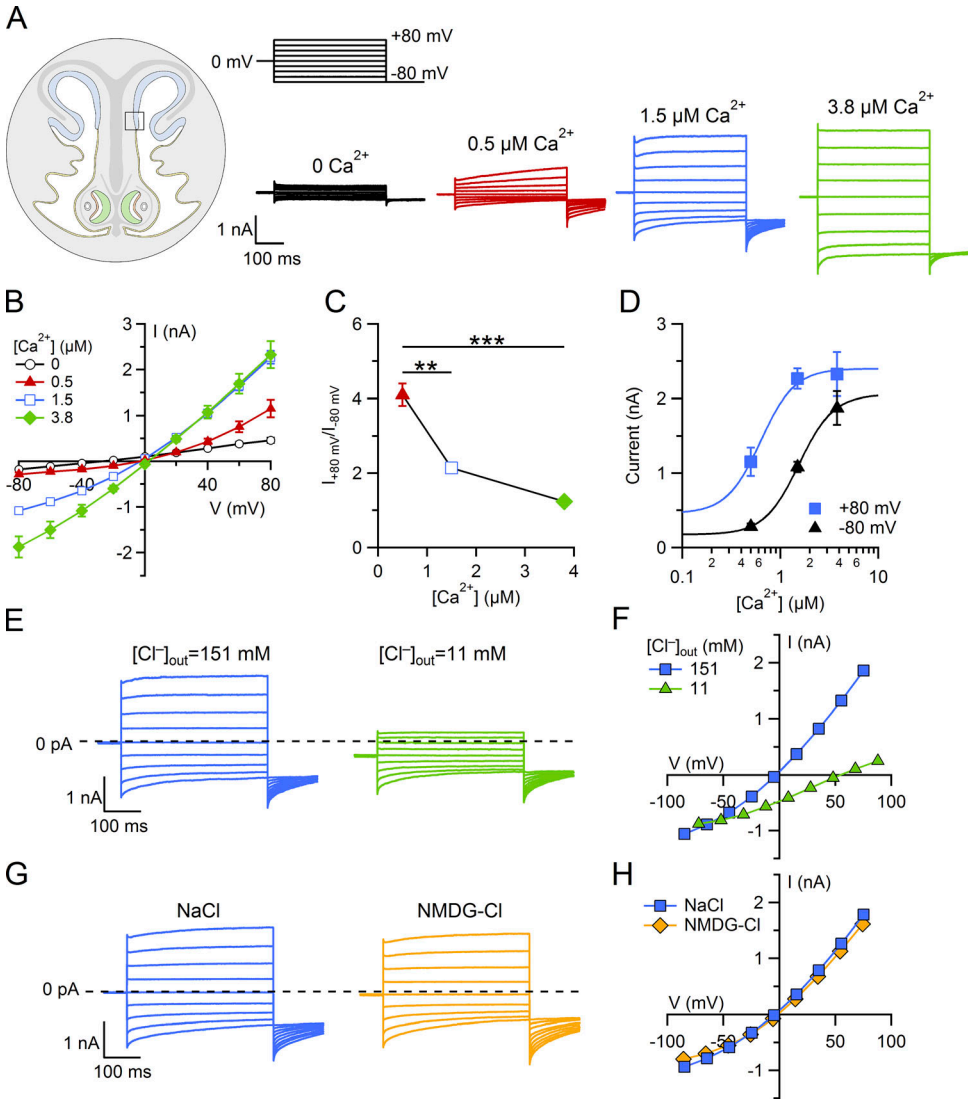

Figure 3. **Ca^{2+}-activated Cl^- currents in supporting cells from a region of the olfactory epithelium near the transition zone with the respiratory epithelium. (A)** Representative whole-cell currents recorded from different supporting cells with pipette solutions containing the indicated $[Ca^{2+}]_i$. The holding potential was 0 mV, and voltage steps from −80 mV to +80 mV with 20-mV increments, followed by a step to −80 mV, were applied as indicated at the top of the panel. **(B)** Average ± SEM of steady-state I-V relations in the presence of the following $[Ca^{2+}]_i$: nominally 0 (n = 17), 0.5 µM (n = 5), 1.5 µM (n = 33), and 3.8 µM (n = 7). **(C)** Average ± SEM of ratios between the currents measured at +80 and −80 mV at different $[Ca^{2+}]_i$ from the same experiments shown in B (**, P < 0.01; ***, P < 0.001, Dunn–Holland–Wolfe test after Kruskal–Wallis test). **(D)** Comparison of dose–responses at +80 and −80 mV, from the same experiments shown in B, fitted to the Hill equation (Eq. 1). The error bars indicate SEM. **(E and F)** Representative whole-cell currents recorded with pipette solution containing 1.5 µM Ca^{2+}. **(E and G)** Extracellular ion concentrations were modified by replacing 140 mM NaCl in the Ringer's solution with sucrose, reducing the extracellular $[Cl^-]$ to the indicated concentrations (E) or with NMDG-Cl (G). **(F–H)** Current amplitudes measured at the end of voltage pulses versus the test potential from the cells shown respectively in E–G.

potent selective blocker for TMEM16A (Seo et al., 2016). Indeed, it has been shown that 1 µM Ani9 does not significantly affect TMEM16B channel activity while it almost completely blocks TMEM16A-mediated currents (Seo et al., 2016). Fig. 5 (A–C) shows that 1 µM Ani9 reduced current amplitudes activated by 1.5 µM Ca^{2+} of 62 ± 3% at +80 mV and 61 ± 3% at −80 mV (n = 10, P < 0.001, one-sample t test), inducing a significant block of the current. The blockage by Ani9 supports the hypothesis that TMEM16A mediates the measured Ca^{2+}-activated Cl^- currents.

To determine the contribution of TMEM16A to Ca^{2+}-activated Cl^- currents in supporting cells, we compared currents from WT and TMEM16A KO mice (Rock et al., 2008). Fig. 6 A shows the comparison between representative recordings from supporting cells from WT (black and blue traces) or TMEM16A KO (orange and red traces) mice. Current amplitudes in the presence of 1.5 µM Ca^{2+} from TMEM16A KO mice (red) were not significantly different from currents measured in the absence of Ca^{2+} (orange; P > 0.05, Tukey test after one-way ANOVA; Fig. 6 B), showing the absence of Ca^{2+}-activated currents in TMEM16A KO mice. The same experiments were performed also in supporting cells in the dorsal zone and yielded similar results. These data demonstrate that TMEM16A is a necessary component of the

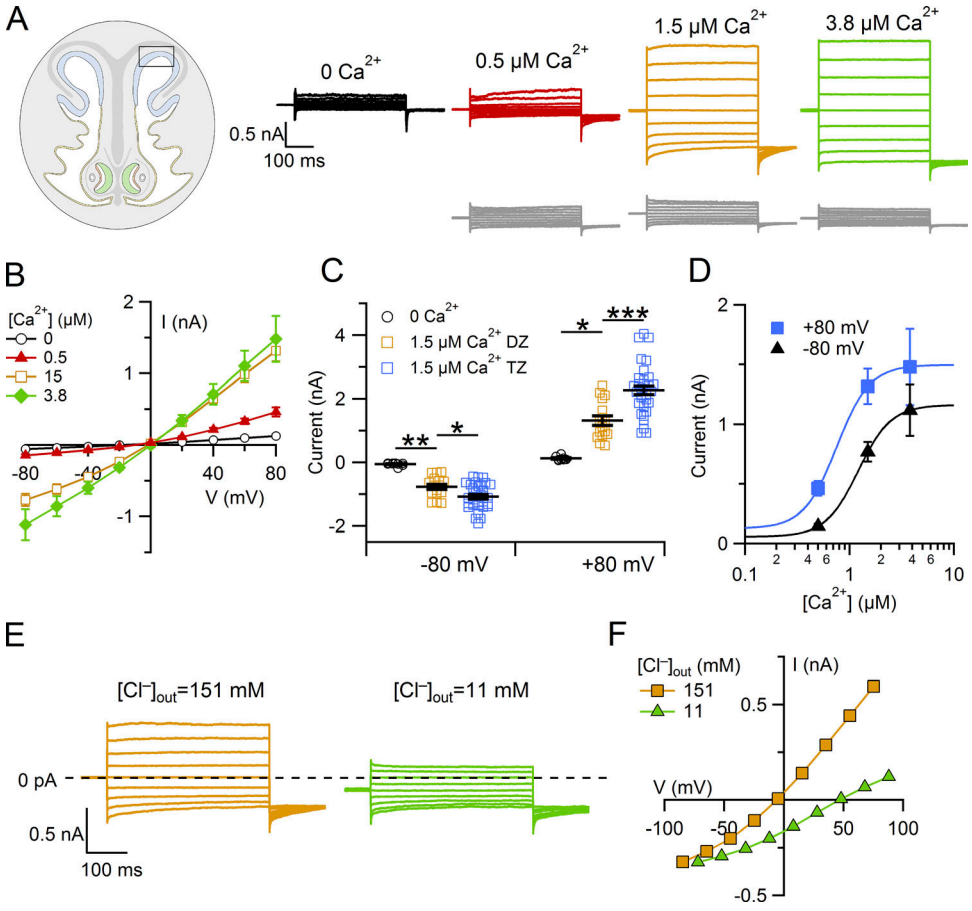

Figure 4. **Ca^{2+}-activated chloride current in supporting cells from the dorsal zone of the olfactory epithelium. (A)** Representative whole-cell currents recorded from different supporting cells from the dorsal zone with pipette solutions containing the indicated $[Ca^{2+}]$. The holding potential was 0 mV, and voltage steps from −80 mV to +80 mV with 20-mV increments, followed by a step to −80 mV, were applied as shown in the top panel of Fig. 3 A. **(B)** Average ± SEM of steady-state I-V relations in the presence of the following $[Ca^{2+}]_i$: nominally 0 (n = 9), 0.5 µM (n = 9), 1.5 µM (n = 16), and 3.8 µM (n = 4). **(C)** Scatter dot plot with average ± SEM showing current amplitudes measured at −80 and +80 mV with the indicated $[Ca^{2+}]_i$ in the dorsal zone (DZ) or transition zone (TZ). Number of cells indicated in the legends of Fig. 3 B or 4 B for the TZ or DZ, respectively. *, P < 0.05; **, P < 0.01; ***, P < 0.001; Tukey test after one way ANOVA. **(D)** Comparison of dose–responses at +80 and −80 mV, from the same experiments shown in B, fitted to the Hill equation (Eq. 1). The error bars indicate SEM. **(E)** Representative whole-cell currents recorded with pipette solution containing 1.5 µM Ca^{2+}. Extracellular ion concentrations were modified by replacing 140 mM NaCl in the Ringer's solution with sucrose, reducing the extracellular $[Cl^-]$ to the indicated concentrations. **(F)** Current amplitudes measured at the end of voltage pulses versus the test potential from the cell shown in E.

Ca^{2+}-activated Cl^- currents in supporting cells of the olfactory epithelium.

ATP activates TMEM16A-dependent currents in supporting cells

As extracellular ATP elicits a transient increase in intracellular Ca^{2+} through activation of G-protein–coupled P2Y receptors and Ca^{2+} release from intracellular stores in olfactory supporting cells (Czesnik et al., 2006; Hassenklöver et al., 2008; Hegg et al., 2009), we hypothesized that ATP stimulation could activate a Ca^{2+}-activated Cl^- current in these cells. Therefore, we first used confocal Ca^{2+} imaging to determine if ATP could elicit an increase in intracellular Ca^{2+} in our experimental conditions. Fig. 7 (A and B) shows that 30 µM ATP induced a significant transient increase of the intracellular Ca^{2+} concentration that returned to baseline level after several seconds in three selected supporting cells. Recordings from several slices showed that 95% of the supporting cells (80 of 84 cells from four slices) responded to ATP stimulation with a transient increase of intracellular Ca^{2+}.

Next, we used whole-cell recordings to test whether the Ca^{2+} increase induced by ATP stimulation could activate Ca^{2+}-activated Cl^- channels in supporting cells. We lowered the intracellular concentration of HEDTA from 10 to 2 mM to reduce Ca^{2+} buffering that could decrease the intracellular Ca^{2+} increase. 30 µM ATP at the holding potential of −80 mV induced large inward currents that slowly recovered to baseline (Fig. 8 A, black trace). The I-V relation measured close to the peak of the response to ATP (Fig. 8 B, indicated as b) showed an outward rectification, resembling the outward rectification of the Ca^{2+}-activated Cl^- current measured in the presence of 1.5 µM Ca^{2+} (Fig. 3 B).

To determine the contribution of TMEM16A to the ATP-induced current, we recorded responses to ATP in supporting cells from TMEM16A KO mice (Fig. 8 A, orange trace). Our experiments show that the average peak inward current induced

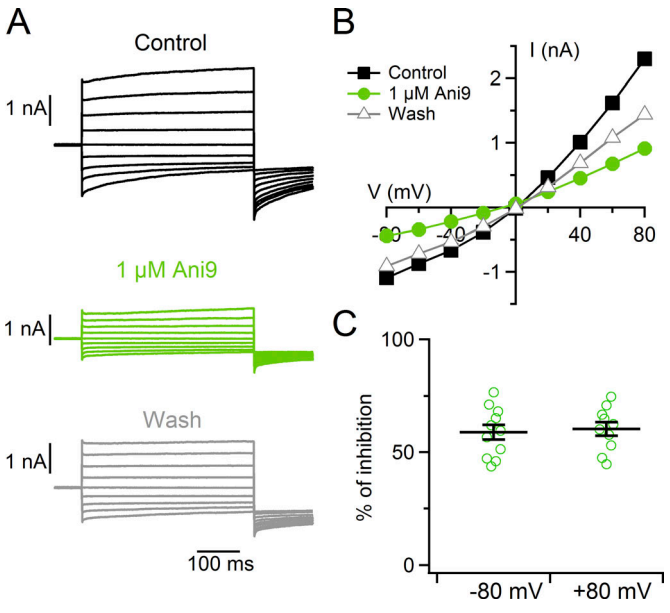

Figure 5. **Ca^{2+}-activated currents in supporting cells are blocked by the TMEM16A inhibitor Ani9. (A)** Representative whole-cell recordings obtained with an intracellular solution containing 1.5 μM Ca^{2+} (voltage protocol as in Fig. 3 A). The cell was exposed to Ringer's solution (black) and 1 μM Ani9 (green) and washed in Ringer's solution (gray). **(B)** I-V relationships measured at the end of the voltage steps from the recordings shown in A. **(C)** Scatter dot plot with average ± SEM of the percentage of current inhibition measured at −80 and +80 mV (n = 11).

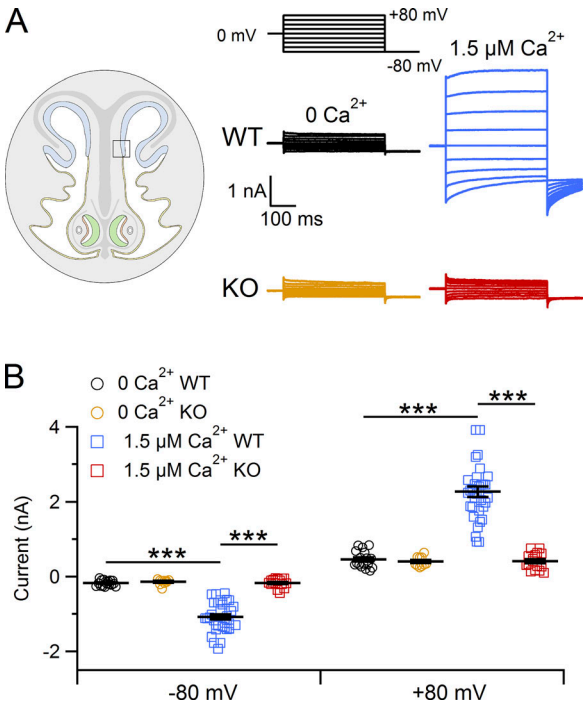

Figure 6. **Lack of Ca^{2+}-activated currents in supporting cells from TMEM16A KO mice. (A)** Representative whole-cell recordings obtained with pipette solutions containing 0 or 1.5 μM Ca^{2+}, as indicated. The voltage protocol is reported at the top of the panel. **(B)** Scatter dot plot with average ± SEM showing current amplitudes measured at −80 and +80 mV in the presence of the following $[Ca^{2+}]_i$: for WT mice nominally 0 (n = 17), 1.5 μM (n = 33) or for TMEM16A KO mice nominally 0 (n = 10), 1.5 μM (n = 16). ***, P < 0.001, Tukey test after one-way ANOVA. Recordings were obtained from supporting cells located close to the transition zone with the respiratory epithelium.

by ATP in WT mice at −80 mV (−438 ± 94 pA, n = 28) was significantly reduced (−6 ± 10 pA, n = 16, Wilcoxon–Mann–Whitney U test) in TMEM16A KO mice (Fig. 8 C).

These results indicate that the transient Ca^{2+} increase elicited by 30 μM ATP activates a TMEM16A-dependent current in supporting cells of the olfactory epithelium.

Discussion

Our results provide the first demonstration that supporting cells of the mouse olfactory epithelium have functional Ca^{2+}-activated Cl^- channels that can be activated by purinergic stimulation producing large Cl^- currents. Recordings from TMEM16A KO mice show that TMEM16A is a necessary component of the Ca^{2+}-activated Cl^- currents in olfactory supporting cells.

An important preliminary step to understand the possible physiological roles of TMEM16A in supporting cells is to estimate equilibrium potential for Cl^- (E_{Cl}) to determine the direction of the Cl^- flux. The apical part of supporting cells and their microvilli are immersed in the mucus (Menco and Farbman, 1992; Menco et al., 1998). The concentrations of various ions in the olfactory mucus, dendritic knobs of sensory neurons, and cytosol of supporting cells from rats have been measured by Reuter et al. (1998) using energy-dispersive x-ray microanalysis. They reported that the average concentration of Cl^- was 55 ± 11 mM in the mucus and 32 ± 12 mM in the cytosol of supporting cells (Reuter et al., 1998). Thus, we estimated E_{Cl} at the apical part of supporting cells, where TMEM16A is localized, assuming that (1) the values of Cl^- concentrations in mouse are the same of those measured in rats and (2) the Cl^- concentration at the apical part of supporting cells and at the proximal part of their microvilli is the same as that in the cytosol. In these conditions, we obtained a value for E_{Cl} of −14 mV (at room temperature 20–25°C). Taking into account that we measured an average value for resting membrane potential of supporting cells of −41 ± 1 mV (that is in agreement with previously measured values in the range between −50 mV and −30 mV; Vogalis et al., 2005a), the calculated electrochemical driving force for Cl^- is −27 mV. Thus, the opening of TMEM16A Cl^- channels by Ca^{2+} at the apical part of supporting cells causes an efflux of Cl^-, contributing to control Cl^- homeostasis and dynamics in the mucus covering the olfactory epithelium.

The mucus composition is fundamental to maintain the ionic environment necessary for olfactory transduction. Indeed, the binding of odorant molecules to odorant receptors in the cilia of olfactory sensory neurons leads to a transduction cascade that includes the activation of CNG channels and the Ca^{2+}-activated Cl^- channels TMEM16B, whose function depends on the Cl^- electrochemical gradient between the mucus and the intraciliary compartment (Pifferi et al., 2009; Stephan et al., 2009; Billig et al., 2011; Pietra et al., 2016; Dibattista et al., 2017; Neureither et al., 2017; Li et al., 2018; Zak et al., 2018; Reisert and Reingruber, 2019). Thus, the Cl^- concentration regulated by

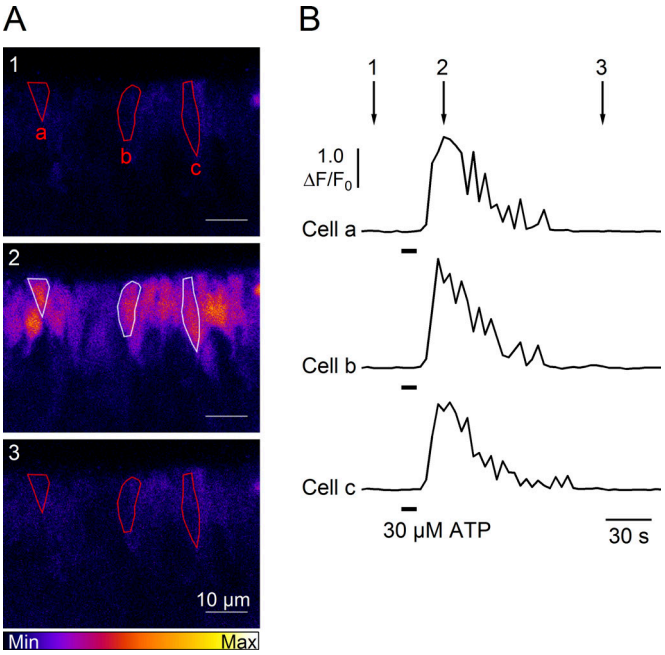

Figure 7. **ATP stimulation induces an increase of $[Ca^{2+}]_i$ in supporting cells. (A)** Representative sequences of confocal images in pseudocolor from a slice of the olfactory epithelium loaded with Cal520-AM before (1), at the peak (2), and after (3) the response activated by application of 30 µM ATP for 10 s. **(B)** Ca^{2+} transients recorded in the cells highlighted in A responding to 30 µM ATP stimulation. Time points indicated by arrows correspond to frame numbers in A.

TMEM16A would affect the TMEM16B-mediated current, modifying the odorant response of the olfactory sensory neurons.

He et al. (2017) have shown that TMEM16A in epithelial cells is necessary to control the cytoplasmic Cl^- concentration and that an adequate level of Cl^- is necessary for proper endocytic trafficking. In olfactory supporting cells, xenobiotic-metabolizing enzymes are localized in the intracellular compartments, and therefore, the engulfing of xenobiotics is a required step for their detoxification (Ling et al., 2004; Zhuo et al., 2004; Asakawa et al., 2017). It is of interest to note that some toxic chemicals, such as dichlobenil and methyl iodide, have a more severe noxious effect in the dorsal portion of the olfactory epithelium, where TMEM16A is less expressed (Robinson et al., 2003; Franceschini et al., 2009). Moreover, the endocytosis activity in supporting cells is massively increased by stimulation with acetylcholine via the activation of M3 muscarinic receptors, generating an increase of intracellular Ca^{2+} concentration that could activate the TMEM16A-mediated current (Hegg et al., 2009; Ogura et al., 2011; Fu et al., 2018). The most likely sources of acetylcholine are the microvillous cells, a still poorly understood population of cells that respond to high odorant concentrations and xenobiotic chemicals (Lin et al., 2008; Menini and Pifferi, 2008; Ogura et al., 2011; Fu et al., 2018). In this scenario, the interplay between the acetylcholine response and regulation of Cl^- homeostasis by TMEM16A could regulate the endocytosis and the subsequent xenobiotic detoxification mediated by supporting cells.

Another role of TMEM16A could be the modulation of the purinergic signaling. Supporting cells express metabotropic purinergic P2Y receptors, and extracellular ATP can induce Ca^{2+} release from intracellular stores (Gayle and Burnstock, 2005; Czesnik et al., 2006; Hassenklöver et al., 2008; Hegg et al., 2009). Here, we have shown that ATP produces an intracellular Ca^{2+} increase sufficient to activate the Ca^{2+}-activated Cl^- currents mediated by TMEM16A. Hayoz et al. (2012) reported evidence that ATP is released both through constitutive and evoked release in the olfactory epithelium of neonatal mice. Moreover, the olfactory epithelium receives extensive innervation by various branches of trigeminal nerves (Finger et al., 1990; Schaefer et al., 2002), and these fibers could release ATP through axonal reflex. Interestingly, TMEM16A can amplify the ATP-mediated Ca^{2+} signal by interacting directly with the IP_3R on the ER membrane (Cabrita et al., 2017). Therefore, we can speculate that TMEM16A could be involved in the cascade of the ATP transduction pathway in the olfactory epithelium. In particular, ATP modulates the neuroproliferation partially by the increase of NPY expression in supporting cells (Hassenklöver

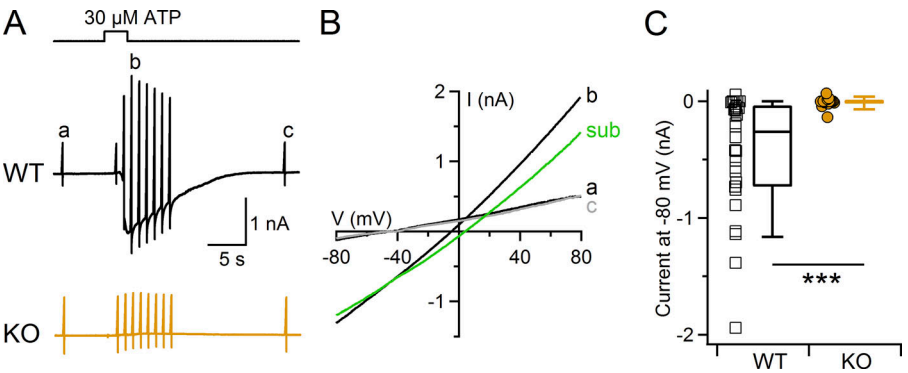

Figure 8. **ATP activates a TMEM16A-dependent current in supporting cells. (A)** Whole-cell currents activated by 30 µM ATP from supporting cells located close to the transition zone with the respiratory epithelium from WT (black trace) or TMEM16A KO (orange trace) mice. ATP was applied for the time indicated in the upper trace. The holding potential was −80 mV, and voltage ramps from −80 to +80 mV before (a), during (b), and after (c) the ATP response were used to measure the I-V relations. **(B)** I-V relations from the WT cell shown in A. The green trace (sub) was obtained by subtracting the average between traces a and c from the trace in the presence of ATP (b). **(C)** Scatter dot plot and box plot showing the peak amplitude of ATP-activated currents measured at −80 mV in WT (n = 28) or TMEM16A KO mice (n = 16). ***, $P < 0.001$, Wilcoxon–Mann–Whitney U test.

et al., 2008; Jia et al., 2009; Jia and Hegg, 2010). It has been also proposed that ATP could have a neuroprotective function by mediating the expression of HSP25 in supporting cells upon exposure to high odorant concentrations (Hegg and Lucero, 2006).

Conclusions

In summary, our data provide a definitive demonstration that TMEM16A-mediated currents are functional in olfactory supporting cells and provide a foundation for future work investigating the precise physiological role of TMEM16A, possibly using conditional KO mice for TMEM16A, as the constitutive TMEM16A knockout mice used in our study die soon after birth.

Acknowledgments

We thank Anna Boccaccio, Michele Dibattista, and all members of the laboratory for discussions. We also thank Elettra Grdina, Angel Pascual Camerota, Lorenzo Maschietto, and Giovanni Tamburin for mice handling and Helena Krmac and Christina Vlachouli for mice genotyping.

This study was supported by a grant from the Italian Ministry of Education, University, and Research (2010599KBR to A. Menini).

The authors declare no competing financial interests.

Author contributions: T. Henriques and E. Agostinelli performed and analyzed the electrophysiological recordings. A. Hernandez-Clavijo and E. Agostinelli performed and analyzed the Ca^{2+} imaging experiments. D. Kumar Maurya performed and analyzed the immunohistochemistry experiments. J.R. Rock and B.D. Harfe generated and provided the TMEM16A KO mouse model. S. Pifferi contributed to the analysis data. T. Henriques, E. Agostinelli, A. Hernandez-Clavijo, D. Kumar Maurya, S. Pifferi, and A. Menini contributed to the experimental design and manuscript writing. All authors agreed with the final version of the manuscript.

Merritt C. Maduke served as editor.

Submitted: 20 December 2018
Revised: 8 March 2019
Accepted: 15 April 2019

References

Ablimit, A., T. Matsuzaki, Y. Tajika, T. Aoki, H. Hagiwara, and K. Takata. 2006. Immunolocalization of water channel aquaporins in the nasal olfactory mucosa. *Arch. Histol. Cytol.* 69:1–12. https://doi.org/10.1679/aohc.69.1

Amjad, A., A. Hernandez-Clavijo, S. Pifferi, D.K. Maurya, A. Boccaccio, J. Franzot, J. Rock, and A. Menini. 2015. Conditional knockout of TMEM16A/anoctamin1 abolishes the calcium-activated chloride current in mouse vomeronasal sensory neurons. *J. Gen. Physiol.* 145: 285–301. https://doi.org/10.1085/jgp.201411348

Asakawa, M., Y. Fukutani, A. Savangsuksa, K. Noguchi, H. Matsunami, and M. Yohda. 2017. Modification of the response of olfactory receptors to acetophenone by CYP1a2. *Sci. Rep.* 7:10167. https://doi.org/10.1038/s41598-017-10862-5

Barry, P.H. 1994. JPCalc, a software package for calculating liquid junction potential corrections in patch-clamp, intracellular, epithelial and bilayer measurements and for correcting junction potential measurements. *J. Neurosci. Methods.* 51:107–116. https://doi.org/10.1016/0165-0270(94)90031-0

Benedetto, R., J. Ousingsawat, P. Wanitchakool, Y. Zhang, M.J. Holtzman, M. Amaral, J.R. Rock, R. Schreiber, and K. Kunzelmann. 2017. Epithelial Chloride Transport by CFTR Requires TMEM16A. *Sci. Rep.* 7:12397. https://doi.org/10.1038/s41598-017-10910-0

Benedetto, R., I. Cabrita, R. Schreiber, and K. Kunzelmann. 2019. TMEM16A is indispensable for basal mucus secretion in airways and intestine. *FASEB J.* 33:4502–4512. https://doi.org/10.1096/fj.201801333RRR

Betto, G., O.L. Cherian, S. Pifferi, V. Cenedese, A. Boccaccio, and A. Menini. 2014. Interactions between permeation and gating in the TMEM16B/anoctamin2 calcium-activated chloride channel. *J. Gen. Physiol.* 143: 703–718. https://doi.org/10.1085/jgp.201411182

Billig, G.M., B. Pál, P. Fidzinski, and T.J. Jentsch. 2011. Ca2+-activated Cl− currents are dispensable for olfaction. *Nat. Neurosci.* 14:763–769. https://doi.org/10.1038/nn.2821

Breipohl, W., H.J. Laugwitz, and N. Bornfeld. 1974. Topological relations between the dendrites of olfactory sensory cells and sustentacular cells in different vertebrates. An ultrastructural study. *J. Anat.* 117:89–94.

Breunig, E., I. Manzini, F. Piscitelli, B. Gutermann, V. Di Marzo, D. Schild, and D. Czesnik. 2010. The endocannabinoid 2-arachidonoyl-glycerol controls odor sensitivity in larvae of Xenopus laevis. *J. Neurosci.* 30: 8965–8973. https://doi.org/10.1523/JNEUROSCI.4030-09.2010

Cabrita, I., R. Benedetto, A. Fonseca, P. Wanitchakool, L. Sirianant, B.V. Skryabin, L.K. Schenk, H. Pavenstädt, R. Schreiber, and K. Kunzelmann. 2017. Differential effects of anoctamins on intracellular calcium signals. *FASEB J.* 31:2123–2134. https://doi.org/10.1096/fj.201600797RR

Cenedese, V., G. Betto, F. Celsi, O.L. Cherian, S. Pifferi, and A. Menini. 2012. The voltage dependence of the TMEM16B/anoctamin2 calcium-activated chloride channel is modified by mutations in the first putative intracellular loop. *J. Gen. Physiol.* 139:285–294. https://doi.org/10.1085/jgp.201110764

Chen, Y., M.L. Getchell, X. Ding, and T.V. Getchell. 1992. Immunolocalization of two cytochrome P450 isozymes in rat nasal chemosensory tissue. *Neuroreport.* 3:749–752. https://doi.org/10.1097/00001756-199209000-00007

Czesnik, D., J. Kuduz, D. Schild, and I. Manzini. 2006. ATP activates both receptor and sustentacular supporting cells in the olfactory epithelium of Xenopus laevis tadpoles. *Eur. J. Neurosci.* 23:119–128. https://doi.org/10.1111/j.1460-9568.2005.04533.x

Czesnik, D., D. Schild, J. Kuduz, and I. Manzini. 2007. Cannabinoid action in the olfactory epithelium. *Proc. Natl. Acad. Sci. USA.* 104:2967–2972. https://doi.org/10.1073/pnas.0609067104

Dauner, K., J. Lissmann, S. Jeridi, S. Frings, and F. Möhrlen. 2012. Expression patterns of anoctamin 1 and anoctamin 2 chloride channels in the mammalian nose. *Cell Tissue Res.* 347:327–341. https://doi.org/10.1007/s00441-012-1324-9

Davidson, J.S., and I.M. Baumgarten. 1988. Glycyrrhetinic acid derivatives: a novel class of inhibitors of gap-junctional intercellular communication. Structure-activity relationships. *J. Pharmacol. Exp. Ther.* 246:1104–1107.

Dibattista, M., A. Mazzatenta, F. Grassi, R. Tirindelli, and A. Menini. 2008. Hyperpolarization-activated cyclic nucleotide-gated channels in mouse vomeronasal sensory neurons. *J. Neurophysiol.* 100:576–586. https://doi.org/10.1152/jn.90263.2008

Dibattista, M., S. Pifferi, A. Boccaccio, A. Menini, and J. Reisert. 2017. The long tale of the calcium activated Cl^- channels in olfactory transduction. *Channels (Austin).* 11:399–414. https://doi.org/10.1080/19336950.2017.1307489

Finger, T.E., V.L. St Jeor, J.C. Kinnamon, and W.L. Silver. 1990. Ultrastructure of substance P- and CGRP-immunoreactive nerve fibers in the nasal epithelium of rodents. *J. Comp. Neurol.* 294:293–305. https://doi.org/10.1002/cne.902940212

Franceschini, V., S. Bettini, S. Pifferi, A. Rosellini, A. Menini, R. Saccardi, E. Ognio, R. Jeffery, R. Poulsom, and R.P. Revoltella. 2009. Human cord blood CD133+ stem cells transplanted to nod-scid mice provide conditions for regeneration of olfactory neuroepithelium after permanent damage induced by dichlobenil. *Stem Cells.* 27:825–835. https://doi.org/10.1002/stem.11

Fu, Z., T. Ogura, W. Luo, and W. Lin. 2018. ATP and Odor Mixture Activate TRPM5-Expressing Microvillous Cells and Potentially Induce Acetylcholine Release to Enhance Supporting Cell Endocytosis in Mouse Main Olfactory Epithelium. *Front. Cell. Neurosci.* 12:71. https://doi.org/10.3389/fncel.2018.00071

Gayle, S., and G. Burnstock. 2005. Immunolocalisation of P2X and P2Y nucleotide receptors in the rat nasal mucosa. *Cell Tissue Res.* 319:27–36. https://doi.org/10.1007/s00441-004-0979-2

Grubb, B.R., T.D. Rogers, H.M. Kulaga, K.A. Burns, R.L. Wonsetler, R.R. Reed, and L.E. Ostrowski. 2007. Olfactory epithelia exhibit progressive functional and morphological defects in CF mice. *Am. J. Physiol. Cell Physiol.* 293:C574–C583. https://doi.org/10.1152/ajpcell.00106.2007

Gu, J., Q.Y. Zhang, M.B. Genter, T.W. Lipinskas, M. Negishi, D.W. Nebert, and X. Ding. 1998. Purification and characterization of heterologously expressed mouse CYP2A5 and CYP2G1: role in metabolic activation of acetaminophen and 2,6-dichlorobenzonitrile in mouse olfactory mucosal microsomes. *J. Pharmacol. Exp. Ther.* 285:1287–1295.

Hassenklöver, T., S. Kurtanska, I. Bartoszek, S. Junek, D. Schild, and I. Manzini. 2008. Nucleotide-induced Ca2+ signaling in sustentacular supporting cells of the olfactory epithelium. *Glia.* 56:1614–1624. https://doi.org/10.1002/glia.20714

Hassenklöver, T., P. Schwartz, D. Schild, and I. Manzini. 2009. Purinergic signaling regulates cell proliferation of olfactory epithelium progenitors. *Stem Cells.* 27:2022–2031. https://doi.org/10.1002/stem.126

Hayoz, S., C. Jia, and C. Hegg. 2012. Mechanisms of constitutive and ATP-evoked ATP release in neonatal mouse olfactory epithelium. *BMC Neurosci.* 13:53. https://doi.org/10.1186/1471-2202-13-53

He, M., W. Ye, W.-J. Wang, E.S. Sison, Y.N. Jan, and L.Y. Jan. 2017. Cytoplasmic Cl^- couples membrane remodeling to epithelial morphogenesis. *Proc. Natl. Acad. Sci. USA.* 114:E11161–E11169. https://doi.org/10.1073/pnas.1714448115

Hegg, C.C., and M.T. Lucero. 2006. Purinergic receptor antagonists inhibit odorant-induced heat shock protein 25 induction in mouse olfactory epithelium. *Glia.* 53:182–190. https://doi.org/10.1002/glia.20258

Hegg, C.C., D. Greenwood, W. Huang, P. Han, and M.T. Lucero. 2003. Activation of purinergic receptor subtypes modulates odor sensitivity. *J. Neurosci.* 23:8291–8301. https://doi.org/10.1523/JNEUROSCI.23-23-08291.2003

Hegg, C.C., M. Irwin, and M.T. Lucero. 2009. Calcium store-mediated signaling in sustentacular cells of the mouse olfactory epithelium. *Glia.* 57:634–644. https://doi.org/10.1002/glia.20792

Huang, F., X. Wong, and L.Y. Jan. 2012. International Union of Basic and Clinical Pharmacology. LXXXV: calcium-activated chloride channels. *Pharmacol. Rev.* 64:1–15. https://doi.org/10.1124/pr.111.005009

Jia, C., and C.C. Hegg. 2010. NPY mediates ATP-induced neuroproliferation in adult mouse olfactory epithelium. *Neurobiol. Dis.* 38:405–413. https://doi.org/10.1016/j.nbd.2010.02.013

Jia, C., J.P. Doherty, S. Crudgington, and C.C. Hegg. 2009. Activation of purinergic receptors induces proliferation and neuronal differentiation in Swiss Webster mouse olfactory epithelium. *Neuroscience.* 163:120–128. https://doi.org/10.1016/j.neuroscience.2009.06.040

Jia, C., C. Roman, and C.C. Hegg. 2010. Nickel sulfate induces location-dependent atrophy of mouse olfactory epithelium: protective and proliferative role of purinergic receptor activation. *Toxicol. Sci.* 115:547–556. https://doi.org/10.1093/toxsci/kfq071

Keller, A., and F.L. Margolis. 1975. Immunological studies of the rat olfactory marker protein. *J. Neurochem.* 24:1101–1106. https://doi.org/10.1111/j.1471-4159.1975.tb03883.x

Kunzelmann, K., I. Cabrita, P. Wanitchakool, J. Ousingsawat, L. Sirianant, R. Benedetto, and R. Schreiber. 2016. Modulating Ca^{2+} signals: a common theme for TMEM16, Ist2, and TMC. *Pflugers Arch.* 468:475–490. https://doi.org/10.1007/s00424-015-1767-4

Lacroix, M.-C., K. Badonnel, N. Meunier, F. Tan, C. Schlegel-Le Poupon, D. Durieux, R. Monnerie, C. Baly, P. Congar, R. Salesse, and M. Caillol. 2008. Expression of insulin system in the olfactory epithelium: first approaches to its role and regulation. *J. Neuroendocrinol.* 20:1176–1190. https://doi.org/10.1111/j.1365-2826.2008.01777.x

Li, R.-C., C.-C. Lin, X. Ren, J.S. Wu, L.L. Molday, R.S. Molday, and K.-W. Yau. 2018. Ca^{2+}-activated Cl current predominates in threshold response of mouse olfactory receptor neurons. *Proc. Natl. Acad. Sci. USA.* 115:5570–5575. https://doi.org/10.1073/pnas.1803443115

Lin, W., T. Ogura, R.F. Margolskee, T.E. Finger, and D. Restrepo. 2008. TRPM5-expressing solitary chemosensory cells respond to odorous irritants. *J. Neurophysiol.* 99:1451–1460. https://doi.org/10.1152/jn.01195.2007

Ling, G., J. Gu, M.B. Genter, X. Zhuo, and X. Ding. 2004. Regulation of cytochrome P450 gene expression in the olfactory mucosa. *Chem. Biol. Interact.* 147:247–258. https://doi.org/10.1016/j.cbi.2004.02.003

Lu, D.C., H. Zhang, Z. Zador, and A.S. Verkman. 2008. Impaired olfaction in mice lacking aquaporin-4 water channels. *FASEB J.* 22:3216–3223. https://doi.org/10.1096/fj.07-104836

Maurya, D.K., and A. Menini. 2014. Developmental expression of the calcium-activated chloride channels TMEM16A and TMEM16B in the mouse olfactory epithelium. *Dev. Neurobiol.* 74:657–675. https://doi.org/10.1002/dneu.22159

Maurya, D.K., T. Henriques, M. Marini, N. Pedemonte, L.J.V. Galietta, J.R. Rock, B.D. Harfe, and A. Menini. 2015. Development of the Olfactory Epithelium and Nasal Glands in TMEM16A−/− and TMEM16A+/+ Mice. *PLoS One.* 10:e0129171. https://doi.org/10.1371/journal.pone.0129171

Menco, B.P., and A.I. Farbman. 1992. Ultrastructural evidence for multiple mucous domains in frog olfactory epithelium. *Cell Tissue Res.* 270:47–56. https://doi.org/10.1007/BF00381878

Menco, B.P., G.B. Birrell, C.M. Fuller, P.I. Ezeh, D.A. Keeton, and D.J. Benos. 1998. Ultrastructural localization of amiloride-sensitive sodium channels and Na+,K(+)-ATPase in the rat's olfactory epithelial surface. *Chem. Senses.* 23:137–149. https://doi.org/10.1093/chemse/23.2.137

Menini, A., and S. Pifferi. 2008. New whiffs about chemesthesis. Focus on "TRPM5-expressing solitary chemosensory cells respond to odorous irritants". *J. Neurophysiol.* 99:1055–1056. https://doi.org/10.1152/jn.00043.2008

Merigo, F., C. Mucignat-Caretta, M. Cristofoletti, and C. Zancanaro. 2011. Epithelial membrane transporters expression in the developing to adult mouse vomeronasal organ and olfactory mucosa. *Dev. Neurobiol.* 71:854–869. https://doi.org/10.1002/dneu.20944

Neureither, F., N. Stowasser, S. Frings, and F. Möhrlen. 2017. Tracking of unfamiliar odors is facilitated by signal amplification through anoctamin 2 chloride channels in mouse olfactory receptor neurons. *Physiol. Rep.* 5:e13373. https://doi.org/10.14814/phy2.13373

Ogura, T., S.A. Szebenyi, K. Krosnowski, A. Sathyanesan, J. Jackson, and W. Lin. 2011. Cholinergic microvillous cells in the mouse main olfactory epithelium and effect of acetylcholine on olfactory sensory neurons and supporting cells. *J. Neurophysiol.* 106:1274–1287. https://doi.org/10.1152/jn.00186.2011

Patton, C., S. Thompson, and D. Epel. 2004. Some precautions in using chelators to buffer metals in biological solutions. *Cell Calcium.* 35:427–431. https://doi.org/10.1016/j.ceca.2003.10.006

Pedemonte, N., and L.J.V. Galietta. 2014. Structure and function of TMEM16 proteins (anoctamins). *Physiol. Rev.* 94:419–459. https://doi.org/10.1152/physrev.00039.2011

Pfister, S., T. Weber, W. Härtig, C. Schwerdel, R. Elsaesser, I. Knuesel, and J.-M. Fritschy. 2015. Novel role of cystic fibrosis transmembrane conductance regulator in maintaining adult mouse olfactory neuronal homeostasis. *J. Comp. Neurol.* 523:406–430. https://doi.org/10.1002/cne.23686

Pietra, G., M. Dibattista, A. Menini, J. Reisert, and A. Boccaccio. 2016. The Ca2+-activated Cl- channel TMEM16B regulates action potential firing and axonal targeting in olfactory sensory neurons. *J. Gen. Physiol.* 148:293–311. https://doi.org/10.1085/jgp.201611622

Pifferi, S., G. Pascarella, A. Boccaccio, A. Mazzatenta, S. Gustincich, A. Menini, and S. Zucchelli. 2006. Bestrophin-2 is a candidate calcium-activated chloride channel involved in olfactory transduction. *Proc. Natl. Acad. Sci. USA.* 103:12929–12934. https://doi.org/10.1073/pnas.0604505103

Pifferi, S., M. Dibattista, and A. Menini. 2009. TMEM16B induces chloride currents activated by calcium in mammalian cells. *Pflugers Arch.* 458:1023–1038. https://doi.org/10.1007/s00424-009-0684-9

Piperno, G., and M.T. Fuller. 1985. Monoclonal antibodies specific for an acetylated form of alpha-tubulin recognize the antigen in cilia and flagella from a variety of organisms. *J. Cell Biol.* 101:2085–2094. https://doi.org/10.1083/jcb.101.6.2085

Rash, J.E., K.G.V. Davidson, N. Kamasawa, T. Yasumura, M. Kamasawa, C. Zhang, R. Michaels, D. Restrepo, O.P. Ottersen, C.O. Olson, and J.I. Nagy. 2005. Ultrastructural localization of connexins (Cx36, Cx43, Cx45), glutamate receptors and aquaporin-4 in rodent olfactory mucosa, olfactory nerve and olfactory bulb. *J. Neurocytol.* 34:307–341. https://doi.org/10.1007/s11068-005-8360-2

Reisert, J., and J. Reingruber. 2019. Ca^{2+}-activated Cl^- current ensures robust and reliable signal amplification in vertebrate olfactory receptor neurons. *Proc. Natl. Acad. Sci. USA.* 116:1053–1058. https://doi.org/10.1073/pnas.1816371116

Reuter, D., K. Zierold, W.H. Schröder, and S. Frings. 1998. A depolarizing chloride current contributes to chemoelectrical transduction in olfactory sensory neurons in situ. *J. Neurosci.* 18:6623–6630. https://doi.org/10.1523/JNEUROSCI.18-17-06623.1998

Robinson, D.A., J.R. Foster, J.A. Nash, and C.J. Reed. 2003. Three-dimensional mapping of the lesions induced by beta-beta'-iminodiproprionitrile, methyl iodide and methyl methacrylate in the rat nasal cavity. *Toxicol. Pathol.* 31:340–347. https://doi.org/10.1080/01926230390204388

Rochelle, L.G., D.C. Li, H. Ye, E. Lee, C.R. Talbot, and R.C. Boucher. 2000. Distribution of ion transport mRNAs throughout murine nose and lung. *Am. J. Physiol. Lung Cell. Mol. Physiol.* 279:L14–L24. https://doi.org/10.1152/ajplung.2000.279.1.L14

Rock, J.R., C.R. Futtner, and B.D. Harfe. 2008. The transmembrane protein TMEM16A is required for normal development of the murine trachea. *Dev. Biol.* 321:141–149. https://doi.org/10.1016/j.ydbio.2008.06.009

Rock, J.R., W.K. O'Neal, S.E. Gabriel, S.H. Randell, B.D. Harfe, R.C. Boucher, and B.R. Grubb. 2009. Transmembrane protein 16A (TMEM16A) is a Ca2+-regulated Cl- secretory channel in mouse airways. *J. Biol. Chem.* 284:14875–14880. https://doi.org/10.1074/jbc.C109.000869

Schaefer, M.L., B. Böttger, W.L. Silver, and T.E. Finger. 2002. Trigeminal collaterals in the nasal epithelium and olfactory bulb: a potential route for direct modulation of olfactory information by trigeminal stimuli. *J. Comp. Neurol.* 444:221–226. https://doi.org/10.1002/cne.10143

Seo, Y., H.K. Lee, J. Park, D.-K. Jeon, S. Jo, M. Jo, and W. Namkung. 2016. Ani9, A Novel Potent Small-Molecule ANO1 Inhibitor with Negligible Effect on ANO2. *PLoS One.* 11:e0155771. https://doi.org/10.1371/journal.pone.0155771

Shimazaki, R., A. Boccaccio, A. Mazzatenta, G. Pinato, M. Migliore, and A. Menini. 2006. Electrophysiological properties and modeling of murine vomeronasal sensory neurons in acute slice preparations. *Chem. Senses.* 31:425–435. https://doi.org/10.1093/chemse/bjj047

Stephan, A.B., E.Y. Shum, S. Hirsh, K.D. Cygnar, J. Reisert, and H. Zhao. 2009. ANO2 is the cilial calcium-activated chloride channel that may mediate olfactory amplification. *Proc. Natl. Acad. Sci. USA.* 106:11776–11781. https://doi.org/10.1073/pnas.0903304106

Suzuki, Y., M. Takeda, and A.I. Farbman. 1996. Supporting cells as phagocytes in the olfactory epithelium after bulbectomy. *J. Comp. Neurol.* 376: 509–517. https://doi.org/10.1002/(SICI)1096-9861(19961223)376:4<509::AID-CNE1>3.0.CO;2-5

Thomas, D., S.C. Tovey, T.J. Collins, M.D. Bootman, M.J. Berridge, and P. Lipp. 2000. A comparison of fluorescent Ca2+ indicator properties and their use in measuring elementary and global Ca2+ signals. *Cell Calcium.* 28: 213–223. https://doi.org/10.1054/ceca.2000.0152

Vogalis, F., C.C. Hegg, and M.T. Lucero. 2005a. Ionic conductances in sustentacular cells of the mouse olfactory epithelium. *J. Physiol.* 562: 785–799. https://doi.org/10.1113/jphysiol.2004.079228

Vogalis, F., C.C. Hegg, and M.T. Lucero. 2005b. Electrical coupling in sustentacular cells of the mouse olfactory epithelium. *J. Neurophysiol.* 94: 1001–1012. https://doi.org/10.1152/jn.01299.2004

Whitby-Logan, G.K., M. Weech, and E. Walters. 2004. Zonal expression and activity of glutathione S-transferase enzymes in the mouse olfactory mucosa. *Brain Res.* 995:151–157. https://doi.org/10.1016/j.brainres.2003.09.012

Wong, W.M., M. Nagel, A. Hernandez-Clavijo, S. Pifferi, A. Menini, M. Spehr, and J.P. Meeks. 2018. Sensory Adaptation to Chemical Cues by Vomeronasal Sensory Neurons. *eNeuro.* 5:ENEURO.0223-18.2018. https://doi.org/10.1523/ENEURO.0223-18.2018

Zak, J.D., J. Grimaud, R.-C. Li, C.-C. Lin, and V.N. Murthy. 2018. Calcium-activated chloride channels clamp odor-evoked spike activity in olfactory receptor neurons. *Sci. Rep.* 8:10600. https://doi.org/10.1038/s41598-018-28855-3

Zhuo, X., J. Gu, M.J. Behr, P.J. Swiatek, H. Cui, Q.-Y. Zhang, Y. Xie, D.N. Collins, and X. Ding. 2004. Targeted disruption of the olfactory mucosa-specific Cyp2g1 gene: impact on acetaminophen toxicity in the lateral nasal gland, and tissue-selective effects on Cyp2a5 expression. *J. Pharmacol. Exp. Ther.* 308:719–728. https://doi.org/10.1124/jpet.103.060301

7. Conclusions:

We provided a comprehensive investigation of the expression and functional activity of two proteins highly expressed in two different cell populations of the MOE. We confirmed that stomatin-like protein-3 (STOML-3) is specifically expressed at a high level in the ciliary compartment of the mouse OSNs, where the olfactory transduction takes place. Moreover, we discovered that the Ca^{2+}-activated Cl^- channel TMEM16A has a peculiar expression pattern in SCs of the mouse MOE. Indeed, TMEM16A is highly expressed in the apical portion of SCs within the transition region in contact with the respiratory epithelium, and it is lower expressed in the dorsal part of the epithelium.

The high rate of expression of these two proteins within the MOE suggests that they could contribute to the regulation of important aspects of the MOE physiology. However, their possible roles were unknown since their contribution to the OS has never been studied before. To assess these points, we took advantage of a loss of expression approach using two constitutive knock-out mice models in which the STOML-3 or TMEM16A gene has been deleted, respectively.

We found that the number of mature OSNs, and their cilia number and length were not affected in STOML-3 KO mice. These results strongly suggest that STOML-3 does not modulate the physiological development of OSNs. Interestingly, several members of the olfactory transduction machinery are normally targeted to the cilia in the mouse model lacking STOML-3. Moreover, patch-clamp experiments revealed that also the active and passive membrane properties of OSNs are unalerted in STOML-3 KO mice.

Nevertheless, extracellular single-cell recordings achieved in the loose-patch modality clearly showed that OSNs not expressing STOML-3 have a significantly lower frequency rate of their spontaneous firing activity. Moreover, upon stimulation with an odorant mix and IBMX, the OSNs from STOML-3 KO mice responded with a significantly lower number of action potentials, and this determined that the duration of their responses was significantly shorter compared to those from WT mice. Since it is well-known that STOML-3 physically and functionally interacts with different types of ion channels (Lapatsina et al., 2012; Qi et al., 2015; Wetzel et al., 2007), we hypothesize that STOML-3 affects the olfactory transduction likely by directly regulating the activity of the CNG and/or TMEM16B channels. Further experiments, such as co-immunoprecipitation assays and investigations of the olfactory transduction current, will be necessary to fully clarify the role of STOML-3 in the regulation of odorant response.

By whole-cell patch-clamp experiments, we found that SCs from both transition and dorsal zone of the mouse MOE showed Ca^{2+}-activated currents when recorded with different amounts of free intracellular Ca^{2+}. However, the amplitude of the current was significantly higher in the transition zone, where TMEM16A is highly expressed. Ion substitution and pharmacology revealed that the Ca^{2+}- activated current was mediated by Cl^- ions and that Ani9, a specific inhibitor of TMEM16A, strongly reduced the current. Importantly, the Ca^{2+}-activated current was completely abolished in SCs from TMEM16A KO mice, confirming that TMEM16A is a necessary component of the Ca^{2+}-activated Cl^- currents in olfactory SCs. Finally, we showed that the extracellular ATP application induced PLC-regulated intracellular Ca^{2+} increase in mouse SCs that led to the activation of a robust TMEM16A-mediated current.

SCs play a crucial role in preserving the MOE integrity and functionality (Hegg et al., 2009; Lucero, 2013; Rafols and Getchell, 1983; Suzuki et al., 1996), and they continuously renovate the mucus layer that covers the epithelium (Menco and Farbman, 1985; Menco and Morrison, 2003; Okano and Takagi, 1974), regulating its ionic composition and metabolizing toxicants trapped into it (Bannister and Dodson, 1992; Getchell, 1986; Trotier, 1998; Vogalis et al., 2005a). For these reasons, we speculate that TMEM16A could have a role in the regulation of the Cl^- concentration, an important anion involved in the olfactory transduction (Dibattista et al., 2017; Kleene, 2008; Li et al., 2018; Reisert and Reingruber, 2019; Schild and Restrepo, 1998), in the mucus, and it could modulate the endocytic trafficking in SCs, a necessary step for

the mucus detoxification since it is known that TMEM16A controls endocytosis in other epithelia (Asakawa et al., 2017; Dahl, 1988; He et al., 2017). Finally, TMEM16A may be involved in the olfactory purinergic cascade by increasing the Ca^{2+} signalling from the intracellular stores in SCs. Indeed, there is evidence that TMEM16A interacts with IP_3 receptors in nociceptive sensory neurons (Jin et al., 2013), and the Ca^{2+} release from internal stores is disrupted in intestinal crypt cells knocked down for TMEM16A (Schreiber et al., 2015). Additional work is required to elucidate the role of the TMEM16A channel in SCs of the MOE and to investigate more in detail the scenario depicted above.

The results in this thesis establish the first evidence that STOML-3 modulates the odorant response in mice and that TMEM16A channels are functionally expressed in mouse SCs mediating large Cl^- currents in response to purinergic receptors stimulations with ATP. These works provide the foundation for future studies aimed at clarifying the physiological role of STOML-3 and TMEM16A in the olfactory system.

References:

Adomaviciene, A., Smith, K.J., Garnett, H., and Tammaro, P. (2013). Putative pore-loops of TMEM16/anoctamin channels affect channel density in cell membranes. J. Physiol. *591*, 3487–3505.

Albeanu, D.F., Provost, A.C., Agarwal, P., Soucy, E.R., Zak, J.D., and Murthy, V.N. (2018). Olfactory marker protein (OMP) regulates formation and refinement of the olfactory glomerular map. Nat. Commun. *9*, 5073.

Altman, J. (1962). Are New Neurons Formed in the Brains of Adult Mammals? Science *135*, 1127–1128.

Alvites, R.D., Caseiro, A.R., Pedrosa, S.S., Branquinho, M.E., Varejão, A.S.P., and Maurício, A.C. (2018). The Nasal Cavity of the Rat and Mouse—Source of Mesenchymal Stem Cells for Treatment of Peripheral Nerve Injury. Anat. Rec. *301*, 1678–1689.

Andres, K.H. (1966). Der Feinbau der Regio olfactoria von Makrosmatikern. Z. Für Zellforsch. Mikrosk. Anat. *69*, 140–154.

Asakawa, M., Fukutani, Y., Savangsuksa, A., Noguchi, K., Matsunami, H., and Yohda, M. (2017). Modification of the response of olfactory receptors to acetophenone by CYP1a2. Sci. Rep. *7*, 10167.

Ayoub, C., Wasylyk, C., Li, Y., Thomas, E., Marisa, L., Robé, A., Roux, M., Abecassis, J., de Reyniès, A., and Wasylyk, B. (2010). ANO1 amplification and expression in HNSCC with a high propensity for future distant metastasis and its functions in HNSCC cell lines. Br. J. Cancer *103*, 715–726.

Baig, A.A., Haining, E.J., Geuss, E., Beck, S., Swieringa, F., Wanitchakool, P., Schuhmann, M.K., Stegner, D., Kunzelmann, K., Kleinschnitz, C., et al. (2016). TMEM16F-Mediated Platelet Membrane Phospholipid Scrambling Is Critical for Hemostasis and Thrombosis but not Thromboinflammation in Mice-Brief Report. Arterioscler. Thromb. Vasc. Biol. *36*, 2152–2157.

Bakalyar, H.A., and Reed, R.R. (1990). Identification of a specialized adenylyl cyclase that may mediate odorant detection. Science *250*, 1403–1406.

Bannister, L.H., and Dodson, H.C. (1992). Endocytic pathways in the olfactory and vomeronasal epithelia of the mouse: ultrastructure and uptake of tracers. Microsc. Res. Tech. *23*, 128–141.

Barnes, T.M., Jin, Y., Horvitz, H.R., Ruvkun, G., and Hekimi, S. (1996). The Caenorhabditis elegans Behavioral Gene unc-24 Encodes a Novel Bipartite Protein Similar to Both Erythrocyte Band 7.2 (Stomatin) and Nonspecific Lipid Transfer Protein. J. Neurochem. *67*, 46–57.

Benzing, T. (2004). Signaling at the slit diaphragm. J. Am. Soc. Nephrol. JASN *15*, 1382–1391.

Bera, T.K., Das, S., Maeda, H., Beers, R., Wolfgang, C.D., Kumar, V., Hahn, Y., Lee, B., and Pastan, I. (2004). NGEP, a gene encoding a membrane protein detected only in prostate cancer and normal prostate. Proc. Natl. Acad. Sci. *101*, 3059–3064.

Billig, G.M., Pál, B., Fidzinski, P., and Jentsch, T.J. (2011). Ca2+-activated Cl− currents are dispensable for olfaction. Nat. Neurosci. *14*, 763–769.

Boccaccio, A., and Menini, A. (2007). Temporal development of cyclic nucleotide-gated and Ca2+ -activated Cl- currents in isolated mouse olfactory sensory neurons. J. Neurophysiol. *98*, 153–160.

Bolduc, V., Marlow, G., Boycott, K.M., Saleki, K., Inoue, H., Kroon, J., Itakura, M., Robitaille, Y., Parent, L., Baas, F., et al. (2010). Recessive mutations in the putative calcium-activated chloride channel Anoctamin 5 cause proximal LGMD2L and distal MMD3 muscular dystrophies. Am. J. Hum. Genet. *86*, 213–221.

Bolz, F., Kasper, S., Bufe, B., Zufall, F., and Pyrski, M. (2017). Organization and Plasticity of Sodium Channel Expression in the Mouse Olfactory and Vomeronasal Epithelia. Front. Neuroanat. *11*.

Bönigk, W., Bradley, J., Müller, F., Sesti, F., Boekhoff, I., Ronnett, G.V., Kaupp, U.B., and Frings, S. (1999). The native rat olfactory cyclic nucleotide-gated channel is composed of three distinct subunits. J. Neurosci. Off. J. Soc. Neurosci. *19*, 5332–5347.

Borisy, F.F., Ronnett, G.V., Cunningham, A.M., Juilfs, D., Beavo, J., and Snyder, S.H. (1992). Calcium/calmodulin-activated phosphodiesterase expressed in olfactory receptor neurons. J. Neurosci. Off. J. Soc. Neurosci. *12*, 915–923.

Boute, N., Gribouval, O., Roselli, S., Benessy, F., Lee, H., Fuchshuber, A., Dahan, K., Gubler, M.C., Niaudet, P., and Antignac, C. (2000). NPHS2, encoding the glomerular protein podocin, is mutated in autosomal recessive steroid-resistant nephrotic syndrome. Nat. Genet. *24*, 349–354.

Brann, J.H., and Firestein, S.J. (2014). A lifetime of neurogenesis in the olfactory system. Front. Neurosci. *8*.

Brann, D.H., Tsukahara, T., Weinreb, C., Lipovsek, M., Van den Berge, K., Gong, B., Chance, R., Macaulay, I.C., Chou, H., Fletcher, R., et al. (2020). Non-neuronal expression of SARS-CoV-2 entry genes in the olfactory system suggests mechanisms underlying COVID-19-associated anosmia (Neuroscience).

Breipohl, W., Laugwitz, H.J., and Bornfeld, N. (1974). Topological relations between the dendrites of olfactory sensory cells and sustentacular cells in different vertebrates. An ultrastructural study. J. Anat. *117*, 89–94.

Breunig, E., Czesnik, D., Piscitelli, F., Di Marzo, V., Manzini, I., and Schild, D. (2010a). Endocannabinoid modulation in the olfactory epithelium. Results Probl. Cell Differ. *52*, 139–145.

Breunig, E., Manzini, I., Piscitelli, F., Gutermann, B., Di Marzo, V., Schild, D., and Czesnik, D. (2010b). The endocannabinoid 2-arachidonoyl-glycerol controls odor sensitivity in larvae of Xenopus laevis. J. Neurosci. Off. J. Soc. Neurosci. *30*, 8965–8973.

Browman, D.T., Resek, M.E., Zajchowski, L.D., and Robbins, S.M. (2006). Erlin-1 and erlin-2 are novel members of the prohibitin family of proteins that define lipid-raft-like domains of the ER. J. Cell Sci. *119*, 3149–3160.

Browman, D.T., Hoegg, M.B., and Robbins, S.M. (2007). The SPFH domain-containing proteins: more than lipid raft markers. Trends Cell Biol. *17*, 394–402.

Brunner, J.D., Lim, N.K., Schenck, S., Duerst, A., and Dutzler, R. (2014). X-ray structure of a calcium-activated TMEM16 lipid scramblase. Nature *516*, 207–212.

Buck, L.B. (2000). The Molecular Architecture of Odor and Pheromone Sensing in Mammals. Cell *100*, 611–618.

Buck, L., and Axel, R. (1991). A novel multigene family may encode odorant receptors: a molecular basis for odor recognition. Cell *65*, 175–187.

Buiakova, O.I., Krishna, N.S.R., Getchell, T.V., and Margolis, F.L. (1994). Human and Rodent OMP Genes: Conservation of Structural and Regulatory Motifs and Cellular Localization. Genomics *20*, 452–462.

Buiakova, O.I., Baker, H., Scott, J.W., Farbman, A., Kream, R., Grillo, M., Franzen, L., Richman, M., Davis, L.M., Abbondanzo, S., et al. (1996). Olfactory marker protein (OMP) gene deletion causes altered physiological activity of olfactory sensory neurons. Proc. Natl. Acad. Sci. *93*, 9858–9863.

Butowt, R., and Bilinska, K. (2020). SARS-CoV-2: Olfaction, Brain Infection, and the Urgent Need for Clinical Samples Allowing Earlier Virus Detection. ACS Chem. Neurosci.

Caggiano, M., Kauer, J.S., and Hunter, D.D. (1994). Globose basal cells are neuronal progenitors in the olfactory epithelium: a lineage analysis using a replication-incompetent retrovirus. Neuron *13*, 339–352.

Caputo, A., Caci, E., Ferrera, L., Pedemonte, N., Barsanti, C., Sondo, E., Pfeffer, U., Ravazzolo, R., Zegarra-Moran, O., and Galietta, L.J.V. (2008). TMEM16A, a membrane protein associated with calcium-dependent chloride channel activity. Science *322*, 590–594.

Carr, V.M., Menco, B.P.M., Yankova, M.P., Morimoto, R.I., and Farbman, A.I. (2001). Odorants as cell-type specific activators of a heat shock response in the rat olfactory mucosa. J. Comp. Neurol. *432*, 425–439.

Carr, V.McM., Farbman, A.I., Colletti, L.M., and Morgan, J.I. (1991). Identification of a new non-neuronal cell type in rat olfactory epithelium. Neuroscience *45*, 433–449.

Castoldi, E., Collins, P.W., Williamson, P.L., and Bevers, E.M. (2011). Compound heterozygosity for 2 novel TMEM16F mutations in a patient with Scott syndrome. Blood *117*, 4399–4400.

Cau, E., Gradwohl, G., Fode, C., and Guillemot, F. (1997). Mash1 activates a cascade of bHLH regulators in olfactory neuron progenitors. Dev. Camb. Engl. *124*, 1611–1621.

Chamanza, R., and Wright, J.A. (2015). A Review of the Comparative Anatomy, Histology, Physiology and Pathology of the Nasal Cavity of Rats, Mice, Dogs and Non-human Primates. Relevance to Inhalation Toxicology and Human Health Risk Assessment. J. Comp. Pathol. *153*, 287–314.

Chamova, T., Florez, L., Guergueltcheva, V., Raycheva, M., Kaneva, R., Lochmüller, H., Kalaydjieva, L., and Tournev, I. (2012). ANO10 c.1150_1151del is a founder mutation causing autosomal recessive cerebellar ataxia in Roma/Gypsies. J. Neurol. *259*, 906–911.

Chapuis, J., and Wilson, D.A. (2011). Bidirectional plasticity of cortical pattern recognition and behavioral sensory acuity. Nat. Neurosci. *15*, 155–161.

Chen, C., Nakamura, T., and Koutalos, Y. (1999). Cyclic AMP diffusion coefficient in frog olfactory cilia. Biophys. J. *76*, 2861–2867.

Chen, X., Fang, H., and Schwob, J.E. (2004). Multipotency of purified, transplanted globose basal cells in olfactory epithelium. J. Comp. Neurol. *469*, 457–474.

Chen, Y., Getchell, M.L., Ding, X., and Getchell, T.V. (1992). Immunolocalization of two cytochrome P450 isozymes in rat nasal chemosensory tissue. Neuroreport *3*, 749–752.

Cho, H., Yang, Y.D., Lee, J., Lee, B., Kim, T., Jang, Y., Back, S.K., Na, H.S., Harfe, B.D., Wang, F., et al. (2012). The calcium-activated chloride channel anoctamin 1 acts as a heat sensor in nociceptive neurons. Nat. Neurosci. *15*, 1015–1021.

Cole, P. (1993). The respiratory role of the upper airways. 42–46.

Cornell-Bell, A.H., Finkbeiner, S.M., Cooper, M.S., and Smith, S.J. (1990). Glutamate induces calcium waves in cultured astrocytes: long-range glial signaling. Science *247*, 470–473.

Corotto, F.S., Piper, D.R., Chen, N., and Michel, W.C. (1996). Voltage- and Ca(2+)-gated currents in zebrafish olfactory receptor neurons. J. Exp. Biol. *199*, 1115–1126.

Cross, N.L., and Elinson, R.P. (1980). A fast block to polyspermy in frogs mediated by changes in the membrane potential. Dev. Biol. *75*, 187–198.

Cui, Z., Zhang, L., Hua, Z., Cao, W., Feng, W., and Liu, Z. (2007). Stomatin-like protein 2 is overexpressed and related to cell growth in human endometrial adenocarcinoma. Oncol. Rep. *17*, 829–833.

Cygnar, K.D., and Zhao, H. (2009). Phosphodiesterase 1C is dispensable for rapid response termination of olfactory sensory neurons. Nat. Neurosci. *12*, 454–462.

Da Cruz, S., Xenarios, I., Langridge, J., Vilbois, F., Parone, P.A., and Martinou, J.-C. (2003). Proteomic analysis of the mouse liver mitochondrial inner membrane. J. Biol. Chem. *278*, 41566–41571.

Dacie, J.V. (1970). Autoimmune haemolytic anaemias. Br. Med. J. *2*, 381–386.

Dahl, A. (1988). The effect of cytochrome P-450-dependent metabolism and other enzyme activities on olfaction. in" Molecular Neurobiology of the Olfactory System.". Plenum Press N. Y.

Dahl, A.R., and Hadley, W.M. (1991). Nasal cavity enzymes involved in xenobiotic metabolism: effects on the toxicity of inhalants. Crit. Rev. Toxicol. *21*, 345–372.

Dang, P., Fisher, S.A., Stefanik, D.J., Kim, J., and Raper, J.A. (2018). Coordination of olfactory receptor choice with guidance receptor expression and function in olfactory sensory neurons. PLOS Genet. *14*, e1007164.

Dang, S., Feng, S., Tien, J., Peters, C.J., Bulkley, D., Lolicato, M., Zhao, J., Zuberbühler, K., Ye, W., Qi, L., et al. (2017). Cryo-EM structures of the TMEM16A calcium-activated chloride channel. Nature *552*, 426–429.

Dauner, K., Lißmann, J., Jeridi, S., Frings, S., and Möhrlen, F. (2012). Expression patterns of anoctamin 1 and anoctamin 2 chloride channels in the mammalian nose. Cell Tissue Res. *347*, 327–341.

Davidson, J.S., and Baumgarten, I.M. (1988). Glycyrrhetinic acid derivatives: a novel class of inhibitors of gap-junctional intercellular communication. Structure-activity relationships. J. Pharmacol. Exp. Ther. *246*, 1104–1107.

DeMaria, S., and Ngai, J. (2010). The cell biology of smell. J. Cell Biol. *191*, 443–452.

De Palo, G., Boccaccio, A., Miri, A., Menini, A., and Altafini, C. (2012). A Dynamical Feedback Model for Adaptation in the Olfactory Transduction Pathway. Biophys. J. *102*, 2677–2686.

Dibattista, M., Pifferi, S., Boccaccio, A., Menini, A., and Reisert, J. (2017). The long tale of the calcium activated Cl- channels in olfactory transduction. Channels Austin Tex *11*, 399–414.

Doucette, R. (1993). Glial cells in the nerve fiber layer of the main olfactory bulb of embryonic and adult mammals. Microsc. Res. Tech. *24*, 113–130.

Døving, K.B., and Trotier, D. (1998). Structure and function of the vomeronasal organ. J. Exp. Biol. *201*, 2913–2925.

Duran, C., Thompson, C.H., Xiao, Q., and Hartzell, H.C. (2010). Chloride Channels: Often Enigmatic, Rarely Predictable. Annu. Rev. Physiol. *72*, 95–121.

Duran, C., Qu, Z., Osunkoya, A.O., Cui, Y., and Hartzell, H.C. (2011). ANOs 3–7 in the anoctamin/Tmem16 Cl– channel family are intracellular proteins. Am. J. Physiol.-Cell Physiol. *302*, C482–C493.

Duvvuri, U., Shiwarski, D.J., Xiao, D., Bertrand, C., Huang, X., Edinger, R.S., Rock, J.R., Harfe, B.D., Henson, B.J., Kunzelmann, K., et al. (2012). TMEM16A induces MAPK and contributes directly to tumorigenesis and cancer progression. Cancer Res. *72*, 3270–3281.

Eber, S.W., Lande, W.M., Iarocci, T.A., Mentzer, W.C., Höhn, P., Wiley, J.S., and Schröter, W. (1989). Hereditary stomatocytosis: consistent association with an integral membrane protein deficiency. Br. J. Haematol. *72*, 452–455.

Eiting, T.P., Smith, T.D., Perot, J.B., and Dumont, E.R. (2014). The role of the olfactory recess in olfactory airflow. J. Exp. Biol. *217*, 1799–1803.

Evans, H.E., and Lahunta, A. de (2013). Miller's Anatomy of the Dog - E-Book (Elsevier Health Sciences).

Fallah, G., Römer, T., Detro-Dassen, S., Braam, U., Markwardt, F., and Schmalzing, G. (2011). TMEM16A(a)/anoctamin-1 shares a homodimeric architecture with CLC chloride channels. Mol. Cell. Proteomics MCP *10*, M110.004697.

Falzone, M.E., Malvezzi, M., Lee, B.-C., and Accardi, A. (2018). Known structures and unknown mechanisms of TMEM16 scramblases and channels. J. Gen. Physiol. *150*, 933–947.

Farbman, A.I. (1994). The cellular basis of olfaction. Endeavour *18*, 2–8.

Farbman, A.I., and Margolis, F.L. (1980). Olfactory marker protein during ontogeny: Immunohistochemical localization. Dev. Biol. *74*, 205–215.

Feinstein, P., Bozza, T., Rodriguez, I., Vassalli, A., and Mombaerts, P. (2004). Axon guidance of mouse olfactory sensory neurons by odorant receptors and the beta2 adrenergic receptor. Cell *117*, 833–846.

Ferrera, L., Caputo, A., Ubby, I., Bussani, E., Zegarra-Moran, O., Ravazzolo, R., Pagani, F., and Galietta, L.J.V. (2009). Regulation of TMEM16A chloride channel properties by alternative splicing. J. Biol. Chem. *284*, 33360–33368.

Ferrero, D.M., and Liberles, S.D. (2010). The secret codes of mammalian scents. Wiley Interdiscip. Rev. Syst. Biol. Med. *2*, 23–33.

Finkbeiner, S. (1992). Calcium waves in astrocytes-filling in the gaps. Neuron *8*, 1101–1108.

Firestein, S. (2001). How the olfactory system makes sense of scents. Nature *413*, 211–218.

Firestein, S., and Werblin, F. (1989). Odor-induced membrane currents in vertebrate-olfactory receptor neurons. Science *244*, 79–82.

Firestein, S., and Werblin, F.S. (1987). Gated currents in isolated olfactory receptor neurons of the larval tiger salamander. Proc. Natl. Acad. Sci. *84*, 6292–6296.

Fletcher, R.B., Das, D., Gadye, L., Street, K.N., Baudhuin, A., Wagner, A., Cole, M.B., Flores, Q., Choi, Y.G., Yosef, N., et al. (2017). Deconstructing Olfactory Stem Cell Trajectories at Single-Cell Resolution. Cell Stem Cell *20*, 817-830.e8.

Fluegge, D., Moeller, L.M., Cichy, A., Gorin, M., Weth, A., Veitinger, S., Cainarca, S., Lohmer, S., Corazza, S., Neuhaus, E.M., et al. (2012). Mitochondrial Ca 2+ mobilization is a key element in olfactory signaling. Nat. Neurosci. *15*, 754–762.

Fodoulian, L., Tuberosa, J., Rossier, D., Landis, B.N., Carleton, A., and Rodriguez, I. (2020). SARS-CoV-2 receptor and entry genes are expressed by sustentacular cells in the human olfactory neuroepithelium. BioRxiv 2020.03.31.013268.

Forrest, A.S., Joyce, T.C., Huebner, M.L., Ayon, R.J., Wiwchar, M., Joyce, J., Freitas, N., Davis, A.J., Ye, L., Duan, D.D., et al. (2012). Increased TMEM16A-encoded calcium-activated chloride channel activity is associated with pulmonary hypertension. Am. J. Physiol. Cell Physiol. *303*, C1229-1243.

Foster, J.D., Getchell, M.L., and Getchell, T.V. (1991). Identification of sugar residues in secretory glycoconjugates of olfactory mucosae using lectin histochemistry. Anat. Rec. *229*, 525–544.

Fricke, B., Argent, A.C., Chetty, M.C., Pizzey, A.R., Turner, E.J., Ho, M.M., Iolascon, A., von Düring, M., and Stewart, G.W. (2003). The "stomatin" gene and protein in overhydrated hereditary stomatocytosis. Blood *102*, 2268–2277.

Frings, S., and Lindemann, B. (1988). Odorant response of isolated olfactory receptor cells is blocked by amiloride. J. Membr. Biol. *105*, 233–243.

Frings, S., Seifert, R., Godde, M., and Kaupp, U.B. (1995). Profoundly different calcium permeation and blockage determine the specific function of distinct cyclic nucleotide-gated channels. Neuron *15*, 169–179.

Fu, Z., Ogura, T., Luo, W., and Lin, W. (2018). ATP and Odor Mixture Activate TRPM5-Expressing Microvillous Cells and Potentially Induce Acetylcholine Release to Enhance Supporting Cell Endocytosis in Mouse Main Olfactory Epithelium. Front. Cell. Neurosci. *12*.

Gallagher, P.G., and Forget, B.G. (1995). Structure, Organization, and Expression of the Human Band 7.2b Gene, a Candidate Gene for Hereditary Hydrocytosis. J. Biol. Chem. *270*, 26358–26363.

Genter, M.B. (2004). Update on olfactory mucosal metabolic enzymes: Age-related changes and N-acetyltransferase activities. J. Biochem. Mol. Toxicol. *18*, 239–244.

Getchell, T.V. (1986). Functional properties of vertebrate olfactory receptor neurons. Physiol. Rev. *66*, 772–818.

Getchell, M.L., and Getchell, T.V. (1992). Fine structural aspects of secretion and extrinsic innervation in the olfactory mucosa. Microsc. Res. Tech. *23*, 111–127.

Ghiaroni, V., Fieni, F., Tirindelli, R., Pietra, P., and Bigiani, A. (2003). Ion Conductances in Supporting Cells Isolated From the Mouse Vomeronasal Organ. J. Neurophysiol. *89*, 118–127.

Giannetti, N., Pellier, V., Oestreicher, A.B., and Astic, L. (1995). Immunocytochemical study of the differentiation process of the septal organ of Masera in developing rats. Brain Res. Dev. Brain Res. *84*, 287–293.

Giaume, C., and Venance, L. (1998). Intercellular calcium signaling and gap junctional communication in astrocytes. Glia *24*, 50–64.

Glusman, G., Yanai, I., Rubin, I., and Lancet, D. (2001). The complete human olfactory subgenome. Genome Res. *11*, 685–702.

Goldstein, B.J., and Schwob, J.E. (1996). Analysis of the Globose Basal Cell Compartment in Rat Olfactory Epithelium Using GBC-1, a New Monoclonal Antibody against Globose Basal Cells. J. Neurosci. *16*, 4005–4016.

Goldstein, B.J., Kulaga, H.M., and Reed, R.R. (2003). Cloning and Characterization of SLP3: a Novel Member of the Stomatin Family Expressed by Olfactory Receptor Neurons. JARO J. Assoc. Res. Otolaryngol. *4*, 74–82.

Graziadei, P.P.C. (1973). Cell dynamics in the olfactory mucosa. Tissue Cell *5*, 113–131.

Graziadei, P.P.C., and Graziadei, G.A.M. (1979). Neurogenesis and neuron regeneration in the olfactory system of mammals. I. Morphological aspects of differentiation and structural organization of the olfactory sensory neurons. J. Neurocytol. *8*, 1–18.

Graziadei, G.A.M., Stanley, R.S., and Graziadei, P.P.C. (1980). The olfactory marker protein in the olfactory system of the mouse during development. Neuroscience *5*, 1239–1252.

Green, J.B., and Young, J.P.W. (2008). Slipins: ancient origin, duplication and diversification of the stomatin protein family. BMC Evol. Biol. *8*, 44.

Gross, E.A., Swenberg, J.A., Fields, S., and Popp, J.A. (1982). Comparative morphometry of the nasal cavity in rats and mice. J. Anat. *135*, 83–88.

Guilmette, R.A., Wicks, J.D., and Wolff, R.K. (1989). Morphometry of Human Nasal Airways In Vivo Using Magnetic Resonance Imaging. J. Aerosol Med. *2*, 365–377.

Guo, Z., Packard, A., Krolewski, R.C., Harris, M.T., Manglapus, G.L., and Schwob, J.E. (2010). Expression of pax6 and sox2 in adult olfactory epithelium. J. Comp. Neurol. *518*, 4395–4418.

Haberly, L.B., and Price, J.L. (1977). The axonal projection patterns of the mitral and tufted cells of the olfactory bulb in the rat. Brain Res. *129*, 152–157.

Hansel, D.E., Eipper, B.A., and Ronnett, G.V. (2001). Neuropeptide Y functions as a neuroproliferative factor. Nature *410*, 940–944.

Hansen, A., and Finger, T.E. (2008). Is TrpM5 a reliable marker for chemosensory cells? Multiple types of microvillous cells in the main olfactory epithelium of mice. BMC Neurosci. *9*, 115.

Harkema, J.R., and Morgan, K.T. (1996). Normal Morphology of the Nasal Passages in Laboratory Rodents. In Respiratory System, T.C. Jones, D.L. Dungworth, and U. Mohr, eds. (Berlin, Heidelberg: Springer), pp. 3–17.

Harkema, J.R., Carey, S.A., and Wagner, J.G. (2006). The Nose Revisited: A Brief Review of the Comparative Structure, Function, and Toxicologic Pathology of the Nasal Epithelium. Toxicol. Pathol. *34*, 252–269.

Hartzell, C., Putzier, I., and Arreola, J. (2005). CALCIUM-ACTIVATED CHLORIDE CHANNELS. Annu. Rev. Physiol. *67*, 719–758.

Hartzell, H.C., Yu, K., Xiao, Q., Chien, L.-T., and Qu, Z. (2009). Anoctamin/TMEM16 family members are Ca2+-activated Cl− channels. J. Physiol. *587*, 2127–2139.

Hassenklöver, T., Kurtanska, S., Bartoszek, I., Junek, S., Schild, D., and Manzini, I. (2008). Nucleotide-induced Ca2+ signaling in sustentacular supporting cells of the olfactory epithelium. Glia *56*, 1614–1624.

Hayoz, S., Jia, C., and Hegg, C. (2012). Mechanisms of constitutive and ATP-evoked ATP release in neonatal mouse olfactory epithelium. BMC Neurosci. *13*, 53.

He, M., Ye, W., Wang, W.-J., Sison, E.S., Jan, Y.N., and Jan, L.Y. (2017). Cytoplasmic Cl− couples membrane remodeling to epithelial morphogenesis. Proc. Natl. Acad. Sci. *114*, E11161–E11169.

Hegg, C.C., and Lucero, M.T. (2006). Purinergic receptor antagonists inhibit odorant-induced heat shock protein 25 induction in mouse olfactory epithelium. Glia *53*, 182–190.

Hegg, C.C., Greenwood, D., Huang, W., Han, P., and Lucero, M.T. (2003a). Activation of Purinergic Receptor Subtypes Modulates Odor Sensitivity. J. Neurosci. *23*, 8291–8301.

Hegg, C.C., Au, E., Roskams, A.J., and Lucero, M.T. (2003b). PACAP is present in the olfactory system and evokes calcium transients in olfactory receptor neurons. J. Neurophysiol. *90*, 2711–2719.

Hegg, C.C., Irwin, M., and Lucero, M.T. (2009). Calcium store-mediated signaling in sustentacular cells of the mouse olfactory epithelium. Glia *57*, 634–644.

Hiebl-Dirschmied, C.M., Entler, B., Glotzmann, C., Maurer-Fogy, I., Stratowa, C., and Prohaska, R. (1991a). Cloning and nucleotide sequence of cDNA encoding human erythrocyte band 7 integral membrane protein. Biochim. Biophys. Acta BBA - Gene Struct. Expr. *1090*, 123–128.

Hiebl-Dirschmied, C.M., Adolf, G.R., and Prohaska, R. (1991b). Isolation and partial characterization of the human erythrocyte band 7 integral membrane protein. Biochim. Biophys. Acta *1065*, 195–202.

Hill, R.W., Wyse, G.A., and Anderson, M. (2004). Animal Physiology, Third Edition.

Hoffmann, M., Kleine-Weber, H., Schroeder, S., Krüger, N., Herrler, T., Erichsen, S., Schiergens, T.S., Herrler, G., Wu, N.-H., Nitsche, A., et al. (2020). SARS-CoV-2 Cell Entry Depends on ACE2 and TMPRSS2 and Is Blocked by a Clinically Proven Protease Inhibitor. Cell *181*, 271-280.e8.

Holbrook, E.H., Szumowski, K.E.M., and Schwob, J.E. (1995). An immunochemical, ultrastructural, and developmental characterization of the horizontal basal cells of rat olfactory epithelium. J. Comp. Neurol. *363*, 129–146.

Holbrook, E.H., Wu, E., Curry, W.T., Lin, D.T., and Schwob, J.E. (2011). Immunohistochemical characterization of human olfactory tissue. The Laryngoscope *121*, 1687–1701.

Holl, A.-M. (2018). Survival of mature mouse olfactory sensory neurons labeled genetically perinatally. Mol. Cell. Neurosci. *88*, 258–269.

Hopkins, C., Surda, P., and Kumar, N. (2020). Presentation of new onset anosmia during the COVID-19 pandemic. Rhinology.

Huang, F., Wong, X., and Jan, L.Y. (2012a). International Union of Basic and Clinical Pharmacology. LXXXV: calcium-activated chloride channels. Pharmacol. Rev. *64*, 1–15.

Huang, F., Wang, X., Ostertag, E.M., Nuwal, T., Huang, B., Jan, Y.-N., Basbaum, A.I., and Jan, L.Y. (2013). TMEM16C facilitates Na(+)-activated K+ currents in rat sensory neurons and regulates pain processing. Nat. Neurosci. *16*, 1284–1290.

Huang, M., Gu, G., Ferguson, E.L., and Chalfie, M. (1995). A stomatin-like protein necessary for mechanosensation in C. elegans. Nature *378*, 292–295.

Huang, W.C., Xiao, S., Huang, F., Harfe, B.D., Jan, Y.N., and Jan, L.Y. (2012b). Calcium-activated chloride channels (CaCCs) regulate action potential and synaptic response in hippocampal neurons. Neuron *74*, 179–192.

Huang, X., Godfrey, T.E., Gooding, W.E., McCarty, K.S., and Gollin, S.M. (2006). Comprehensive genome and transcriptome analysis of the 11q13 amplicon in human oral cancer and synteny to the 7F5 amplicon in murine oral carcinoma. Genes. Chromosomes Cancer *45*, 1058–1069.

Huard, J.M.T., and Schwob, J.E. (1995). Cell cycle of globose basal cells in rat olfactory epithelium. Dev. Dyn. *203*, 17–26.

Huber, T.B., and Benzing, T. (2005). The slit diaphragm: a signaling platform to regulate podocyte function. Curr. Opin. Nephrol. Hypertens. *14*, 211–216.

Huber, T.B., Schermer, B., Müller, R.U., Höhne, M., Bartram, M., Calixto, A., Hagmann, H., Reinhardt, C., Koos, F., Kunzelmann, K., et al. (2006). Podocin and MEC-2 bind cholesterol to regulate the activity of associated ion channels. Proc. Natl. Acad. Sci. U. S. A. *103*, 17079–17086.

Hutch, C.R., and Hegg, C.C. (2016). Cannabinoid receptor signaling induces proliferation but not neurogenesis in the mouse olfactory epithelium. Neurogenesis *3*, e1118177.

Hutch, C., Hillard, C.J., Jia, C., and Hegg, C.C. (2015). An endocannabinoid system is present in the mouse olfactory epithelium but does not modulate olfaction. Neuroscience *300*, 539–553.

Hwang, C.-S. (2006). Olfactory neuropathy in severe acute respiratory syndrome: report of A case. Acta Neurol. Taiwanica *15*, 26–28.

Imai, T., Suzuki, M., and Sakano, H. (2006). Odorant receptor-derived cAMP signals direct axonal targeting. Science *314*, 657–661.

Iwai, N., Zhou, Z., Roop, D.R., and Behringer, R.R. (2008). Horizontal Basal Cells Are Multipotent Progenitors in Normal and Injured Adult Olfactory Epithelium. STEM CELLS *26*, 1298–1306.

Jeng, G., Aggarwal, M., Yu, W.-P., and Chen, T.-Y. (2016). Independent activation of distinct pores in dimeric TMEM16A channels. J. Gen. Physiol. *148*, 393–404.

Jia, C., and Hegg, C.C. (2010). NPY mediates ATP-induced neuroproliferation in adult mouse olfactory epithelium. Neurobiol. Dis. *38*, 405–413.

Jin, X., Shah, S., Liu, Y., Zhang, H., Lees, M., Fu, Z., Lippiat, J.D., Beech, D.J., Sivaprasadarao, A., Baldwin, S.A., et al. (2013). Activation of the Cl- channel ANO1 by localized calcium signals in nociceptive sensory neurons requires coupling with the IP3 receptor. Sci. Signal. *6*, ra73.

John, J.A.S., and Key, B. (2005). Olfactory marker protein modulates primary olfactory axon overshooting in the olfactory bulb. J. Comp. Neurol. *488*, 61–69.

Johnson, N.T., Villalón, M., Royce, F.H., Hard, R., and Verdugo, P. (1991). Autoregulation of beat frequency in respiratory ciliated cells. Demonstration by viscous loading. Am. Rev. Respir. Dis. *144*, 1091–1094.

Jones, D.T., and Reed, R.R. (1989). Golf: an olfactory neuron specific-G protein involved in odorant signal transduction. Science *244*, 790–795.

Kanageswaran, N., Demond, M., Nagel, M., Schreiner, B.S.P., Baumgart, S., Scholz, P., Altmüller, J., Becker, C., Doerner, J.F., Conrad, H., et al. (2015). Deep Sequencing of the Murine Olfactory Receptor Neuron Transcriptome. PLOS ONE *10*, e0113170.

Kaneko, H., Putzier, I., Frings, S., Kaupp, U.B., and Gensch, T. (2004). Chloride Accumulation in Mammalian Olfactory Sensory Neurons. J. Neurosci. *24*, 7931–7938.

Kanzaki, A., and Yawata, Y. (1992). Hereditary stomatocytosis: phenotypical expression of sodium transport and band 7 peptides in 44 cases. Br. J. Haematol. *82*, 133–141.

Kass, M.D., Moberly, A.H., Rosenthal, M.C., Guang, S.A., and McGann, J.P. (2013). Odor-Specific, Olfactory Marker Protein-Mediated Sparsening of Primary Olfactory Input to the Brain after Odor Exposure. J. Neurosci. *33*, 6594–6602.

Keller, A., and Margolis, F.L. (1975). Immunological studies of the rat olfactory marker protein. J. Neurochem. *24*, 1101–1106.

Kepler, G.M., Joyner, D.R., Fleishman, A., Richardson, R., Gross, E.A., Morgan, K.T., Kimbell, J.S., and Godo, M.N. (1995). Method for obtaining accurate geometrical coordinates of nasal airways for computer dosimetry modeling and lesion mapping. Inhal. Toxicol. *7*, 1207–1224.

Kim, H., Kim, H., Lee, J., Lee, B., Kim, H.-R., Jung, J., Lee, M.-O., and Oh, U. (2018). Anoctamin 9/TMEM16J is a cation channel activated by cAMP/PKA signal. Cell Calcium *71*, 75–85.

Kimbell, J.S. (2016). Nasal Dosimetry of Inhaled Gases and Particles: Where Do Inhaled Agents Go in the Nose?: Toxicol. Pathol.

Kirchhof, M.G., Chau, L.A., Lemke, C.D., Vardhana, S., Darlington, P.J., Márquez, M.E., Taylor, R., Rizkalla, K., Blanca, I., Dustin, M.L., et al. (2008). Modulation of T Cell Activation by Stomatin-Like Protein 2. J. Immunol. *181*, 1927–1936.

Kleene, S.J. (2008). The Electrochemical Basis of Odor Transduction in Vertebrate Olfactory Cilia. Chem. Senses *33*, 839–859.

Kleene, S.J., and Gesteland, R.C. (1991). Calcium-activated chloride conductance in frog olfactory cilia. J. Neurosci. *11*, 3624–3629.

Kobayakawa, K., Hayashi, R., Morita, K., Miyamichi, K., Oka, Y., Tsuboi, A., and Sakano, H. (2002). Stomatin-Related Olfactory Protein, SRO, Specifically Expressed in the Murine Olfactory Sensory Neurons. J. Neurosci. *22*, 5931–5937.

Kramer, R.H., and Siegelbaum, S.A. (1992). Intracellular Ca2+ regulates the sensitivity of cyclic nucleotide-gated channels in olfactory receptor neurons. Neuron *9*, 897–906.

Kurahashi, T. (1989). Activation by odorants of cation-selective conductance in the olfactory receptor cell isolated from the newt. J. Physiol. *419*, 177–192.

Kurahashi, T., and Menini, A. (1997). Mechanism of odorant adaptation in the olfactory receptor cell. Nature *385*, 725–729.

Kurahashi, T., and Shibuya, T. (1989). Membrane resonses and permeability changes to odorants in the solitary olfactory receptor cells of newt. Zoolog. Sci. *6*, p19-30.

Lacroix, M.-C., Badonnel, K., Meunier, N., Tan, F., Schlegel-Le Poupon, C., Durieux, D., Monnerie, R., Baly, C., Congar, P., Salesse, R., et al. (2008). Expression of insulin system in the olfactory epithelium: first approaches to its role and regulation. J. Neuroendocrinol. *20*, 1176–1190.

Lagostena, L., and Menini, A. (2003). Whole-cell Recordings and Photolysis of Caged Compounds in Olfactory Sensory Neurons Isolated from the Mouse. Chem. Senses *28*, 705–716.

Lande, W.M., Thiemann, P.V., and Mentzer, W.C. (1982). Missing band 7 membrane protein in two patients with high Na, low K erythrocytes. J. Clin. Invest. *70*, 1273–1280.

Lapatsina, L., Brand, J., Poole, K., Daumke, O., and Lewin, G.R. (2012). Stomatin-domain proteins. Eur. J. Cell Biol. *91*, 240–245.

Le, S.C., Jia, Z., Chen, J., and Yang, H. (2019). Molecular basis of PIP 2 -dependent regulation of the Ca 2+ -activated chloride channel TMEM16A. Nat. Commun. *10*, 3769.

Lee, A.C., He, J., and Ma, M. (2011). Olfactory Marker Protein Is Critical for Functional Maturation of Olfactory Sensory Neurons and Development of Mother Preference. J. Neurosci. *31*, 2974–2982.

Leung, C.T., Coulombe, P.A., and Reed, R.R. (2007). Contribution of olfactory neural stem cells to tissue maintenance and regeneration. Nat. Neurosci. *10*, 720–726.

Li, R.-C., Ben-Chaim, Y., Yau, K.-W., and Lin, C.-C. (2016). Cyclic-nucleotide-gated cation current and Ca2+-activated Cl current elicited by odorant in vertebrate olfactory receptor neurons. Proc. Natl. Acad. Sci. U. S. A. *113*, 11078–11087.

Li, R.-C., Lin, C.-C., Ren, X., Wu, J.S., Molday, L.L., Molday, R.S., and Yau, K.-W. (2018). Ca2+-activated Cl current predominates in threshold response of mouse olfactory receptor neurons. Proc. Natl. Acad. Sci. U. S. A. *115*, 5570–5575.

Li, Y.-C., Bai, W.-Z., and Hashikawa, T. (2020). The neuroinvasive potential of SARS-CoV2 may play a role in the respiratory failure of COVID-19 patients. J. Med. Virol.

Lim, N.K., Lam, A.K.M., and Dutzler, R. (2016). Independent activation of ion conduction pores in the double-barreled calcium-activated chloride channel TMEM16A. J. Gen. Physiol. *148*, 375–392.

Lin, W., Ogura, T., Margolskee, R.F., Finger, T.E., and Restrepo, D. (2008). TRPM5-expressing solitary chemosensory cells respond to odorous irritants. J. Neurophysiol. *99*, 1451–1460.

Lindemann, B. (2001). Predicted profiles of ion concentrations in olfactory cilia in the steady state. Biophys. J. *80*, 1712–1721.

Liu, B., Linley, J.E., Du, X., Zhang, X., Ooi, L., Zhang, H., and Gamper, N. (2010). The acute nociceptive signals induced by bradykinin in rat sensory neurons are mediated by inhibition of M-type K+ channels and activation of Ca2+-activated Cl- channels. J. Clin. Invest. *120*, 1240–1252.

Liu, C.Y., Fraser, S.E., and Koos, D.S. (2009). Grueneberg ganglion olfactory subsystem employs a cGMP signaling pathway. J. Comp. Neurol. *516*, 36–48.

Lledo, P.-M., Gheusi, G., and Vincent, J.-D. (2005). Information Processing in the Mammalian Olfactory System. Physiol. Rev. *85*, 281–317.

Lock, S.P., Smith, R.S., and Hardisty, R.M. (1961). Stomatocytosis: a hereditary red cell anomally associated with haemolytic anaemia. Br. J. Haematol. *7*, 303–314.

Lowe, G., and Gold, G.H. (1993). Contribution of the ciliary cyclic nucleotide-gated conductance to olfactory transduction in the salamander. J. Physiol. *462*, 175–196.

Lu, D.C., Zhang, H., Zador, Z., and Verkman, A.S. (2008). Impaired olfaction in mice lacking aquaporin-4 water channels. FASEB J. Off. Publ. Fed. Am. Soc. Exp. Biol. *22*, 3216–3223.

Lucero, M.T. (2013). Peripheral modulation of smell: Fact or fiction? Semin. Cell Dev. Biol. *24*, 58–70.

Lynch, J.W., and Barry, P.H. (1989). Action potentials initiated by single channels opening in a small neuron (rat olfactory receptor). Biophys. J. *55*, 755–768.

Lynch, J.W., and Barry, P.H. (1991). Properties of transient K+ currents and underlying single K+ channels in rat olfactory receptor neurons. J. Gen. Physiol. *97*, 1043–1072.

Mackay-Sim, A., John, J.S., and Schwob, J.E. (2015). Neurogenesis in the Adult Olfactory Epithelium. In Handbook of Olfaction and Gustation, (John Wiley & Sons, Ltd), pp. 133–156.

Mairhofer, M., Steiner, M., Salzer, U., and Prohaska, R. (2009). Stomatin-like protein-1 interacts with stomatin and is targeted to late endosomes. J. Biol. Chem. *284*, 29218–29229.

Manglapus, G.L., Youngentob, S.L., and Schwob, J.E. (2004). Expression patterns of basic helix-loop-helix transcription factors define subsets of olfactory progenitor cells. J. Comp. Neurol. *479*, 216–233.

Mannsfeldt, A.G., Carroll, P., Stucky, C.L., and Lewin, G.R. (1999). Stomatin, a MEC-2 like protein, is expressed by mammalian sensory neurons. Mol. Cell. Neurosci. *13*, 391–404.

Manoury, B., Tamuleviciute, A., and Tammaro, P. (2010). TMEM16A/Anoctamin 1 protein mediates calcium-activated chloride currents in pulmonary arterial smooth muscle cells. J. Physiol. *588*, 2305–2314.

Marconi, C., Brunamonti Binello, P., Badiali, G., Caci, E., Cusano, R., Garibaldi, J., Pippucci, T., Merlini, A., Marchetti, C., Rhoden, K.J., et al. (2013). A novel missense mutation in ANO5/TMEM16E is causative for gnathodiaphyseal dyplasia in a large Italian pedigree. Eur. J. Hum. Genet. EJHG *21*, 613–619.

Marinosci, A., Landis, B.N., and Calmy, A. (2020). Possible link between anosmia and COVID-19: sniffing out the truth. Eur. Arch. Otorhinolaryngol. 1–2.

Martinez, A.D., Hayrapetyan, V., Moreno, A.P., and Beyer, E.C. (2002). Connexin43 and connexin45 form heteromeric gap junction channels in which individual components determine permeability and regulation. Circ. Res. *90*, 1100–1107.

Martinez-Salgado, C., Benckendorff, A.G., Chiang, L.-Y., Wang, R., Milenkovic, N., Wetzel, C., Hu, J., Stucky, C.L., Parra, M.G., Mohandas, N., et al. (2007). Stomatin and Sensory Neuron Mechanotransduction. J. Neurophysiol. *98*, 3802–3808.

Mason, R.J. (2020). Pathogenesis of COVID-19 from a cell biologic perspective. Eur. Respir. J.

Masukawa, L.M., Kauer, J.S., and Shepherd, G.M. (1983). Intracellular recordings from two cell types in an in vitro preparation of the salamander olfactory epithelium. Neurosci. Lett. *35*, 59–64.

Masukawa, L.M., Hedlund, B., and Shepherd, G.M. (1985). Electrophysiological properties of identified cells in the in vitro olfactory epithelium of the tiger salamander. J. Neurosci. *5*, 128–135.

Maue, R.A., and Dionne, V.E. (1987). Patch-clamp studies of isolated mouse olfactory receptor neurons. J. Gen. Physiol. *90*, 95–125.

Maurya, D.K., and Menini, A. (2014). Developmental expression of the calcium-activated chloride channels TMEM16A and TMEM16B in the mouse olfactory epithelium. Dev. Neurobiol. *74*, 657–675.

Maurya, D.K., Henriques, T., Marini, M., Pedemonte, N., Galietta, L.J.V., Rock, J.R., Harfe, B.D., and Menini, A. (2015). Development of the Olfactory Epithelium and Nasal Glands in TMEM16A-/- and TMEM16A+/+ Mice. PloS One *10*, e0129171.

Mayer, M.L. (1985). A calcium-activated chloride current generates the after-depolarization of rat sensory neurones in culture. J. Physiol. *364*, 217–239.

Menco, B.Ph.M. (1980). Qualitative and quantitative freeze-fracture studies on olfactory and nasal respiratory structures of frog, ox, rat, and dog. Cell Tissue Res. *207*, 183–209.

Menco, B.P., and Farbman, A.I. (1985). Genesis of cilia and microvilli of rat nasal epithelia during pre-natal development. I. Olfactory epithelium, qualitative studies. J. Cell Sci. *78*, 283–310.

Menco, B.P., and Farbman, A.I. (1992). Ultrastructural evidence for multiple mucous domains in frog olfactory epithelium. Cell Tissue Res. *270*, 47–56.

Menco, B.Ph.M., and Jackson, J.E. (1997). Cells resembling hair cells in developing rat olfactory and nasal respiratory epithelia. Tissue Cell *29*, 707–713.

Menco, B.P.M., and Morrison, E.E. (2003). Morphology of the Mammalian Olfactory Epithelium: Form, Fine Structure, Function, and Pathology. 17–49.

Menco, B.P., Birrell, G.B., Fuller, C.M., Ezeh, P.I., Keeton, D.A., and Benos, D.J. (1998). Ultrastructural localization of amiloride-sensitive sodium channels and Na+,K(+)-ATPase in the rat's olfactory epithelial surface. Chem. Senses *23*, 137–149.

Menini, A., Lagostena, L., and Boccaccio, A. (2004). Olfaction: From Odorant Molecules to the Olfactory Cortex. Physiology *19*, 101–104.

Mery, S., Gross, E.A., Joyner, D.R., Godo, M., and Morgan, K.T. (1994). Nasal Diagrams: A Tool for Recording the Distribution of Nasal Lesions in Rats and Mice: Toxicol. Pathol.

Miledi, R. (1982). A calcium-dependent transient outward current in Xenopus laevis oocytes. Proc. R. Soc. Lond. B Biol. Sci. *215*, 491–497.

Milenkovic, V.M., Brockmann, M., Stöhr, H., Weber, B.H., and Strauss, O. (2010). Evolution and functional divergence of the anoctamin family of membrane proteins. BMC Evol. Biol. *10*, 319.

Mills, R.P., and Christmas, H.E. (1990). Applied comparative anatomy of the nasal turbinates. Clin. Otolaryngol. Allied Sci. *15*, 553–558.

Miragall, F., Hwang, T.-K., Traub, O., Hertzberg, E.L., and Dermietzel, R. (1992). Expression of connexins in the developing olfactory system of the mouse. J. Comp. Neurol. *325*, 359–378.

Mombaerts, P. (1999). Seven-Transmembrane Proteins as Odorant and Chemosensory Receptors. Science *286*, 707–711.

Mombaerts, P. (2004). Genes and ligands for odorant, vomeronasal and taste receptors. Nat. Rev. Neurosci. *5*, 263–278.

Montel-Hagen, A., Kinet, S., Manel, N., Mongellaz, C., Prohaska, R., Battini, J.-L., Delaunay, J., Sitbon, M., and Taylor, N. (2008). Erythrocyte Glut1 triggers dehydroascorbic acid uptake in mammals unable to synthesize vitamin C. Cell *132*, 1039–1048.

Moran, D.T., Rowley, J.C., Jafek, B.W., and Lovell, M.A. (1982). The fine structure of the olfactory mucosa in man. J. Neurocytol. *11*, 721–746.

Morgan, K.T., Jiang, X.Z., Patterson, D.L., and Gross, E.A. (1984). The nasal mucociliary apparatus. Correlation of structure and function in the rat. Am. Rev. Respir. Dis. *130*, 275–281.

Mori, K., Campenhausen, H. von, and Yoshihara, Y. (2000). Zonal organization of the mammalian main and accessory olfactory systems. Philos. Trans. R. Soc. Lond. B. Biol. Sci. *355*, 1801–1812.

Morrison, E.E., and Costanzo, R.M. (1990). Morphology of the human olfactory epithelium. J. Comp. Neurol. *297*, 1–13.

Morrow, I.C., and Parton, R.G. (2005). Flotillins and the PHB domain protein family: rafts, worms and anaesthetics. Traffic Cph. Den. *6*, 725–740.

Murrell, W., Bushell, G.R., Livesey, J., McGrath, J., MacDonald, K.P., Bates, P.R., and Mackay-Sim, A. (1996). Neurogenesis in adult human. Neuroreport *7*, 1189–1194.

Nakamura, T., and Gold, G.H. (1987). A cyclic nucleotide-gated conductance in olfactory receptor cilia. Nature *325*, 442–444.

Neureither, F., Stowasser, N., Frings, S., and Möhrlen, F. (2017). Tracking of unfamiliar odors is facilitated by signal amplification through anoctamin 2 chloride channels in mouse olfactory receptor neurons. Physiol. Rep. *5*.

Newman, M.P., Féron, F., and Mackay-Sim, A. (2000). Growth factor regulation of neurogenesis in adult olfactory epithelium. Neuroscience *99*, 343–350.

Ogura, T., Szebenyi, S.A., Krosnowski, K., Sathyanesan, A., Jackson, J., and Lin, W. (2011). Cholinergic microvillous cells in the mouse main olfactory epithelium and effect of acetylcholine on olfactory sensory neurons and supporting cells. J. Neurophysiol. *106*, 1274–1287.

Ohloff, G. (1994). Scent and fragrances: the fascination of odors and their chemical perspectives (Springer-Verlag).

Okada, Y., Fujiyama, R., Miyamoto, T., and Sato, T. (2000). Comparison of a Ca(2+)-gated conductance and a second-messenger-gated conductance in rat olfactory neurons. J. Exp. Biol. *203*, 567–573.

Okano, M., and Takagi, S.F. (1974). Secretion and electrogenesis of the supporting cell in the olfactory epithelium. J. Physiol. *242*, 353–370.

Otowa, T., Yoshida, E., Sugaya, N., Yasuda, S., Nishimura, Y., Inoue, K., Tochigi, M., Umekage, T., Miyagawa, T., Nishida, N., et al. (2009). Genome-wide association study of panic disorder in the Japanese population. J. Hum. Genet. *54*, 122–126.

Parma, V., Ohla, K., Veldhuizen, M.G., Niv, M.Y., Kelly, C.E., Bakke, A.J., Cooper, K.W., Bouysset, C., Pirastu, N., Dibattista, M., et al. (2020). More Than Smell—COVID-19 Is Associated With Severe Impairment of Smell, Taste, and Chemesthesis. Chem. Senses *45*, 609–622.

Paulino, C., Kalienkova, V., Lam, A.K.M., Neldner, Y., and Dutzler, R. (2017a). Activation mechanism of the calcium-activated chloride channel TMEM16A revealed by cryo-EM. Nature *552*, 421–425.

Paulino, C., Neldner, Y., Lam, A.K., Kalienkova, V., Brunner, J.D., Schenck, S., and Dutzler, R. (2017b). Structural basis for anion conduction in the calcium-activated chloride channel TMEM16A. ELife *6*.

Pedemonte, N., and Galietta, L.J.V. (2014). Structure and Function of TMEM16 Proteins (Anoctamins). Physiol. Rev. *94*, 419–459.

Peters, C.J., Gilchrist, J.M., Tien, J., Bethel, N.P., Qi, L., Chen, T., Wang, L., Jan, Y.N., Grabe, M., and Jan, L.Y. (2018). The Sixth Transmembrane Segment Is a Major Gating Component of the TMEM16A Calcium-Activated Chloride Channel. Neuron *97*, 1063-1077.e4.

Pietra, G., Dibattista, M., Menini, A., Reisert, J., and Boccaccio, A. (2016). The Ca2+-activated Cl- channel TMEM16B regulates action potential firing and axonal targeting in olfactory sensory neurons. J. Gen. Physiol. *148*, 293–311.

Pifferi, S., and Menini, A. (2015). The Olfactory System: From Odorant Molecules to Perception. In Aromatherapy: Basic Mechanisms and Evidence Based Clinical Use, G. Bagetta, M. Cosentino, and T. Sakurada, eds. (CRC Press), pp. 17–42.

Pifferi, S., Boccaccio, A., and Menini, A. (2006). Cyclic nucleotide-gated ion channels in sensory transduction. FEBS Lett. *580*, 2853–2859.

Pifferi, S., Dibattista, M., and Menini, A. (2009). TMEM16B induces chloride currents activated by calcium in mammalian cells. Pflüg. Arch. Eur. J. Physiol. *458*, 1023–1038.

Pifferi, S., Menini, A., and Kurahashi, T. (2010). Signal Transduction in Vertebrate Olfactory Cilia. In The Neurobiology of Olfaction, A. Menini, ed. (Boca Raton (FL): CRC Press/Taylor & Francis), pp. 203–223.

Pifferi, S., Cenedese, V., and Menini, A. (2012). Anoctamin 2/TMEM16B: a calcium-activated chloride channel in olfactory transduction. Exp. Physiol. *97*, 193–199.

Price, J.L. (1973). An autoradiographic study of complementary laminar patterns of termination of afferent fibers to the olfactory cortex. J. Comp. Neurol. *150*, 87–108.

Price, M.P., Thompson, R.J., Eshcol, J.O., Wemmie, J.A., and Benson, C.J. (2004). Stomatin modulates gating of acid-sensing ion channels. J. Biol. Chem. *279*, 53886–53891.

Pun, R.Y.K., and Kleene, S.J. (2004). An estimate of the resting membrane resistance of frog olfactory receptor neurones. J. Physiol. *559*, 535–542.

Pusch, M., and Neher, E. (1988). Rates of diffusional exchange between small cells and a measuring patch pipette. Pflüg. Arch. *411*, 204–211.

Qi, Y., Andolfi, L., Frattini, F., Mayer, F., Lazzarino, M., and Hu, J. (2015). Membrane stiffening by STOML3 facilitates mechanosensation in sensory neurons. Nat. Commun. *6*, 8512.

Rafols, J.A., and Getchell, T.V. (1983). Morphological relations between the receptor neurons, sustentacular cells and Schwann cells in the olfactory mucosa of the salamander. Anat. Rec. *206*, 87–101.

Rasche, S., Toetter, B., Adler, J., Tschapek, A., Doerner, J.F., Kurtenbach, S., Hatt, H., Meyer, H., Warscheid, B., and Neuhaus, E.M. (2010). Tmem16b is specifically expressed in the cilia of olfactory sensory neurons. Chem. Senses *35*, 239–245.

Reese, T.S. (1965). OLFACTORY CILIA IN THE FROG. J. Cell Biol. *25*, 209–230.

Reifschneider, N.H., Goto, S., Nakamoto, H., Takahashi, R., Sugawa, M., Dencher, N.A., and Krause, F. (2006). Defining the Mitochondrial Proteomes from Five Rat Organs in a Physiologically Significant Context Using 2D Blue-Native/SDS-PAGE. J. Proteome Res. *5*, 1117–1132.

Reisert, J. (2010). Origin of basal activity in mammalian olfactory receptor neurons. J. Gen. Physiol. *136*, 529–540.

Reisert, J., and Reingruber, J. (2019). Ca2+-activated Cl- current ensures robust and reliable signal amplification in vertebrate olfactory receptor neurons. Proc. Natl. Acad. Sci. U. S. A. *116*, 1053–1058.

Reisert, J., and Zhao, H. (2011). Response kinetics of olfactory receptor neurons and the implications in olfactory coding. J. Gen. Physiol. *138*, 303–310.

Reisert, J., Bauer, P.J., Yau, K.-W., and Frings, S. (2003). The Ca-activated Cl Channel and its Control in Rat Olfactory Receptor Neurons. J. Gen. Physiol. *122*, 349–364.

Reisert, J., Lai, J., Yau, K.-W., and Bradley, J. (2005). Mechanism of the Excitatory Cl− Response in Mouse Olfactory Receptor Neurons. Neuron *45*, 553–561.

Reisert, J., Yau, K.-W., and Margolis, F.L. (2007). Olfactory marker protein modulates the cAMP kinetics of the odour-induced response in cilia of mouse olfactory receptor neurons. J. Physiol. *585*, 731–740.

Ressler, K.J., Sullivan, S.L., and Buck, L.B. (1993). A zonal organization of odorant receptor gene expression in the olfactory epithelium. Cell *73*, 597–609.

Reuter, D., Zierold, K., Schröder, W.H., and Frings, S. (1998). A depolarizing chloride current contributes to chemoelectrical transduction in olfactory sensory neurons in situ. J. Neurosci. Off. J. Soc. Neurosci. *18*, 6623–6630.

Reznik, G.K. (1990). Comparative Anatomy, Physiology, and Function of the Upper Respiratory Tract. Environ. Health Perspect. *85*, 171–176.

Rivera-Milla, E., Stuermer, C. a. O., and Málaga-Trillo, E. (2006). Ancient origin of reggie (flotillin), reggie-like, and other lipid-raft proteins: convergent evolution of the SPFH domain. Cell. Mol. Life Sci. CMLS *63*, 343–357.

Rock, J.R., Futtner, C.R., and Harfe, B.D. (2008). The transmembrane protein TMEM16A is required for normal development of the murine trachea. Dev. Biol. *321*, 141–149.

Roselli, S., Heidet, L., Sich, M., Henger, A., Kretzler, M., Gubler, M.-C., and Antignac, C. (2004). Early glomerular filtration defect and severe renal disease in podocin-deficient mice. Mol. Cell. Biol. *24*, 550–560.

Rubin, D., and Ismail-Beigi, F. (2003). Distribution of Glut1 in detergent-resistant membranes (DRMs) and non-DRM domains: effect of treatment with azide. Am. J. Physiol. Cell Physiol. *285*, C377-383.

Ruiz, C., Martins, J.R., Rudin, F., Schneider, S., Dietsche, T., Fischer, C.A., Tornillo, L., Terracciano, L.M., Schreiber, R., Bubendorf, L., et al. (2012). Enhanced expression of ANO1 in head and neck squamous cell carcinoma causes cell migration and correlates with poor prognosis. PloS One *7*, e43265.

Sagheddu, C., Boccaccio, A., Dibattista, M., Montani, G., Tirindelli, R., and Menini, A. (2010). Calcium concentration jumps reveal dynamic ion selectivity of calcium-activated chloride currents in mouse olfactory sensory neurons and TMEM16b-transfected HEK 293T cells. J. Physiol. *588*, 4189–4204.

Saleem, M.A., Ni, L., Witherden, I., Tryggvason, K., Ruotsalainen, V., Mundel, P., and Mathieson, P.W. (2002). Co-Localization of Nephrin, Podocin, and the Actin Cytoskeleton. Am. J. Pathol. *161*, 1459–1466.

Salzer, U., and Prohaska, R. (2001). Stomatin, flotillin-1, and flotillin-2 are major integral proteins of erythrocyte lipid rafts. Blood *97*, 1141–1143.

Salzer, U., Ahorn, H., and Prohaska, R. (1993). Identification of the phosphorylation site on human erythrocyte band 7 integral membrane protein: implications for a monotopic protein structure. Biochim. Biophys. Acta *1151*, 149–152.

Salzer, U., Mairhofer, M., and Prohaska, R. (2007). Stomatin: A new paradigm of membrane organization emerges. Dyn. Cell Biol. *1*, 20–33.

Saraiva, L.R., Ibarra-Soria, X., Khan, M., Omura, M., Scialdone, A., Mombaerts, P., Marioni, J.C., and Logan, D.W. (2015). Hierarchical deconstruction of mouse olfactory sensory neurons: from whole mucosa to single-cell RNA-seq. Sci. Rep. *5*, 18178.

Scemes, E., and Giaume, C. (2006). Astrocyte calcium waves: what they are and what they do. Glia *54*, 716–725.

Schild, D. (1989). Whole-cell currents in olfactory receptor cells of Xenopus laevis. Exp. Brain Res. *78*, 223–232.

Schild, D., and Restrepo, D. (1998). Transduction Mechanisms in Vertebrate Olfactory Receptor Cells. Physiol. Rev. *78*, 429–466.

Schild, D., Jung, A., and Schultens, H.A. (1994). Localization of calcium entry through calcium channels in olfactory receptor neurones using a laser scanning microscope and the calcium indicator dyes Fluo-3 and Fura-Red. Cell Calcium *15*, 341–348.

Schlosser, G. (2006). Induction and specification of cranial placodes. Dev. Biol. *294*, 303–351.

Schmitt, S., Prokisch, H., Schlunck, T., Camp, D.G., Ahting, U., Waizenegger, T., Scharfe, C., Meitinger, T., Imhof, A., Neupert, W., et al. (2006). Proteome analysis of mitochondrial outer membrane from Neurospora crassa. Proteomics *6*, 72–80.

Schneppenheim, R., Castaman, G., Federici, A.B., Kreuz, W., Marschalek, R., Oldenburg, J., Oyen, F., and Budde, U. (2007). A common 253-kb deletion involving VWF and TMEM16B in German and Italian patients with severe von Willebrand disease type 3. J. Thromb. Haemost. JTH *5*, 722–728.

Schreiber, R., Uliyakina, I., Kongsuphol, P., Warth, R., Mirza, M., Martins, J.R., and Kunzelmann, K. (2010). Expression and function of epithelial anoctamins. J. Biol. Chem. *285*, 7838–7845.

Schreiber, R., Faria, D., Skryabin, B.V., Wanitchakool, P., Rock, J.R., and Kunzelmann, K. (2015). Anoctamins support calcium-dependent chloride secretion by facilitating calcium signaling in adult mouse intestine. Pflugers Arch. *467*, 1203–1213.

Schreiber, S., Fleischer, J., Breer, H., and Boekhoff, I. (2000). A Possible Role for Caveolin as a Signaling Organizer in Olfactory Sensory Membranes. J. Biol. Chem. *275*, 24115–24123.

Schroeder, B.C., Cheng, T., Jan, Y.N., and Jan, L.Y. (2008). Expression cloning of TMEM16A as a calcium-activated chloride channel subunit. Cell *134*, 1019–1029.

Scott, J.W., McBride, R.L., and Schneider, S.P. (1980). The organization of projections from the olfactory bulb to the piriform cortex and olfactory tubercle in the rat. J. Comp. Neurol. *194*, 519–534.

Sedensky, M.M., Siefker, J.M., Koh, J.Y., Miller, D.M., and Morgan, P.G. (2004). A stomatin and a degenerin interact in lipid rafts of the nervous system of Caenorhabditis elegans. Am. J. Physiol.-Cell Physiol. *287*, C468–C474.

Sepahi, A., Kraus, A., Casadei, E., Johnston, C.A., Galindo-Villegas, J., Kelly, C., García-Moreno, D., Muñoz, P., Mulero, V., Huertas, M., et al. (2019). Olfactory sensory neurons mediate ultrarapid antiviral immune responses in a TrkA-dependent manner. Proc. Natl. Acad. Sci. U. S. A. *116*, 12428–12436.

Sheridan, J.T., Worthington, E.N., Yu, K., Gabriel, S.E., Hartzell, H.C., and Tarran, R. (2011). Characterization of the oligomeric structure of the Ca(2+)-activated Cl- channel Ano1/TMEM16A. J. Biol. Chem. *286*, 1381–1388.

Shono, A., Tsukaguchi, H., Yaoita, E., Nameta, M., Kurihara, H., Qin, X.-S., Yamamoto, T., and Doi, T. (2007). Podocin Participates in the Assembly of Tight Junctions between Foot Processes in Nephrotic Podocytes. J. Am. Soc. Nephrol. *18*, 2525–2533.

Smith, R.L., Baker, H., Kolstad, K., Spencer, D.D., and Greer, C.A. (1991). Localization of tyrosine hydroxylase and olfactory marker protein immunoreactivities in the human and macaque olfactory bulb. Brain Res. *548*, 140–148.

Snyers, L., Thinès-Sempoux, D., and Prohaska, R. (1997). Colocalization of stomatin (band 7.2b) and actin microfilaments in UAC epithelial cells. Eur. J. Cell Biol. *73*, 281–285.

Snyers, L., Umlauf, E., and Prohaska, R. (1998). Oligomeric nature of the integral membrane protein stomatin. J. Biol. Chem. *273*, 17221–17226.

Snyers, L., Umlauf, E., and Prohaska, R. (1999). Association of stomatin with lipid-protein complexes in the plasma membrane and the endocytic compartment. Eur. J. Cell Biol. *78*, 802–812.

Song, Y., Cygnar, K.D., Sagdullaev, B., Valley, M., Hirsh, S., Stephan, A., Reisert, J., and Zhao, H. (2008). Olfactory CNG channel desensitization by Ca2+/CaM via the B1b subunit affects response termination but not sensitivity to recurring stimulation. Neuron *58*, 374–386.

Sorokin, S., and Weiss, L. (1988). Cell and tissue biology. Textb. Histol. 211–254.

Spassova, M.A., Hewavitharana, T., Xu, W., Soboloff, J., and Gill, D.L. (2006). A common mechanism underlies stretch activation and receptor activation of TRPC6 channels. Proc. Natl. Acad. Sci. *103*, 16586–16591.

Stephan, A.B., Shum, E.Y., Hirsh, S., Cygnar, K.D., Reisert, J., and Zhao, H. (2009). ANO2 is the cilial calcium-activated chloride channel that may mediate olfactory amplification. Proc. Natl. Acad. Sci. U. S. A. *106*, 11776–11781.

Stephan, A.B., Tobochnik, S., Dibattista, M., Wall, C.M., Reisert, J., and Zhao, H. (2012). The Na + /Ca 2+ exchanger NCKX4 governs termination and adaptation of the mammalian olfactory response. Nat. Neurosci. *15*, 131–137.

Stewart, G.W., Hepworth-Jones, B.E., Keen, J.N., Dash, B.C., Argent, A.C., and Casimir, C.M. (1992). Isolation of cDNA coding for an ubiquitous membrane protein deficient in high Na+, low K+ stomatocytic erythrocytes. Blood *79*, 1593–1601.

Stewart, G.W., Argent, A.C., and Dash, B.C.J. (1993). Stomatin: a putative cation transport regulator in the red cell membrane. Biochim. Biophys. Acta BBA - Mol. Basis Dis. *1225*, 15–25.

Stöhr, H., Heisig, J.B., Benz, P.M., Schöberl, S., Milenkovic, V.M., Strauss, O., Aartsen, W.M., Wijnholds, J., Weber, B.H.F., and Schulz, H.L. (2009). TMEM16B, a novel protein with calcium-dependent chloride channel activity, associates with a presynaptic protein complex in photoreceptor terminals. J. Neurosci. Off. J. Soc. Neurosci. *29*, 6809–6818.

Storan, M.J., and Key, B. (2006). Septal organ of Grüneberg is part of the olfactory system. J. Comp. Neurol. *494*, 834–844.

Sun, H., Xia, Y., Paudel, O., Yang, X.-R., and Sham, J.S.K. (2012). Chronic hypoxia-induced upregulation of Ca2+-activated Cl- channel in pulmonary arterial myocytes: a mechanism contributing to enhanced vasoreactivity. J. Physiol. *590*, 3507–3521.

Suzuki, J., Umeda, M., Sims, P.J., and Nagata, S. (2010). Calcium-dependent phospholipid scrambling by TMEM16F. Nature *468*, 834–838.

Suzuki, Y., Takeda, M., and Farbman, A.I. (1996). Supporting cells as phagocytes in the olfactory epithelium after bulbectomy. J. Comp. Neurol. *376*, 509–517.

Ta, C.M., Acheson, K.E., Rorsman, N.J.G., Jongkind, R.C., and Tammaro, P. (2017). Contrasting effects of phosphatidylinositol 4,5-bisphosphate on cloned TMEM16A and TMEM16B channels. Br. J. Pharmacol. *174*, 2984–2999.

Tavernarakis, N., Driscoll, M., and Kyrpides, N.C. (1999). The SPFH domain: implicated in regulating targeted protein turnover in stomatins and other membrane-associated proteins. Trends Biochem. Sci. *24*, 425–427.

Tembo, M., and Carlson, A.E. (2018). PIP2 and CA2+ are Both Required to Open TMEM16a Channels in Xenopus Laevis Oocytes. Biophys. J. *114*, 610a.

Terashima, H., Picollo, A., and Accardi, A. (2013). Purified TMEM16A is sufficient to form Ca2+-activated Cl-channels. Proc. Natl. Acad. Sci. U. S. A. *110*, 19354–19359.

Theiler, K. (1972). The house mouse. Development and normal stages from fertilization to 4 weeks of age. House Mouse Dev. Norm. Stages Fertil. 4 Weeks Age.

Tien, J., Lee, H.Y., Minor, D.L., Jan, Y.N., and Jan, L.Y. (2013). Identification of a dimerization domain in the TMEM16A calcium-activated chloride channel (CaCC). Proc. Natl. Acad. Sci. U. S. A. *110*, 6352–6357.

Tondera, D., Grandemange, S., Jourdain, A., Karbowski, M., Mattenberger, Y., Herzig, S., Da Cruz, S., Clerc, P., Raschke, I., Merkwirth, C., et al. (2009). SLP-2 is required for stress-induced mitochondrial hyperfusion. EMBO J. *28*, 1589–1600.

Treloar, H.B., Miller, A.M., Ray, A., and Greer, C.A. (2010). Development of the Olfactory System. In The Neurobiology of Olfaction, A. Menini, ed. (Boca Raton (FL): CRC Press/Taylor & Francis), pp. 130–157.

Trotier, D. (1998). Electrophysiological Properties of Frog Olfactory Supporting Cells. Chem. Senses *23*, 363–369.

Trotier, D., and MacLeod, P. (1986). Intracellular recordings from salamander olfactory supporting cells. Brain Res. *374*, 205–211.

Trudeau, M.C., and Zagotta, W.N. (2003). Calcium/Calmodulin Modulation of Olfactory and Rod Cyclic Nucleotide-gated Ion Channels. J. Biol. Chem. *278*, 18705–18708.

Tsukaguchi, H., Sudhakar, A., Le, T.C., Nguyen, T., Yao, J., Schwimmer, J.A., Schachter, A.D., Poch, E., Abreu, P.F., Appel, G.B., et al. (2002). NPHS2 mutations in late-onset focal segmental glomerulosclerosis: R229Q is a common disease-associated allele. J. Clin. Invest. *110*, 1659–1666.

Unfried, I., Entler, B., and Prohaska, R. (1995). The organization of the gene (EPB72) encoding the human erythrocyte band 7 integral membrane protein (protein 7.2b). Genomics *30*, 521–528.

Uraih, L.C., and Maronpot, R.R. (1990). Normal Histology of the Nasal Cavity and Application of Special Techniques. Environ. Health Perspect. *85*, 187–208.

Vaira, L.A., Deiana, G., Fois, A.G., Pirina, P., Madeddu, G., De Vito, A., Babudieri, S., Petrocelli, M., Serra, A., Bussu, F., et al. (2020). Objective evaluation of anosmia and ageusia in COVID-19 patients: Single-center experience on 72 cases. Head Neck.

Verkhratsky, A., and Kettenmann, H. (1996). Calcium signalling in glial cells. Trends Neurosci. *19*, 346–352.

Vogalis, F., Hegg, C.C., and Lucero, M.T. (2005a). Ionic conductances in sustentacular cells of the mouse olfactory epithelium. J. Physiol. *562*, 785–799.

Vogalis, F., Hegg, C.C., and Lucero, M.T. (2005b). Electrical coupling in sustentacular cells of the mouse olfactory epithelium. J. Neurophysiol. *94*, 1001–1012.

Vollrath, M., Altmannsberger, M., Weber, K., and Osborn, M. (1985). An ultrastructural and immunohistological study of the rat olfactory epithelium: Unique properties of olfactory sensory cells. Differentiation *29*, 243–253.

Wang, Y., and Morrow, J.S. (2000). Identification and Characterization of Human SLP-2, a Novel Homologue of Stomatin (Band 7.2b) Present in Erythrocytes and Other Tissues. J. Biol. Chem. *275*, 8062–8071.

Wang, Y.-X., and Kotlikoff, M.I. (1997). Inactivation of calcium-activated chloride channels in smooth muscle by calcium/calmodulin-dependent protein kinase. Proc. Natl. Acad. Sci. *94*, 14918–14923.

Wang, M., Yang, H., Zheng, L.-Y., Zhang, Z., Tang, Y.-B., Wang, G.-L., Du, Y.-H., Lv, X.-F., Liu, J., Zhou, J.-G., et al. (2012). Downregulation of TMEM16A calcium-activated chloride channel contributes to cerebrovascular remodeling during hypertension by promoting basilar smooth muscle cell proliferation. Circulation *125*, 697–707.

Wemmie, J.A., Price, M.P., and Welsh, M.J. (2006). Acid-sensing ion channels: advances, questions and therapeutic opportunities. Trends Neurosci. *29*, 578–586.

West, R.B., Corless, C.L., Chen, X., Rubin, B.P., Subramanian, S., Montgomery, K., Zhu, S., Ball, C.A., Nielsen, T.O., Patel, R., et al. (2004). The novel marker, DOG1, is expressed ubiquitously in gastrointestinal stromal tumors irrespective of KIT or PDGFRA mutation status. Am. J. Pathol. *165*, 107–113.

Wetzel, C., Hu, J., Riethmacher, D., Benckendorff, A., Harder, L., Eilers, A., Moshourab, R., Kozlenkov, A., Labuz, D., Caspani, O., et al. (2007). A stomatin-domain protein essential for touch sensation in the mouse. Nature *445*, 206–209.

Whisman, M.L., Goetzinger, J.W., Cotton, F.O., and Brinkman, D.W. (1978). Odorant evaluation: a study of ethanethiol and tetrahydrothiophene as warning agents in propane. Environ. Sci. Technol. *12*, 1285–1288.

Whitlock, J.M., and Hartzell, H.C. (2017). Anoctamins/TMEM16 Proteins: Chloride Channels Flirting with Lipids and Extracellular Vesicles. Annu. Rev. Physiol. *79*, 119–143.

Wilson, D.A. (2009). Olfactory Cortex Physiology. In Encyclopedia of Neuroscience, L.R. Squire, ed. (Oxford: Academic Press), pp. 95–100.

Wolozin, B., Sunderland, T., Zheng, B.B., Resau, J., Dufy, B., Barker, J., Swerdlow, R., and Coon, H. (1992). Continuous culture of neuronal cells from adult human olfactory epithelium. J. Mol. Neurosci. MN *3*, 137–146.

Wysocki, C.J. (1979). Neurobehavioral evidence for the involvement of the vomeronasal system in mammalian reproduction. Neurosci. Biobehav. Rev. *3*, 301–341.

Xiao, Q., Yu, K., Perez-Cornejo, P., Cui, Y., Arreola, J., and Hartzell, H.C. (2011). Voltage- and calcium-dependent gating of TMEM16A/Ano1 chloride channels are physically coupled by the first intracellular loop. Proc. Natl. Acad. Sci. U. S. A. *108*, 8891–8896.

Xydakis, M.S., Dehgani-Mobaraki, P., Holbrook, E.H., Geisthoff, U.W., Bauer, C., Hautefort, C., Herman, P., Manley, G.T., Lyon, D.M., and Hopkins, C. (2020). Smell and taste dysfunction in patients with COVID-19. Lancet Infect. Dis.

Yan, C., Zhao, A.Z., Bentley, J.K., Loughney, K., Ferguson, K., and Beavo, J.A. (1995). Molecular cloning and characterization of a calmodulin-dependent phosphodiesterase enriched in olfactory sensory neurons. Proc. Natl. Acad. Sci. U. S. A. *92*, 9677–9681.

Yan, C.H., Faraji, F., Prajapati, D.P., Boone, C.E., and DeConde, A.S. (2020). Association of chemosensory dysfunction and Covid-19 in patients presenting with influenza-like symptoms. Int. Forum Allergy Rhinol.

Yang, Y.D., Cho, H., Koo, J.Y., Tak, M.H., Cho, Y., Shim, W.-S., Park, S.P., Lee, J., Lee, B., Kim, B.-M., et al. (2008). TMEM16A confers receptor-activated calcium-dependent chloride conductance. Nature *455*, 1210–1215.

Yokoyama, H., Fujii, S., and Matsui, I. (2008). Crystal structure of a core domain of stomatin from Pyrococcus horikoshii Illustrates a novel trimeric and coiled-coil fold. J. Mol. Biol. *376*, 868–878.

Yu, K., Jiang, T., Cui, Y., Tajkhorshid, E., and Hartzell, H.C. (2019). A Network of Phosphatidylinositol 4,5-bisphosphate Binding Sites Regulate Gating of the Ca2+-activated Cl− Channel ANO1 (TMEM16A). BioRxiv 625897.

Zak, J.D., Grimaud, J., Li, R.-C., Lin, C.-C., and Murthy, V.N. (2018). Calcium-activated chloride channels clamp odor-evoked spike activity in olfactory receptor neurons. Sci. Rep. *8*, 10600.

Zamparo, I., Francia, S., Franchi, S.A., Redolfi, N., Costanzi, E., Kerstens, A., Fukutani, Y., Battistutta, R., Polverino de Laureto, P., Munck, S., et al. (2019). Axonal Odorant Receptors Mediate Axon Targeting. Cell Rep. *29*, 4334-4348.e7.

Zhang, C., and Restrepo, D. (2002). Expression of connexin 45 in the olfactory system. Brain Res. *929*, 37–47.

Zhang, X., and Firestein, S. (2002). The olfactory receptor gene superfamily of the mouse. Nat. Neurosci. *5*, 124–133.

Zhang, J.Z., Abbud, W., Prohaska, R., and Ismail-Beigi, F. (2001). Overexpression of stomatin depresses GLUT-1 glucose transporter activity. Am. J. Physiol. Cell Physiol. *280*, C1277-1283.

Zhang, L., Ding, F., Cao, W., Liu, Z., Liu, W., Yu, Z., Wu, Y., Li, W., Li, Y., and Liu, Z. (2006). Stomatin-like Protein 2 Is Overexpressed in Cancer and Involved in Regulating Cell Growth and Cell Adhesion in Human Esophageal Squamous Cell Carcinoma. Clin. Cancer Res. *12*, 1639–1646.

Zhang, Y., Zhang, Z., Xiao, S., Tien, J., Le, S., Le, T., Jan, L.Y., and Yang, H. (2017). Inferior Olivary TMEM16B Mediates Cerebellar Motor Learning. Neuron *95*, 1103-1111.e4.

Zheng, J. (2020). SARS-CoV-2: an Emerging Coronavirus that Causes a Global Threat. Int. J. Biol. Sci. *16*, 1678–1685.

Zheng, J., and Zagotta, W.N. (2004). Stoichiometry and assembly of olfactory cyclic nucleotide-gated channels. Neuron *42*, 411–421.

Zhou, P., Yang, X.-L., Wang, X.-G., Hu, B., Zhang, L., Zhang, W., Si, H.-R., Zhu, Y., Li, B., Huang, C.-L., et al. (2020). A pneumonia outbreak associated with a new coronavirus of probable bat origin. Nature *579*, 270–273.

Zhu, Y., Paszty, C., Turetsky, T., Tsai, S., Kuypers, F.A., Lee, G., Cooper, P., Gallagher, P.G., Stevens, M.E., Rubin, E., et al. (1999). Stomatocytosis is absent in "stomatin"-deficient murine red blood cells. Blood *93*, 2404–2410.

Ziegler, C.G.K., Allon, S.J., Nyquist, S.K., Mbano, I.M., Miao, V.N., Tzouanas, C.N., Cao, Y., Yousif, A.S., Bals, J., Hauser, B.M., et al. (2020). SARS-CoV-2 receptor ACE2 is an interferon-stimulated gene in human airway epithelial cells and is detected in specific cell subsets across tissues. Cell.

Zufall, F., Shepherd, G.M., and Firestein, S. (1991). Inhibition of the olfactory cyclic nucleotide gated ion channel by intracellular calcium. Proc. R. Soc. Lond. B Biol. Sci. *246*, 225–230.

Zufall, F., Firestein, S., and Shepherd, G.M. (1994). Cyclic Nucleotide-Gated Ion Channels and Sensory Transduction in Olfactory Receptor Neurons. Annu. Rev. Biophys. Biomol. Struct. *23*, 577–607.